Alma Mater Studiorum – Università di Bologna

DOTTORATO DI RICERCA IN

FISICA

Ciclo 33

Settore Concorsuale: 02/B1 – FISICA SPERIMENTALE DELLA MATERIA

Settore Scientifico Disciplinare: FIS/03 – FISICA DELLA MATERIA

Novel Semiconducting Materials and Thin Film Technologies for High Energy Radiation Detection

Presentata da: Ilaria Fratelli

Coordinatore Dottorato
Prof. Michele Cicoli

Supervisore
Prof. Beatrice Fraboni

Co-supervisore
Dr. Laura Basiricò

Esame finale anno 2021

Abstract

Nowadays the development of real-time ionizing radiation detection system operating over large areas is crucial. Despite the excellent detecting performance exhibited by inorganic semiconductors (e.g. a-Se, CZT…) as direct solid state detectors, the increasing quest for flexible, portable, low cost and low power consumption sensors pushed the scientific community to look for alternative materials and technologies able to fulfill these new requirements. In this thesis the potentiality of organic semiconductors and metal oxides as material platforms for novel ionizing radiation sensors is demonstrated. In particular, organic semiconductors are human tissue-equivalent in terms of radiation absorption and this represents a unique and desirable property for the development of dosimeters to be employed in the medical field. The ionizing radiation sensors described in this thesis have been designed, fabricated and characterized during my PhD research and are realized onto thin polymeric foils leading to flexible devices operating at low voltages, in ambient condition and able to directly detect X-rays, gamma-rays and protons. Following the study of the properties and of the mechanisms of interaction between the ionizing radiation and the active layers of the sensors, several strategies have been put in place in order to enhance the efficiency of these novel radiation detectors. Innovative real-time X-rays dosimeters based on organic semiconductors have been realized presenting record sensitivity values compared with the state of the art for large area radiation detection. The unprecedentedly reported performance led to the possibility to testing these devices in actual medical (dental radiography) environments. Moreover, the proof-of-principle demonstration of a real-time dosimetric detection of high energy proton beam (5Mev and 70MeV) by organic-based sensors is reported. Finally, a new sensing platform based on metal oxides is introduced. Combining the advantages of amorphous high mobility oxide semiconductors with a novel stacked multilayer dielectric, new devices have been designed, capable of providing a sensitivity one order of magnitude higher than the one shown by the standard CMOS RADFETs. Thanks to their unique properties, these sensors have been integrated with a wireless readout system based on a commercial RFID tag and its assessment is presented.

Contents

List of Acronyms

AFM – Atomic Force Microscopy

AMA – Active Matrix Array

AMLCD – Active Matrix Liquid Crystal Display

AO – Atomic Orbital

AOS – Amorphous Oxide Semiconductor

BAMS – Bar Assisted Meniscus Shearing

BGBC – Bottom-Gate Bottom-Contacts

BGTC – Bottom-Gate Top-Contacts

CCE – Charge Collection Efficiency

CMOS – Complementary Metal-Oxide Semiconductor

CVD – Chemical Vapor Deposition

diF-TEG-ADT – 5,11-bis(triethylgermylethynyl)anthra- dithiophene

diF-TES-ADT – 2,8-difluoro-5,11-bis(triethylsilylethynyl)anthradithiophene

E_G – Energy Gap

FPXI – Flat Panel X-ray Imager

G – Gain factor

HMOS – High Mobility Oxide Semiconductors

HOMO – Highest Occupied Molecular Orbital

IC – Integrated Circuit

INAF – Istituto Nazionale di Astrofisica

IRCP – International Commission on Radiological Protection

IUPAC – International Union of Pure and Applied Chemestry

KERMA – Kinetic Energy released per unit Mass in matter

L – Length

LABEC – Laboratory of Nuclear techniques for Environment and Cultural Heritage

LCAO – Linear Combination of Atomic Orbitals

LET – Linear Transfer Energy

LINAC – Linear particle accelerator

LOD – Limit of Detection

LUMO – Lowest Unoccupied Molecular Orbital

MO – Molecular Orbitals

MOSFET – Metal-Oxide-Semiconductor Field Effect Transistor

OFET – Organic Field Effect Transistor

OSC – Organic Semiconductor

PC – Photocurrent Spectroscopy

PECVD- Plasma- enhanced chemical vapor deposition

PEN – Polyethylene naphthalate

PET – Polyethylene

PFBT – Pentafluorobenzenethiolo

PG – Photoconductive Gain

PS – Polystyrene

PVD – Physical Vapor Deposition

QE – Quantum Efficiency (QE_E – external, QE_I - internal)

RADFET - radiation-sensitive Field Effect Transistor

RF – Radio-frequency

RFID – Radio-frequency identification

RMS – Root Mean Square

RT – Room Temperature

SAC – Solvent-Assisted Crystallization

SAM – Self Assembled Monolayer

SNR – Signal to Noise Ratio

SRIM – Stopping and Range of Ions in Matter

τ_t – Transit Time

τ_r – Recombination Time

TFT – Thin Film Transistor

TGBC – Top-Gate Bottom-Contacts

TGTC – Top-Gate Top-Contacts

TIFPA – Trento Institute for Fundamental Physics and Applications

TIPGe-Pn – triisopropyl- germanylethynylpentacene

TIPS-Pn – 6,13-bis(triisopropylsilylethynyl)pentacene

UV – ultraviolet

VAC – Vibration-Assisted Crystallization

V_{th} – Threshold Voltage

W – Width

$W_{\pm}$ – Electron-Hole Pair Generation Energy

Z – atomic number

Introduction

The detection of ionizing radiation is a crucial task in several fields of human society. In many applications, novel requirements are emerging such as mechanical flexibility and conformability, portability, ease of fabrication processes, stability in ambient conditions and low production cost. For these reasons, in the last decades several efforts have been done by the scientific community to find new materials, processes and technologies able to fulfill these novel emerging necessities. The development of flexible and large area electronics offered new opportunities for the implementation of innovative radiation sensors. The active materials used for such devices are processable by low-cost fabrication techniques at low temperatures, leading to the possibility to deposit them onto polymeric and flexible foils and to scale up the devices onto large areas.

In this thesis I focused my research on the study of two classes of materials that possess the above described features and that can be implemented as active layer in high-energy radiation sensors. In particular, I investigated organic small-molecules semiconductors and metal oxides thin films employed to fabricate large-area and flexible detectors. These two material platforms demonstrated to be promising candidates to overcome the main limitations imposed by the existing solid-state sensors based on bulky and rigid inorganic materials. They offered the chance to develop conformable and large area sensing platforms formed by thin film-based devices able to detect X-rays, gamma-rays, and protons.

In the first chapter, a general introduction to flexible and large area electronics is given with a particular focus on the employment of organic semiconductors and

metal oxide semiconducting materials. Their charge transport mechanisms and the main deposition techniques implemented for the fabrication of thin film transistors are discussed, together with their operation characteristics and non-idealities.

The second chapter is dedicated to ionizing radiation detectors. After a first brief summary about ionizing radiation sources, the main mechanisms of interaction with matter and the definition of important physical quantities adopted in this field, ionizing radiation detectors based on semiconducting materials are introduced. The figures of merit employed to describe the capability of detection are listed together with the main architectures employed to realize this class of sensors and a critical comparative discussion of the advantages and disadvantages. This chapter illustrates the state of the art regarding flexible and large area direct ionizing radiation detectors focusing both on organic semiconductor based and on metal oxide-based devices. Finally, the state of the art for proton detection is presented.

The materials and experimental tools used for the devices under study are described in chapter three. Besides, the main fabrication techniques employed for the realization of these sensors are shown.

Chapter four is dedicated to the experimental results achieved by the ionizing radiation detectors fabricated in this research work, based on organic semiconductors. A deep study regarding the mechanism of detection occurring in these sensors is illustrated and several strategies adopted in order to tune the sensing capability are proved. The assessment of the detection performances of this class of devices for X-ray medical applications (dental radiography) is reported. Finally, the results achieved by organic semiconductor-based devices for the detection of proton beams is discussed.

The ionizing radiation detection performance of high mobility metal oxide semiconductor-based devices are described in chapter five and the proof of concept for the detection of gamma-rays is also reported. Here the implementation of a wireless readout system based on a CMOS RFID (Radio-frequency identification) tag is demonstrated.

This study has been carried out at the Department of Physics and Astronomy of the University of Bologna, Italy, in close cooperation with several international research groups. In particular, I collaborated with Prof. J. E. Anthony from the *University of Kentucky (U.S.A)*, Dr. M. Mas Torrent's group at *Institut de Ciència de Materials de Barcelona* (Spain) and Prof. P. Baquinha's group at *Faculdade de Ciências e Tecnologia, Universidade Nova de Lisboa* (Portugal). I performed some measurements at the *Compagnia Elettronica Italiana* (Bologna, Italy) using irradiating setups employed in the field of dental radiography and commercialized by *Skanray Europe srl* and *Skan-X Radiology Devices S.p.A,* and also at the *LABEC* (Laboratory of Nuclear techniques for Environment and Cultural Heritage, INFN Firenze, Italy) and *TIFPA* Proton Therapy Center (Trento, Italy). Finally, part of this work has been conducted during my exchange semester spent at the *Columbia University* (New York City, USA) hosted by Prof. I. Kymissis' research group.

1.

Flexible and large area electronics: organic and high-mobility oxide semiconductors

In this first chapter, an introduction about flexible and large area electronics is given. At the beginning, a brief history of flexible electronics is presented. The core of the chapter is focused on the description of two classes of materials: organic semiconductors and amorphous oxide semiconductors. Finally, the main applications of flexible and large-area electronics are summarized with a particular attention on thin film transistors.

1.1. Brief history of flexible electronics

Flexible and large-area electronics has been deeply investigated in the last decades by the scientific community and industry. These studies aim to the development of new technologies able to fulfill new devices' requirements for several applications such as the low cost of fabrication, the portability and conformability, the

lightweight, the robustness and the scalability onto large areas. Even if the push in this field has been particularly emerged in the last years, the beginning of this story dates back to the 1960s [1].

The main driving force at that time was the solar industry and the need to produce solar cells able to lower the cost of photovoltaic energy. The first tentative was made by thinning a crystal silicon wafer but soon the researchers moved their efforts on a new material processable at low temperature and thus compatible with plastic and flexible substrates: the hydrogenated amorphous silicon (a-Si:H). In the 1980s the first cells based on a-Si:H were produced [2] [3] and the era of flexible and large-area electronics started. A second context in which the flexibility and large-area were ambitious and appealing properties was the displays market. In the 1980s, the active-matrix liquid-crystal display (AMLCD) industry started in Japan by adopting the same fabrication techniques used for the flexible solar cells. Here in fact, a-Si:H was implemented as the active material of the transistor (thin film transistors – TFTs) constituting the active backplane of the displays. From that moment, the research on flexible electronics has rapidly expanded and many research groups and companies have developed flexible displays on plastic foil substrates.

From the beginning, the development of this new branch of electronics has covered several topics of the research: from the materials, process to the systems and applications. As a matter of fact, the choice of the materials is for sure the heart of this technology. In fact, in order to directly pattern the electronic system onto a flexible foil, materials compatible with low temperature processes must be chosen. In particular, physical vapor deposition or solution-based printing technique are the two options which allow the development of a flexible system.

In fact, even if some examples are reported in literature, the use of a-Si:H and polycrystalline-Si [4] [5] directly printed on polymeric substrates is still limited because of the need of high temperature processing. On the contrary, other materials don't present this necessity and they have been largely employed for the development of large-area and flexible electronics such as organic materials and metal oxides. Important to notice is the fact that, hybrid solution-processable materials have recently received a lot of interest, with the aim to combine the best features of different materials, such as mechanical flexibility and processability of polymers, with high performance of 1D or 2D structures (e.g. graphene [6], carbon nano-tubes (CNTs) [7], [8]). Notably, a new emerging class of solution-processable materials, called hybrid metal-organic perovskites, has opened up vast opportunities for low-temperature fabrication of efficient flexible solar cells [9] and solution-processable optoelectronic devices and sensors [10]. The studies concerning the mechanical flexibility of this novel class of materials started some years ago in the field of solar cells and involved other applications only more recently. In particular, still few works demonstrating the development flexible radiation sensors based on halide-perovskites are reported in literature and deeper investigations are ongoing [11]–[14].

1.2. Materials for flexible electronics

As it has just been shown in the previous section, several materials have been employed in order to develop flexible and large-area devices. All these classes of

materials share an important property: the possibility to process them at low temperature and deposit them directly onto large-area polymeric foils.

In particular, in the next sections two of these materials which are fully compatible with circuit fabrication on foil will be introduced: the organic semiconductors (OSCs) and the amorphous oxide semiconductors (AOSs). In fact, in the recent years both these two types of semiconductor families have reached a transport performance level superior to amorphous silicon, which has long been the technology benchmark for flexible electronics [15]. (***Table 1.1***)

	a – Si	*poly - Si*	*AOS*	*OSC*
Mobility (cm^2 V^{-1} s^{-1})	<1	50-100	1-50	<10
Channel polarity	n	n and p	N	n and p
Reliability	moderate	high	High	moderate/high
Process Temperature (°C)	250-350	<500	RT - 250	RT - 100
Flexibility ε_{max} (%)	0.2 – 0.4	0.1 – 0.5	0.7	1 – 2

Table 1.1 *Comparison of key performance parameters of organic and high mobility amorphous oxide semiconductors with benchmark technologies. Adapted from* [15]

1.2.1. Organic semiconductors

Organic semiconductors (OSs) are carbon-based materials. For this reason, to understand the properties of organic compounds it is important to see the electronic structure of the carbon atom and the possible bonds that it can form. Carbon is a IV group material and so it has four electrons in the outer energy level (i.e. it can form four bonds with other atoms). In particular, the IUPAC electron configuration of Carbon is $1s^2 2s^2 2p^2$. An important property of the carbon atom is that it can

hybridize in several forms. The concept of hybridization was introduced by Linus Pauling in 1931 and it describes the linear combination between different atomic orbitals. VESPR theory indicates that carbon can form three different kinds of hybrid orbitals named *sp*, sp^2 and sp^3. These represent the combination of *s* and *p* orbitals. Let's consider as an example the sp^2 hybridization shown in **Figure 1.1a**. In this case, the *2s* orbital combines with two of the *2p* orbitals (e.g. $2p_x$ and $2p_y$) forming three hybrid sp^2 orbitals which lie in the XY plane. The fourth unhybridized orbital (in this case $2p_z$) places orthogonal to the XY plane as depicted in **Figure 1.1b**. If we consider now two sp^2-hybridised carbon atoms coming into close contact, they can form two different kinds of chemical bonds. On one hand, the overlap between two sp^2 orbitals leads to a covalent bond called *σ-bond* formed along the line joining the two carbon atoms' nuclei. On the other hand, the partial overlap between the two unhybridized $2p_z$ orbitals forms another type of covalent bond called *π-bond* (see **Figure 1.1c**). Energetically speaking, the much larger overlap between the two sp^2 orbitals if compared with the two unhybridized $2p_z$ orbitals leads to a difference in strength between these two: the *σ-bond* is a stronger bond that the *π-bond.* This aspect has very important consequences for the electrical behavior of the organic molecules: in *σ-bond*, the involved electrons (*σ-electrons*) are too localized to be free to move while the electrons involved in *π-bond* (*π-electrons*) are much more delocalized. As a result, the *σ-electrons* forms the skeleton of the molecules while the *π-electrons* are free to move across the molecule and they contribute to the electrical properties of the material.

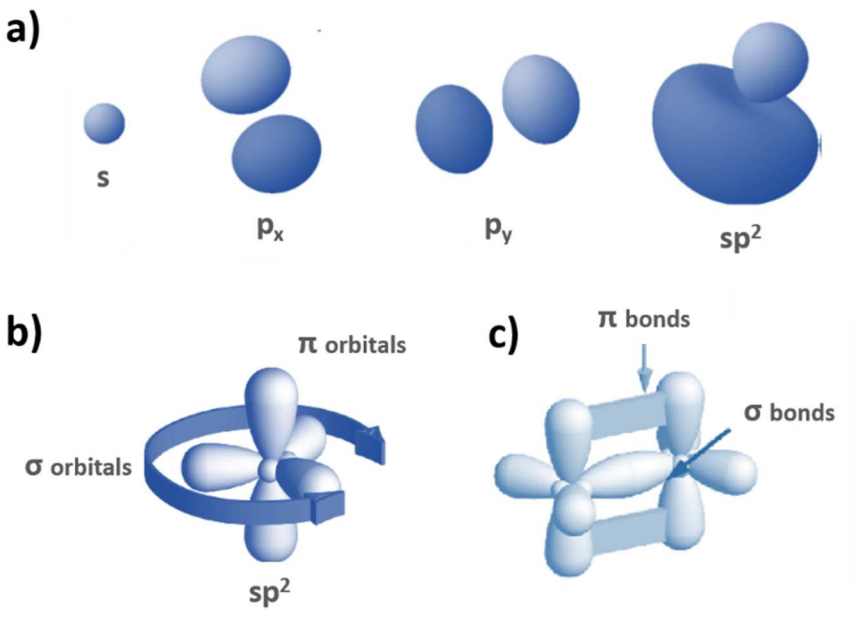

Figure 1.1 *a) electron density probability surfaces for the constituent components of the sp^2 hybridization. b) Schematically show the geometry of the sp2 orbital structures. c) Two sp2 bonded carbon atoms. Adapted from* [16]

Typically, the organic semiconductors are formed by a repetition of conjugated units in which single and double *π-bond* alternate. Depending on the length of the π-conjugated systems (i.e. the number of conjugated units) one can distinguish small molecules and polymers (**Figure 1.2**). The organic small molecules are compounds with a well-defined molecular weight while polymers are long-chain molecules consisting of an indeterminate number of molecular repeat units. Despite this, these compounds share more similarities than differences especially in terms of both optical and electrical properties [17][18].

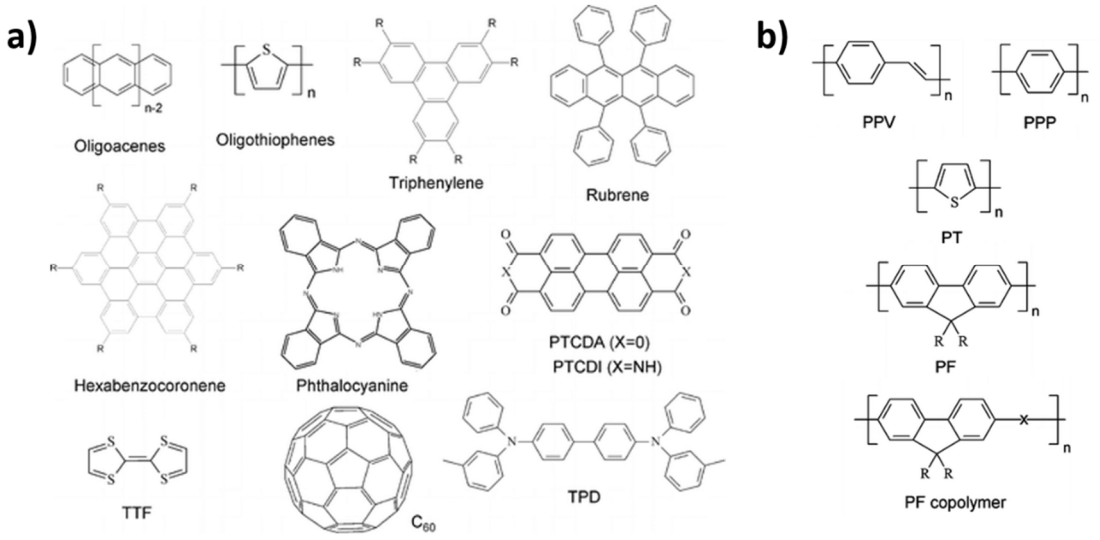

Figure 1.2 *Chemical structure of the most studied (a) Organic Small Molecules and (b) polymers semiconductor. Adapted from* [19].

A quantitative description of the energetic structure of the organic semiconductors can be provided by the theory of Molecular Orbitals (MOs) [20]. According to this theory, the orbitals of a complex molecule can be described as a linear combination of the atomic orbitals (AOs) corresponding to the single constituents. This approach is known as LCAO (Linear Combination of Atomic Orbitals) and it provides the mathematical calculations regarding the energetic structure of molecular systems. This method identifies two categories of energy levels: the bonding (π) and the anti-bonding (π^*) which together form a band-like structure. In particular, the occupied π levels form the HOMO (*Highest Occupied Molecular Orbital*) and the unoccupied π^* form the LUMO (*Lowest Unoccupied Molecular Orbital*). These represent respectively the outer shell occupied by electrons (the analogue of the valence band) and the lowest energy level unoccupied (the correspondent to the conduction band). The energy difference between the HOMO

and LUMO represents the energy gap (E_G) of the semiconductor. It has been proved that in conjugated molecules, for longer chain the energy gap results lower.

In order to describe the charge transport in organic semiconductors, one should note that while in the inorganic semiconductors the atoms are bonded with covalent bonds, the organic molecules aggregate in a solid through the weak Van der Waals interaction. Such a weak intermolecular force lowers the conductivity of the organic semiconductors and determine the need of new models able to describe the charge transport within these solids.

1.2.1.1. Charge transport in organic small molecules semiconductors

As it has been introduced in the previous section, while the charge transport in inorganic semiconductors occurs through delocalized states and can be described by a band transport, in organic semiconductors the molecular units are connected by weak Van der Waals interactions and the transport occurs between localized states. The transport, in this latter case, depends on the overlap between the π orbitals and for this reason it is deeply related to the structural characteristic of the organic film. Depending on the degree of order of the organic system the charge transport can be described by the band theory (for the organic single crystals i.e. long-range ordered systems) or by the hopping model (for the amorphous or poly-crystalline systems).

Even if a complete knowledge is still lacking, several models have been introduced in the last decades in order to describe the charge transport in amorphous or

disordered materials and some reviews described them in details [19], [21]–[26]. Here the most used models will be illustrated.

Hopping Transport

The hopping model was firstly introduced by Mott [27] and Conwell [28] and later it was revisited by Mills and Abrahams [29]. This model assesses that while in an ordered system, the electrons are free to move along delocalized states, in disordered or amorphous solids the charges move hopping between localized states. To determine which is the best model to describe a system, one must observe how the electrical mobility varies with the temperature. In fact, in the band-like model the increase of temperature leads to an increase in the scattering occurring between the charges and the phonon and consequently it leads to a drop of the mobility ($\mu \propto T^{-n}\,; 0 < n < 3$) (**Figure 1.3**).

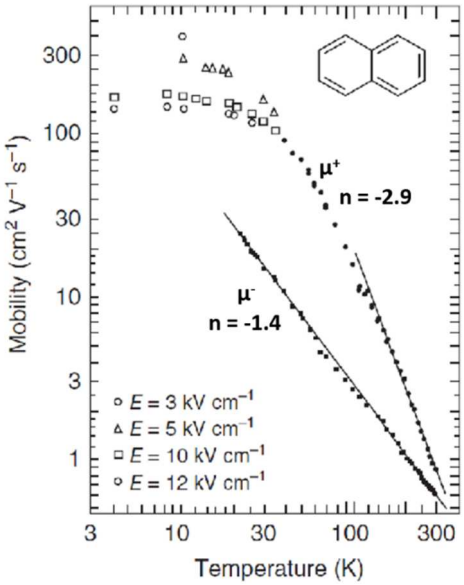

Figure 1.3 *Hole and electron mobility in ultrapure naphtalene organic single crystal as a function of Temperature. The trend of the curves ($\mu \propto T^{-n}$) is a proof of a band-like transport in organic ordered systems. Adapted from* [30].

On the opposite side, the hopping mechanism is thermally assisted and therefore the mobility increases with temperature. In particular, in the hopping model the mobility is proportional to the transition rate between two different states W_{ij} (e.g. from i to j) which is defined by the Mills-Abrahams expression (Eq. 1.1).

$$W_{ij} = \upsilon_0 \, exp\left(-2\gamma\left|R_{ij}\right|\right)\begin{cases} exp\left(-\dfrac{\varepsilon_j - \varepsilon_i}{K_B T}\right) & \forall\ \varepsilon_j > \varepsilon_i \\ 1 & else \end{cases} \qquad (1.1)$$

where υ_0 is the phonon vibration frequency, γ^{-1} is the wavefunctions overlap between the two states R_{ij} is the distance between the two states and ε_i and ε_j are the energy respectively of the initial and final states.

Small Polaron model

To identify the nature of the localized states in organic materials, Holstein introduced in 1959 the theory of the Small Polaron [31]. When a charge flows across the conjugate chain of an organic materials, because of its long-range interaction it polarizes and deforms the molecular system itself. The result of this deformation is called polaron and it provokes the self-trapping of the charges responsible of the effect.

The Holstein model is a one-dimension, one-electron model in which the total energy of the system can be obtained by the sum of three terms. The lattice energy E_L is given by the sum of N harmonic oscillators that vibrate at the frequency ω_0 (Eq. 1.2):

$$E_L = \sum_{n=1}^{N} \frac{1}{2M}\left(\frac{\hbar}{i}\frac{\partial}{\partial u_n}\right)^2 + \frac{1}{2} M \omega_0^2 u_n^2 \qquad (1.2)$$

where u_n is the displacement of the nth molecule from its equilibrium position and M is the reduced mass of the nth molecular site.

The energy of the electrons is calculated in the tight binding approximation and it assumes that the potential at each chain site affects only the nearest neighbor (Eq. 1.3 where J is the electron transfer energy and a is the lattice constant). And finally, the electrons-lattice coupling is expressed in Eq.1.4 where A is a constant.

$$E_k = E_0 - 2J\cos(ka) \tag{1.3}$$

$$\varepsilon_n = -Au_n \tag{1.4}$$

An important parameter in this model is the polaron binding energy E_B which is defined as $E_B = A^2/2M\omega_0^2$ and indicates the energy gain of an infinitely slow carrier due to the polarization of the lattice. Then the mobility (Eq. 1.5) of the small polaron is determined by solving the time-dependent Schrödinger equation [23].

$$\mu = \sqrt{\frac{\pi}{2}}\frac{ea^2}{\hbar}\frac{J^2}{\sqrt{E_B}}(K_BT)^{-3/2}exp\left(-\frac{E_B}{2K_BT}\right) \tag{1.5}$$

Multiple Trapping and Release

The *Multiple Trapping and Release* is a model able to describe the charge transport in polycrystalline semiconductors [32], [33]. In this kind of materials, crystalline regions form domains which are divided each other by amorphous grain boundaries. While within the same microcrystal the transport occurs across delocalized states and can be described by the band-like model, when the charges reach the grain boundaries they are trapped, and the electrical mobility drops down.

Depending on the dimension on the grains, Horowitz et al. proposed a step forward in this model [34]. The polycrystalline system can be illustrated as many resistors (i.e. the single grains and the grain boundaries) connected in series. According to this point, the mobility can be expressed as:

$$\frac{1}{\mu} = \frac{1}{\mu_G} + \frac{1}{\mu_B} \tag{1.6}$$

where μ_G and μ_B are the mobilities respectively within the grains and at the grain boundaries.

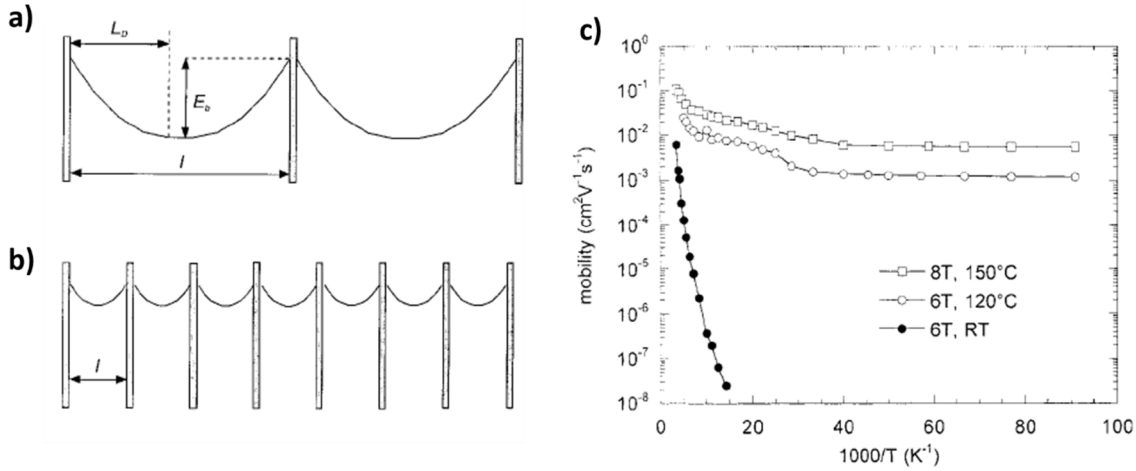

Figure 1.4 *Energy scheme of a polycrystalline materials in two extreme cases: (a) when the grain size (l) is higher than the Debye Length (big grains) and (b) when l<L_D. (c) Arrhenius plot of the mobility as a function of the temperature for sexithiophene (6T) and octothiophene (8T) based thin film devices. The samples deposited at higher T, present bigger grains while the one fabricated at room temperature (RT) is formed by small crystalline grains.* [34]

Depending on the dimensions of the grains (l) with respect to the Debye Length (L_D) one can distinguish two different regimes:

1. When $l > 2L_D$ (**Figure 1.4a**): the traps are located only at the grain boundaries and the mobility is expressed by the Eq. 1.7.

$$\mu = \mu_B = \frac{q\bar{v}l}{8K_BT} exp\left(-\frac{E_B}{K_BT}\right) \tag{1.7}$$

   where q is the electrical charge, $\bar{v}$ is the mean velocity of the charge and E_B is the height of the energy barrier induced by the trapped charges at the grain boundaries. In this case the mobility is linearly proportional to the dimensions

of the grains. Moreover, for low temperature, the transport is dominated by the tunneling of the charges across the energy barriers and the mobility results independent from the temperature (see **Figure 1.4c**);

2. When $l < L_D$ (**Figure 1.4b**): the traps at the grain boundaries can be thought as uniformly distributed and the mobility can be described by the Eq.1.8.

$$\mu \propto \mu_0 \, exp\left(-\frac{E_B}{K_B T}\right) \tag{1.8}$$

where μ_0 is the mobility within the grain. In this case, the transport can be considered as thermal activated and the mobility increases with the temperature. In particular, the energy barrier induced by the trapped charges at the grain boundaries (E_B) can be estimated looking at the mobility as a function of the temperature (**Figure 1.4c**).

1.2.1.2. Deposition techniques

Organic semiconductors can be deposited either from the vapor or solution phase, depending on their vapor pressure and solubility. Depending on the technique of deposition, it is possible to obtain different morphologies and molecular structures which, as it has been illustrated in the previous sections, can strongly influence the transport properties of the materials.

Although the pioneering studies on organic semiconducting materials have been conducted on organic single crystals deposited by vapor phase [35], for the development of flexible and large-area electronics looking at devices based on organic thin films deposited by solution technique is more suitable. In fact, solution

growth allows to obtain uniform and large area films at low temperature (i.e. making possible to fabricate devices onto polymeric foils) leading to scalable and flexible technologies at low cost of production. Moreover, even if the good performance in terms of transport properties have been reached thanks to evaporated semiconductors, the great progresses regarding the deposition methods achieved in the past decades, lead to an incredible improvement of the devices fabricated by solution [36]–[40].

Many reviews have been published in the last years in order to illustrate all the fabrication processes exploited for the fabrication of organic devices and to figure out some strategies in order to optimize and control the film growth [35], [41]–[43]. Here the most used technique of deposition by solution developed in the last decades are summarized (see **Figure 1.5**).

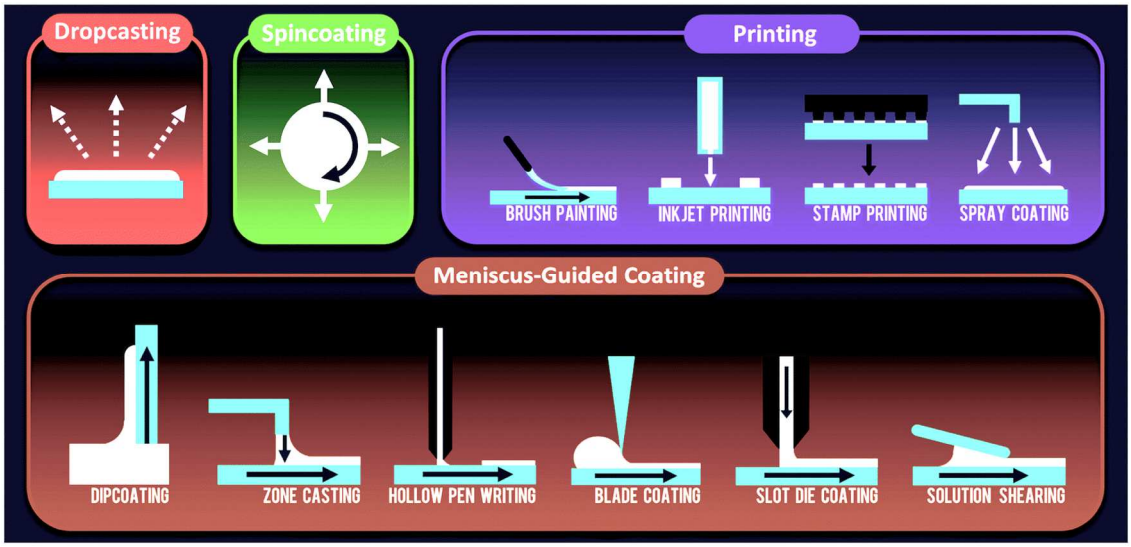

Figure 1.5 *A schematic summary of the most used deposition technique by solution.* [35]

Drop casting

Drop casting is the simplest technique of deposition by solution. It consists in dropping the solution (i.e. the organic semiconductor dissolved in an appropriate solvent) directly onto the substrate. The spontaneous evaporation of the solvent leaves behind individual crystals or thin films. In the last years, some modifications to the standard technique have been proposed in order to optimize the crystallization of the organic semiconductor. For instance, with the *Vibration-Assisted-Crystallization* (VAC), applying to the substrate a controlled gentle vibration lets the molecules acquire sufficient energy in order to pass from a metastable state to a minimum potential energy configuration with the highest degree of order [44]. Moreover, by the *Solvent-Assisted-Crystallization* (SAC) [45] or by surface treatments [46] it is possible to slow down the evaporation rate of the solvent improving the crystallization of the semiconducting film.

Spin coating

Spin coating is the most used technique to deposit organic semiconductors by solution in research laboratories. The organic solution is deposited onto the substrate which is rotated at high speed (>1000 rpm). The centripetal acceleration induces the uniform spread of the solution over the substrate and the evaporation of the solvent left the organic semiconducting film. The properties of the film (e.g. thickness, uniformity, film microstructures...) depend on several parameters such as the spinning velocity and acceleration, the concentration of the solute in the solution, the nature of the solvent. Even in this case, modification of the standard spin coating technique leaded optimized film in terms of transport and morphological properties. Yuan et al. [47] developed an off-centered spinning technique in which the substrate is placed apart from the rotational center.

Therefore, the solution is no longer spread radially but aligned in a specific direction.

Meniscus-guided technique

Many solution-based deposition techniques use the linear translation of either the substrate or the coating tool to induce aligned crystallite growth in the deposited thin films. These methods involve the evolution of a solution meniscus, which induces the solvent evaporation. Indeed, the solution concentrates with the removal of solvent, and once the point of supersaturation is reached, the solute precipitates and is deposited as thin film. Due to the linear motion of the solution with respect to the substrate, in many of these techniques the alignment of the microstructure in the organic thin film is achieved. Several parameters can influence the film crystallization (e.g. the velocity and the temperature of deposition [48]) and depending on the tool used for the shearing it is possible to identify many different techniques.

Dip-coating consists in the immersion of the substrate in the organic solution and the following withdrawal of the sample at controlled velocity. Depending on the evaporation rate of the solvent and on the velocity of the substrate, different thicknesses and crystalline packings are achievable. [49]

Blade coating is the most popular meniscus-guided technique. Depending on the shape of the tool used to spread the solution on the substrate, it is possible to distinguish several methods such as doctor blading, bar coating… Passing on the top of a reservoir of organic solution, the spreading element (i.e. the bar, the blade, the knife…) leaves a wet thin film on the top of the substrate which crystalize after the evaporation of the solvent. The velocity and the temperature of deposition are, also in this case, the key parameters to tune the properties of the organic thin film.

Blading is one of the most scalable deposition technique and it has been adapted to roll-to-roll process [50]. A particular blading developed by Marta Mas Torrent et al. [51], [52] is called Bar Assisted Meniscus Shearing (BAMS) and it demonstrated to offer optimal performance organic thin films formed by small molecules semiconductors blended with polymers.

Printing technique

Printing techniques allow to deposit organic thin films spatially confined making possible a direct pattern of the semiconducting layer.

Inkjet printing is the most famous printing technique for organic electronics. This consists in the jetting of the organic ink in the form of small droplets thanks to a piezoelectric or thermal process. The key parameters of this deposition technique are related to the ink-substrate interaction: the surface energy of the substrate and the viscosity of the solution. A promising optimization of this technique has been developed by Kymissis et al. [53] and it is called Pneumatic Nozzle Printing. This is a combination between a inkjet printing and a meniscus guided technique in which the solution is printed by a nozzle placed very close to the surface in order to create a meniscus. Thanks to this method it is possible to obtain a patterned organic thin film which present ultra-aligned microcrystallites.

Spray Coating is another example of printing technique based on the ejection from a nozzle of small droplets aerosolized by an inert carrier gas. The aerosolized particles then hit the substrate and dry rapidly, forming homogeneous films. Several parameters can influence the properties of the films such as the pressure of the inert gas, the shape and dimension of the nozzle, the concentration of the solution and the duration time of deposition. Also this technique is easily scalable and high-quality thin films have been produced onto large-area substrates [54].

1.2.1.3. Charge carrier traps in Organic Semiconductors

As it has been introduced in the previous sections, the weak intermolecular interactions in organic semiconductors (i.e. Van der Waals forces) make them very susceptible to defect formation, resulting in localized states in the band-gap that can trap charge carriers [55]. Indeed, charge carrier traps influence the transport mechanism of organic semiconductors and they can deeply affect the electrical and optoelectronic properties of the devices based on this class of materials.

An electronic trap is an imperfection in the semiconductor that creates localized states laying within the energy band gap of the semiconductor. Depending on the distance from the band edges in terms of energy, one can distinguish shallow traps (i.e. the ones placed few K_BT far from the HOMO/LUMO edge) and deep traps (i.e. the traps placed several K_BT away from the HOMO/LUMO edge). As depicted in **Figure 1.6**, the shallow traps can be activated by thermal effect and they play and important role in the mechanism of transport in the semiconductor. On the opposite side, the deep traps can't be thermally excited, and they often act as recombination centers.

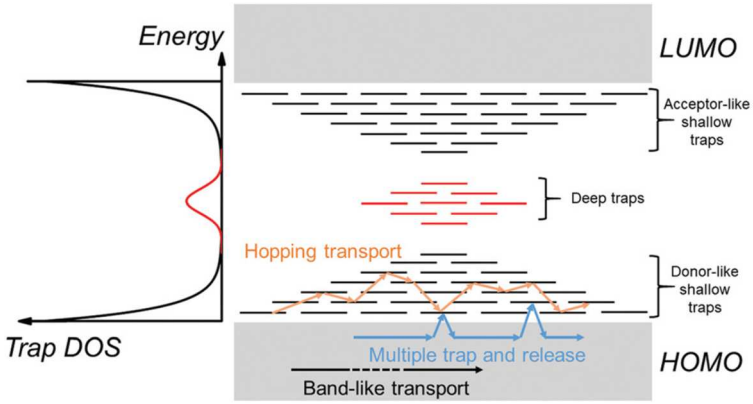

Figure 1.6 *Trap Density Of State (left) and schematic and spatial diagram of shallow and deep traps in organic semiconductors* [55].

In this section the possible sources of traps in organic semiconductors are summarized and it is discussed how they can affect the transport properties in these materials. Moreover, a deepening on their effects on the electrical parameters of a specific electronic device (i.e. thin film transistor) is presented in **Section 1.3.1.1**.

Sources of traps in organic semiconductors

The sources of electron traps in organic semiconductors can be divided in intrinsic and extrinsic ones. In fact, while the disorder can be considered an intrinsic source, on the opposite side dopants, interfacial, environmental, and bias stress effects are considered extrinsic sources.

Disorder

The disorder can be dynamic or static. The dynamic disorder is caused by thermal motions of the molecules and it is time dependent involving the entire molecular system. On the other side, static disorder is caused by structural defects or by chemical impurities, it is time-independent and it involves only the location where the defects are present. Both induce localized tail states in the band gap.

In particular, structural defects are mainly related to the growth of the organic semiconductors (i.e. the growth rate, method of fabrication) and they are present both in organic single crystals and in thin films. The spatial deviation from the crystal lattice order induces a variation in the local electronic polarization energies for the charge carriers in the vicinity of such defects causing the formation of localized trapping states. As far as the organic poly-crystalline thin films concerned, another important source of traps is related to the grain boundaries [56]. In fact, they act both as trap states and as energy barriers for charge carriers.

Interfacial Effects

In all the devices based on organic semiconductors, the organic films are always interposed between other kind of materials forming interfaces OSC/dielectric, OSC/metal or OSCs/OSC.

In particular, the dielectric/OSCs interface can be source of trap states because of non-uniform topology, surface energy, chemistry, roughness of the dielectric and finally it can be related to the adsorption of impurities such as water, oxygen or hydroxyl groups.

Also, the OSC/metal contact interfaces can induce several trap states which affect in particular the injection/collection of charge carriers. This effect can be observed by an high contact resistance in electronic devices [57].

Environmental Effects

Exposure to environmental either during the device fabrication, handling, and characterization, often affects the quality of the organic semiconductor and can lead to trap formation. Temperature, moisture (H_2O), ambient gases (O_2) and electromagnetic radiation such as light or X-rays are some other possible sources of traps [55].

1.2.2. High mobility amorphous oxide semiconductors

Amorphous Oxide Semiconductors (AOSs) are other promising materials employed for the development of large-scale flexible electronics. In fact, on one side the

amorphous phase ensures the uniformity of the materials over a large-area (avoiding the presence of grain boundaries) and on the other side, despite the structural disorder, AOSs maintain a high electrical mobility (i.e. μ >10 $cm^2V^{-1}s^{-1}$). To better understand the peculiarity of these semiconductors, their molecular structure and their electronic configuration are here described.

AOSs are multicomponent compounds in which the mixing of different oxides ensures the amorphous phase. In fact, as depicted in **Figure 1.7a**, the assembly of different cations with different sizes and ionic charges prevent the crystallization of the material and leads to the existence of a high number of AOSs species. In particular indium, gallium, zinc and tin are the major constituents of the most studied AOSs. Besides, from the graph reported in **Figure 1.7b**, it is possible to see how the incorporation of a stabilizer cation (such as Gallium) is a crucial point for the formation of a good semiconductor. In fact, the Ga-O bond is stronger than the Zn-O and the In-O ones and it allows to lower the oxygen vacancies and consequently offers the possibility to have a higher control of the charge densities.

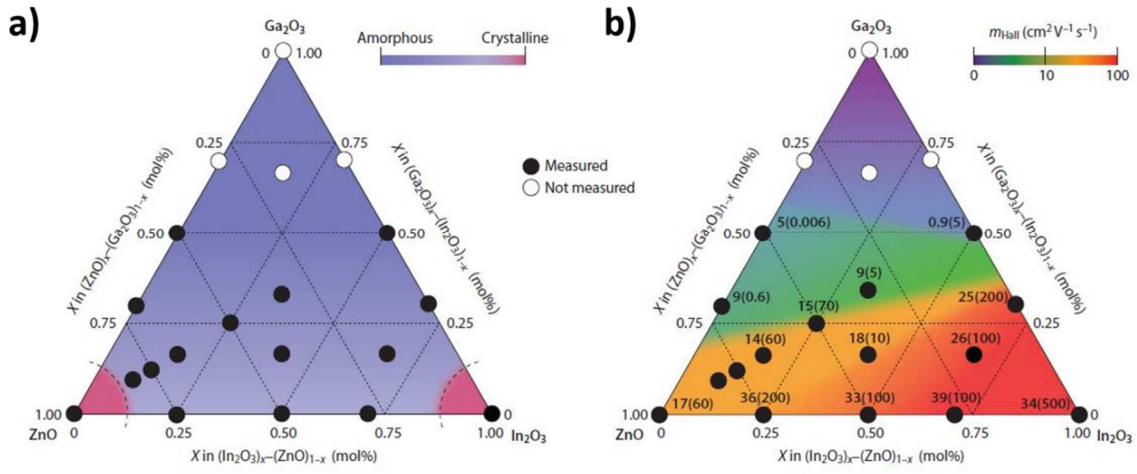

Figure 1.7 (a) Amorphous formation and (b) electron transport properties of In_2O_3-Ga_2O_3-ZnO thin films. The values in (b) denote the electron Hall mobility ($cm^2V^{-1}s^{-1}$) with density (10^{18} cm^{-3}) in parenthesis. Adapted from [58].

Considering the standard covalent semiconductors, we are used to think that the switch from a crystalline phase to an amorphous phase brings a dramatic degradation of the charge transport in the material (e.g. for Silicon $\mu_{c\text{-}Si} \approx 1500$ $cm^2V^{-1}s^{-1}$ while $\mu_{a\text{-}Si} < 1$ $cm^2V^{-1}s^{-1}$). On the contrary, in AOSs the electrical mobility remains unchanged despite the amorphous structure and the reason of this property is based on the strong ionicity of these compounds and on their electronic structures.

If we look at Silicon, the conduction band minimum and the valence band maximum are formed respectively by the anti-bonding (sp^3 σ^*) and bonding (sp^3 σ) states of Si sp^3 hybridized orbitals and the corresponding energy band gap is formed by the energy splitting of these two (see **Figure 1.8a**). On the contrary, when a metal comes in the vicinity of oxygen in order to form oxides, charge transfer occurs from the former to the last due to the different electron affinities. In particular, as it is shown in **Figure 1.8b,c**, the electronic structure of the ionic compound is stabilized by the Madelung potential formed by these ions, raising the energy levels of the metallic cations and lowering the ones of the oxygen. Thus, here the maximum of the valence band is formed by the fully occupied oxygen 2p orbitals while the minimum of the conduction band is composed by the empty metal cation s orbitals. The difference between these two edges forms the energy band gap of the AOSs. [59]

The electronic configuration described above, explains why AOSs maintain high electrical mobility even if they present an amorphous structure. Since the minimum of the conduction band is mainly formed by the spherical s orbitals of the metal cations, when the radius of these orbitals exceeds the inter-cation distance the overlap between these leads to a broad band dispersion (i.e. a small electron

effective mass). Moreover, while the sp^3 orbitals forming the conduction band in Silicon are strongly unidirectional, the spherical s orbitals involved in the formation of the conduction band in AOSs are not affected by the structural disorder maintaining a good overlap also in amorphous materials (**Figure 1.8d, e, f, g**).

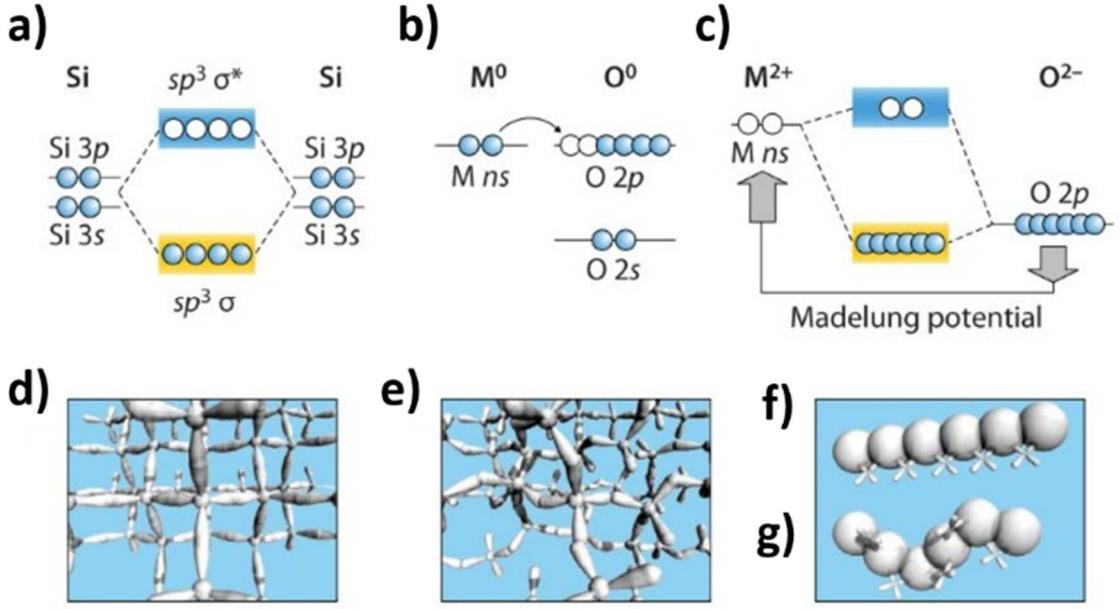

Figure 1.8 *Schematic electronic structures in Silicon and in ionic oxide semiconductors. Band-gap formation mechanisms in (a) covalent and (b, c) ionic semiconductors. Carrier transport paths in (d) c-Si, (e) a-Si, (f) c-oxides and (g) AOSs.* [58]

1.2.2.1. Charge transport in AOS

In AOSs the transport mechanism can be described using a band-like transport. In fact, as it has been discussed in the previous section, despite the amorphous structure presented by this class of materials, the electronic configuration forming the conduction band of AOSs does not affect the formations of bands. In **Figure 1.9a** the pseudo-band structures of a-Indium Gallium Zinc Oxide (a-IGZO i.e. a ternary AOS) and a-Si obtained through DFT calculations are depicted. As it is

shown, while the a-Si presents very small width bands, on the opposite side in the a-IGZO the conduction band has a large dispersion with a bandwidth ≈1eV indicating that the electrons in a-IGZO are delocalized [60].

Moreover, AOSs present two unusual carrier transport properties:

- The electron mobility increases with the free electron charge density (**Figure 1.9b**) both in amorphous and crystalline material while in the typical crystalline semiconductor this trend is the opposite. In fact, typically the increasing of charge density is due to an increase of the materials doping and thus to an increase in the scattering of the free charges with the impurities. On the opposite side, in AOSs the doping of the materials mainly occurs through a modulation of the oxygen vacancy density avoiding the introduction of impurities in the material.

- The electron mobility increases with the temperature both in amorphous and crystalline material despite the degeneration of the density of charges [59]. This thermally activated mechanism suggests that the transport of free carriers in the conduction band is limited by potential barriers above the band edge. These are well explained in the percolation transport model [61] depicted in **Figure 1.9c**. With the increasing of temperature, the charges acquired enough energy to pass over the potential barriers and take the shorter path, enhancing the electrical mobility of the AOSs.

Finally, AOSs present very high values of electrical mobility (i.e. >10 $cm^2V^{-1}s^{-1}$) which can be explained by the charge transport mechanism occurring and by the low density of sub-gap defects states [62].

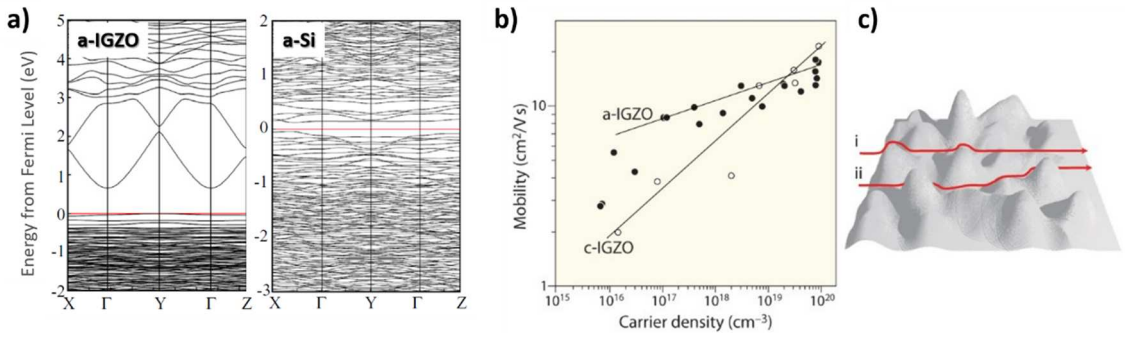

Figure 1.9 *a) Pseudo band-structure of a-IGZO (left) and a-Si (right). b) The relation between electrical mobility and charge carrier density for a-IGZO and c-IGZO. c) Schematic of the percolation conduction showing the short (i) and the long (ii) pathways. The isosurface represents the electron potential in the conduction band. Adapted from* [58], [63]

1.2.2.2. Deposition techniques

As for the organic semiconductors, the AOSs can be deposited both by solution and by vacuum deposition techniques.

Vacuum deposition processes are widely used in flat-panel display manufacturing and in particular sputtering technology is one of the most employed techniques among the others [10], [64]–[68]. In fact, this method of deposition offers several advantages such as the possibility to operate at low-temperature (i.e. RT) and it allows to obtain a good adhesion of uniform and dense films onto large-area substrates [69].

In order to focus on the development on scalable and flexible system based on AOSs in the last years several works and reviews have been published about the possibility to employ the traditional technique of deposition by solution (i.e. the ones discussed for the OSCs) also for this class of materials [70]–[73].

1.3. Large-area and flexible devices: applications

In recent years, large-area and flexible electronics have developed at an unprecedented rate. In fact, the increasing quest of scalable and stretchable devices forced the scientific community and the industries to look for alternative pathways in order to find new materials able to address these necessities.

Large area and flexible devices are employed in several applications such as in personal devices (e.g. wearable health monitoring devices), large-area sensors (e.g. electronic skin, biomedical devices, digital medical imagers), rollable displays, solar cells and smart tagging of products with radio-frequencies identification tags (see **Figure 1.10**) [10], [74].

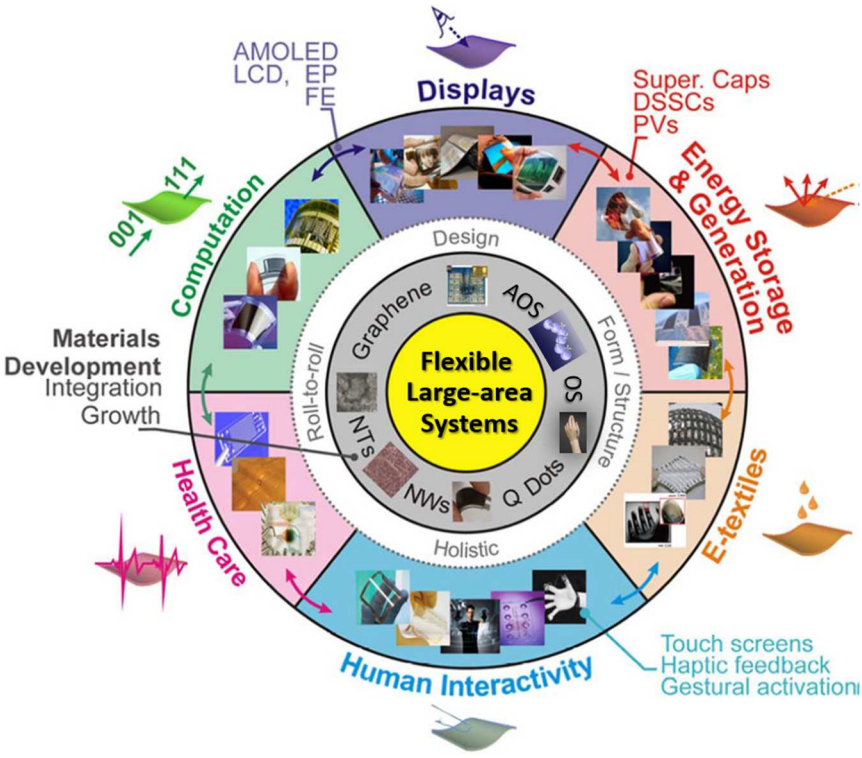

Figure 1.10 *Applications of flexible and Large-area Electronics. Adapted from* [75].

1.3.1. Thin Film Transistors (TFTs)

Among this wide range of possible applications, flexible and scalable technologies have been implemented for the development of thin film transistors (TFTs). In particular, organic semiconductors [16], [24], [25], [38], [41], [43], [45], [76]–[78] and amorphous oxide semiconductors [60], [70], [79]–[86] have been both exploited as materials forming the semiconducting layer of the device (see **Section 1.3.1.2**).

The TFT is a three terminal device where it is possible to tune the current flowing in a semiconductor placed between two electrodes (i.e. source and drain). A dielectric layer is inserted between the semiconductor and a third electrode named gate, being the current modulation achieved by the capacitive injection of carriers at the interface between the semiconductor and the dielectric layers. This effect is turned possible due to the parallel plate capacitor structure formed by the gate electrode, insulator and semiconductor and it is known as *field effect*.

Depending on the position of the semiconducting layer respect to the electrodes, four different configurations can be distinguished: bottom gate-bottom contact (BGBC), bottom gate-top contact (BGTC), top gate-bottom contact (TGBC) and top gate-top contact (TGTC) (see **Figure 1.11**). The TFTs reported in this thesis are all in the bottom gate bottom contact configuration.

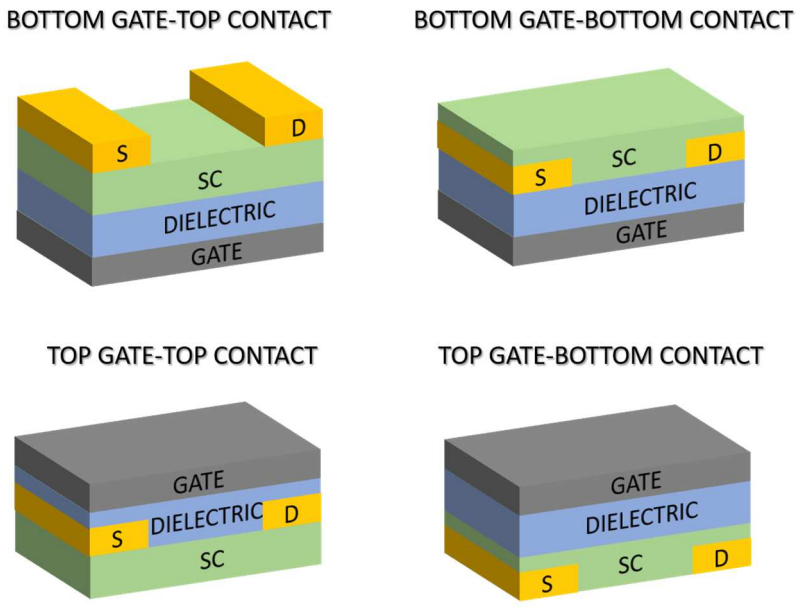

Figure 1.11 *Thin film transistor structures*

While the typical field effect devices (e.g. MOSFETs) operation is based on the inversion regime, the working principle of the TFTs is based on the creation of a conductive channel at the interface between the semiconductor and the dielectric layer (i.e. accumulation regime). Let us consider as an example a TFT based on an n-type (p-type) semiconductor. When a positive (negative) bias is applied through the gate electrode (i.e. V_{GS}), electrons (holes) are attracted at the interface between the insulator and the semiconductor and a conductive channel is created. Applying then a bias between the source and drain electrodes leads the flowing of these charges across the channel length and a current (i.e. I_{DS}) can be measured. On the opposite side, when a negative (positive) bias is applied at the gate terminal, the interface between the semiconductor and the insulator is depleted and no electrical currents can be measured between the source and drain electrodes. The former denotes the ON-state of the transistor while the last is the OFF-state of the device. Ideally, the switching from the ON-state to the OFF-state should happen at $V_{GS} =$

0V. Indeed, in a real device the switching between these two regimes of operation does not occur at $V_{GS} = 0V$ but at a threshold voltage (i.e. V_{th}) which depends on the background carrier concentration of the semiconductor, the charge density residing within the dielectric and the trap density at the interface and within the semiconductor.

Considering now the ON-state of the transistor (i.e. $|V_{GS}| > |V_{th}|$), depending on the intensity of the bias applied at the drain electrode (i.e. V_{DS}), two different regimes can be distinguished:

- **Linear Regime** $V_{DS} < (V_{GS} - V_{th})$

In this regime, the charges accumulated in the channel are spatially uniformly distributed and the I_{DS} increases linearly with the V_{GS} as expressed by the following Equation 1.9:

$$I_{DS} = C_i \mu \frac{W}{L}\left[(V_{GS} - V_{th})V_{DS} - \frac{1}{2}V_{DS}^2\right] \sim C_i \mu \frac{W}{L}(V_{GS} - V_{th})V_{DS} \quad (1.9)$$

Where C_i is the capacitance per unit of area of the dielectric layer, W is the width of the channel and L is the length of the channel.

- **Saturation Regime** $V_{DS} > (V_{GS} - V_{th})$

When the V_{DS} is higher that $(V_{GS} - V_{th})$, the region close to the drain electrode becomes depleted leading to the saturation of I_{DS} (i.e. pinch-off of the conductive channel). In this regime the drain current can be expressed by the following Equation 1.10:

$$I_{DS} = C_i \mu \frac{W}{2L}(V_{GS} - V_{th})^2 \quad (1.10)$$

Both these regimes of operation are depicted in **Figure 1.12** where the Output and the transfer characteristic curves are reported.

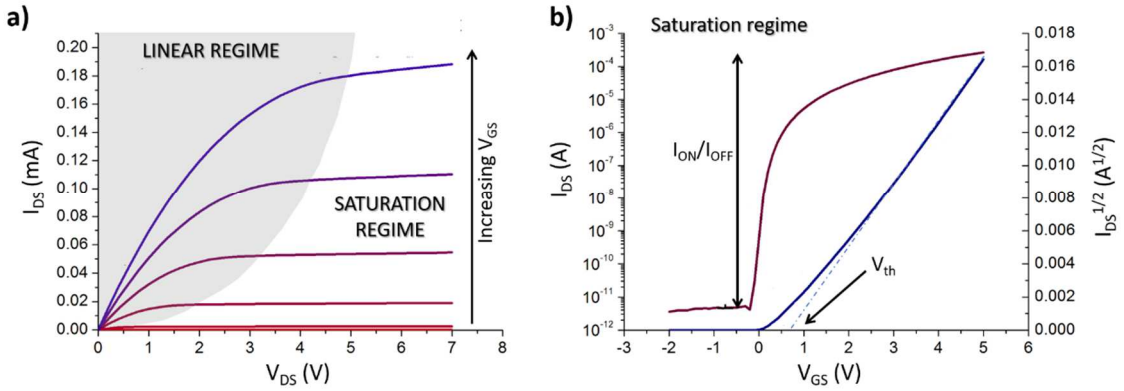

Figure 1.12 *a) Output characteristic. Both the linear and saturation regimes are indicated. b) Transfer characteristic in saturation regime.*

The electrical performance of the TFTs can be described by several parameters which can be extracted from the graphs reported in **Figure 1.12**.

- I_{ON}/I_{OFF} ratio indicates the ratio between the maximum and the minimum value of I_{DS}. A high value is desirable for a good operation of the device as an electronic switch.

- The Threshold Voltage (V_{th}) indicates the value of V_{GS} at which the TFT changes the status between ON-state and OFF-state. It can be extrapolated from the transfer characteristic as it is depicted in the graph (**Figure 1.12**). It strongly depends on the trap states for majority carriers being present at the semiconducting layer and for this reason, an estimation of the density of interfacial traps (N_{it}) can be calculated observing the variation of the threshold voltage with the temperature (Eq. 1.11):

$$N_{it} = \frac{C_i}{K_B T} \frac{\partial V_{th}}{\partial T} \tag{1.11}$$

- The sub-threshold swing slope (S) indicates how fast the TFT switches from the OFF-state to the ON-state changing the V_{GS}. It can be extracted from the transfer characteristic in the LOG-LIN plot as the inverse of the maximum slope (Eq. 1.12):

$$S = \left(\frac{\partial \log(I_{DS})}{\partial V_{GS}} \bigg|_{max} \right)^{-1} \tag{1.12}$$

  It strongly depends on the on the majority carriers trap states as well, as highlighted by the following Equation (Eq. 1.13):

$$S = \frac{K_B T ln(10)}{q} \left(\frac{N_{it} q^2}{C_i} + 1 \right) \tag{1.13}$$

- The Mobility (μ) represents how quickly a charge carrier moves in response to an electric field. Ideally the mobility extracted from the TFTs characteristic curves and the intrinsic mobility of the material would be the same. As a matter of fact, the mobility in TFTs strongly depends on structural defects of the semiconducting layer and on interface states and roughness. Therefore, in this case, it is reasonable thinking about the mobility as a property of the device more than of the material. Moreover, the mobility depends on the V_{GS} applied and for this reason it is possible to calculate this parameter both in linear (Eq. 1.14) and in saturation regime (Eq. 1.15).

$$\mu_{FE,lin} = \frac{\frac{\partial I_{DS}}{\partial V_{GS}}}{C_i \frac{W}{L} V_{DS}} \tag{1.14}$$

$$\mu_{FE,sat} = \frac{\left(\frac{\partial \sqrt{I_{DS}}}{\partial V_{GS}}\right)^2}{\frac{1}{2} C_i \frac{W}{L}} \tag{1.15}$$

1.3.1.1. The role of trap states: TFTs non idealities

As it has been introduced in **Section 1.2.1.3**, the presence of traps has a profound impact on the performance of electronic devices such as TFTs. This effect can be studied through the analysis of the electrical parameters [55] and the characteristic curves discussed in the previous section. The main nonidealities induced by traps are summarized in **Figure 1.13**. Recent reviews by H. I. Un et al. [87] and T. Yang et al. [88] provide a complete discussion on this topic.

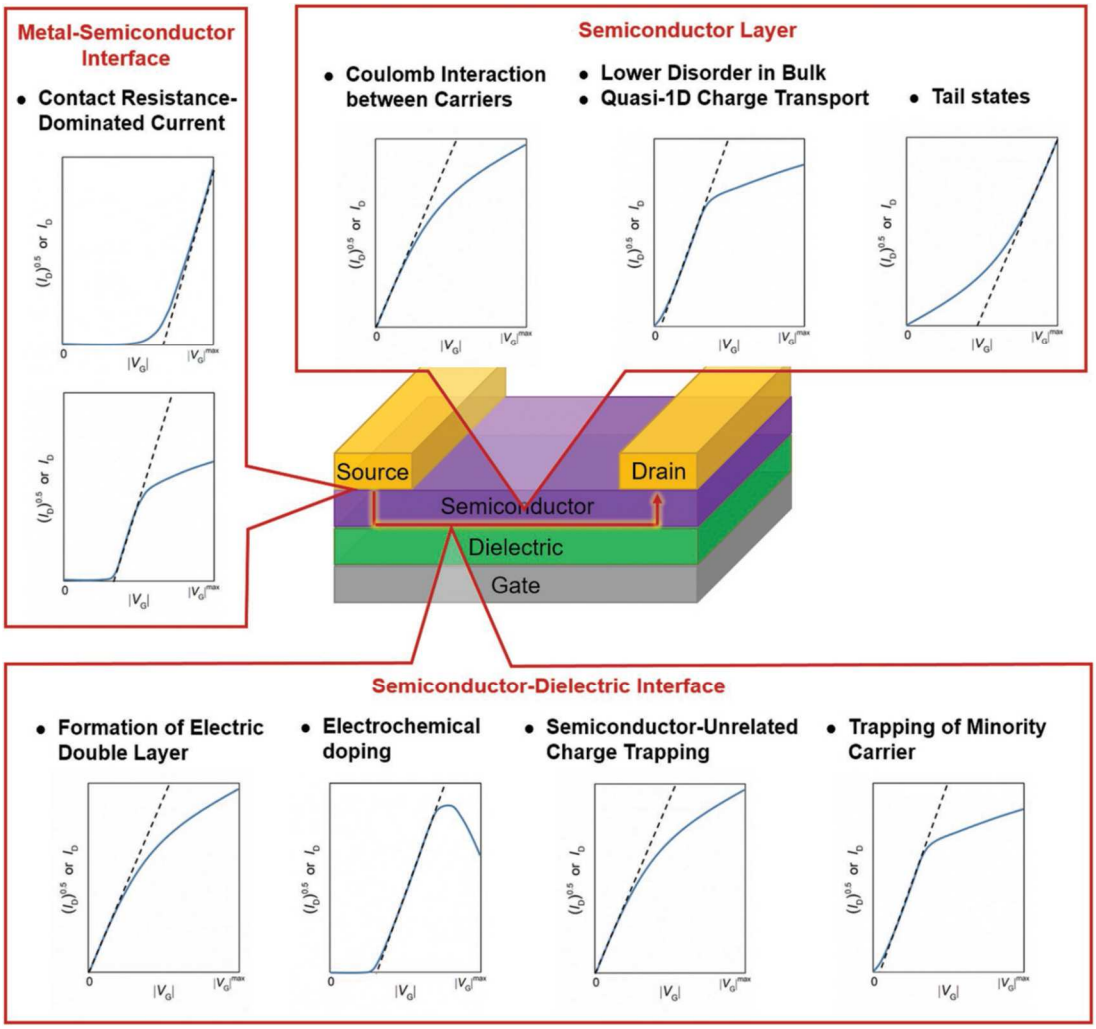

Figure 1.13 *Summary of the relationship between the origins of nonidealities and the resulting shapes of the transfer characteristics.*

First of all, the trap charge carriers reduce the electrical mobility with the density of traps and trapping timescale. In fact, in this case the mobility is V_{GS} dependent. In particular, at low V_{GS}, the injected/accumulated charges occupy the available trap states, and the electrical conduction is based on the thermally-activated hoping/tunneling between these states. For higher V_{GS}, the trap states are filled and the charge carriers can finally occupy the extended states and consequently increase the mobility. This is the reason for the deviation of the V_{th} from 0 V which can be observed as non-idealities in TFTs [89]. The most relevant sources of

trapping in this case are the ones induced in the semiconductor bulk or at the semiconductor/dielectric interface. For example, the presence of functional groups (e.g. -OH, -NH_2, -COOH) on the dielectric surface, can lead to a reaction with water molecules eventually present near the metal contacts bringing the formation of charge trapping layers. One possible solution to this issue is offered by the employment of surface treatments (e.g. hexamethyldisilzane (HMDS) treatment for the passivation of SiO2 surface) or by the use of polymer dielectric which does not contain functional groups (e.g. polystyrene).

Contact resistance is another crucial aspect which can strongly affect the transport properties of the TFTs inducing a downward bending of the transfer characteristic and a consequent non-linearity of the curve. This can have both an electrical and/or a structural origin. In fact, on one side the surface of organic materials is full of defects and when they are kept in contact with metallic materials localized states are induced at the interface. These states bring a surface potential which increases the injection barrier interposed between the electrodes and the conductive channel. On the other hand, also the semiconductor morphology plays a crucial role in this sense. For example, in BGBC TFTs the higher contact resistance is due the discontinuous coverage and poor film morphology of the semiconductor layer near the edge of the contacts. Also in this case, some strategies can be adopted in order to overcome this issue. For instance, organic self-assembled monolayer (e.g. pentafluorobenzenethiol (PFBT), see **Section 3.3.3**) can be employed to modify the Au electrodes for achieving a more uniform orientation of the organic semiconducting film.

Besides, another salient feature in practical OFETs, resulting from the existence of traps, is the bias stress effect. This phenomenon is represented by a shift of V_{th} or

V_{ON} (which is modeled by a stretched exponential) due to the continuous application of a V_{GS}. The causes of this can be several such as the charge trapping within the semiconductor bulk, in the dielectric or at the semiconductor/dielectric interface. Many strategies have been tested in the past decades in order to reduce this effect. For example, Kippelen et al. [90] have recently demonstrated remarkable bias stress stability employing an ultrathin bilayer dielectric formed by CYTOP and Al2O3. In this case, the best device showed ΔV_{th} below 0.2 V when it was kept in saturation condition for 40 hours (V_{GS} = -10 V; V_{DS} = -10 V) and in linear regime for 100 hours (V_{GS} = -10 V; V_{DS} = -2 V).

Finally, hysteresis in the current-voltage characteristics is another clear indication of the existence of traps. In this case, the charge carriers are trapped in the semiconductor or at the semiconductor/dielectric interface during the forward voltage sweep and are then released during the reverse voltage sweep causing a differential current. Also to correct this nonidealities, several methods can be adopted such as using different crystallization techniques [91] or employing post-deposition thermal annealing [92].

1.3.1.2. Flexible TFTs: State of Art

As large-area and flexible electronics continue to advance, the research on TFTs becomes more elaborate and divergent, extending to new materials, device concepts, manufacturing processes, and integrated systems that offer improved performance and more functionalities, ultimately leading to new markets [93].

As it has been anticipated at the beginning of this section, both organic semiconductors and amorphous oxide semiconductors have been employed as active layer in this class of devices.

In this paragraph some examples of the advances of these two technologies are illustrated with a particular focus on flexible systems.

As far as the OFETs concern, several efforts have been done in the last years in order to push the electrical performances of these devices and to adapt and implement them in several fields of applications. The intense work has been conducted on several aspects such as the improvement and the scalability of the fabrication techniques, the implementation of the devices onto new platforms, and the creation of novel architectures. In **Figure 1.14** some recent examples reported in literature are shown. In particular, **Figure 1.14a,b,c** report three different architectures which can offer several advantages. The first one is reported in a recent review by Kleemann et al. where the main aspects of the vertical organic transistors are summarized [94]. Here it is illustrated how, exploiting this architecture it is possible to fabricate OFETs with a very short channel length leading to the possibility of increase the transition frequency up to 40 MHz. The second option is reported by Wakayama et al. in [95] where they show the potentiality of an antiambipolar architecture for recording a steep increase and decrease in drain current within a certain range of gate bias voltage. And finally, another new architecture proposed by Cosseddu et al. and implemented for sensing application is called *organic charge modulated field effect transistor* (i.e. *OCMFET*) [96]. This device is based on a floating gate transistor and it is biased through a control capacitor. In the meanwhile, part of the floating gate is exposed to the environment forming the sensing area of this technology.

Moreover, OFETs have been fabricated using exotic substrates such as ultrathin polymeric foils [97] or paper [98]. In particular, this latter possibility opens the way for tattoo-paper transfer electronics and edible electronics [99].

Finally, scalability onto large area and flexible substrates have been the main aspect which have driven the evolution of the fabrication techniques [100]. In **Figure 1.14e** an example of the adaptation of the standard photolithography process in order to produce a large-area and flexible pixelated matrix composed by OFETs is reported. Moreover, other studies as the one reported by M. Mas Torrent et al. [101] regarding the modulation of the organic semiconductor deposition for the enhancement of the bendability properties are central for the development of flexible technology systems.

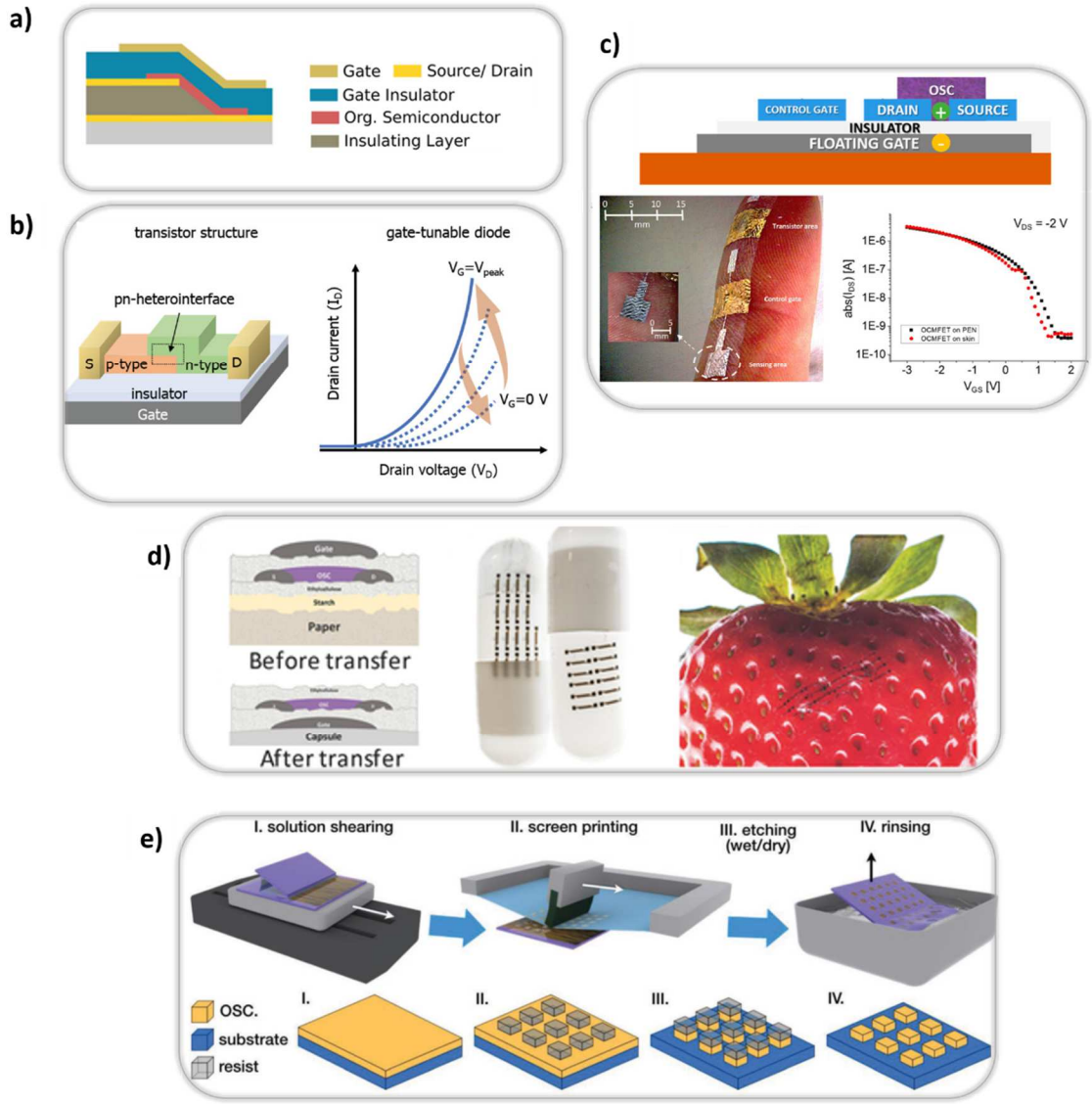

Figure 1.14 *Flexible and large-area OFETs: state of art. New architectures have been implemented such as a) the vertical organic transistors*[94]*, b) the antiambipolar OFET* [95]*, and c) the Organic Charge Modulated Field Effect Transistor (OCMFET)* [96]*. d) Novel substrates have been employed opening the way to the tattoo-paper transfer electronics and edible electronics* [99]*. e) New fabrication techniques have been invented in order to scale onto flexible and large area substrates pixelated matrix for sensing and electronic applications* [102]*.*

For what the amorphous oxide semiconductor-based TFTs concern, similar approaches to the ones described for OFETs have been followed in order to adapt these systems to scalable and flexible technologies. In **Figure 1.15** some examples of the main strategies employed are shown [70], [103].

For example, in **Figure 1.15a**, Kim et al. [104] showed the fabrication of an a-IGZO-based TFT implemented onto an ultrathin 1.5 µm-thick PI foil. They demonstrated the enhancement of the folding stability of the devices thank to the use of an additional 1.5 µm-thick PI deposited on the top which ensure that the devices are located at the neutral plane. Moreover, several efforts have been done to improve the deposition techniques from solution dedicated to the production of flexible devices to be implemented in several technologies such as sensors, displays and circuits. In **Figure 1.15b** for example it is shown an ultrathin (3.5 nm) In_2O_3 films prepared for a biosensor application, using a one-step spin-coating process and an aqueous In_2O_3 solution. The resulting biosensor platform was used to detect pH and glucose [105]. Moreover, different architecture (e.g. vertical TFT, see **Figure 1.15c**) [106] or bilayer-structured organic/oxide material (see **Figure 1.15d**) [107] have been reported in literature in order enhance the efficiency of flexible phototransistor for light sensing.

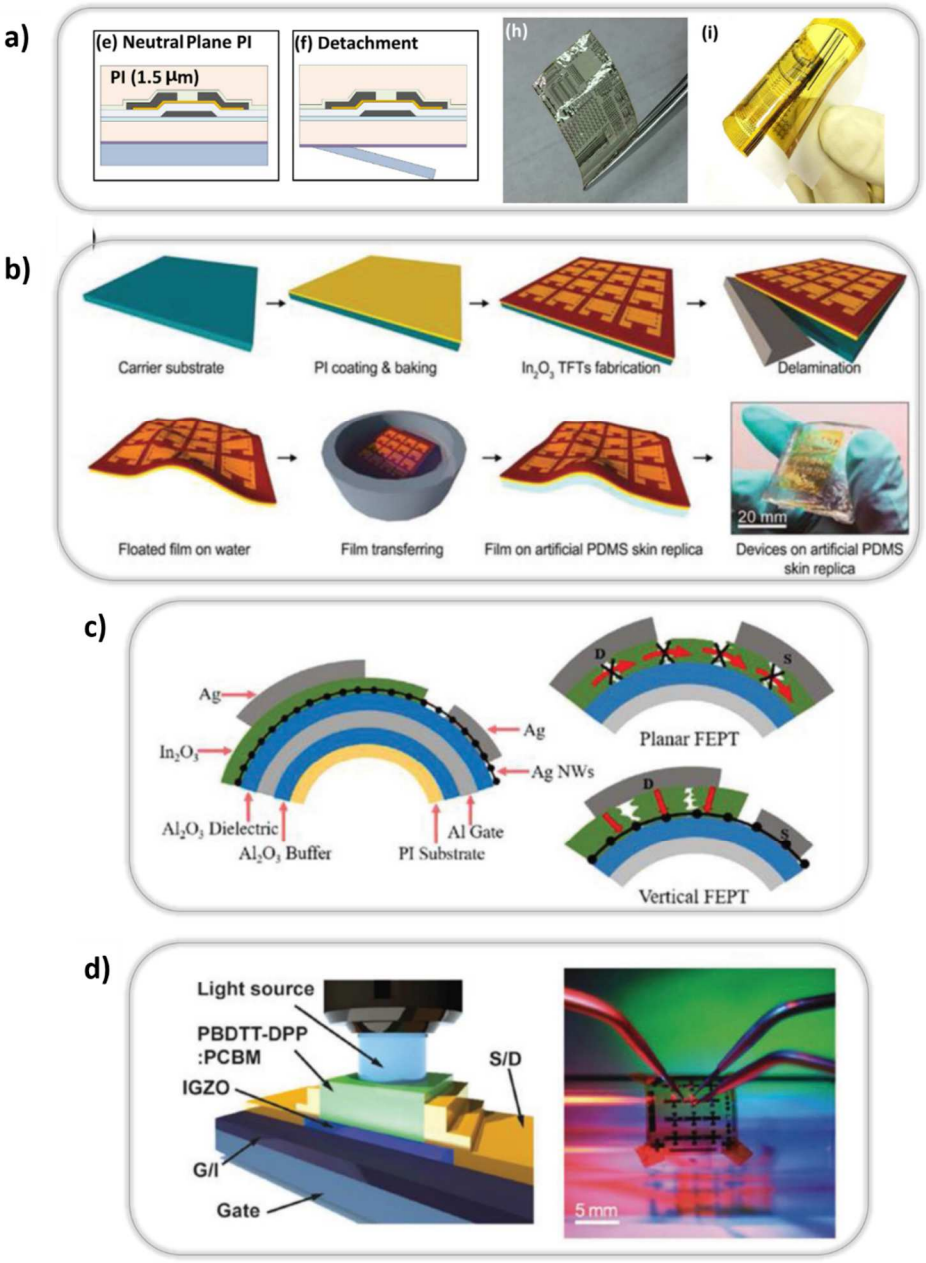

Figure 1.15 *Flexible and large area a-oxide-based TFTs: state of the art. a) Fabrication of neutral plane TFTs based on a-IGZO on a 1.5 µm thick PI substrate* [104]. *b) fabrication process of a ultra-flexible and conformable biosensor based on In_2O_3 3.5 nm thick* [105]. *c) Schematic layout of the cross section of a flexible vertical field effect phototransistor, and illustration of the current transport of conventional planar type and vertical type TFTs* [106]. *d) Bilayer-structured TFT based on both a-oxide and organic semiconductors for the visible-light detection; schematic structure of the device and picture of the bended device under test* [107].

2.

Solid State Ionizing Radiation Detectors based on Thin Film Devices

In this second chapter, an overview on solid state ionizing radiation detectors is reported. The first part is focused on the radiation sources and in particular on X-Rays, Gamma-Rays and protons production. After, the main mechanisms of interaction between radiation and matter and the most important physical quantities related to the radiation are described. The following part of the chapter is focused on the description of the main properties of a radiation detector, the figures of merit used to describe the quality of such a detector and finally the possible architectures used for the realization of a solid state sensor. Finally, at the end of the chapter, the state-of-the-art for the direct solid state and large area radiation detectors and for proton detectors employed in medical field is presented.

2.1. Ionizing Radiation Sources

The radiation can be conventionally divided into two general categories: charged particles radiation which includes fast electrons and heavy charged particles, and uncharged radiation where electromagnetic radiation and neutrons can be placed.

Depending on the type of radiation, different sources can be identified and moreover several kinds of interaction with matter can occur.

Hereafter, the sources of electromagnetic radiation (i.e. X- and Gamma Rays) and heavy charged particles are introduced.

2.1.1. Electromagnetic Radiation

In this thesis I focused only on specific ranges of the electromagnetic spectrum. In particular, I worked on sensors able to detect high energy electromagnetic radiation such as X-Rays and Gamma-Rays. These classes of radiation present an energy laying in the range between 120 eV and 120 keV and a wavelength in the range between 0.1 and 100 Å. The main difference between the two is related to the sources as it is shown in the next paragraphs. [108]

2.1.1.1. X-Rays

X-Rays can be produced by three different sources exploiting different physical effects.

Bremsstrahlung radiation (see **Figure 2.16a**) is a broad spectrum generated by the deceleration of fast electrons impinging on a solid. The energy of the photons consists in a continuous spectrum which extends as high as the energy of the fast electrons and it depends also on the atomic number of the absorber material (i.e. higher is Z, higher is the mean energy of the produced radiation beam).

Characteristic X-Rays (see **Figure 2.16b**) are produced by atomic transitions. In fact, when an atom is excited by a radiation decay or by an external radiation (i.e. the electrons occupy higher energy orbitals) there is a natural tendency for the electrons to rearrange in order to come back to the ground energy configuration. The transition of the electrons from an outer shell to an inner shell produces photons with a discrete and well-defined energy that corresponds to the difference between the final and the initial state. Depending on the shells involved in the transition, it is possible to distinguish K, L, M emissions all identified by the specific energy of the element involved.

Bremsstrahlung and characteristic radiation are the main two phenomena occurring in the production of X-Rays by typical X-Ray tubes (see **Figure 2.16c**). Here, a beam of monoenergetic electrons is accelerated at tens of kV from a heated filament (i.e. cathode) to a target material (i.e. anode). The impact of the electrons to the target excites the elements forming the target (typically W, Mo or Cu) and the following relaxation of the atoms produces the characteristic radiation described above. Besides, the deceleration of the fast electrons produces the Bremsstrahlung radiation. Indeed, the produced radiation is a convolution of these two.

Finally, another important source of X-Rays is the synchrotron radiation [109], [110]. From the classical electrodynamics an accelerated charged particle emits radiation. In particular, if this particle is forced in a circular orbit at relativistic

speed ($\gamma \approx 10^3$ - 10^4), it loses energy (i.e. synchrotron radiation) tangent to the orbit and with an angular dispersion $\Delta\varphi = 1/\gamma$. In order to produce synchrotron radiation, several facilities have been built up in the last decades all over the world. One example is depicted in **Figure 2.16d**. Here, a LINAC accelerates the electrons firstly in a booster ring and later the beam of particles is introduced in the main accelerator called storage ring. Here the particles are forced in the circular orbit thanks to bending magnets. Tangentially to the ring, following the trajectory of the synchrotron radiation, several experimental lines (i.e. beamline) are present. Three kinds of insertion devices are used along the ring to generate the X-rays: bending magnet, undulators and wigglers. In general, the synchrotron radiation is very collimated, very intense and with a broad energy spectrum (i.e. between few eV and 104 eV) which can be monochromatized.

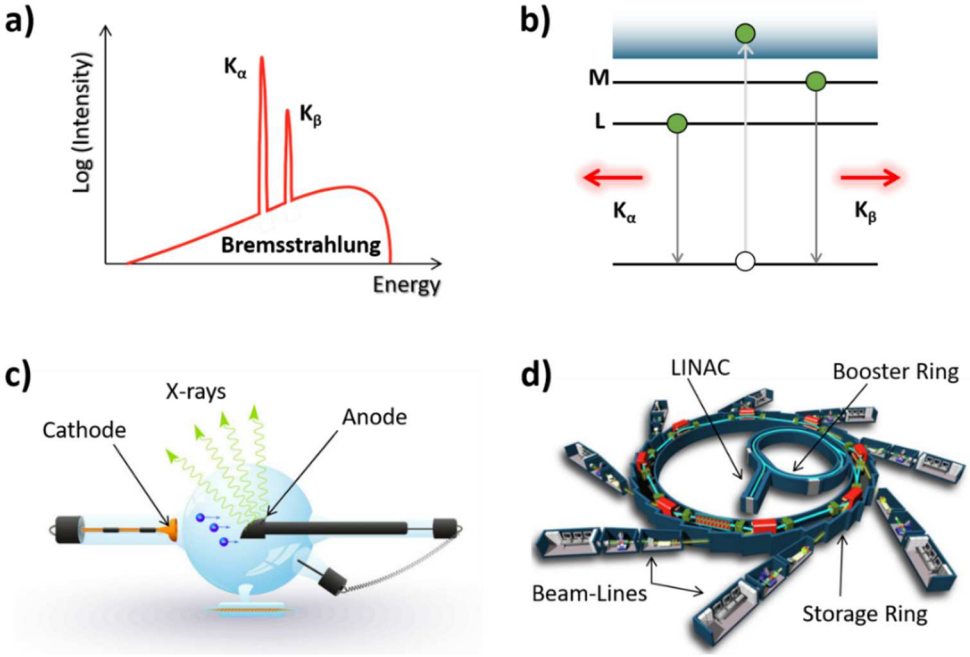

Figure 2.16 *a) Spectrum from an X-Ray tube formed by both the Bremsstrahlung and the characteristic radiation. b) schematic of the atomic energy shell transitions which produce characteristic radiation. c) schematic of an X-ray tube and d) of a Synchrotron facility. Adapted from* [110].

2.1.1.2. Gamma-Rays

Gamma Rays can be produced by three different sources all related to nuclear physics.

Firstly, they can come from β decays. When a parent radionucleus decays, it leads to a daughter nucleus in an excited nuclear state. The transition of the latter to a lower-lying nuclear level produces a gamma ray whose energy is equal to the difference in energy between the initial and the final nuclear state. While the half-life of the parent nuclei is of the order of hundreds of days, the transition of the daughter elements is much faster with an average lifetime of the order of picoseconds. Because of the well-defined energies of the nuclear states, this source of radiation is nearly monoenergetic and for this reason it is often employed for the calibration of detectors with very good energy resolution. The energy of the produced photons can have a maximum energy of 2.8 MeV.

Second, gamma rays can be produced by annihilation. In fact, when a β+ decay occurs, a positron is produced and it can easily recombine within the same material with an electron. This recombination leads two 0.511 MeV photons with opposite directions known as annihilation radiation.

Finally, other nuclear reactions can be exploited to produce gamma rays with energies higher than 2.8 MeV. Typically, alpha emitters are involved in this kind of reactions where a stable element is transformed in a product nucleus in an excited state which decaying emits gamma rays. Unfortunately, due to the short lifetime of these states, the energy of this gamma rays spreads of about 1%.

2.1.2. Heavy Charged Particles

Depending on the kind of heavy charged particles, several sources are present such as alpha decay for the alpha particles or spontaneous fission for heavier particles. In this paragraph I will briefly introduce the two main sources of protons because these are the only heavy charged particles treated in this thesis.

2.1.2.1. Protons

The main source for high energy proton beams is based on particle accelerators. These can be divided in several categories depending on the shapes, dimensions, energy delivered. Despite the differences, all of them share three important properties: the existence of a proton source, the use of electric and a magnetic fields in order to respectively accelerate and guide the particles and finally a good vacuum through which the beam travels avoiding scattering events. In order to generate protons, a hydrogen gas is employed and ionized in order to strip the electron from the atoms. Then, to accelerate the charged particles, electric fields are used and in particular, in order to obtain high energy beams (i.e. >MeV) very high difference of potential has to be applied. Working with such high voltages is not easy and for this reason, several technologies exploit instead several repetitions of weaker electric fields. In particular, linear accelerators (LINACs) and cyclic accelerators (e.g. Cyclotrons and Synchrotrons) have been developed. In cyclotrons, the accelerating electric field oscillates at fixed frequency between the two dees (see **Figure 2.17**) and the guiding magnetic field has a fixed intensity which forces the particles in a

spiral motion before their extraction. On the opposite side, in the synchrotrons as the protons are accelerated, the magnetic field is increased in order to maintain the radius of the orbit approximately constant. [111]

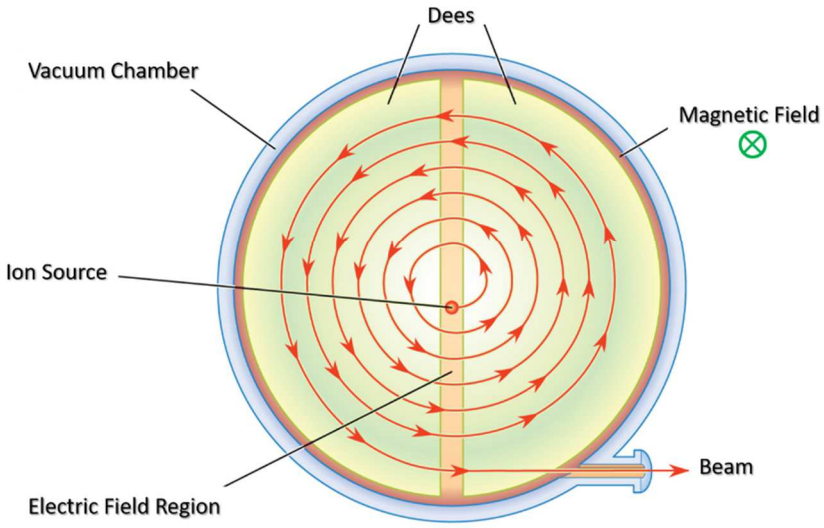

Figure 2.17 *Schematic of a Cyclotron for the production of ion beams*

2.2. Ionizing Radiation interaction with matter

The operation of the radiation detectors depends on the mechanism of interaction between the active material forming the sensor and the radiation impinging on it. For this reason, in this section I will summarize the main manners in which the high energy photons and the protons interact with matter.

2.2.1. Interaction of high energy photons

High Energy Photons (i.e. X-Rays and Gamma-Rays) interact with matter mainly through three different mechanisms: photoelectric absorption, Compton scattering and pair production. In all of them, the energy of the photons is partially or totally transferred to the atoms forming the material.

The photoelectric absorption consists in the complete absorption of a photon by an atom. The absorbed energy causes the ejection of an electron of the inner shell (e.g. K shell) which escapes from the atom with a kinetic energy $E_{e^-} = h\nu$ - E_b where $h\nu$ is the photon energy and E_b is the binding energy of the electron. The vacancy left by the electron is quickly filled by the capture of a free electron or by the rearrangement of the electronic configuration of the atom itself. This process, as it has been explained in the previous section, generates a characteristic X-Ray or in some case an Auger electron. In both cases, the ejected primary electron and the Auger electron or the X-rays characteristic are often reabsorbed by the material inducing a cascade of events.

As in the photoelectric absorption, also in the Compton Scattering the high energy photons interact with the electrons of the material. In this case, the transfer of energy from the photon to the electron is partial and the photon is not totally absorbed but it is only deviated. The probability of Compton scattering increases with the number of electrons per atom (i.e. Z number) and it is common for photons with energy of the order of 1 MeV.

The pair production occurs for photons with higher energies. When the photon exceeds several MeV it is able to interact within the electrical field built up by

nuclei and it can form an electron-positron pair. When the two particles slow down, the positron annihilates and two photons are generated as secondary products.

In ***Figure 2.18*** the probability of these main three mechanisms of interaction is depicted as a function of the photon energies and the atomic number of the material.

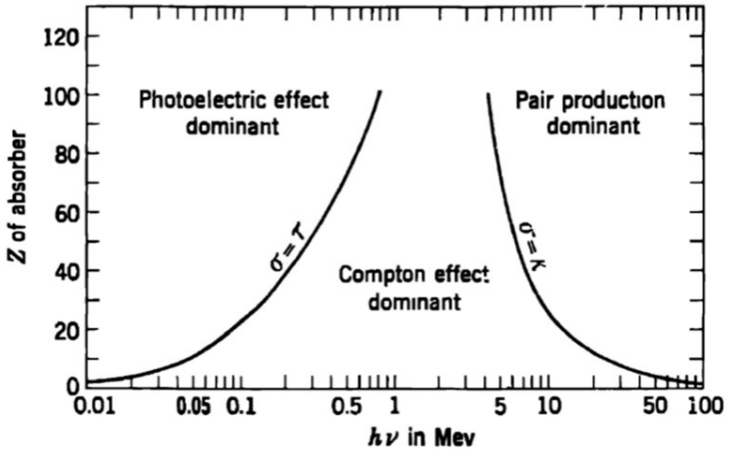

Figure 2.18 *The relative importance of the three major types of high energy radiation interaction. The lines show the values of Z and hυ for which the two mechanism have the same probability to occur.* [112]

2.2.2. Interaction of protons

Protons interact with matter in three distinct ways. Due to the electromagnetic interaction, they can slow down after inelastic collisions with the atomic electrons of the material or they can be slightly deflected by elastic scattering with nuclei. More rarely, they can also have head-on collisions with nuclei setting secondary particles in motion. [113]

Due to the myriad of inelastic collisions with electrons, the protons lose energy along their pathways within the material. The stopping power S is the quantity which expresses the energy loss per unit path length and it can be defined by the Bethe-Bloch equation (Eq. 2.1) [114]

$$S = -\frac{dE}{dx} = \frac{4\pi e^4 z^2}{m_0 v^2} NB \tag{2.1}$$

$$B = Z\left[ln\frac{2m_0v^2}{I} - ln\left(1-\frac{v^2}{c^2}\right) - \frac{v^2}{c^2}\right]$$

where v and ze are the velocity and the charge of the primary particle, N and Z are the density and the atomic number of the absorber atoms, m_0 and e are respectively the electron rest mass and charge and I is the average excitation and ionization potential of absorber. For a non-relativistic proton, the stopping power varies inversely with particle energy. This can be explained by noting that a slower proton spends much more time in the vicinity of electrons, and it is able to transfer to them much more energy. The Bethe-Bloch equation begins to fail at low particle energies where charge exchange between the particle and the absorber becomes important. In **Figure 2.19** the stopping power as a function of the penetration depth is depicted both for photons and for protons. In the case of charged particles, this plot is named *Bragg Curve* and the sharp peak depicts exactly the large dose enhancement just before the protons stop. In fact, while photons exhibit a dose buildup followed by an exponential decay, in the charged particles (e.g. protons) where electromagnetic interaction occurs, the energy of each one decreases continuously and so the entire beam stops at more or less the same depth. This feature has great consequence in the field of radiotherapy/proton therapy as it will be illustrated in the following sections.

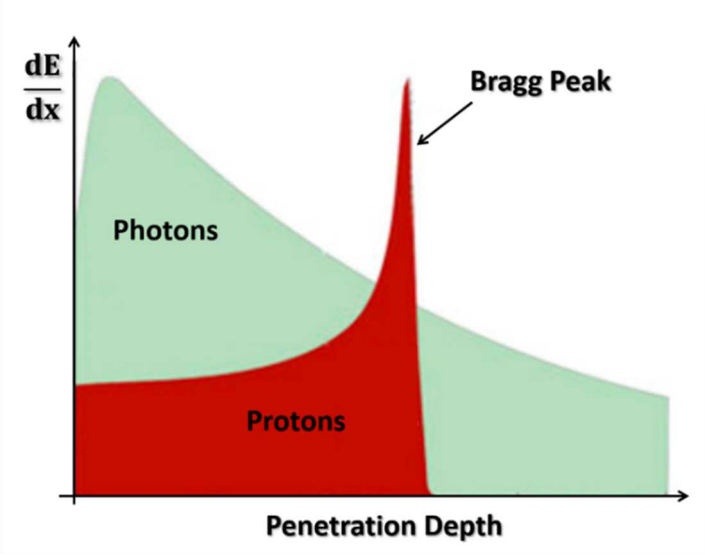

Figure 2.19 *Stopping power as a function of penetration depth for both high-energy photons and proton radiation. Adapted from* [115].

2.3. Ionizing radiation physical quantities

In this section the main quantities describing ionizing radiation (or charged particles) and the corresponding units of measurements are summarized. [116][117]

Activity

This quantity described the number of decays per second for a specific radioactive material. It is expressed in Becquerel (Bq) which is defined as one disintegration per second. The corresponding CGS unit of measurement is the Curie (Ci) which is equal to $3.7 \cdot 10^{10}$ decays per second ($1\ \text{Ci} = 3.7 \cdot 10^{10}$ Bq).

Fluence and Flux

The fluence of radiation is defined as the number of photons (or protons, or charged particles in general) per unit of area (Eq. 2.2) while the flux is equal to the fluence per unit of time (Eq. 2.3).

$$Fluence\ [cm^{-2}] = {}^{N}/_{A} \tag{2.2}$$

$$Flux\ [cm^{-2}s^{-1}] = {}^{N}/_{A \cdot time} \tag{2.3}$$

Linear Attenuation Coefficient

When the radiation pass through matter, it is attenuated by the interaction mechanisms described above. For photons, the decay of an incident beam of radiation I_0 is described by the exponential law in Eq. 2.4.

$$\frac{I}{I_0} = e^{-\alpha t} \tag{2.4}$$

Where t is the thickness of the material and α is called linear attenuation fraction. This latter indicates the probability of interaction of one photon per unit of pathlength and can be expressed as the inverse of the mean free path λ. The probability of interaction between the photon and the material depends also on the density of matter and for this reason, it is common to use the mass attenuation coefficient α/ρ instead of the linear attenuation coefficient.

KERMA (Kinetic Energy released per unit Mass in matter)

KERMA is a quantity referred only to particles such as photons for which the ionization is an indirect process. In this case, when the photons imping onto matter, they firstly generate primary products (i.e. charged particles such as electrons) and after these charged particles can ionize and excite the atoms of the medium. The

KERMA is related to the first process and it indicates the mean energy transferred to the first products by the radiation per unit of mass (Eq. 2.5).

$$KERMA\ [J\ kg^{-1}] = \frac{d\bar{E}_{tr}}{dm} \tag{2.5}$$

The KERMA can be expressed as a function of radiation flux using Eq. 2.6.

$$KERMA\ = \varphi\left(\frac{\mu\alpha_{tr}}{\rho}\right)E_{tr} \tag{2.6}$$

Where φ is the radiation flux and α_{tr}/ρ is the mass attenuation coefficient.

KERMA is used to express the intensity of the radiation in a specific position in the space. In particular, AIR KERMA is commonly employed and it indicates the energy transferred by the radiation to a unit of mass of air. This value can be converted for any absorber material, just multiplying it for the ratio between the mass attenuation coefficient of the material and of the air.

Absorbed Dose

The Absorbed Dose is a quantity referred to any type of radiation. It indicates the energy absorbed by a medium per unit of mass and it is expressed by Eq. 2.7.

$$Absorbed\ Dose\ [Gy] = \left(\frac{dE_{abs}}{dm}\right) \tag{2.7}$$

The SI unit of measurement for the dose is the *Gray* which is defined as 1 Gy = 1 joule/kg.

Noteworthy for a thick medium, the energy transferred to primary products (E_{tr}) is equal to the one absorbed by the medium and thus KERMA is the same as the absorbed dose.

Equivalent Dose

When the effects of radiation on living organism are evaluated, depending on the nature of radiation it is possible to obtain different biological effects. For this reason, another important quantity considering this aspect has been introduced. The Equivalent Dose ($H_{T,R}$) in a tissue (T) for a given type of radiation (R) is the product of the absorbed dose ($D_{T,R}$) and the radiation weighting factor (w_R) (Eq. 2.8).

$$H_{T,R}\,[Sv] = D_{T,R} \cdot w_R \tag{2.8}$$

The SI unit of measurement of the equivalent dose is the Sievert (Sv) and it is used when the dose is expressed in Gray.

In 1991 The International Commission on Radiological Protection (IRCP) [118] evaluated all the radiation weighting factor that have been tabulated.

2.4. Ionizing radiation detectors

Ionizing radiation detectors are devices able to collect the energy released by radiation into the active volume of the sensor and convert it into an electrical output signal. Depending on the kind of radiation and on the mechanism of detection, several classes of these sensors exist. [119], [120]

The first radiation detectors were gas-based devices (e.g. ionization chamber, Geiger counters) and they are still employed in some specific applications. The main limitations presented by this class of detectors are related to their high ionization energy (≈30 eV) and their low density. This is the reason why in the last

decades, solid-state detectors have replaced gas filled devices in most of the cases. In fact, due to their higher density (≈1000 times) and the lower ionization energy (≈3-6 eV), for the same amount of impinging radiation the absorbed dose results higher and the electron-hole pairs generated as secondary products are achieving better performances in terms of detection.

Solid state ionizing radiation detectors can be divided into two categories (**Figure 2.20**). Indirect detection is based on a two-steps process in which the high energy radiation is firstly converted into visible photons and then these are detected by a photodetector which convert them into an electrical output signal. On the opposite side, direct detectors directly transduce the high energy radiation into an electrical output signal in a one-step process. In the first case, scintillating materials are usually coupled with photodetectors, while in the latter case semiconducting materials are employed.

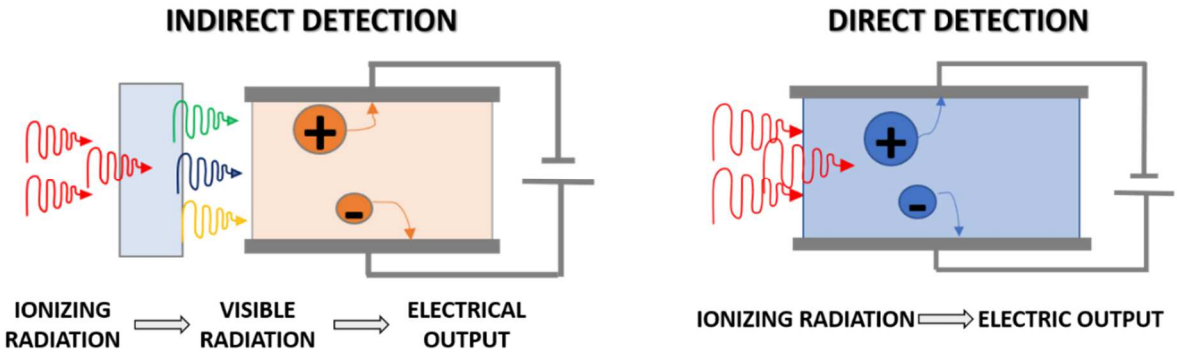

Figure 2.20 *Indirect detection is based onto a two steps conversion process while the direct detectors convert directly the ionizing radiation into an electrical output signal.*

In this thesis I will focus on the direct detection of radiation by semiconducting materials which offers the advantages of a faster response and of an higher signal to noise ratio [121].

In the direct detection, when the high energy radiation impinges onto the sensor, due to the mechanisms of interaction summarized in the previous sections, it generates primary excitons. After that, these primary products interact with the active volume of the sensor (i.e. the semiconductor) inducing a large number of secondary products (i.e. electron/hole pairs). In a semiconductor detector, an electric field is typically imposed to the device to separate the induced charges and to record a photocurrent as the electrical signal produced by the absorbed high energy radiation. To achieve good detecting performances, the semiconductor employed as the active material of the sensor must fulfill some requirements. In particular, it has to present a high Z-number and a great density to maximize the absorption of radiation, its energy gap should be higher than 1.5 eV in order to lower the intrinsic carrier concentration and consequently the dark current, but it has to be lower than 5 eV to minimize the e-h pair generation energy and finally it has to show good transport properties (i.e. high $\mu\tau$ product) to guarantee a good collection of the photogenerated charges. Moreover, depending on the specific application, some other requirements should be satisfied such as the mechanical flexibility, the possibility to fabricate uniform and large area sensing systems at limited costs, the portability and finally the human-tissue equivalence in terms of radiation absorption.

2.4.1. Solid State Ionizing Radiation Detectors: Figures of Merit

In this section, the most significant figure of merits which describe the potentiality of a device implemented as ionizing radiation detector are described. [122], [123]

Quantum Efficiency (QE)

The quantum efficiency, also known as attenuated fraction, indicates the efficiency with which the semiconductor attenuates the radiation. It depends on the linear attenuation coefficient α, which is strongly energy dependent, and it can be expressed by the Equation 2.9.

$$QE = 1 - e^{-\alpha t} \tag{2.9}$$

Where t is the thickness of the semiconductor. Higher is the density and the atomic number Z of the active material, higher is the efficiency of the detector.

To highlight the difference between the External Quantum Efficiency (QE_E) and the Internal Quantum Efficiency (QE_I): in the first case the QE indicates the fraction of the collected charges over the incident radiation while in the second case the QE is calculated over the absorbed radiation.

Electron-Hole Pair Generation Energy ($W_{\pm}$)

The e^-/h pair generation energy indicates the energy needed to create a collectable electron hole pair. In fact, the charge ΔQ induced by the absorption of energy ΔE of radiation is equal to $e\Delta E/W_{\pm}$ where e is the electron charge. To increase the sensitivity of the sensor, low $W_{\pm}$ is required. In many material systems, $W_{\pm}$ is proportional to the bandgap of the semiconductor.

Charge Collection Efficiency (CCE)

The charges generated by the absorbed radiation have to be collected by the electrodes avoiding trapping and recombination effects. The condition to ensure high CCE is $\mu\tau E > L$ where μ is the carrier mobility, τ is the lifetime of the charges before recombination, E is the electrical field imposed, and L is the channel length between the two collecting electrodes.

Dark Current

The dark current represents the current flowing in the semiconductor in absence of any radiation stimulus. It determines the noise of the detector and for this reason should be as small as possible to achieve high signal to noise ratio (SNR) and low minimum detectable dose (LOD). The possible sources of the dark current are three: the presence of defective states, the injection of carriers from the electrodes, and the thermal generation of carriers in the materials. To lower this quantity several strategies can be exploited. First of all, low-defective semiconductors have to be employed such as ultra-pure single crystals or polycrystalline films where passivation treatments can reduce the trap density. Moreover, wider bandgap semiconductor can limit the thermal generation of carriers and non-injecting electrodes are desirable.

Radiation Hardness

During the irradiation, the active material can be damaged temporarily or even permanently by the generation of various defects especially under high radiation doses or for long exposure time. The accumulation of these induced defects can generate two different consequences. First it can lead to a *ghosting effect* in which the photogenerated charges recombine with previously trapped charges without

reaching the collecting electrode. This recombination causes a lowering of the detection response of the sensor. Second, the net space charge due to the trapped carriers modifies the applied electric field modifying the CCE.

Sensitivity

The sensitivity (S) is the quantity which quantifies the charge collected (Q) per unit of radiation (X), often expressed per unit of area irradiated (A). This is expressed by the Equation 2.10 and it indicates the capability of the sensor to detect the radiation and produce an electrical output signal. [123]

$$S = \frac{Q}{X \cdot A} \tag{2.10}$$

Kasap *et al.* introduced a general expression to calculate the theoretical sensitivity of an X-ray detector based on a-Se semiconductor which is equal to the product between the three fundamental steps forming the detection process (Eq. 2.11). [124]

$$S = \left(\frac{5.45 \cdot 10^{13} e}{(\alpha_{en}/\rho)_{air}}\right) \cdot QE \cdot \left(\frac{(\alpha_{en}/\alpha)E_{ph}}{W_{\pm}}\right) \cdot CCE \tag{2.11}$$

In Equation. 2.10, the first term represents the radiation fluence per unit of Roetgen, the second term is the quantum efficiency of the sensing material and it indicates the effective absorption of radiation by the semiconductor, the third term shows the quantity of electron/hole pairs generated by the absorbed radiation and finally the CCE illustrates the capability of the device to collect the photocharges induced by the energy released. [117]

Typically, for a detector operating in current mode, the sensitivity can be extracted from the linear plot of the photocurrent VS dose rate as the slope of the curve.

Limit Of Detection

The limit of detection (LOD) expresses the minimum detectable dose of radiation which a sensor is able to transform in an electrical output signal. This figure of merit can define the range of application of the sensor as each of them operate in different irradiation condition. For example, while in medical diagnostic very low dose rates are employed (e.g. few µGy s^{-1} for mammography [125]), on the opposite side higher doses are used in radiotherapy (tens of mGy s^{-1} with total doses up to few Gy [126]). The definition which I used during the characterization of the detectors here presented, is the one offered by the IUPAC description [127] that corresponds to the minimum radiation which provokes a SNR = 3. Therefore, in order to obtain a low LOD two aspects have to be taken into account: a high sensitivity and a low level of noise (i.e. dark current).

2.4.2. Solid State Ionizing Radiation Detectors: Architectures

The radiation detectors based on semiconducting materials can be divided into three classes depending on their architecture which are depicted in **Figure 2.21**: photoconductors, photodiodes and phototransistors. [123]

The first two are two-terminals devices where the active semiconducting layer is placed between two metal electrodes to collect the induced charges. The geometry of these devices can be both vertical or co-planar (see **Figure 2.21a-b**). In the vertical structures, thicker semiconducting layer can be employed and the implementation of these devices in pixelated matrix can be easier. On the opposite

side, the co-planar geometry results simpler to fabricate and moreover, it ensures a good collection of the induced charges even at low voltages because it depends only on the distance between the metallic electrodes [128]. Moreover, in the photodiodes configuration (see **Figure 2.21c**), the sensor can be operated in reverse polarization inducing a depletion region which minimizes the dark current and leads to an improvement of the SNR and the LOD values.

The transistor architecture (see **Figure 2.21d**) is less implemented for ionizing radiation detection if compared with the other two geometries even if it offers a unique property. In fact, thanks to the gate electrode it is possible to modulate the detecting response by tuning the charge density in the conductive channel of the device. Another appealing peculiarity of this architecture is referred to the pixelated imager and the possibility of avoiding the introduction of addressing TFTs exploiting the capability of switching on and off the sensor itself. The most used transistor in the field of radiation detection is the MOSFET where the active layer in terms of detection is not the semiconductor but the gate dielectric. In fact, as it will be explained in the next sections, the charges induced by radiation within the insulating layer are suddenly trapped and provoke a shift in the V_{th} of the transistor which determine the output signal of the sensor.

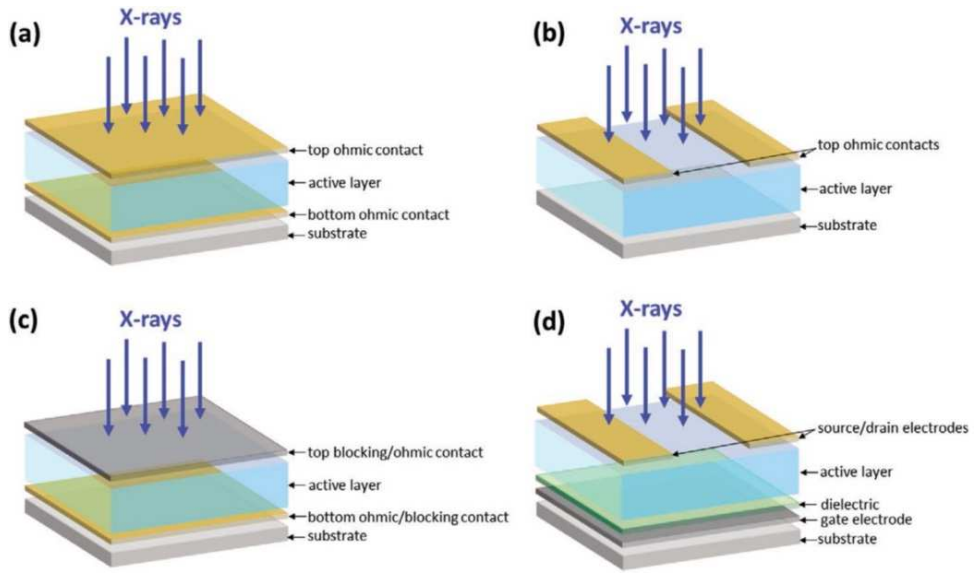

Figure 2.21 *Schematics of the typical architectures employed for direct radiation detectors: a) vertical photoconductor; b) co-planar photoconductor; c) photodiode; d) phototransistor.* [123]

2.5. Solid State Ionizing Radiation Detectors: State Of the Art

As it has already been mentioned in the previous sections, the direct detection of radiation offers two main advantages compared to the indirect process: a faster response and a higher SNR due to the single-step conversion of radiation into electrical output signal. Moreover, the employment of semiconducting active materials instead of gas-phase ones permits the miniaturization of the sensing devices maintaining a high efficiency of conversion of the radiation into electrical photocurrents.

Nowadays, many solid-state radiation detectors based on crystalline inorganic semiconductors such as Silicon, Germanium and other compounds as CdTe, SiC, CdZnTe are employed [129]. In fact, on one side they offer excellent performance

in terms of energy resolution but on the other hand they often have to be operated at cryogenic temperature and moreover they exhibit very high costs of production because of the high purity level necessary to obtain such a good performance.

Besides, in several fields of application (e.g. medical diagnostic and radiotherapy) an important quest is the development of large-area detectors able to cover extended surfaces. To attend this new requirement, as already discussed in the first Chapter, amorphous and polycrystalline materials are the only practical choice. Therefore, in order to fulfill this new necessity, in the last decades the scientific community and the industries focused on the search for alternative and novel materials to be implemented as the active volume of large-area radiation sensors [124].

Among the others (e.g. a-Si:H, and polycrystalline HgI_2, PbI_2, PbO, TIBr), amorphous Selenide (a-Se) is the benchmark material employed for the development of large-area radiation detectors and in particular for the realization of Flat panel X-ray Imagers (FPXIs). The schematic diagram of a FPXI is depicted in **Figure 2.22a**. It is formed by a large array of pixels as part of an active matrix array (AMA). An AMA is a two-dimensional array of single-detector in which each pixel has a TFT that can be externally addressed. The active matrix is then covered by a suitable photo-converting layer (e.g. stabilized a-Se) which is sandwiched with a top electrode in order to be biased. Each pixel contains a storage capacitor which collects the photocharges induced by the absorbed radiation. Then, the photocurrent can flow through the TFT to the multiplexer only when the specific pixel is addressed. In 1995 Rowlands and Zhao employed stabilized a-Se semiconductor layer to develop a FPXI for the first time [130]. Stabilized a-Se (a-Se alloyed with 0.2-0.5% As and doped with 5-20 ppm Cl) is currently the preferred

photoconductor for clinical X-ray image sensors because it can be quickly and easily deposited as a uniform film over large areas by vacuum deposition techniques, it has an acceptable X-ray absorption coefficient, good charge-transport properties for both electrons and holes and finally, thanks to the adding of two blocking layers, it presents a low dark current. The typical sensitivity value reported for a standard X-ray detector based on a-Se is 25 µC Gy^{-1} cm^{-2} [124]. Despite the optimal performances showed by a-Se, some important drawbacks are still present. The main issue is related to the operation voltages used to biasing the semiconducting layer. In fact, the typical value used in a-Se devices is 10 V/µm that means 2000 V of biasing for a 200 µm thick sensor [124].

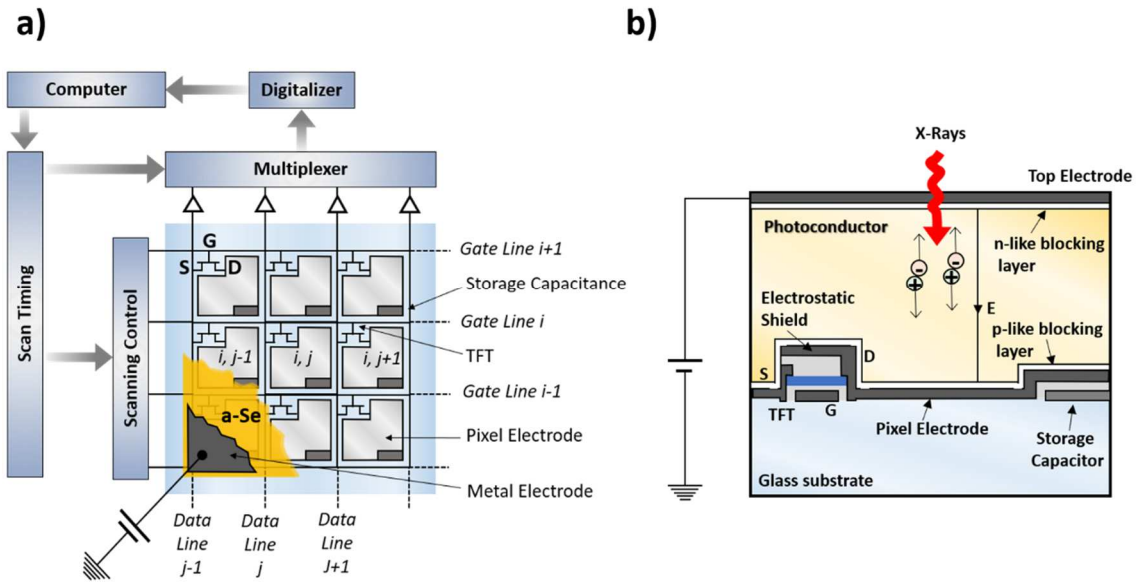

Figure 2.22 *a) schematic representation of a FPXI. The AMA is formed by several identical pixels which are entirely covered by the photoconductor and a top electrode. b) schematic cross section of a single pixel. Adapted from* [124].

In the last few years, thin films based on perovskites gained the interest of the scientific community for their implementation as active layers in large-area direct radiation detectors. The first proof of principle was published by Yakunin et al. in 2015 [131] and after that a huge improvement of this technology has been already achieved. The highest sensitivity value for this class of sensor has been reported by Hu et al. and it is equal to $1.22 \cdot 10^5$ µC Gy^{-1} cm^{-2} [132].

In this thesis, I present other two classes of materials able to fulfill the main requirements to develop a new generation of large area and flexible radiation detectors: organic semiconductors and amorphous oxide thin films, introduced in the next two sections.

2.5.1. Solid State Ionizing Radiation Detectors based on Organic Semiconductors

In the field of ionizing radiation detection, organic materials have been mainly employed in the indirect detection process. In fact, they have been deeply studied and implemented both as scintillating materials able to convert the high energy photons into visible radiation and also as semiconducting layer in the photodiode used to transduce the visible radiation into an electrical output signal. Only in the last years, they have been investigated for the development of direct detection systems and in this thesis I will deeply discuss this latter approach.

The organic semiconductors offer unique properties [133]. First, as largely discussed in **Chapter 1**, they can be deposited by solution at low temperature onto large areas. This possibility leads to the development of flexible detectors directly printed

onto large polymeric foils and able to cover curved surfaces. Second, they offer the possibility to easily chemically tailor their atomic structure, reaching the desired properties. Finally, their atomic composition mainly formed by low-Z elements (i.e. C, O, H) makes them human tissue equivalent in terms of radiation absorption. This important feature allows to skip all the calibration procedures of the detector during, for instance, the dose monitoring of a patient subjected to a radiation treatment.

Organic single crystals have been firstly employed as the active layer of X-Ray detectors offering a real-time, fast and box-shaped response [121], [134]–[137]. But the development of large-area devices and in particular of large-area ionizing radiation detectors is still not addressable with crystalline materials and for this reason this topic will not be treated in this thesis.

In 2007 Prof. Sellin et al. [138] gave the first proof of principle of direct radiation detection by organic thin film-based devices employing photodiodes with thick conjugated polymer as active layers. He tested several organic polymers such as poly[1-methoxy-4-(2-ethylhexyloxy)-phenylenevinylene] (MEH-PPV) [138], poly(9,9-dictyluorene) (PFO) [138], and poly(triarylamine) (PTAA) [139], [140]. These first devices showed moderate sensitivity values, however they highlighted for the first time the possibility to detect in real-time high energy radiation by organic-based devices.

As illustrated at the beginning of this paragraph, the chemical composition of the organic materials makes them optimal candidate for the radiation detection in medical field because of the human tissue-like behavior in terms of absorption. On the other side, the low-Z elements forming the active layer of this class of sensors poorly absorb high energy radiation and the optimization of the detection response

is the most challenging aspects of this technology. Considering the sensitivity as the most relevant figure of merit able to describe the efficiency of a sensing system, Equation 2.11 indicates that several pathways can be followed to enhance the detection performance. For instance, the active volume of the detector can be increased by employing thicker semiconducting layer but, on the other end this choice could bring to a loose of flexibility, a worse charge collection and an increase in the operating-voltage of the system.

Another strategy to improve the radiation response of organic-based detectors is based on increasing the cross section of interaction between the high energy photons and the active layer of the detector. With this aim, many researchers employed the blending of organic semiconductors with high-Z nanocomposites leading to an increase of the attenuation fraction of the device. Several examples based on this approach are reported in literature. First, Intaniwet et al. [141] tested a blend of bismuth oxide (Bi_2O_3) nanoparticles (NPs) and PTAA 20 µm thick active layer arranged in a photodiode geometry (**Figure 2.23a**). The sensitivity reached with the blended devices was 2.5 times higher than the PTAA-pure photodiode ($2 \cdot 10^2$ µC Gy^{-1} cm^{-3}). In a following work [142], they highlighted the differences between the introduction of metallic Ta NPs and insulating Bi_2O_3 NPs in organic polymers (PTAA and poly([9,9-dioctylfluorenyl-2,7-diyl]-cobithiophene) (F8T2) fabricating devices with the same architecture as the previously reported. Despite the higher attenuation mass of the Bi_2O_3 NPs, the Ta NPs based devices offered higher sensitivity, up to $4.34 \cdot 10^2$ µC Gy^{-1} cm^{-3}, probably due to a better charge transfer from the metallic nanostructures and the polymeric matrix.

Ciavatti et al. [143] reached a very high sensitivity ($S = 2.4 \cdot 10^5$ µC Gy^{-1} cm^{-3}) employing an organic photodiode doped with high-Z Bi_2O_3 NPs (**Figure 2.23b**).

Further, a comparison between the charge-injection condition (forward bias) and charge-collection condition (reverse bias) is reported.

A similar approach was followed by Ankah et al. [144] who reported the results obtained with a bulk heterojunction (BHJ) fabricated blending inorganic lead sulfide (PbS) nanocrystal quantum dots in a semiconducting polymer matrix of P3HT:PCBM (**Figure 2.23c**). More recently, Thirimanne et al. [145] reported the results achieved with a similar BHJ photodiode with a 10-30 µm thick active layer made of organic P3HT:PCBM blended with Bi_2O_3 NPs (**Figure 2.23d**).

Buchele et al. [146] proposed a different strategy in order to push the sensing performances by organic devices, employing a quasi-direct mechanism of detection. They showed the results obtained with a photodiode formed by an active layer based on scintillating terbium-doped gadolinium oxysulfide (GOS:Tb) X-ray absorbers blended in a polymer BHJ (P3HT:PCBM) (**Figure 2.23e**). They reported sensitivities up to $S = 7.3 \cdot 10^3$ µC Gy^{-1} cm^{-3}.

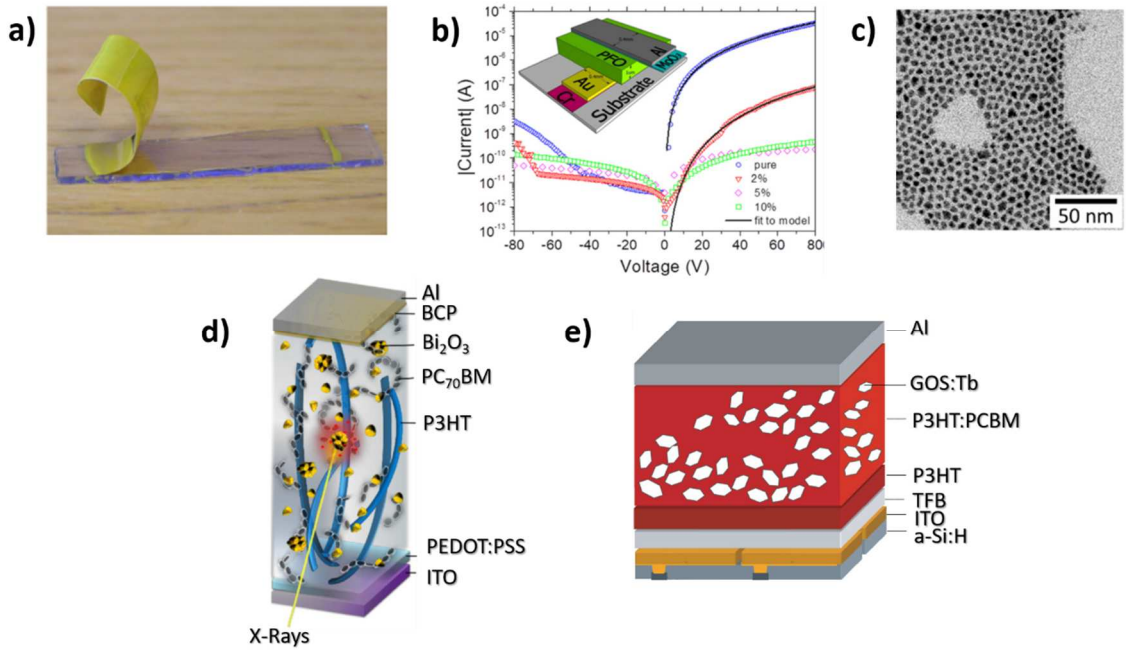

Figure 2.23 *Blending of inorganic high-Z nanostructures in polymeric matrixes. a) Picture of the blended PTAA with bismuth oxide (Bi_2O_3) nanoparticles (NPs) pilled of from the glass-ITO substrate* [141]*. b) Schematic and Current-Voltage curve of an organic photodiode doped with high-Z Bi_2O_3 NPs* [143]*. c) HR-TEM image of PbS quantum dots embedded in a P3HT:PCBM bulk hetero-junction* [144]*. d) schematic of a bulk heterojunction photodiode with a 10-30 µm thick active layer made of organic P3HT:PCBM blended with Bi_2O_3 NPs* [145] *and e) of a photodiode formed by an active layer based on scintillating terbium-doped gadolinium oxysulfide (GOS:Tb) X-ray absorbers blended in a polymer BHJ (P3HT:PCBM)* [146]*.*

The major limit of this approach is related to the charge collection efficiency of these devices. In fact, the introduction of nanostructures in polymeric matrixes often degrades the transport properties of the latter and moreover, aggregates and clusters have been observed trying to increase over a certain percentage the concentration of the NPs. Second, the blending of the organic polymers with inorganic nanocomposites leads the loose of human-like absorption which is a peculiarity of organic-based sensors. Finally, the thick active layers employed in these devices imposes very high voltage operation.

In order to overcome these limitations, other approaches have been proposed. For instance, to maintain the human-tissue equivalence, blending of the organic active layer with other organic compounds has been tested. This strategy can improve the transport properties of the device by enhancing the charge collection of the sensor. Some examples are reported in literature such as the blend of PTAA with TIPS-pentacene [147] and a polymer matrix blended with carbon nanotubes [148].

Finally, a novel strategy to enhance the efficiency of the organic radiation detectors is based on the exploiting of the physical phenomenon that occurs when the high energy photons interact with organic thin film devices. This is known as Photoconductive Gain Effect (PG) and it will be deeply discussed in the next paragraph.

Following all these enhancement strategies, organic detectors reached a good level of performances and they have been recently tested under actual irradiation conditions used in medical diagnostic (e.g. radiography) and radiotherapy demonstrating the potentiality of this technology in order to develop a new generation of medical dosimeters and imagers. [149]–[151]

In this thesis I will show additional and very effective strategies exploited to further boosting the detection performance of organic thin film-based devices (see **Chapter 4**).

2.5.1.1. Photoconductive Gain Effect

In highly ordered crystalline semiconductors and in polycrystalline film-based photodiodes, the detection of high energy photons is ruled by charge collection (see

Figure 2.24a). On the opposite side, Photoconductive Gain [123] is the physical phenomenon occurring in a semiconductor thin film-based radiation detector. As it is depicted in **Figure 2.24b**, when the electron-hole pairs are generated by the absorbed radiation, the trapping of minority carriers can induce an amplification of the collected photocharges by a gain factor G. In order to maintain the charge neutrality, the majority carriers are continuously re-injected from the ohmic contact inside the conductive channel contributing more than one time to the total photocurrent. Thus, the internal quantum efficiency of the detector exceeds 100% and the sensitivity values result very high. The inner amplification process can be described using the factor G (Eq. 2.12) which is expressed as the ratio between the recombination time (τ_r) and the transit time (τ_t) (Eq. 2.13 and 2.14 respectively).

$$G = \frac{\tau_r}{\tau_t} \tag{2.12}$$

$$\tau_r = \frac{\alpha}{\gamma}\left[\alpha\, ln\left(\frac{\rho_0}{\rho_X}\right)\right]^{\frac{1-\gamma}{\gamma}} \tag{2.13}$$

$$\tau_t = \frac{L^2}{\mu\, V} \tag{2.14}$$

where α, γ and ρ_0 are material-specific constants describing the characteristic time-scale and the dispersion of trap states, and a reference carrier density respectively, ρ_X is the photogenerated carrier concentration, L is the channel length, μ is the electrical mobility and V is the applied bias.

The recombination and the transit time are the two characteristic times of the system describing the time-scale of recombination of the trapped minority carriers and the time of transit of the majority carriers through the conductive channel respectively.

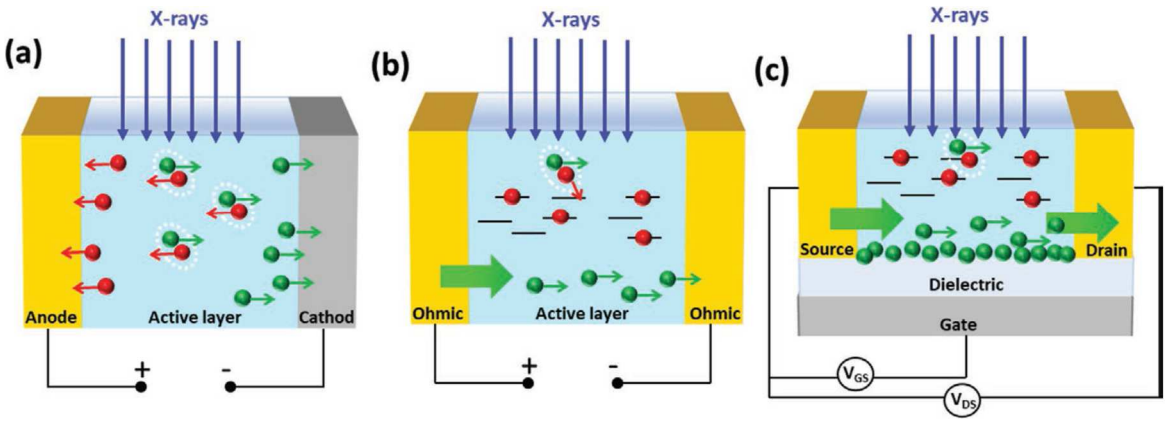

Figure 2.24 *Schematics of the direct X-ray detection processes. a) Charge collection in photodiode architecture. b) Photoconductive gain in photoconductor architecture. c) Photoconductive gain in phototransistor architecture.* [152]

In 2016, the photoconductive gain effect model has been introduced by Basiricò et al. in order to modelling the high X-ray response of an organic thin film photoconductor based on TIPS-pentacene and derivatives [153]. In this work, they demonstrated how, despite the extremely low X-ray absorption (about 0.0015% for 100 nm thick TIPS-pentacene polycrystalline film) due to the low-Z elements forming the absorbing material and the low thickness of active layer, it was possible to record very high photocurrents resulting in very high sensitivity values ($S = 7.7 \cdot 10^4$ μC Gy^{-1} cm^{-3}). Moreover, developing the analytic kinetic model, the authors explained the slow recombination dynamics through stretched exponential curves and they calculated gain values up to $4.7 \cdot 10^4$.

A first strategy to maximize and exploit the photoconductive gain mechanism is based on the employment of a phototransistor architecture. In fact, as it is depicted in **Figure 2.24c**, the use of the gate polarization allows to increase the charge density in the OFET channel (i.e. ρ_0), leading to an enhancement of minority carriers trapping and majority carriers conduction. Further in over-threshold condition τ_t decreases. Thanks to these effects, in 2017 Lai et al. reported a higher

gain factor ($G = 3 \cdot 10^5$) and an higher sensitivity $4.8 \cdot 10^5$ $\mu C\ Gy^{-1}\ cm^{-3}$ with respect for what it was obtained with a coplanar architecture [154].

2.5.2. Solid State Ionizing Radiation Detectors based on High Mobility Oxide Thin Films

Many microelectronic dosimeters are realized in silicon-based complementary metal-oxide semiconductor (CMOS) technology and consist in diode or transistor structures. In this paragraph I will focus on the radiation-sensitive Field Effect Transistor (RADFET) which employs a thick silicon oxide (SiO_2) layer as the active volume for high-energy radiation detection. When a standard Metal-Oxide-Semiconductor Field Effect Transistor (MOSFET) is irradiated by high-energy photons, electron-hole pairs are generated within the dielectric SiO_2 layer due to the absorption of energy from the radiation. While the electrons either recombine or are collected by the gate electrode in a timescale of a few picoseconds, holes have lower mobility and remain trapped in long-term sites inside the insulator longer. These trapped holes build-up a net positive charge in the SiO_2 which interferes with the electric field imposed by the gate electrode and causing a negative shift of the MOSFET Threshold Voltage (V_{th}) (see **Figure 2.25a, b**). The Threshold voltage shift (ΔV_{th}) is proportional to the dose absorbed (D) in the oxide and can be monitored during irradiation or at any time after irradiation due to the integration of the information about the radiation exposure history [155]. The RADFET sensitivity is defined as it is reported in Equation 2.15 [156].

$$S\left(\frac{V}{Gy}\right) = \frac{\Delta V_{th}}{D} \tag{2.15}$$

Typical values of sensitivity reported for commercial devices span between 0.05 and 0.3 V/Gy depending on oxide thickness and photon energy [155].

Assuming that the holes are uniformly distributed within the dielectric layer, the ΔV_{th} can also be expressed as in Equation 2.16.

$$\Delta V_{th} = -\frac{qN_{Ox}}{C_{Ox}} \tag{2.16}$$

where q is the electronic charge, N_{Ox} is the number of trapped holes per unit area inside the SiO_2 layer and C_{Ox} is the capacitance per unit area of the oxide.

The finite number of traps in the oxide layer leads to a saturation of the RADFET effect and the reaching of a threshold voltage plateaus. Several studies reported in literature illustrate some strategies to recycle the saturated RADFETs employing current or thermal annealing [157], [158].

The RADFETs can be operated both in passive mode or by applying a positive voltage to the gate electrode in order to inhibit the recombination of pairs and enhance the sensitivity and the storage capacity of the sensor. Besides, the incorporation of a floating gate in monolithic MOSFET has been achieved, and the integrated chip was employed in miniaturized, low-power dosimeters with wireless data transmission [159]–[161].

The small size of dosimetric volume, ability to permanently store accumulated dose, dose-rate independence and ease of readout make RADFET ideal for many applications [120]. They have been employed in space mission to detect the space radiation on satellites [162] (**Figure 2.25c**) and in particular they have shown particular strengths for in vivo dosimetry during radiotherapy [163]. In fact, they

can be placed on the patient's skin to monitor the delivery dose on a patient subjected to radiation treatments. For instance the *MOSkin* is a MOSFET mounted underneath a thin plastic layer which has been tested for several in-vivo dosimetry application (**Figure 2.25d**) and other radiation diagnostic applications [164]–[169].

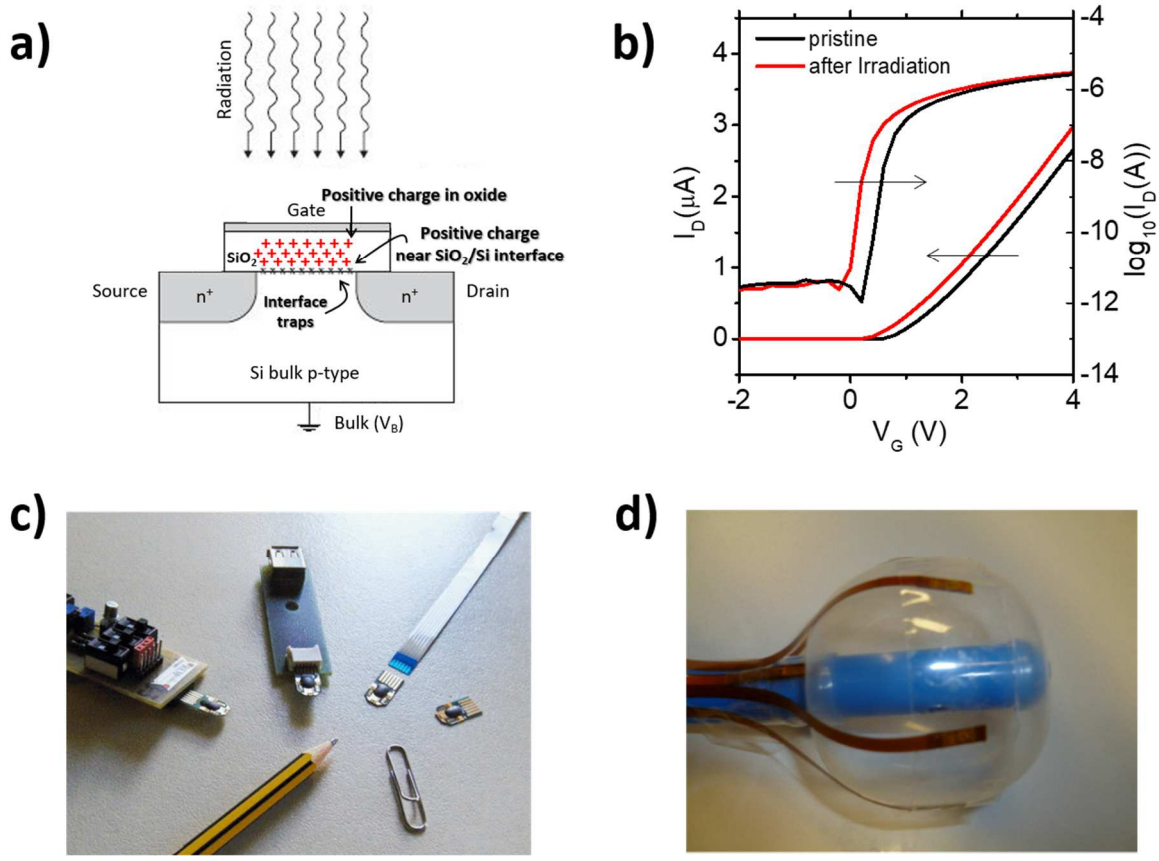

Figure 2.25 *a) Holes trapping in the SiO2 dielectric induced by radiation* [170]. *b)Shift of the RADFET threshold Voltage (V_{th}) due to the absorption of radiation. b) RADFET employed in space missions* [162] *and c) MOSkin mounted over an endorectal balloon for in-vivo dosimetry* [165].

The main limitation presented by the RADFET technology is related to the low stopping power of SiO_2. Moreover, the CMOS technology is incompatible with the development of large area and flexible devices. For these reasons, the search of new materials is essential to enhance the efficiency of this class of radiation detectors.

In **Chapter 5**, I will illustrate how to implement amorphous oxide thin films to overcome these two major limitations achieving an enhancement of the detection performance of the RADFET technology.

2.6. Proton Detectors: State Of the Art

The development of detectors for protons is a long-lasting research topic not only for fundamental applications, but also, more recently, for monitoring energy and fluences of particles in ion beam applications. Among the others, the most demanding application for which accurate measurements are needed is hadron therapy of cancer. In this application, ion beams (and in particular proton beams) are used for the controlled treatment of cancer by the delivery of the prescribed amount of dose to the tumor, sparing the surrounding healthy tissues as much as possible [171]. Hadron therapy and proton therapy are preferred to radiotherapy to treat all those tumors close to organs at risk because of the different releasing of energy depicted in **Figure 2.19**. In order to assure the safe, effective and consistent radiation delivery, accurate monitoring of the beams and measurements of the absorbed dose are essential. In this paragraph, the main proton detectors employed nowadays with this aim are briefly described. For a complete discussion, the reader can refer to several reviews and books reported in literature [113], [120], [172], [173].

The detectors employed for the monitoring of the proton beams have the crucial role to continuously measure the proton fluences and the transversal distribution to guide the irradiation. Arrays of parallel plate ionization chambers, with either a

single large electrode or electrodes segmented in strips or pixels [174], together with multi-wire ionization chambers [175] are the most employed detectors for this purpose. These beam position monitors are characterized by 1.5-5 mm strips/wires pitch aiming a spatial resolution below 0.3 mm. Moreover, they must be able to detect continuous or pulsed irradiations (1–10 μs) with proton fluxes in the range from 10^8 to 10^{11}–10^{12} protons/s. Also, Faraday cups and calorimeters are widely used to monitor the proton beam fluences with a high accuracy.

Other detectors are employed to monitor the dose distribution delivered to the patients. The main characteristics of these sensors are:

- The tissue equivalence to limit the perturbation of the beams.
- The active volume shall be small enough to provide good spatial resolution and to be able to detect steep gradient of doses.
- They should feature 2D mapping capabilities.
- Energy and dose rate independence.
- Real-time monitoring to speed up the verification and improve the effectiveness.

So far, a single sensor which fulfil all these requirements does not exist and different detectors are used for the monitoring of the delivered dose at single point or the longitudinal and transverse profile.

The most widely employed dosimeters for point dose measurements are pinpoint, cylindrical and plane-parallel integrate circuits (ICs) properly calibrated and embedded within water or plastic phantoms [176].

The longitudinal profile of the delivered dose is defined by the trend of the ionization charges integrated over a plane perpendicular to the proton beam as a function of the penetration depth. This profile is mainly adopted to monitor the range and the Bragg peak depth of the irradiating beam. For the measurement of the Integrated Depth-Dose (IDD) profile, plane-parallel ICs are commonly used because of their high accuracy and their independence from the energy. The main drawback related to this technology is the difficulty to cover a large enough area to be able to detect all the secondary scattered products coming from the primary beam (Ø ≈ 8-12 cm). To achieve the longitudinal profile, the movement of the sensor is employed [177] or alternatively Multi-Layer Ionization Chambers (MLICs) which let measure the dose simultaneously at different depth can be used [178].

The transversal dose distribution is commonly measured in to assess the spatial homogeneity and dimension of the beam. Here the spatial resolution is the key-point and it can span in the range between 10 mm to 0.1 mm. Several dosimeters can be employed with this aim such as radiochromic or radiographic films [179], scintillating screens [180], silicon microstrips, MOSFETs [166], [181] and diamond array detectors [182].

Both radiographic and radiochromic films produce a relative dose-induced map which has to be read by a photometric device and need to be calibrated in terms of absorbed dose. the main difference between the two is that radiochromic films can be operated in the daylight while the radiographic is highly light sensitive and must be kept in dark. The main advantages related to these technologies are the human tissue equivalence, the weak energy dependence, a linear response over a large dose range, a good spatial resolution (0.1-0.2 mm) and the mechanical flexibility. On the other side, the main drawback presented by these films is related

to the readout system which is not in real-time and it has to follow a complex protocol for the calibration.

Scintillating screens are formed by a plate coated with a scintillating material (e.g. Gd_2O_2S:Tb) and are typically coupled with a CCD camera used to acquire the emitted light. The luminescence distribution results proportional to the absorbed dose, presenting a high spatial resolution (0.5 mm) and a good linearity up to high proton fluences. While radiochromic films provide a single integrated transversal dose at the end of the delivery and must be digitalized and analyzed off-line, the scintillating screens can be operated in a real-time mode employing an instantaneous optical-electrical readout. Plastic scintillators are also employed for beam diagnostics and in particular, scintillating fibers recently showed very good results [183]. The main drawback presented by this class of sensors is related to the light detection which has to be very sensitive in order to obtain reliable results. For this reason, a complex readout chain must be implemented to this system including photomultiplier tubes and photomultipliers.

Two-D arrays of ionization chamber can also be employed as dosimeter [184]. The main limitation here is determined by the poor spatial resolution.

Silicon-based solid-state detectors (e.g. MOSFETs, Si microstrip) are largely used as dosimeters for proton beams offering high signals and a very high spatial resolution ($<$ mm). The main limitations presented by this class of detectors are the non-water equivalence, the energy-dependent response, the impossibility to realize large area and flexible detecting systems.

In this thesis (see **Section 4.4**) I will discuss the potentiality of organic semiconductors as active material of a novel generation of direct proton detectors for flexible and large area sensing during medical treatment.

3.

Materials and Methods

In this third chapter, the materials and the experimental methods involved in this dissertation are presented. In the first Section, a graphical summary of the several device architectures of the sensors tested is shown. The second Section is dedicated to the different materials implemented in these devices while in the third section, some on the fabrication techniques are discussed. Finally, all the characterization methods followed in this thesis are summarized. In particular, the electrical and morphological characterizations are presented. Besides, an entire section is dedicated to the photocurrent spectroscopy experiment. In conclusion, all the experimental setups employed for the characterization of the radiation sensing performance are described.

3.1. Devices structure and architecture

In this dissertation, the results obtained by several solid-state detectors are shown. In this paragraph a summary of the different geometries, materials and fabrication techniques that I implemented is given.

I mainly tested two different geometries which have been already presented in **Section 2.4.2**: the two-terminals co-planar architecture and the Bottom Gate-Bottom Contacts (BGBC) thin film transistor configuration. A comparison between these two structures is shown in **Section 4.1**.

In **Figure 3.26** the typical two-terminals co-planar architecture is depicted, and the main materials and deposition techniques employed are listed [153]. This kind of samples has been used to achieve the results shown in **Section 4.3** and **Section 4.4**.

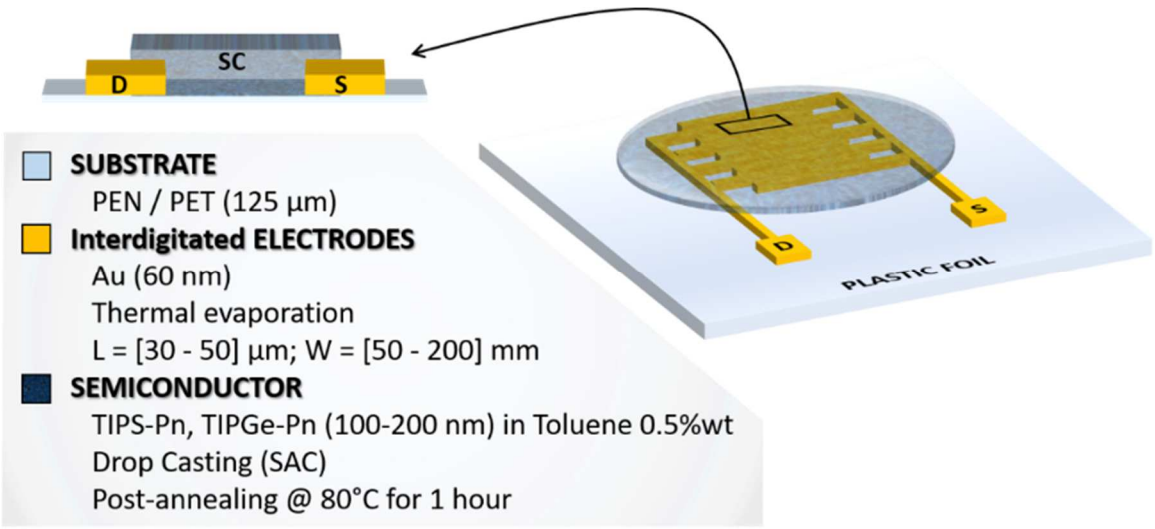

Figure 3.26 *Two-terminal co-planar device based on organic semiconductors.*

In **Figure 3.27** the Bottom Gate – Bottom Contacts Organic Field Effect Transistor structures realized for several classes of detectors are shown and a list of the materials and the main fabrication techniques is provided.

In particular, the OFETs depicted in **Figure 3.27a** have been fabricated at the *University of Cagliari* by Prof. A. Bonfiglio's research group and they have been employed to reach the results reported in **Section 4.2.2**.

The transistors shown in **Figure 3.27b** have been produced at the *Institut de Ciència de Materials de Barcelona* (ICMAB, Spain) by Dr. M. Mas Torrent's research group and these allowed us to conduct the studies discussed in **Section 4.2.1.1** and **Section 4.2.3**.

Finally, I realized the devices depicted in **Figure 3.27c** during my six-months stay at the *Columbia University* (New York, USA) hosted by Prof. I. Kymissis. By these OFETs I obtained the results described in **Section 4.2.1.2** and **Section 4.2.5**.

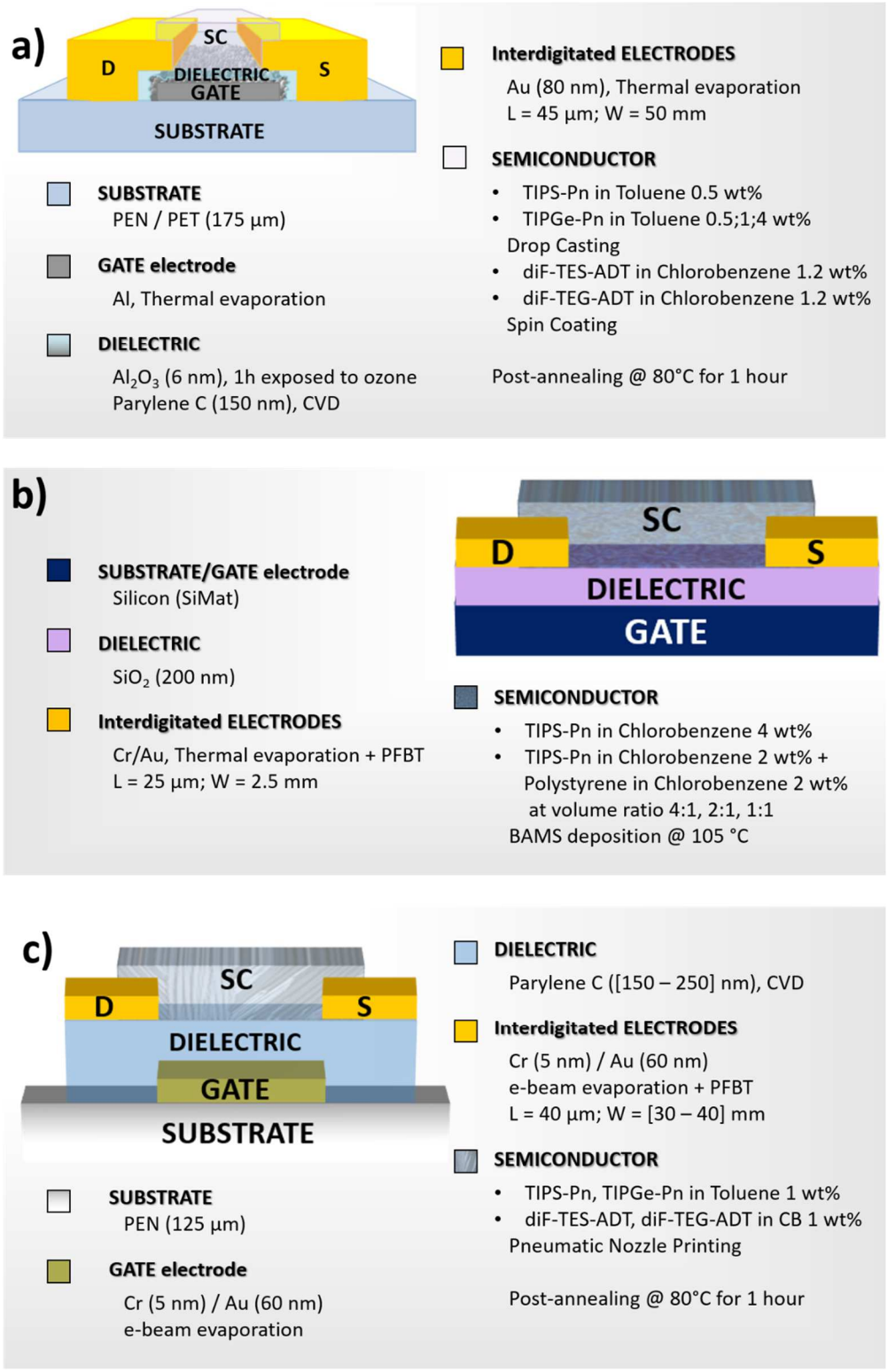

Figure 3.27 *Three different OFET structures employed in this dissertation. a) Ultra-low voltage OFET designed and fabricated by Cosseddu et al.* [185]*. b) OFETs fabricated at ICMAB (Barcelona, Spain) employed the BAMS technique developed by Mas-Torrent et al.* [52]*. c) OFETs designed and fabricated at Columbia University during my 6-months spent in the laboratories of professor Kymissis.*

Finally, in **Figure 3.28** the Bottom Gate - Bottom Contacts Thin Film Transistor based on HMAOs is reported. These devices have been fabricated at the *Faculdade de Ciências e Tecnologia, Universidade Nova de Lisboa* (FCT UNINOVA, Portugal) and the results achieved by this class of sensors are described in **Chapter 5**.

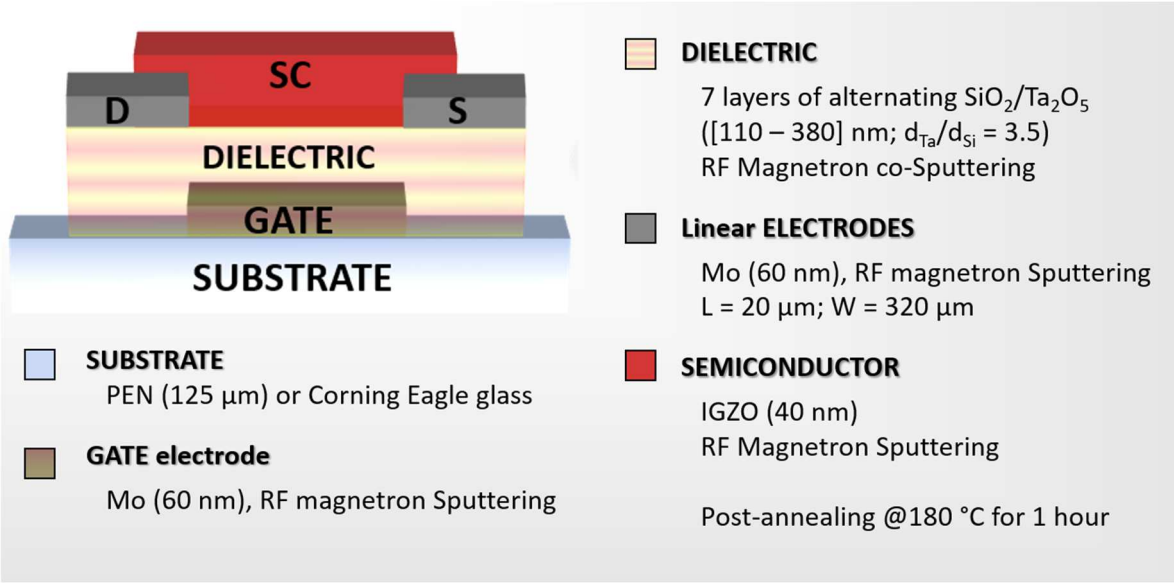

Figure 3.28 *HMAO TFTs realized and characterized as Radiation Detectors. The devices have been fabricated in the clean room of CENIMAT at Uninova (Lisbon, Portugal).*

All the transistor structures have been fabricated following the standard photolithography process (*Karl-Suss MA6* mask aligner). In particular, the different layers have been patterned using positive photoresist (e.g. *S1811*, *AZ6632*), developed by metal ion free developer (e.g. *AZ726MIF*, *AZ300MIF*), and etch by dry or wet etching (*TRION PHANTOM III RIE*).

In particular, in the case of the samples fabricated at the Columbia University I followed the entire process starting from the design of the layout (*LayoutEditor*) and the realization of the photo-lithography masks (*DWL 66+ laser writer*).

3.2. Materials

In the following sections, a brief description is given regarding the main materials implemented to develop the here studied devices. The first paragraph is focused on the flexible substrates, the core is centered on the different semiconducting materials and finally the implemented dielectrics are described.

3.2.1. Plastic substrates: PET and PEN

One of the purposes of this thesis is the demonstration of the radiation detection abilities of solid-state sensors fabricated onto flexible substrates employing deposition techniques scalable onto large areas (see **Figure 3.29a**). With this aim I fabricated the devices preferably onto plastic substrates and in particular onto *Polyethylene* (PET) and *Polyethylene naphthalate* (PEN) 125 µm thick foils. The two chemical structures are reported in **Figure 3.29b,c**. Before the fabrication process, the substrates have been cleaned by a subsequent 15 minutes ultrasonic baths in acetone and isopropyl alcohol followed by a rinsing in de-ionized water and drying under nitrogen flow.

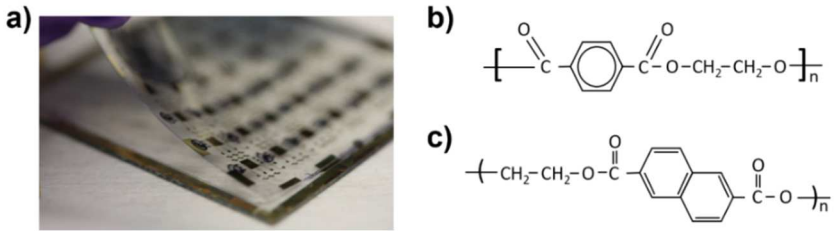

Figure 3.29 *a) Picture of a flexible radiation detector fabricated onto a plastic foil. Chemical structures of b) PET and c) PEN.*

The main properties of the two plastics are reported in **Table 3.2**. The main difference between the two is based on the thermal properties: PEN can be employed for processes which require higher temperatures (if compared with PET) up to 160 °C.

	Properties	*Max Deposition Temperature*
PET	Optical transparent; good chemical resistance; inexpensive; moderate moisture absorption; good flexibility (tensile strength [190-260] MPa)	120 °C
PEN	Optical transparent; good chemical resistance; inexpensive; moderate moisture absorption; Young modulus higher than PET	160 °C

Table 3.2 *Main properties of PET and PEN substrates* [75].

3.2.2. Organic Semiconductors

As organic semiconductors, I mainly focused on acenes [186]. This is a class of organic compounds and polycyclic aromatic hydrocarbons made up of linearly fused *n*-benzene rings. Pentacene (i.e. n=5) is the acene, and more in general one of the organic semiconductors, which exhibits high performances in terms of stability and electrical mobilities (> 1 cm^2 V^{-1} s^{-1}) [187]. Despite the common use as active layer in several electronic applications, it presents two main limitations. First, it is insoluble in the most of organic solvents and for this reason it is not possible to deposit it from solution by the low-cost and scalable techniques described in **Chapter 1**. Also, pentacene crystallize in the *edge to face herringbone* structure

(see **Figure 3.30a**) which provides a poor π-stacking with a consequent poor dispersion of the electronic bands in the solid and limited transport properties.

With the aim of overcome these two main issues, the functionalization of pentacene has been extensively exploited in the last decades by means of the substitution of different functional groups [188]–[191]. These functionalized molecules on one side result soluble in organic solvents making possible to deposit them from solution by spin coating [192], drop casting, meniscus shearing [193] and printing techniques. On the other side, they present a greater π-stacking and an improvement of the transport properties. For instance, the substitution of the bulky trialkylsilylethynyl substituent facilitates the close cofacial face-to-face arrangement of the acene backbone (see **Figure 3.30b**), and results in dramatic improvements in the solubility, stability and electrical properties.

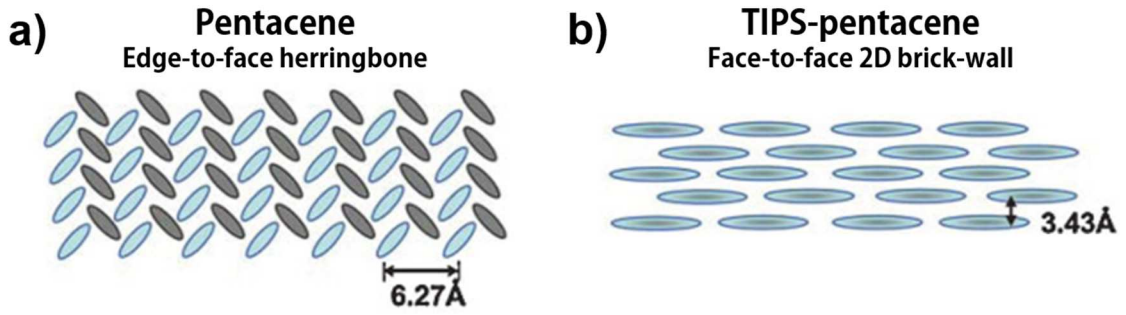

Figure 3.30 *Molecular packing arrangements with average distances between the π-faces in a) Pentacene and b) TIPS-Pn.* [194]

In particular, in this work I employed two functionalized acenes by means 6,13-bis(triisopropylsilylethynyl)pentacene (**TIPS-Pn**, $C_{44}H_{54}Si_2$) [191], [195] and 2,8-difluoro-5,11-bis(triethylsilylethynyl)anthradithiophene (**diF-TES-ADT**, $C_{34}H_{36}F_2S_2Si_2$) [196]–[198]. Their chemical structures are reported in **Figure 3.31a**.

Both these organic small molecules have been extensively studied in the last years because of their good properties among the soluble organic small molecules in terms of transport properties and stability. They have been employed as the active layer of OFETs offering high electrical mobilities up to 20 $cm^2V^{-1}s^{-1}$ [39].

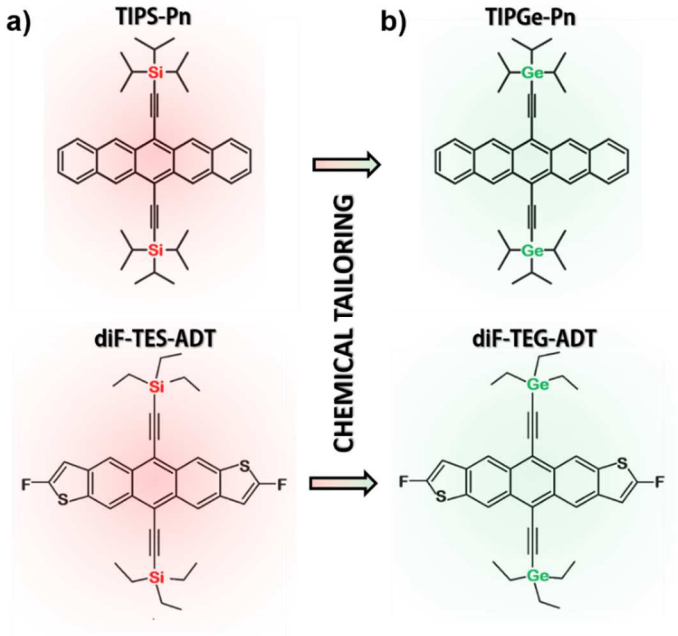

Figure 3.31 *Molecular structure of a) TIPS-Pn, diF-TES-ADT and b) the chemically tailored TIPGe-Pn and diF-TEG-ADT.*

Moreover, in order to enhance the radiation detection performance of the organic-based sensors I exploited another unique characteristic of organic semiconductors that is the possibility to chemically tailor their molecular structure in an easy way. With this purpose, I worked with two synthetized molecules developed by J. E. Anthony et al. (i.e. triisopropyl- germanylethynylpentacene (**TIPGe-Pn**, $C_{44}H_{54}Ge_2$) and 5,11-bis(triethylgermylethynyl)anthra- dithiophene (**diF-TEG-ADT** $C_{34}H_{36}F_2S_2Ge_2$) in which the two Silicon atoms present in TIPS-Pn and diF-

TES-ADT have been substituted with two Germanium atoms. Both the molecular structures of TIPGe-Pn and diF-TEG-ADT are reported in **Figure 3.31b**. Besides, it has been demonstrated that in both these Ge-based molecules the greater molecular packing enhances the transport properties if compared with the standard Silicon-based counterparts [45], [199], [200].

Finally, with the aim to improve the electrical properties of the organic devices, I employed some OFETs in which the active layer is formed by a blend of TIPS-Pn and polystyrene (PS). In fact, it has been demonstrated that the blending of the organic small molecules and inert dielectric polymers (e.g. polystyrene) leads to easier processing, better control of the solution viscosity, greater uniformity throughout the film, and even vertical demixing of the blend constituents [201], [202].

In this thesis, the organic semiconducting layers have been deposited from solution employing several deposition techniques. In particular, among the procedures described in **Chapter 1**, I employed the drop casting, the blade coating, the BAMS technique and the Pneumatic Nozzle Printing. The organic molecules have been dissolved in appropriate organic solvent (e.g. Toluene or Chlorobenzene) in different concentration in the range between 0.5%wt and 4%wt depending on the adopted deposition technique.

3.2.3. High Mobility Amorphous Oxide Semiconductors

As AOS I implemented the amorphous indium-gallium-zinc oxide (a-IGZO). As it has been discussed in **Chapter 1**, in this class of multicomponent oxide

semiconductors, the different cations can be mixed in different percentage and consequently it is possible to tune the properties of the final compound. In particular in a-IGZO, In^{3+} cations are the main elements of the conduction band, Ga^{3+} limits the free charges in the semiconductor creating strong bonds with oxygen and lowering their vacancies and Zn^{2+} prevent the crystallization of the material assuring the maintaining of the amorphous phase.

In this thesis, the a-IGZO has been sputtered from a multi-component target with (2:1:1) (atomic In/Ga/Zn ratio) composition with the addition of oxygen to the argon flow in order to keep controlled the self-doping of the final semiconducting layer.

3.2.4. Dielectric Layers

In this thesis, I employed mainly three different materials as the insulating layers of the developed thin film transistors.

1. **Al_2O_3 + parylene C** in some of the OFETs as deeply discussed by P. Cosseddu et al. in [185];
2. **Parylene C** in some other OFETs fabricated at the Columbia University in New York City;
3. **SiO_2/Ta_2O_5 multilayer dielectric** implemented as the active layer of the radiation detectors based on AOSs.

In the next two sections, a brief description of the Parylene C and the high-k dielectrics are reported.

3.2.4.1. Parylene C

Parylene is a polymer which belongs to the family of poly(p-xylylene). It consists in a linear chain of Benzene rings with two methilene groups replacing two hydrogen atoms on opposite sides of the benzene ring and serving as coupling links for the polymer. Parylene C differs from the standard one because of the substitution of a Cl atom instead of one of the aromatic H. The molecular structure of the monomer is depicted in **Figure 3.32**.

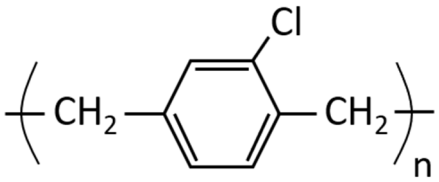

Figure 3.32 *Chemical structure of Parylene C.*

The main properties of Parylene C are the following:

- High crystallinity;
- Low permeability to gases and moisture;
- Optical transparency;
- Biocompatibility;
- Uniform thickness and good dielectric properties ($\varepsilon \sim 3$);
- High mechanical flexibility;
- Compatibility with most of the solvents and fabrication processes employed for the development of electronic devices;

- Capability to form layers perfectly conformable to the substrate.

Accordingly to all these properties, Parylene is often employed in flexible electronic devices both to encapsulate the systems preventing the degradation due to ambient conditions [203], and as dielectric layer in TFTs.

In this thesis, I implemented Parylene C as dielectric layer in several OFETs. It has been deposited by Chemical Vapor Deposition (CVD) as it is deeply discussed in **Section 3.3.2**. The thicknesses of the layers vary in the range between 150nm and 250 nm.

3.2.4.2. SiO_2/Ta_2O_5 multilayer dielectric

In this work, as insulator in AOS TFTs, a multilayer dielectric has been employed using a co-sputtering technique with SiO_2 and Ta_2O_5.

This multilayer structure offers a twofold advantage combining the properties of both the materials employed.

On one side Ta_2O_5 belongs to a class of insulator called *high-k dielectric*. As it has been discussed in **Chapter 1**, in the field effect transistors the creation of the conductive channel of the device is ruled by the capacitive behavior of the gate/insulator/semiconductor structure. In order to achieve a high carrier density with low operative bias, a high capacitance of the insulating layer has to be ensured. For this purpose, one option could be to decrease the dielectric thickness, but this can lead to the increase of the undesired leakage current. As alternative *high-k dielectric* can be employed to increase the capacitance even with the same dielectric

thickness. In fact, these materials show higher dielectric constant than for example SiO_2 and for this reason it is possible to induce a high carrier density in the TFTs channel using minimal gate operating voltage even in thick dielectric which can prevent the leakage current. The main drawback of this class of insulators is linked to their energy bandgap. In fact, usually for most metal oxide dielectric E_G is inversely proportional to the dielectric constant. And so, even if the high-k materials allow the realization of thicker dielectric layer preserving the capacitance, if the E_G is too low, leakage current can still remain an issue.

On the other side, silicon dioxide presents a very high energy bandgap (i.e. $E_G \sim 8.9$ eV) which successfully prevents the leakage current. For this reason, by mixing a high-k/low-E_G oxide (e.g. Ta_2O_5) with a low-k/high-E_G oxide (e.g. SiO_2) it is possible to achieve a gate dielectric which allows low operation voltage, low leakage current and besides it assures an amorphous structure with a smoother surface with improved interface properties [204].

Moreover, this dielectric multilayer can be deposited by RF sputtering (see **Section 3.3.1.1**) without intentional substrate heating during deposition which makes this technique compatible with the fabrication of electronic devices onto flexible polymeric foils.

Finally, it is noteworthy that in this kind of AOS TFTs the active layer in terms of radiation detection is formed by the here described multicomponent insulator, as it will be deeply discussed in **Chapter 5**. As it has been highlighted for the organic semiconducting molecules (**Section 3.2.2**) the adding of a high Z element (e.g. Ta, $Z_{Ta} = 73$) increases the cross section of interaction between the high energy photons and the atoms of the sensor leading to an improvement of the efficiency of the detector.

3.3. Fabrication techniques

In this paragraph, the main fabrication techniques employed in this work are described. In particular, the deposition methods employed for the realization of the devices are discussed and finally, a treatment used for the electrodes' functionalization is illustrated. The deposition techniques from solution employed for the realization of the organic semiconducting layers have already been listed in **Section 3.2.2** and more details will be given in **Chapter 4**.

3.3.1. Physical Vapor Deposition (PVD)

In PVD techniques, atoms or molecules are physically removed from a source material and transported through high-vacuum to a substrate, where they form a thin film. Depending on the mechanism which allows to remove the material atoms from the sources, several techniques can be distinguished. In this research I mainly employed three of these which will be described in the following sections.

3.3.1.1. Sputtering

The sputtering technique is based on the creation of a gaseous plasma and the consequent acceleration of the generated ions in the direction of a target composed by the material to deposit with its consequent erosion. In fact, due to the transfer

of energy, the accelerated ions are able to kick out from the target atoms of the desired material in the form of neutral particles. As it is depicted in **Figure 3.33a**, these ejected atoms reach the substrate placed on the opposite side of the target and they start forming the thin film. This process occurs in a vacuum chamber containing two electrodes: the cathode including the target and the anode covered by the substrate generally grounded. An inert gas (e.g. Argon) is introduced in the chamber and it is suddenly ionized or excited by all the electrons present in the chamber and accelerated between the two electrodes. If the Ar^+ present a kinetic energy higher than a threshold value to achieve a sputter yield (i.e. number of atoms ejected from the target for each bombardment ion) higher than unity, the sputtering deposition takes place.

Three different types of sputtering techniques exist: DC, RF and magnetron. Despite the DC sputtering (i.e a DC bias applied between the anode and the cathode) is the simplest configuration, only RF sputtering (i.e. high frequency voltage supplied to the target) offers the opportunity to deposit also insulating materials. In fact, while in the DC configuration insulators are not able to supply the target surface with sufficient secondary electrons to maintain the plasma in the chamber, in the RF configuration, these are attracted to the target during the positive portion of the RF signal. In this way, a self-biased DC voltage emerges in the target, creating the conditions for sputtering to occur.

Moreover, magnetron sputtering (see **Figure 3.33b**) offers an additive improvement of the technique avoiding the bombardment of the forming thin film with the electrons present in the chamber and increasing the rate of deposition. In fact, it employs magnets behind the cathode to trap free electrons in a magnetic field directly above the target surface. Hence, these electrons are not free to bombard

the substrate and at the same time, they enhance their probability of hitting and ionizing a neutral gas atom [69].

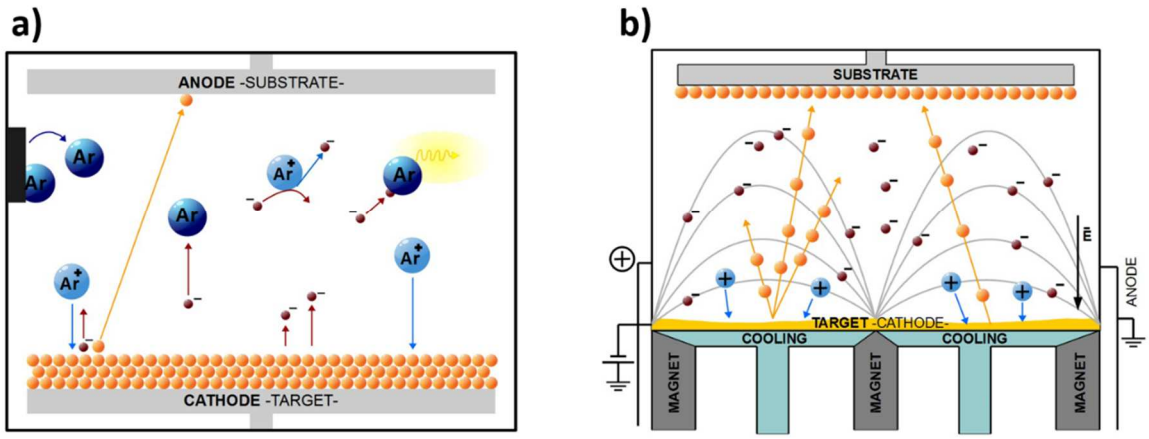

Figure 3.33 *a) Schematic of a typical Sputtering process. b) Magnetron Sputtering.*

RF magnetron Sputtering has been intensively used in this thesis to deposit metallic electrodes made by molybdenum, multilayer SiO_2/Ta_2O_5 dielectric and a-IGZO in AOS TFTs. The procedure took place without intentional substrate heating. *AJA ATC-1300F* and *AJA ATC 1800-S* existent at CEMOP (Universidade Nove de Lisboa, Postugal) have been used for this purpose (see **Figure 3.34a,b**).

3.3.1.2. Electron-beam and thermal Evaporation

Physical evaporation is the oldest and one of the most used deposition techniques especially for metals. This consists essentially in heating the materials who is supposed to be deposited up to its point of vaporization to allow the evaporated molecules to reach the substrate placed close to the source material. In order to

reduce the possibility of scattering and to maximize the probability of reaching the substrate, the evaporation process takes place under high-vacuum.

Depending on the way to induce the evaporation, it is possible to distinguish thermal and electron-beam deposition.

In the first case, the material to deposit is placed on the top of a filament made by a refractory metal (e.g. tungsten or tantalum). Due to the electrical current forced to flow through this filament, it heats up and induces the evaporation of the material. For all those materials which require high temperature to evaporate, a cross-contamination from the material of the filament can occur.

In the electron-beam (e-beam) evaporation, instead of using a heated filament a highly energetic electron beam is employed to induce the evaporation of the material. In particular, the electrons produced by thermoionic emission are accelerated against the material target by a magnetic field. In this way, only the region hit by the beam is heated and thus it is possible to evaporate also material with high melting points, avoiding external contamination.

In this work I used both these two techniques to deposit Chromium and Gold electrodes. For the thermal evaporation I employed a custom tool. For this procedure, the AC current flowing in the tungsten filament is in the range [10 – 20] A and the pressure of the chamber lays in the range [2 - 8] $\cdot$ 10^{-6} mbar. For the e-beam evaporation I employed an *Angstrom EvoVac e-beam deposition system* (see **Figure 3.34c**) located in the CNI cleanroom at the Columbia University (New York, USA). This tool provides a chamber pressure between 1 $\cdot$ 10^{-7} and 8 $\cdot$ 10^{-8} mbar and the possibility to deposit at very low deposition rates down to 1 Å s^{-1}.

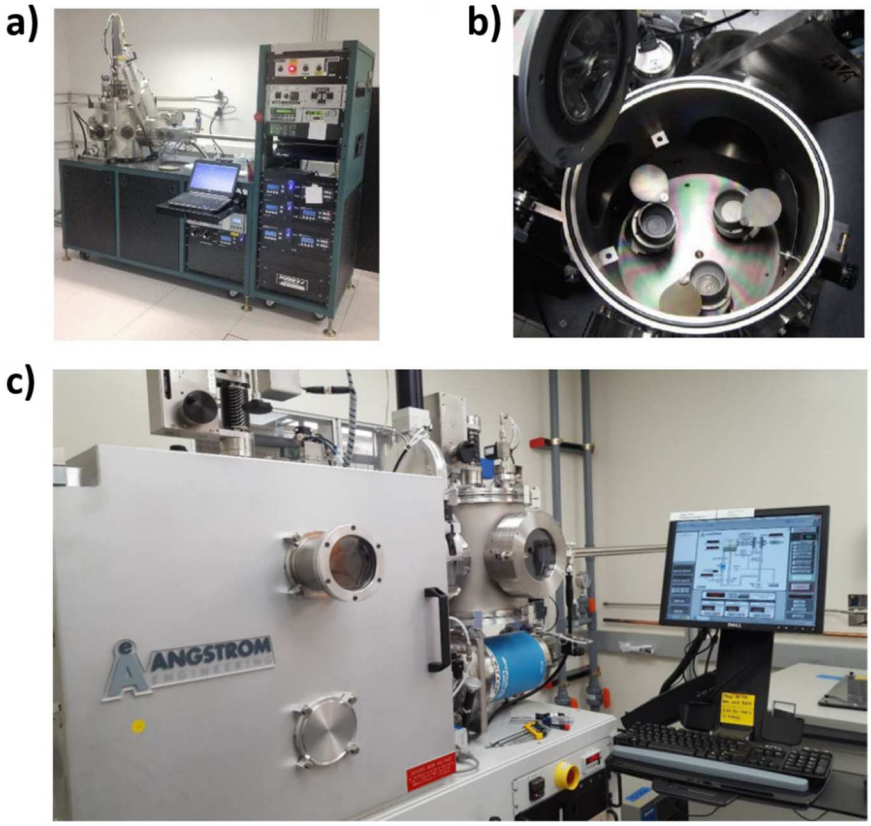

Figure 3.34 *a) Picture of AJA ATC 1800-S sputtering system used for the deposition of metallic contacts. b) detail of the main chamber where the targets are shown. c) Picture of the Angstrom EvoVac e-beam deposition system.*

3.3.2. Chemical Vapor Deposition (CVD)

Chemical vapor deposition (CVD) is referred to as deposition process of thin films and nanostructures through chemical reactions of vapor phase precursors. Since CVD can be conducted using high purity precursors, it likely leads to thin film and nanostructures with high purity [205].

In this work, Parylene C implemented as dielectric layer in some OFETs has been deposited by CVD following the steps depicted in **Figure 3.35a**. In particular, the

process starts from the dimers of the parylene molecule which are firstly sublimated in the vaporizer chamber. After, they are broken into monomers in the Pyrolizer furnace and then deposited as long chain polymers on substrates in the deposition chamber. The exhaust is pumped into a liquid-nitrogen trap by a mechanical oil trap. The cold trap serves to prevent vapors being evacuated from the process from entering the vacuum pump where they would condense and contaminate all the system.

For the realization of the dielectric layer in some of the OFETs here reported I used a *CVD-PDS-2010 SCS Labcoater® Parylene deposition system* located in the CNI cleanroom at the Columbia University (New York, USA) (see **Figure 3.35b**).

An adhesion promoter consisting of sylane was used during the deposition to improve the adhesion between parylene-C and the underlayers.

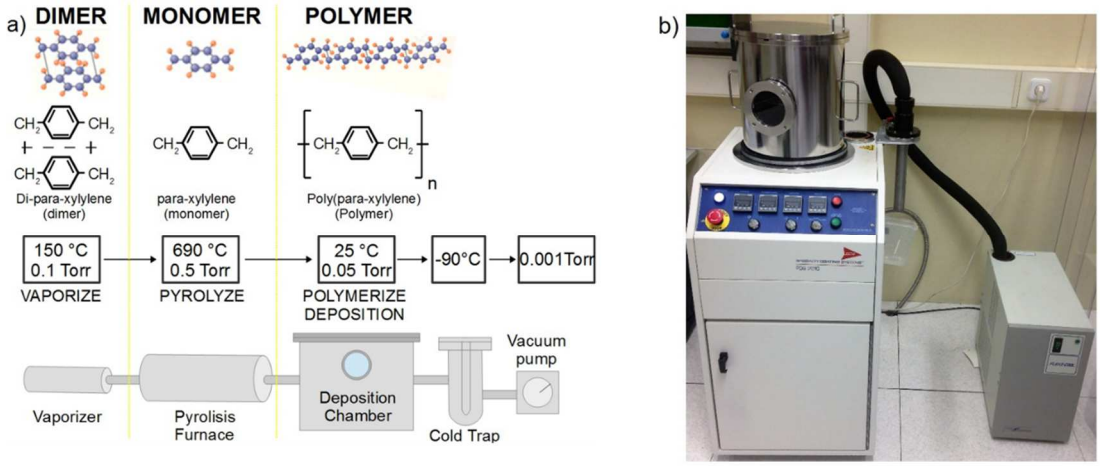

Figure 3.35 *a) Parylene deposition process. b) SCS Labcoater® Parylene deposition system (CVD-PDS-2010).*

3.3.3. Electrodes functionalization

Considering the Organic Field Effect Transistors analyzed in this work, the source and drain electrodes have been fabricated using gold. In fact, this is the metal which better satisfies the matching between the metal work function (φ_{Au} = [-5.10 – -5.47] eV) and the HOMO level of the implemented semiconductor (e.g. $HOMO_{TIPS\text{-}Pn}$ = -5.15 eV; $HOMO_{diF\text{-}TES\text{-}ADT}$ = -5.35 eV), providing a good injection/collection of charge carriers. In order to further improve the coupling between the metallic contact and the semiconducting layer, the approach proposed by Kim et al. has been employed [206]. In fact, he demonstrated that the chemical tailoring of the electrode surface with a SAM (i.e. Self Assembled Monolayer) composed by pentafluorobenzenethiol (PFBT) enhances the injection and the transport properties of OFETs based on diF-TES-ADT. Moreover, it has been demonstrated that this functionalization of the electrodes acts in two parallel directions. On one side, it induces a shift of the metallic work function which leads to a more efficient injection into the HOMO lowering the contact resistance [39]. On the other side, it helps a better crystallization of the organic semiconductor close to the contacts interfaces.

In this work I employed the PFBT treatment on the gold source/drain electrodes present in the OFETs. It consists in a 30 min immersion of the sample in a 30 mM solution of PFBT in isopropyl alcohol (or ethanol) and then the rinse using the same fresh solvent.

3.4. Electrical characterization

Electrical characterizations have been performed in ambient conditions (i.e. in air and at room temperature) in order to assess the transport properties of the tested devices. A customized probe station has been employed equipped with tungsten probe-tips controlled by micro-manipulator and with a metal box acting as Faraday box shielding the external electrical noise and keeping the samples in dark during the measurements. The electrical characterizations have been conducted using a *Keithley 2614B* or a *Keysight B2912* source meter units (see **Figure 3.36a**). Moreover, with the aim to test pixelated geometry acquiring the electrical curves of different devices laying on the same array a customized Analog Multiplexer SPDT (Single Pole Double Throw) 20 channels has been employed (see **Figure 3.36b**). These setups have been used in order to acquire the current-voltage curves (i.e. I-V curves) of the planar devices and the transfer and the output characteristic of the thin film transistors as the ones described in **Chapter 1**. The electrical parameters have been extracted from the acquired curves using a MATLAB script.

Besides, for the characterization of the insulating layers implemented as dielectrics in the TFTs, some impedance measurements have been carried on employing a Metrohm *PGSTAT204*. Both the electrical connections employed for the I-V and C-V curves are summarized in **Figure 3.36c**.

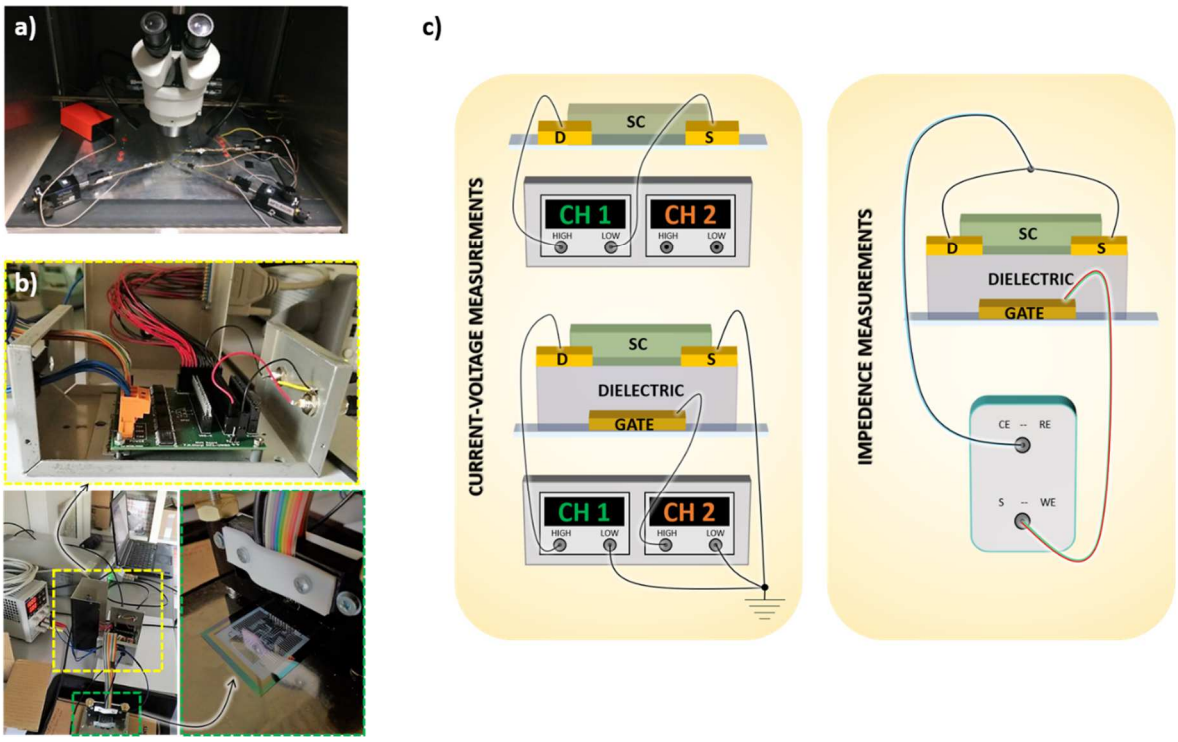

Figure 3.36 *a) Setup employed for the electric characterization of the tested devices. b) Analog customized Multiplexer used for the simultaneous characterization of several devices laying on the same pixelated array. c) Schematics of the electrical connections employed for the acquisition of the IV curves and for the impedance measurements.*

3.5. Morphological characterization

For a macroscopic characterization of the semiconductor morphology, two optical microscopes have been employed: an *OPTIKA zoom stereo microscope SZM* and an *OPTIKA polarization microscope*. Besides, for a microscopic characterization, atomic force microscopy (AFM) has been exploited both to evaluate the thickness of the semiconducting and dielectric layers, the roughness and the microcrystalline structures obtained with different deposition techniques. In the following paragraph, a brief introduction of AFM technique is illustrated.

3.5.1. Atomic Force Microscopy

Atomic Force Microscopy is a high-resolution surface characterization technique employed to image and measure the properties of a material surface. Unlike its precursor Scanning Tunneling Microscopy (STM), AFM can characterize both conducting and insulating materials exploiting the interaction between the atoms of a very sharp tip and the sample surface. The interaction between two atoms separated by a distance r can be expressed using the Lennard-Jones potential which is depicted in **Figure 3.37**. Depending on the distance between the two atoms, compared with the interatomic spacing in equilibrium condition (i.e. r_0), one can distinguish two different forces: for $r < r_0$ the force results repulsive while $r > r_0$ leads to an attractive interaction.

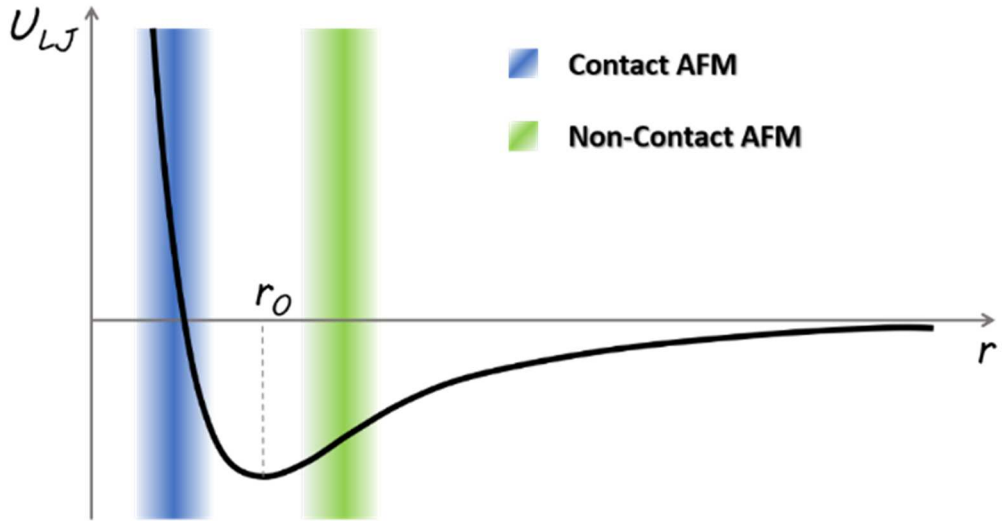

Figure 3.37 *Lennard-Jones Potential. The interaction between two atoms is repulsive or attractive respectively when their distance r is $>r_0$ or $<r_0$.*

These two different regimes can be exploited to implement two AFM operation modes:

Contact Mode

The AFM tip touches the sample surface, and the tip-sample repulsive force deflects the tip cantilever. Here the cantilever deflection is monitored and used as the feedback signal.

Non-Contact Mode

The cantilever is externally oscillated at its resonance frequency. The tip-sample attractive interaction is altered as the tip-sample distance changes, leading to a change in oscillation amplitude and resonance frequency. These deviations from the reference amplitude and frequency are used as feedback signals to obtain the topography of the sample surface.

Even if, as it is shown in **Figure 3.37**, the huge slope presented by the curve in the repulsive interaction region (i.e. in *Contact Mode*) provides a greater resolution, bringing the tip in contact with the sample surface can lead to severe damages both at the tip and at the sample. For this reason, non-contact mode is often preferred even if it presents a lower resolution.

In non-contact mode the surface mapping is carried out by measuring the changes in the phase or in amplitude of the vibration of the cantilever holding the tip due to the attractive force between the probe tip and the sample while the cantilever is mechanically oscillated near its resonant frequency (i.e. ω_0).

The cantilever oscillation can be described by the Eq. 3.1, considering the tip as a point-mass spring.

$$m\ddot{z} + \frac{m\omega_0}{Q}\dot{z} + kz = F_{ts} + F_0\cos(\omega_d t) \qquad (3.1)$$

where k is the elastic constant, Q the quality factor, F_{ts} the tip-sample interaction, F_0 and ω_d the amplitude and the angular frequency of the driving force respectively.

When the tip approaches the sample surface, the attractive force causes a shift of the cantilever resonance curve and for small oscillation, this system can be considered a weakly perturbed harmonic oscillator. The frequency shift can be expressed by the Eq. 3.2 and for attractive forces (i.e. $\partial F_{ts}/\partial z > 0$) the force gradient lowers the resonance frequency.

$$\Delta f_0 = -\frac{f_0}{2k}\frac{\partial F_{ts}}{\partial z} \tag{3.2}$$

where $f_0 = \omega_0/2\pi$.

Hence, to acquire the map of the sample surface, the force gradient has to be recorded scanning the x-y area and so varying the tip-surface distance depending on the morphology of the sample. To measure this quantity, the knowledge of the frequency shift due to the tip-sample interaction is essential. With this aim, the cantilever is forced to vibrate at a frequency f_1 (see **Figure 3.38b**) where the amplitude change (ΔA) is large also with very small shift of intrinsic frequencies due to atomic attraction. Thus, the ΔA measured in f_1 reports the distance change (Δd) between the probe tip and the surface atoms (see **Figure 3.38c**). The non-contact mode feedback loop compensates the change in the oscillation of the cantilever and keeping constant the vibration amplitude and so the distance between the tip and the sample surface. In this way the AFM can acquire the topography of the samples.

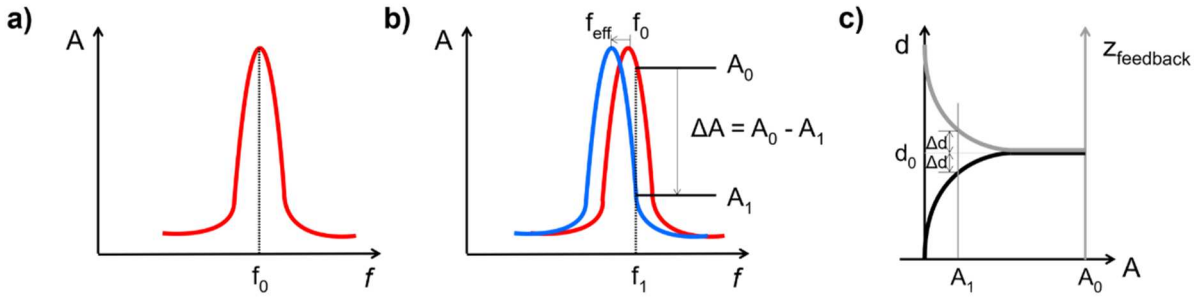

Figure 3.38 *a) Free resonance frequency, b) frequency shift and c) distance of the tip from the sample surface and z-feedback as a function of amplitude modulation. Adapted from [207].*

To characterize the morphology of my samples, I used a *Park NX10* scanning probe microscope operated as AFM in Non-contact Mode. In **Figure 3.39** a scheme of the system is reported.

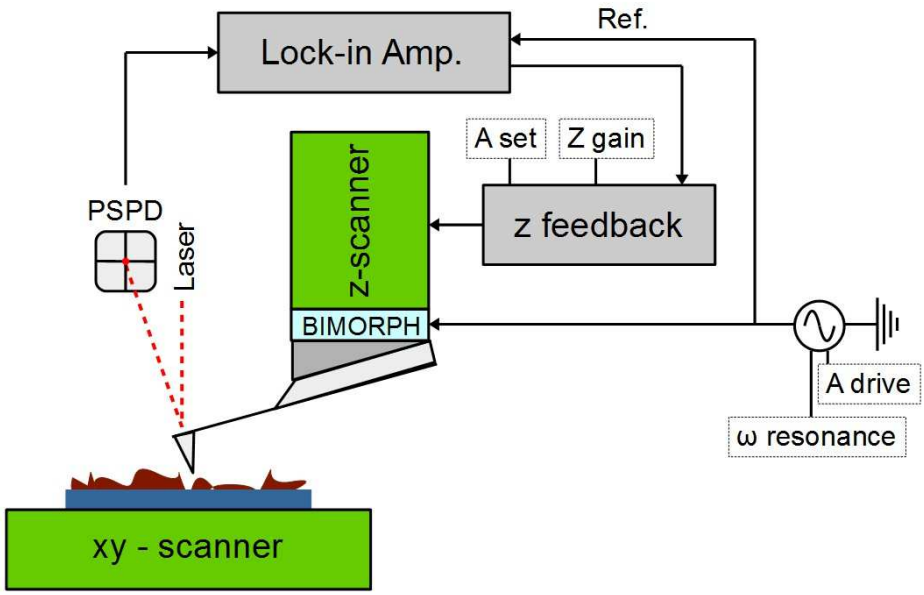

Figure 3.39 *Non-contact AFM system.*

The samples are placed on a piezo tube scanner which allow the scanning in the x,y and z directions. The cantilever is mechanically forced to vibrate near its

resonance frequency (typically between 100 and 400 kHz) by a biomorph. The user can set the vibrational amplitude of the cantilever by applying an AC signal (i.e. Amplitude Drive). The cantilever deflection due to the interaction with the sample surface is acquired by a Position Sensitive Photo Detector (PSPD) which is a four-section split photodiode. It can monitor the cantilever movement changes thank to the reflected beam laser intensity and moreover it can establish a feedback loop which controls and coordinates the piezo tube z-scanner comparing the signal received from the PSPD and the parameters set by the operator (e.g. *Amplitude setpoint* and *Z servo gain*). Finally, the voltage signal used by the z feedback-loop to compensate the deviation of the cantilever oscillation amplitude provides the information to reconstruct the topography of the sample surface.

3.6. Photocurrent Spectroscopy

The photocurrent spectroscopy (PC) is an experimental technique which allows to investigate the optoelectronic properties of a semiconductor. It is based on the photoconductivity phenomenon which indicates the increase of the electrical conductivity as a result of incident electromagnetic radiation (e.g. visible light, ultraviolet light, infra-red light, X-rays). This phenomenon is based on the absorption of a photon by an electron (i.e. *internal photoelectric effect*). If the energy absorbed by the electron is higher than the energy gap of the semiconductor, the photon is able to create excitons promoting the electron in the conduction band (i.e. LUMO for OSC) and leaving an hole in the valence band (i.e. HOMO for OSC). Thus, the density of free electrons and holes changes and the semiconductor

conductivity increases. Also transitions induced by photons with lower or higher energies than E_G are possible respectively if the presence of trap states intra-gap is recorded or if many anti-bonding orbitals are present.

The conductivity of a semiconductor kept in dark, can be expressed by Eq. 3.3

$$\sigma = e(n\mu_n + p\mu_p) \tag{3.3}$$

where e is the electron charge, $\mu_{n/p}$ is the electron/hole mobility and n and p indicate the electron and hole density. When the semiconductor absorbs energy from an impinging electromagnetic radiation, the generation of electron/hole pairs occurs and the conductivity increases:

$$\sigma + \Delta\sigma = e\left[(n + \Delta n)\,\mu_n + (p + \Delta p)\,\mu_p\right] \tag{3.4}$$

Thus, when an electric field E is applied to separate the generated excitons, the current density J increases by a factor J_{ph} which is called *photocurrent*:

$$J = (\sigma + \Delta\sigma)E = J_{bulk} + J_{ph} \tag{3.5}$$

Therefore, the recording of the current flowing in the semiconductor provides information regarding the radiation absorption of the material and consequently about its optoelectronic properties. It is important to notice that the photocurrent is strongly related to the energy band diagram of the tested materials and it can provide important information on the trap states present in the semiconductor which can induce a modification of the recorded photocurrent [208]–[211]. The information provided by this technique are deeply discussed by R.H. Bube in [212].

In order to characterize the optoelectronic properties of the organic semiconductor-based devices, I employed a setup depicted in the schematic in **Figure 3.40**.

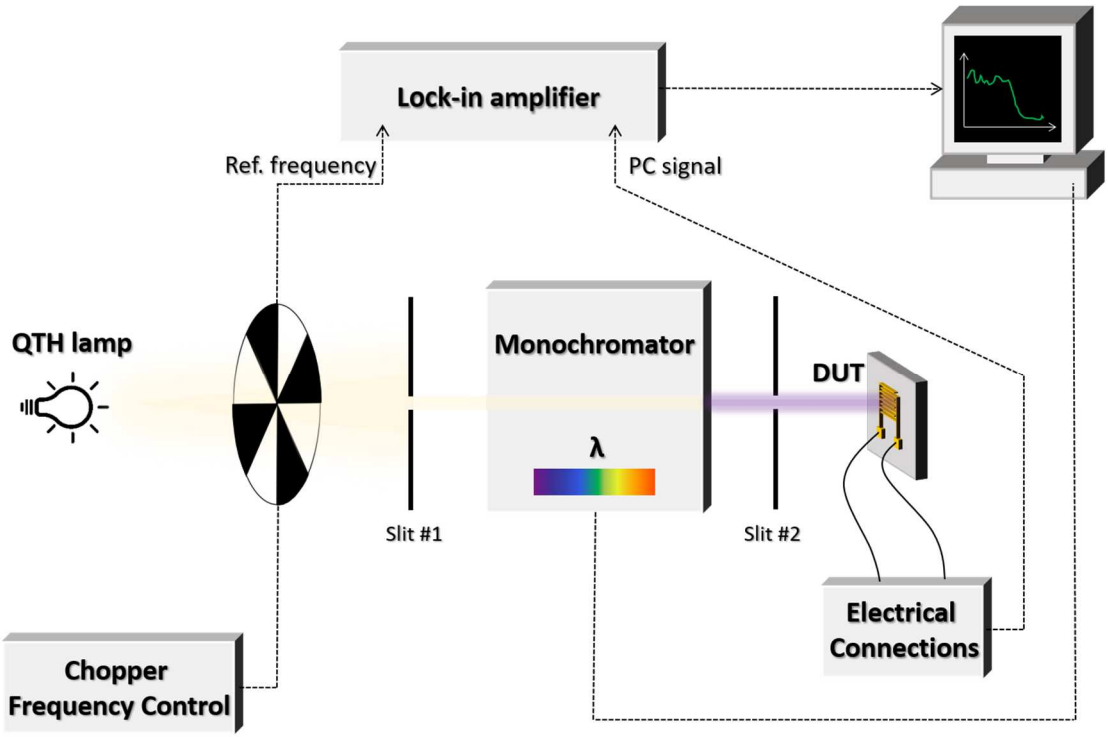

Figure 3.40 *Schematic of photocurrent experimental set-up.*

As radiation source, a QTH (Quartz Tungsten Halogen) lamp (22 V, 150 W) is employed. This source produces a white spectrum which is sent to a *Cornestone 260 monochromator* (resolution $\Delta\lambda = 1\text{nm}$). This is composed by a rotative diffraction grid and a system of mirrors which select a wavelength at a time and focus it on the sample. At the entrance and at the exit of the monochromator, two slits allow the collimation of the light beam for the improvement of the intensity and sensitivity of the irradiation. In order to filter the photo-induced signal and discriminate it from the surrounding electrical noise, a chopper is coupled with a lock-in amplifier. The chopper (i.e. a dark disk with periodic holes) is placed between the lamp and the monochromator and it transforms the incident continuous illumination in a chopped light at a set frequency. This reference frequency (37 Hz) is sent to the *Stanford Research 830 lock-in amplifier* which is

employed to filter the recorded photocurrent. The device is connected to the system as it is shown in **Figure 3.41**. In fact, in order to enhance the measurement of the induced photocurrent, considering the high resistivity of the organic semiconductors (R~1-100 MΩ) a voltage-mode measurement has been acquired. Instead of directly measure the photocurrent flowing in the semiconductor, a load resistance (R_L) of the same order of magnitude of the organic layers is employed and it is connected in parallel with the lock-in amplifier. When a small change in the current is recorded due to the illumination, a relatively high drop of potential is induced in R_L.

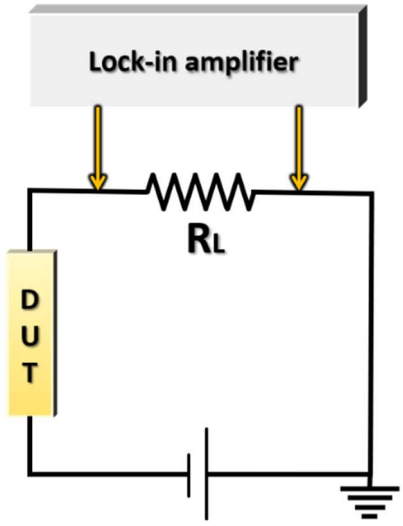

Figure 3.41 *Electrical connection employed during PC experiments.*

The photocurrent spectra have been normalized for the lamp spectrum acquired with a Pyroelectric sensor (*Scitec Instruments, LTQ2 Pyroelectric Single Element Detector for Measurement Applications*) kept in the same experimental conditions. This sensor provides a flat responsivity, independent from the light wavelength.

3.7. Detector characterization

3.7.1. X-ray tubes

In order to assess the X-ray detection performances, I tested the samples under the radiation provided by two different X-ray tubes. In the next two paragraphs they are briefly described.

In both cases, a mechanical shutter has been placed between the X-ray source and the detector in order to acquire dynamical responses by the sensors recorded for ON/OFF cycles of irradiation (i.e. opening/closing the beam).

Moreover, both the X-ray tubes have been calibrated using a *Barracuda radiation detector* (RTI Group, Sweden).

Both the irradiation apparatuses are enclosed in a lead-based screening box which provides the protection of the operator during the measurements.

During the irradiation, the devices have been electrically connected to the source meters as described in **Section 3.4**.

The typical procedure followed for the characterization of the X-rays detectors, the data analysis and the extraction of the fundamental figures of merit are intensively discussed in **Chapter 4** and in particular in **Section 4.2**.

3.7.1.1. Mo-tube

A commercial *PANalytical PW2285/20* X-ray tube with a Molybdenum target has been employed ($K_\alpha \sim 17.4$ keV, $K_\beta \sim 19.6$ keV). The tube has been kept at 35 kVp and the electron current flowing between the anode and the cathode has been tuned in the range [5; 30] mA, corresponding to dose rates of X-ray between 5 and 30 mGy s^{-1}. The samples have been placed 29 cm far from the tube and centered along the beam direction. The X-ray spot at that distance is about $1cm^2$. The samples have been electrically connected in different way depending on the geometry of the sensing system under test. In some cases, the samples have been enclosed in a Faraday box with an aperture covered by a thin Aluminum foil in order to prevent electrical noise, to keep the sample in dark during the measurements and to let the X-ray beam pass through the aperture avoiding its attenuation. In other cases (see **Figure 3.42a**) the samples have been directly connected with the tungsten probe-tips described in **Section 3.4**.

In **Figure 3.42b** the simulated spectrum provided by this X-ray tube kept at 35 kVp is reported. In **Figure 3.42c** the calibration curve acquired by the *Barracuda detector* is shown.

Moreover, interposing several layers of Aluminum between the sensor and the X-ray tube we could attenuate the radiation beam down to (2.32 ± 0.02) µGy s^{-1} and this allows us to measure the limit of detection of the X-rays sensors.

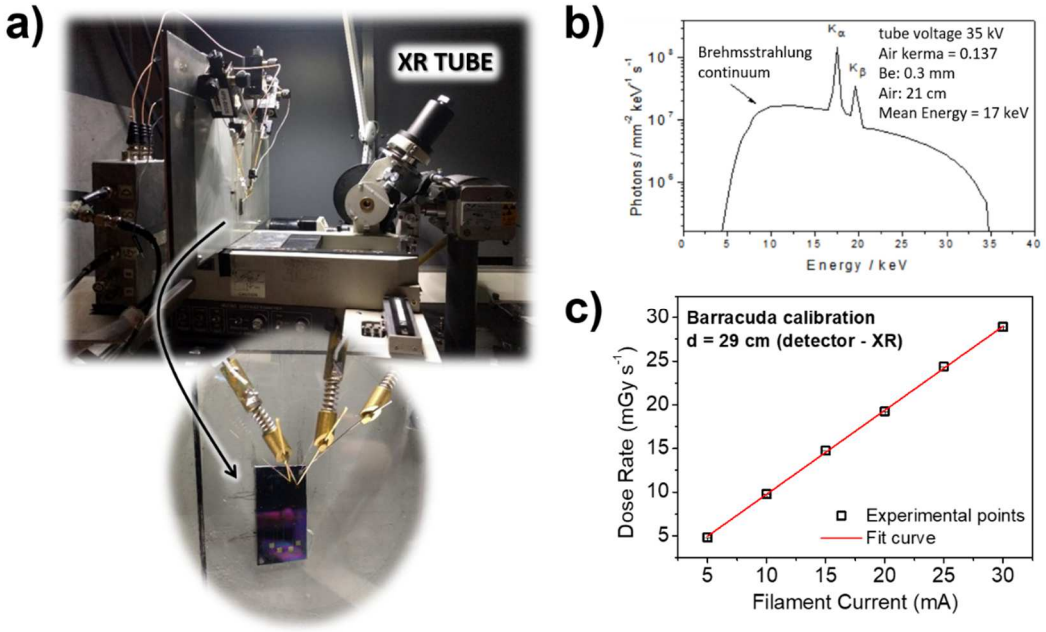

Figure 3.42 *a) samples tested under X-rays produced by the Mo target tube. b) simulated spectra of 35kV, 35 mA Mo-tube. c) calibration of the tube employing a Barracuda detector.*

3.7.1.2. W-tube microfocus

A *L12161-07 150kV Microfocus X-ray tube* with a Tungsten target commercialized by Hamamatsu has been employed (K_α ~ 59.3 keV) (see **Figure 3.43a**). The accelerating voltage applied to the tube spans between 40 kVp and 150 kVp. Depending on the accelerating voltage and the filament current, several dose rates of X-ray have been employed for the irradiation of the sensors as it is indicated in the calibration graph reported in **Figure 3.43b** and performed with the Barracuda detector. The simulated spectrum representing the 150kVp operating condition is illustrated in **Figure 3.43c**.

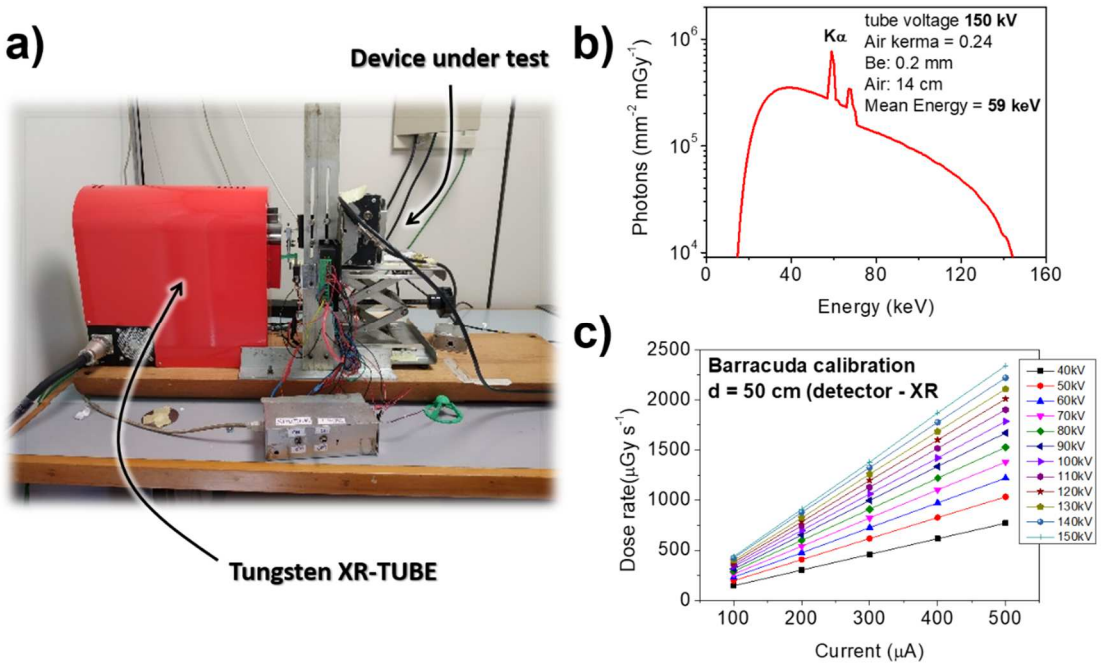

Figure 3.43 *a) sample tested under X-rays produced by the W target tube. b) simulated spectra of 150 kV W-tube. c) calibration of the tube polarized at different voltages acquired by a Barracuda detector.*

3.7.2. Dental X-ray setup by Skanray Europe S.r.l.

To assess the potentiality of the here reported detectors in dental radiography field, we employed two different commercial radiation sources kept in actual medical conditions:

1. A commercial tungsten-target X-ray tube (*OPX/105 Serial Number: 681502 by Skan-X Radiology Devices S.p.A.*, see **Figure 3.44a**) operated at 70 kVp accelerating voltage and 4 mA anodic current. I varied the exposure time between 0.5 s and 2 s obtaining a total dose of irradiation which spans in the range [15.5-64.6] μGy.

2. A commercial dental radiography system (*Interskan DC, SkanRay Europe S.r.l.*, see **Figure 3.44b**). The source has been operated at 70kVp with an anodic current varying in the range [4-8] mA. In this way, the response of the sensors has been tested irradiating them with tunable dose rates of radiation in the range [1.13-2.31] mGy s^{-1} provided in short pulses 100 ms long.

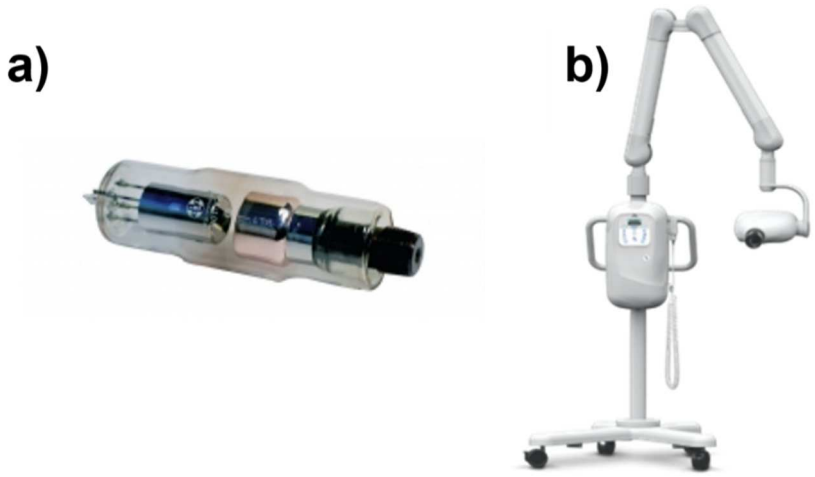

Figure 3.44 *a) dental radiography X-ray tube (OPX/105 Serial Number: 681502 by Skan-X Radiology Devices S.p.A.). b) Dental radiography system (Interskan DC, SkanRay Europe S.r.l.).*

3.7.3. Gamma sources

I tested the detectors based on AOSs under two different gamma sources at Istituto Nazionale di Astrofisica (INAF, Bologna, Italy). To this aim I employed ^{137}Cs and ^{109}Cd radiation sources sealed in a leaded shield. The ^{109}Cd source emits a primary electromagnetic radiation at 22 keV and a secondary at 88 keV with a total activity of 105.1 MBq. On the other side, the ^{137}Cs source emits a primary electromagnetic

radiation between 32 and 36 keV and a secondary at 662 keV with a total activity of 1.6 MBq. The sources have been placed 1 cm far from the sensor. We performed the measurements in ambient condition, and we acquired the electrical output signal connecting the device as illustrated in **Section 3.4**.

3.7.4. Proton Irradiation

With the aim to test the devices based on OSC as proton detectors, I measured their responses under the proton beams provided by two different facilities. The main purpose of this study is the investigation of the potentiality of this sensing technology for its implementation in the medical field as dosimeter employed in proton therapy. For this reason, I tested the performances under proton beams at low (5 MeV) and high (70 MeV) energies in order to investigate their response both under the typical energy employed in radiotherapy (i.e. 70 MeV) and under the end-of-range values of the scattered protons (i.e. 5 MeV).

3.7.4.1. LABEC (Laboratory of Nuclear techniques for Environment and Cultural Heritage, INFN Firenze)

The organic-based sensors have been tested under a 5MeV beam provided by the 3 MV Tandetron accelerator at the LABEC ion beam center. The irradiation system is reported in **Figure 3.45**.

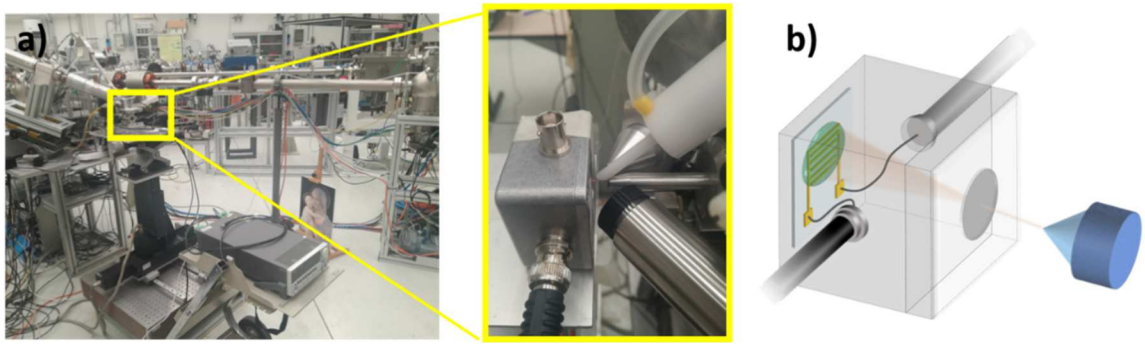

Figure 3.45 *a) Proton beamline at LABEC. b) The detectors have been enclosed in a box during the irradiations in order avoid the illumination of the devices.*

The sample has been centered under the proton beam at 8 mm from the beam's exit and it has been enclosed in a box to keep the dark during the measurements. The sensors have been electrically connected as described in **Section 3.4**. to determine the actual energy of the protons impinging onto the device. The energy loss of the charged particles passing through the several layers interposed between the beam and the sensor (i.e. 200 nm of Si_3N_4 for the beam extraction window, 8 mm of mixed air-He, 14 µm of Al for the entrance window of the box and 14 mm of air inside the box) have been calculated by a SRIM Monte Carlo simulation [213].

The proton beam currents employed are in the range between 1-100 pA which correspond to fluences between 3.5 · 10^{9} $H^{+}cm^{-2}$ and 8.7 · 10^{11} $H^{+}cm^{-2}$. The weak intensity of the beam has been monitored and measured using a rotative chopper placed between the proton source and the sample in order to intercept the beam [214]. The chopper is a graphite vane covered with a thin nickel evaporation, and the Ni X-ray yield is used as an indirect measurement of the proton current.

3.7.4.2. TIFPA (Trento Institute for Fundamental Physics and Applications)

The organic-based detectors have been tested under therapeutic proton beams provided by the Trento Proton Therapy facility and supervised by the Trento Institute for Fundamental Physics and Applications. In this case it has been possible to carry on the measurements under real conditions of irradiation employed during the medical treatments and to test the detection response of our devices under actual proton fluxes and energies recorded for the primary beam.

In this facility, the cyclotron (see **Chapter 2**) accelerates the beam up to a maximum energy of 228 MeV. After the cyclotron exit, a coarse energy selection is carried-out by a rotating degrader of different thicknesses and materials to select the beam energy down to its minimum value of 70 MeV. Moreover, different beam intensities can be requested at the exit of the cyclotron, in the range spanning between 1 and 320 nA. The calibration of the beam is provided by an ionization chamber for the measurements of the fluxes and GAFCHROMIC for the evaluation

of the spot size. Recently, Tommasino et al. reported the main properties of the facility [215].

During my work, I carried on some preliminary test at TIFPA setting the energy of the protons at 70 MeV and looking at the detection response acquired for different proton fluxes. Moreover, I tested the effect of solid waters of different thicknesses interposed between the sensor and the proton source. The experimental setup is depicted in **Figure 3.46**.

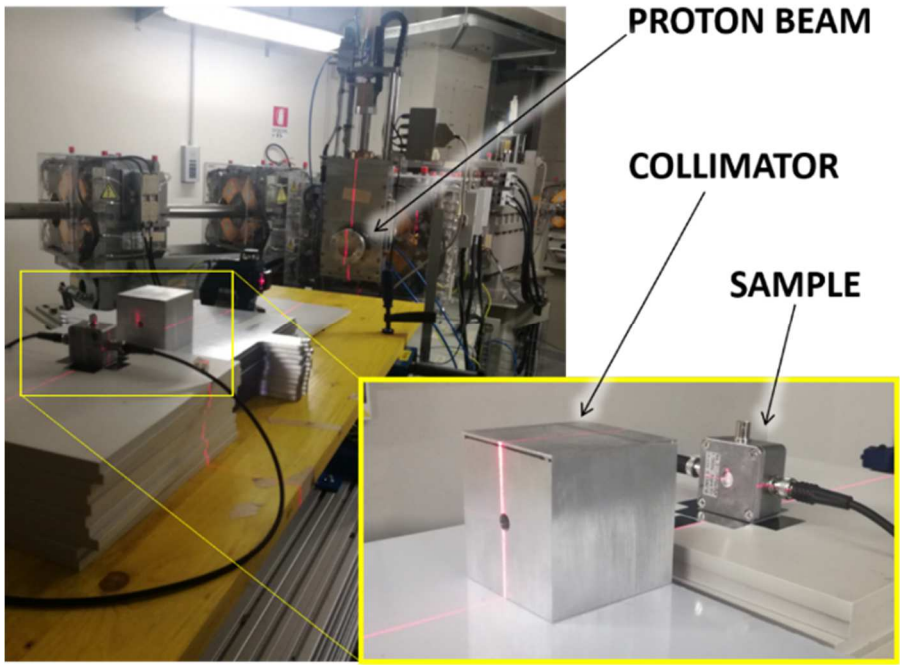

Figure 3.46 *Experimental setup at TIFPA.*

4.

Ionizing radiation detectors based on Organic Semiconductors

In this fourth chapter, the experimental work on organic thin film-based detectors carried on in these three years is illustrated. The chapter is divided in four main sections.

In the first section, the difference in terms of detection between the two main architectures involved in my work are pointed out.

The second section is dedicated to the X-ray detection. After a first summary which describes the main measurements carried on in order to characterize the sensors, several strategies studied and adopted in order to improve the efficiency of this class of detectors are described. Firstly, a deep study of the trap states which rule the detection mechanism is shown. Second, the improvement of the sensing performance achieved by the employment of new high-Z synthesized organic molecules as active layer is discussed. Later, the impact of the transport properties of the devices onto the detection capability is shown. Finally, the role of the device

architectures on the X-ray detection is discussed. In the following section, the results achieved during my six-months period spent at the Columbia University are shown. At the end of this section, a summary about all the strategies adopted in this work is proposed.

The third section illustrates the results achieved testing the organic thin film-based devices in actual clinical environments for their application in the field of dental radiography.

The last section describes the results about the proton detection experiments carried on with organic based devices. The first part of the section is dedicated to the measurements that took place at the LABEC laboratory using 5 MeV protons. While the second part of the paragraph is focused on the preliminary results achieved at the TIFPA Proton Therapy Center employing a therapeutic proton beams at 70 MeV.

4.1. Co-planar and OFET architectures

In order to assess the potentiality of organic-based devices for radiation and proton detection, two main architectures have been tested. In particular, as it has been already discussed in **Chapter 3**, two-terminal coplanar (**Figure 4.47a**) and OFET (**Figure 4.47b**) structures have been realized. The geometry, the materials and the main fabrication techniques employed for the fabrication of the devices are described in **Figure 3.26** and **Figure 3.27**.

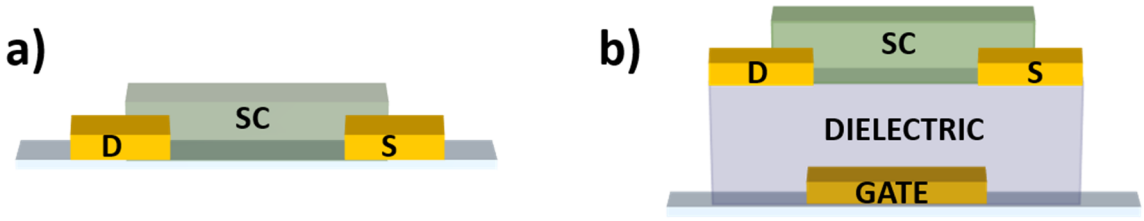

Figure 4.47 *a) Two-terminals coplanar and b) Organic Field Effect Transistor architectures.*

Both architectures present collecting electrodes with an interdigitated geometry in order to maximize the channel width keeping a limited pixel area. This is the optimized option to implement pixelated detectors onto large-area, able to provide a spatial resolution of the impinging radiation signal.

The two-terminal and the three-terminal devices offer different kind of advantages.

On one side, the co-planar architecture is composed by only two layers and this implies an easier fabrication process.

On the other side, the transistor configuration offers several advantages as it has already been reported by S. Lai et al. [154].

1) Transistors are multiparametric devices and for this reason different electrical parameters can be analyzed to study the radiation effect on the detector.

2) Transistors can be employed for transducing the sensing event.

3) The use of the gate electrode can tune the operating condition of both the electrical device and the sensor, as illustrated in **Figure 4.48**. In fact, considering a p-type semiconductor (e.g. TIPS-Pn), when a negative voltage is applied to the gate (i.e. $|V_{GS}| > |V_{th}|$) the OFET is turned on and the

sensor responds to the radiation with an increase of the I_{DS} proportional to the impinging dose rate. On the contrary, when the OFET is turned OFF (i.e. $|V_{GS}| > |V_{th}|$) the sensor is switched off as well providing a poor response to the radiation. This aspect offers an enormous advantage if compared with the performance achieved with the standard two-terminals architecture because it allows to address the single pixel in a matrix structure (e.g. FPXI) avoiding the implementation of an additional TFT (backplane in the FPXI, see **Section 2.5**).

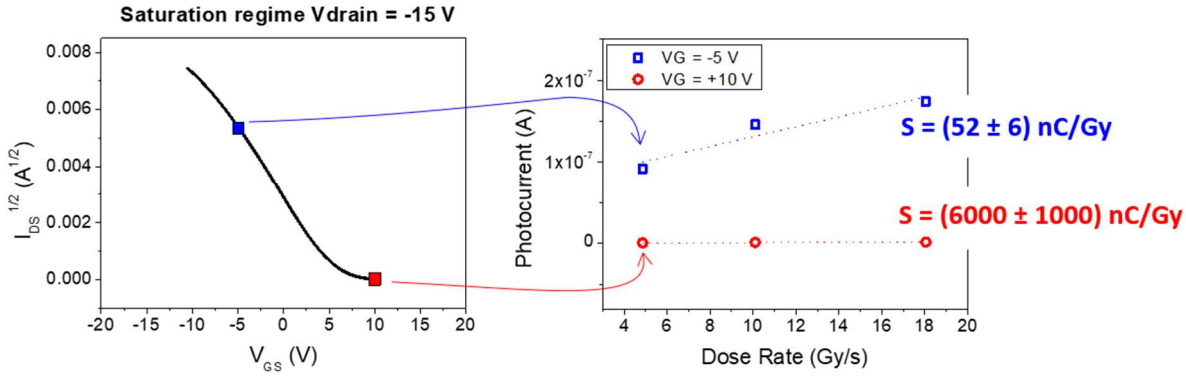

Figure 4.48 *Impact of the gate voltage on the detector performance. When $|V_{GS}| > |V_{th}|$ (here V_{GS} = -5 V) the sensor responds to the radiation providing a IDS proportional to the dose rate of radiation and a sensitivity S = (6 ± 1) μC Gy^{-1}. On the opposite side, when $|V_{GS}| < |V_{th}|$, the sensor is switched off and it shows a very low sensitivity (S = (52 ± 6) nC Gy^{-1}).*

4) The transistor structure permits to enhance the charge density in the channel boosting of the efficiency of both hole conduction and electron accumulation. Now, considering the photoconductive gain effect (see **Section 2.5.1.1**) as the mechanism which rules the detection performance of this class of sensor, an increase of the charge density in the semiconducting

channel brings to an increase of the gain factor which amplify the photocurrent signal.

5) The contact resistance of the device can be tuned by exploiting the polarization condition of the transistor. In particular, as it is shown in **Figure 4.49** , in the saturation regime the injection/collection of the generated charges is facilitated if compared with the linear regime and consequently the recorded sensitivity values are higher.

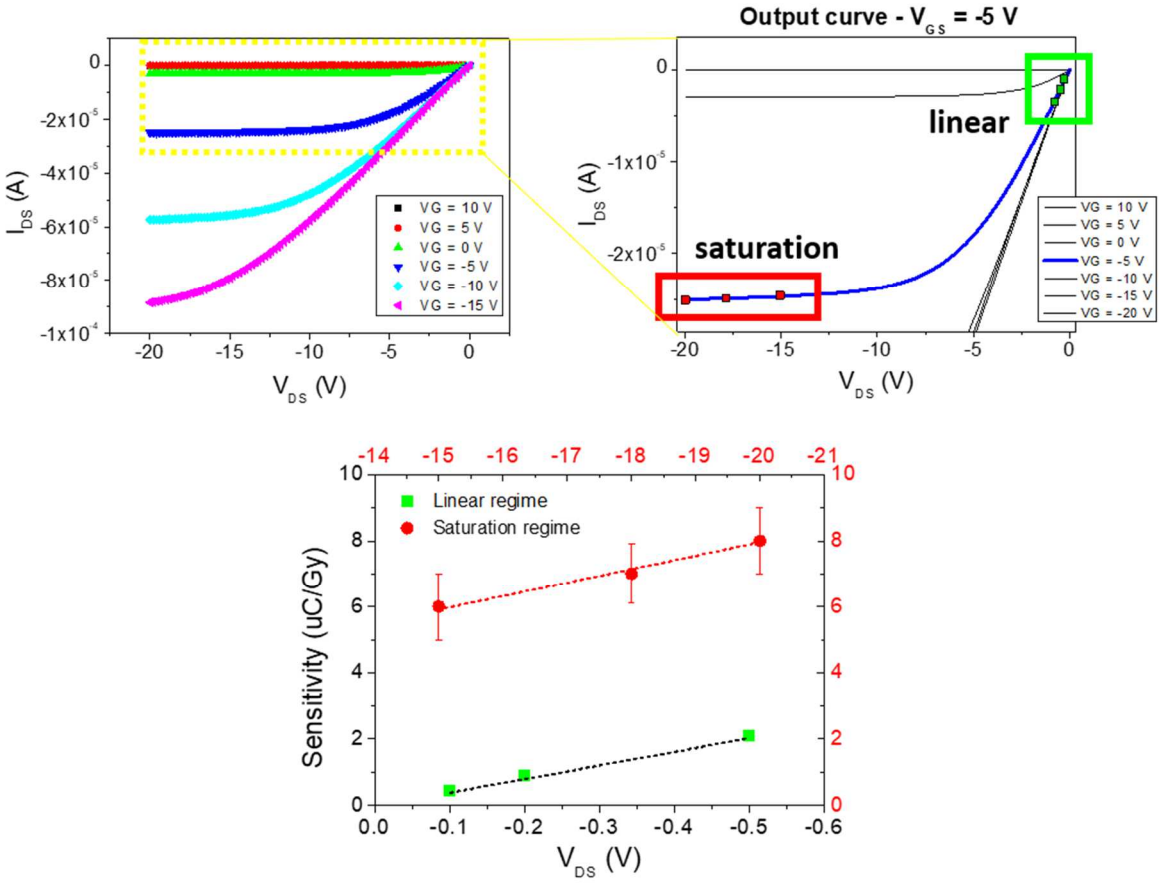

Figure 4.49 *Impact of the drain voltage on the detection performance. Keeping V_{GS} = -5 V constant, the sensitivity of the detector is higher when the OFET is operated in saturation regime in compared with the linear regime.*

4.2. X-ray detection

I have investigated the direct X-ray detection properties of organic semiconductor-based sensors by testing the devices' electrical response under X-ray beams provided by a W-based and a Mo-based X-ray tubes (see **Section 3.7.1.1** and **3.7.1.2**). As it has been extensively discussed in the previous paragraph, in order to have a full and complete characterization on the detection process occurring in organic detectors, I employed OFETs architectures which allowed to monitor the changes of all the transport parameters of the devices during the irradiation.

The transistors were connected as described in **Section 3.4** and the current flowing between the source and drain electrodes has been acquired as a function of time. Changing the intensity of the X-ray beam (i.e. the current imposed between the anode and the cathode of the X-ray tube) it has been possible to monitor the variation of the I_{DS} due to different doses of radiation absorbed by the sensors. In particular, **Figure 4.50** shows the typical dynamic curve acquired using this class of sensors. This measurement consists in the monitoring of I_{DS} during consequent ON/OFF cycles of the X-ray beam. This allows to calculate the photocurrent induced by the radiation as

$$Photocurrent = |I_{ON}| - |I_{OFF}| \tag{4.1}$$

where I_{ON} and I_{OFF} are the current flowing between the source and drain electrodes respectively when the sample is irradiated and kept in the dark condition.

The curve is always acquired for almost four different dose rates in order to observe the different photocurrent induced by diverse amount of absorbed radiation.

I typically acquired at least three consequent photocurrent peaks for each dose rate tested with the aim to check the reproducibility of the radiation induced signal.

In **Figure 4.50** the yellow squares indicate the time during which the shutter is open and the sensor is irradiated.

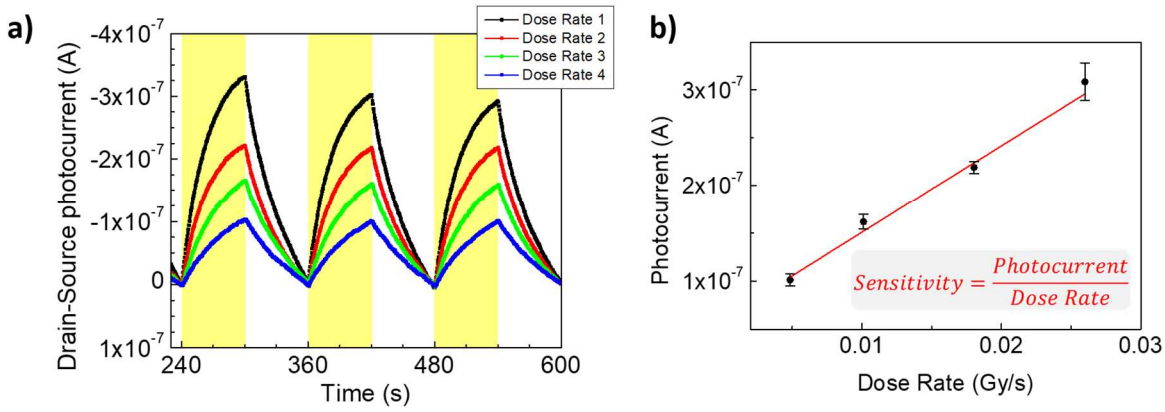

Figure 4.50 *Dynamic measurement of the OFET-based detectors. a) Three consequent photocurrent peaks acquired between the source and drain electrodes as a function of time. The yellow squares indicate the time intervals in which the sample are irradiated, and the ON/OFF cycles correspond to 60 s. The different colors indicate four different dose rates of irradiation (decreased from 1 to 4). b) In this graph the photocurrents as a function of the corresponding dose rates are reported. The slope of the fitting curve represents the sensitivity of the sensor.*

From the dynamic response of the sensor it is possible to plot the photocurrent as a function of the relative dose rate. This is shown in **Figure 4.50 b** from which it is possible to notice that, in this specific range of operation, the response of the sensor increases linearly with the dose rates. Moreover, as it has been discussed in **Section 2.4.1**, by fitting this curve it is possible to extract the sensitivity of the sensor as the slope of the obtained line. This is the most studied figure of merit in this work and it is employed to evaluate the detection performance of the tested devices.

The time of the ON/OFF cycles have been set at 60 s following the study reported by Basiricò et al. [153]. In fact, this time allows to reach a saturation of the detection process and to record the maximized value of photocurrent (see **Figure 4.51**).

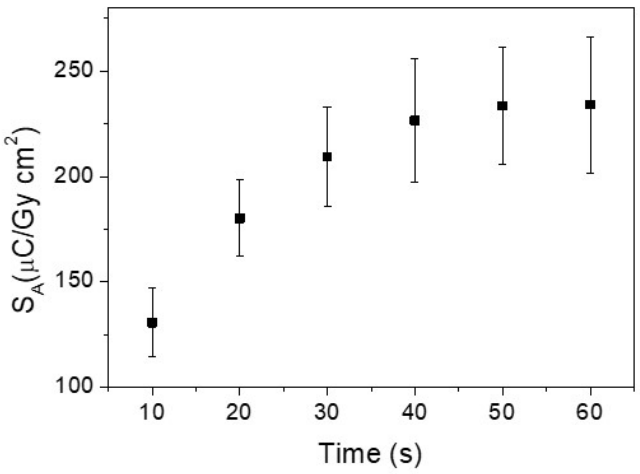

Figure 4.51 *Sensitivity values over time exposure to X-rays. The error bars refer to the fit error over three experimental points (corresponding to three different dose rates), employed for the calculation of the sensitivity values* [216].

Besides, following the considerations reported in the previous section, in order to achieve the best detection responses and to push the sensitivity values I characterized the OFETs keeping them in saturation regime.

As it has been already discussed in **Chapter 2**, organic-based radiation detectors offer a unique advantage among the several existent sensing technologies. In fact, their chemical composition mainly formed by low-Z elements makes them human tissue-equivalent in terms of radiation absorption. This property is very appealing especially for the development of radiation dosimeters to be employed in the medical field because it would offer the advantage to skip the calibration process

and to directly measure the total dose absorbed by the patient during a therapeutic treatment or a diagnostic exam. Besides, they could be interposed between the patient and the radiation source without interfere with the impinging photons letting the beam pass.

If on one side, this aspect renders organic detectors the most suitable technology in the medical field, on the other side it makes the radiation detection challenging. In fact, the low-Z elements forming the active layer of the detector leads to a very poor absorption which provides a very low external quantum efficiency. For this reason, it is important to study and deeply characterize the detection mechanism in order to find possible roots which allow to control and enhance the radiation detection capability.

In the following sections, several pathways experimented during this work are described.

4.2.1. Enhancing and controlling the photoconductive gain effect

As discussed in **Section 2.5.1.1**, the detection mechanism involved in thin film devices based on polycrystalline semiconductors is called *Photoconductive Gain* effect (PG). This consists in an inner amplification process which is activated by trap states for minority carriers (i.e. electrons in the cases here studied). Thus, considering the fact that the photoresponse of these devices is mediated by active traps, the slow rise and decay of the radiation detection signal can be considered the fingerprint of this kind of detectors.

As already shown, the gain factor is represented by the ratio of two characteristic times (Eq. 2.13, 2.14): τ_t which mainly depends on the transport properties and on the geometry of the device and τ_r which is related to the properties of the active electron traps that induce the PG. Then, in order to deeply understand the detection properties of this class of devices a complete characterization of the active material should be carried on. For this reason, in this work, an intense analysis of the possible causes of traps has been conducted.

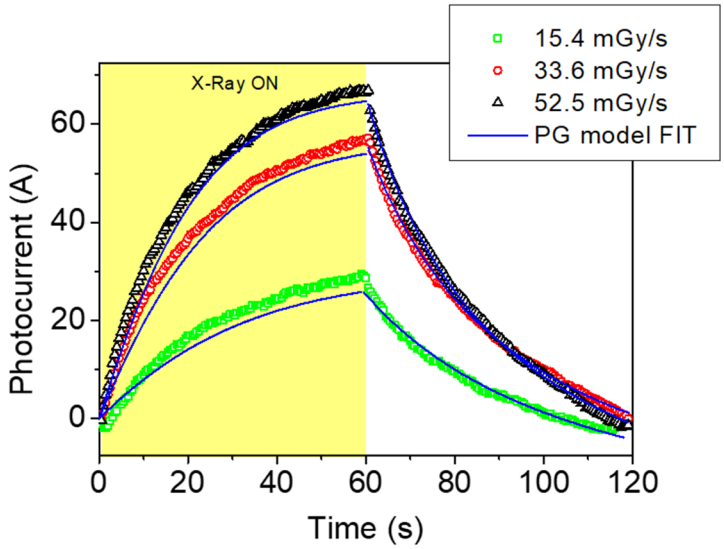

Figure 4.52 *Experimental and fitted curves of the response of an organic detector for three different dose rates of radiation. The fit curves have been obtained by applying the PG analytical model described in* [153]*. Adapted from* [216].

With this aim a MATLAB script has been implemented in order to fit the dynamic curves measured with different OFETs. By this fitting procedure, it has been possible to determine the stretched exponential decay of the photocurrent after the irradiation, due to the slow relaxation of the trapped electrons. Then, the extrapolation of the main parameters which determine the characteristic times has been achieved and then the calculation of the gain factor G has been provided.

In **Figure 4.52** a graph representing the dynamic response of the sensor for different dose rates is reported. As it is possible to notice, the photoconductive gain model greatly fit these curves and it provides a unique set of parameters able to describe the exponential trap distribution.

In the next two paragraphs, two possible sources of active traps which can tune the PG effect, and thus determine the detector response, are discussed.

4.2.1.1. Impact of the morphology of the organic semiconducting layer

The results shown in this section are reported in a recent publication that describes the results obtained from a collaboration with Prof. M. Mas-Torrent's research group at the ICMAB (*Institut de Ciència de Materials de Barcelona, Barcelona, Spain*) [216].

In order to investigate the role that the morphology of the organic thin film plays in the X-ray detection, we tested some BGBC OFETs fabricated onto Si/SiO_2 substrates, with gold interdigitated electrodes and the active layer formed by TIPS-Pn deposited by *Bar Assisted Meniscus Shearing* technique (see **Figure 3.2b**). BAMS has been already mentioned in **Section 1.2.1.2** among the Shearing deposition techniques highlighting the fact that it allows to deposit very high quality organic thin films with a good spatial uniformity. In **Figure 4.53** a sketch of the BAMS setup is reported and a picture of the layout of the final fabricated devices is shown.

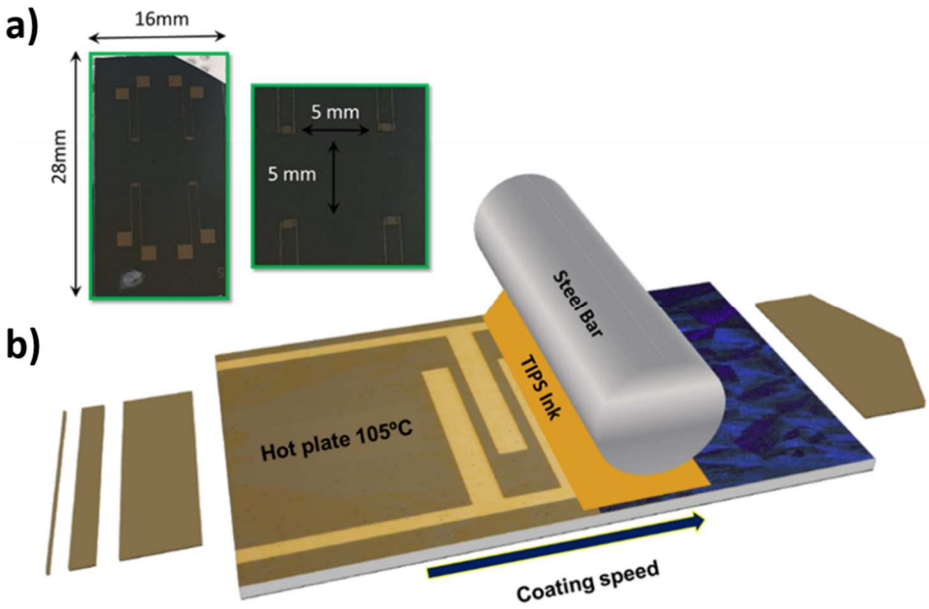

Figure 4.53 *Pictures of the samples indicating the substrate dimensions and the spacing between the devices. b) Sketch of the BAMS setup present at ICMAB (Barcelona, Spain) for the deposition of organic semiconductors* [216].

By exploiting the modification of the deposition parameters we could tune the morphology of the organic thin films. In particular, the modification of the deposition speed impacts on the crystallization regime of the film, affecting the morphology, the domain size, and even the molecular orientation [48], [217]–[219]. In fact, as shown in **Figure 4.54** , by tuning the deposition speed we could vary the crystalline grain dimensions. In particular, coating at a speed of 4-5 mm s^{-1} gives rise to the same spherulitic domains found when coating at a speed of 10-30 mm s^{-1} but with bigger domain size. The polarized optical images of two samples fabricated respectively at 4 mm s^{-1} and 28 mm s^{-1} are reported as an example, in **Figure 4.54 a** and **b**, where the different grain dimensions are clearly visible. We evaluated by Atomic Force Microscopy both the morphology (see **Figure 4.54 c and d**) and the thickness of the two films, which result quite comparable (see **Figure 4.54 e and f**).

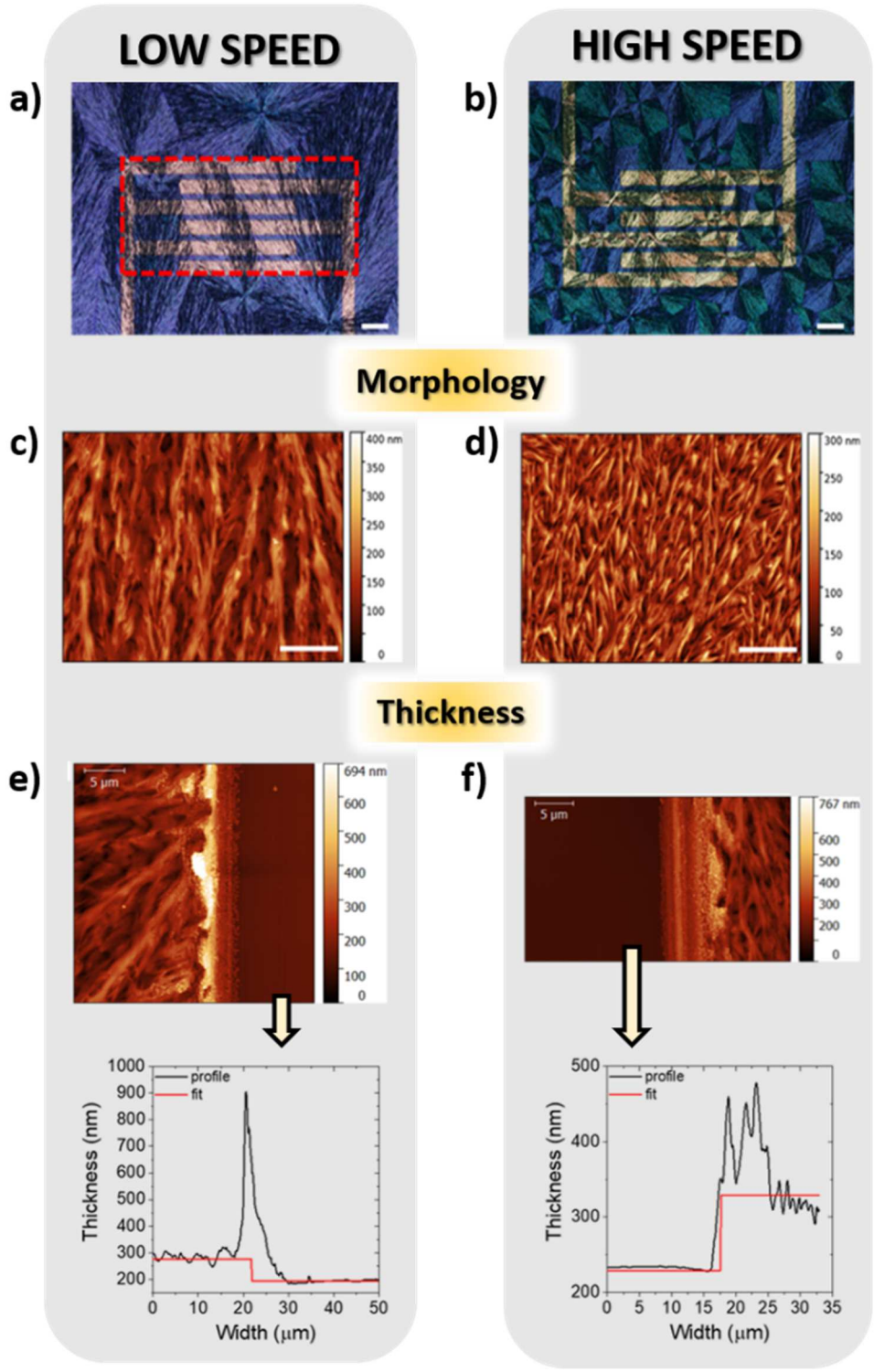

Figure 4.54 *Cross-polarized optical microscope images and AFM topography images of TIPS-Pn thin films deposited at a), c) low speed (4 mm s⁻¹) and b), d) high speed (28 mm s⁻¹). The dashed red box in a) indicated the pixel area used to normalize the following parameters. Scale bar: 10 µm. Topographic AFM images and relative depth profiles for thicknesses estimation for the low-speed and high-speed samples. Adapted from* [216].

Both the thickness and the grain dimensions have been extracted from the AFM images using Gwyddion functions and they are listed in **Table 4.3**.

Deposition Speed (mm s^{-1})	*Grain Size (μm^2)*	*Thickness (nm)*	*Mobility ($cm^2\ V^{-1}\ s^{-1}$)*	*N_T ($10^{12}\ eV^{-1}\ cm^{-2}$)*	*Sensitivity ($\mu C\ Gy^{-1}\ cm^{-2}$)*	*Gain*
Low (4)	17 ± 3	70 ± 20	(2.5 ± 0.7) · 10^{-2}	1.7 ± 0.4	(1.0 ± 0.2) · 10^2	(7 ± 2) · 10^5
Standard (10)	6 ± 2	80 ± 20	(1.7 ± 0.5) · 10^{-2}	1.8 ± 0.5	(3.8 ± 0.1) · 10^2	(20 ± 6) · 10^5
High (28)	6 ± 2	120 ± 50	(2.4 ± 0.6) · 10^{-2}	1.6 ± 0.4	(3.8 ± 1.2) · 10^2	(40 ± 15) · 10^5

Table 4.3 *Structural, electrical and detection parameters for devices based on TIPS-Pn thin films fabricated at different deposition speeds* [216].

It is important to notice that films deposited at a coating speed between 10 and 28 mm s^{-1} did not show great differences in morphology or in grain dimension (see **Figure 4.55**). Higher speeds have not been tested because they provide a non-uniform organic film.

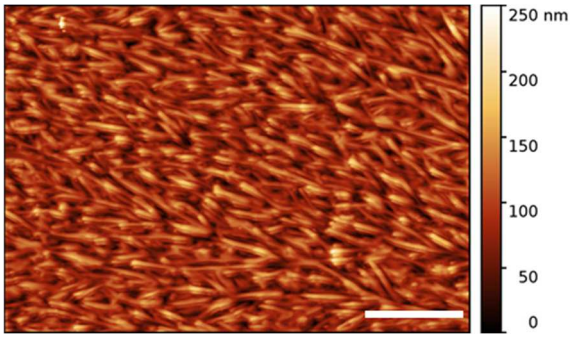

Figure 4.55 *AFM topography image of a TIPS-Pn film deposited at 10 mm s-1 (i.e. standard speed). Scale bar: 10 µm.* [216]

Samples deposited both at high and low deposition speeds have been tested under X-rays produced by a Mo-target tube (see **Section 3.7.1.1**) following the procedure described in **Section 4.2** and keeping them in saturation regime (i.e. V_{GS} = -15 V, V_{DS} = -20 V). From the dynamic response of the sensors we calculated the sensitivity values obtained with these two types of devices, as it is shown in **Figure 4.50**. The graph from which they have been extracted is reported in **Figure 4.56** and it is possible to notice that the sensitivity value varies considerably with the deposition speed.

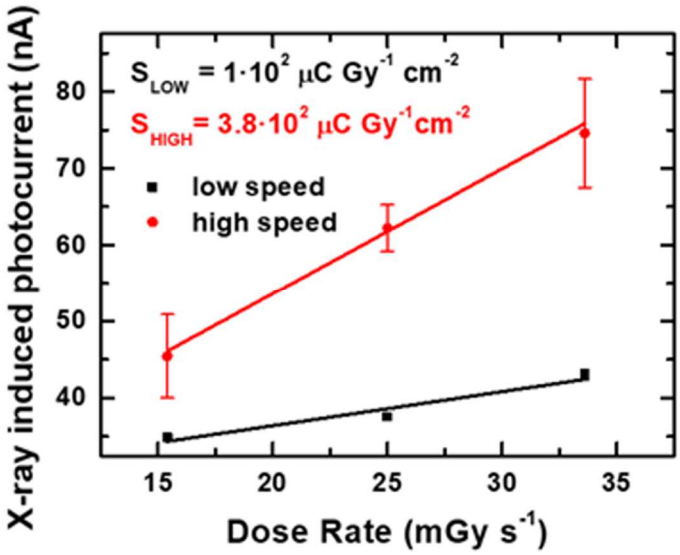

Figure 4.56 *X-ray induced photocurrent versus dose rate plot for the two types of film and relative calculated sensitivity, obtained under irradiation by a Mo-target X-ray tube. The error bars refer to the statistical fluctuations of the signal amplitude over three on/off switching cycles of the X-ray beam in the same condition* [216].

In particular, the devices processed at high-speed show a sensitivity more than three times higher than that of the low-speed processed devices ($3.8 \cdot 10^2$ and $1 \cdot 10^2$ µC Gy^{-1} cm^{-2} respectively). Considering that the transport properties of these

devices are comparable (see the calculated electrical mobilities μ and density of traps for majority carriers N_T reported in **Table 4.3**) the different radiation responses can be ascribed only to the different morphologies and to the different densities of grain boundaries. In fact, as it is shown in **Table 4.3**, the gain factor G calculated for both the *high-speed* and *low-speed* samples results higher for the first, indicating a greater amplification of the photocurrent. This means that the higher is the density of grain boundaries the greater is the density of electron traps which provides the better activation of the photoconductive gain mechanism.

The presence of the electron traps impacts on the recombination time τ_r, i.e., the electron lifetime, which is directly proportional to the gain G (Eq. 2.13). The correlation existing between the electron traps, the density of grain boundaries determined by the deposition speed, and the sensitivity to the radiation can be then explained comparing the experimentally determined sensitivity and hole mobility with the analytical calculation of τ_t and τ_r for different deposition speeds. These calculations have been carried out as it has been described in the previous section. The resulting values are reported in the graphs in **Figure 4.57**: both the recombination time (related to electron traps) and the sensitivity increase with increasing deposition speed, i.e., with the reduction of grain size and thus with the increasing of grain boundary density. A plateau is reached for similar grain sizes (standard and high speed). On the other hand, we could assess how the experimentally measured hole mobility and the related hole transit time show a markedly different trend.

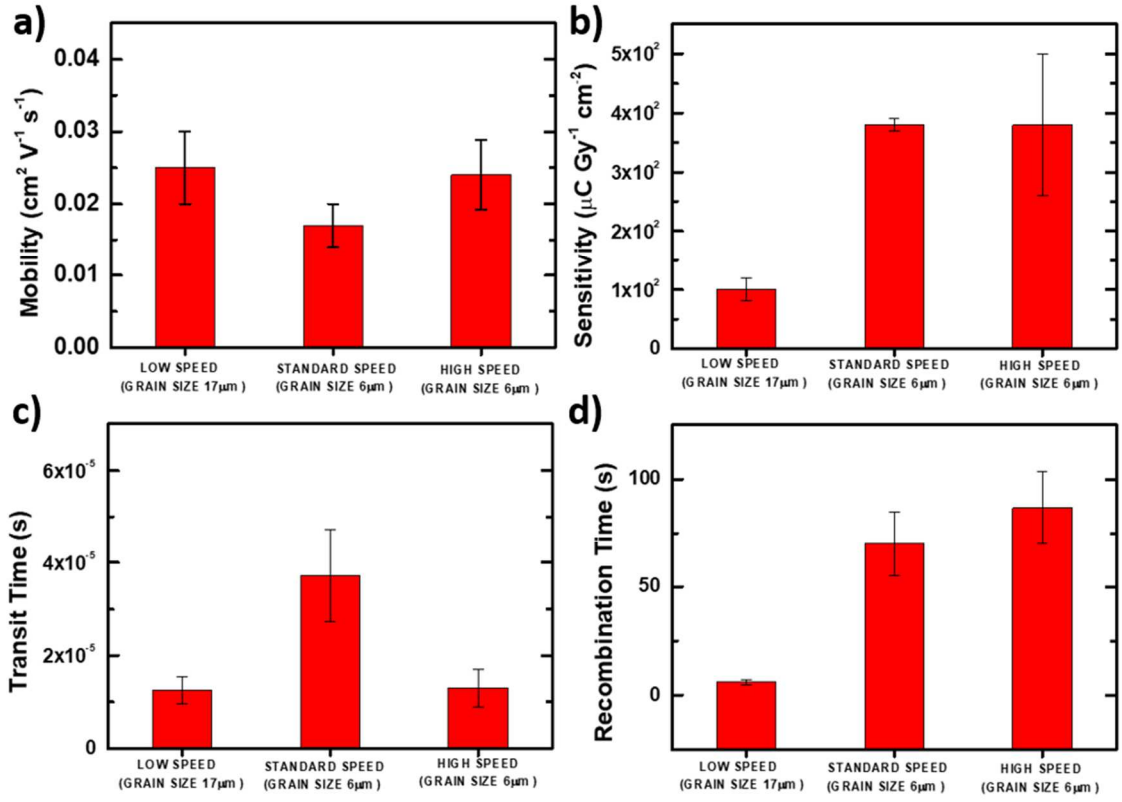

Figure 4.57 *Correlation between mobility, sensitivity, and traps. Experimentally determined hole mobility (a) and sensitivity (b). Analytically determined* τ_t *(c) and* τ_r *(d)for TIPS-Pn thin films deposited at different speeds (i.e. with different density of grain boundaries). The error bars refer to statistical fluctuations of the parameters over four samples for each deposition speed.*[216]

Another important consideration can be extracted by the thickness values reported in **Table 4.3**. in fact, as it is possible to notice, the thicknesses do not strongly affect the radiation detection response of the device. Devices deposited at low and standard deposition speeds have similar thicknesses but different sensitivities and G values. This stems from the fact that in OFETs charge transport occurs at the interface between the organic semiconductor and the dielectric layer, i.e., the few nanometers of the transistor channel. This differs from what happens in a vertical stacked organic detectors (e.g. the heterojunction devices based on P3HT:PCBM:Bi_2O_3 reported by C. A. Mills & S. R. P. Silva et al. [145], [220],

[221]) where charge transport occurs through the bulk of the organic layer, and so its thickness plays a crucial role in the detection process. On the contrary, in our case the radiation-induced charge carriers involved in the photoconductive gain process flow within the OFET channel, meaning that the detection performance is more affected by the efficacy of the transport process at the semiconductor/dielectric interface than by the efficacy of the radiation absorption in the semiconductor bulk. For this reason, increasing the active layer thickness does not represent a winning strategy to improve the X-ray detection properties of OFET-based sensors.

To conclude, in this paragraph I have shown a promising strategy in order to enhance the detection efficiency of this class of sensors. Increasing the grain boundaries density provides a greater number of electron traps which induces a higher activation of the PG mechanism.

4.2.1.2. Impact of the interface dielectric/organic semiconductor

Another frequent source of charge trapping in OFETs structure is the dielectric/organic semiconductor interface (see **Sections 1.2.1.3** and **1.3.1.1)**. In order to relate also this kind of traps to the activation of the PG, analogous samples as the ones described in the previous section have been tested. But, instead of tuning the morphology of the organic films, for this experiment we kept the deposition parameters constant (i.e. 10 mm s^{-1} of deposition speed) while we varied the Si/SiO_2 substrates. In particular, we used two different silicon dioxides provided

by *Bruno Kessler Institute* (FBK, Trento, Italy) and we fabricated on them exactly the same devices as the ones depicted in the previous section.

The silicon dioxides layers have been grown by different techniques:

1) a *PECVD SiO_2* has been evaporated on a Si wafer. This dielectric layer presents a thickness of (304 ± 3) nm. Due to the low process temperature (i.e. 200 °C) and the high deposition rate, this insulator shows the highest trap density.

2) a *TEOS SiO_2* (i.e. *tetraethyl ortosilicate*) deposited at 630 °C has been used (thickness = (299 ± 4) nm) as dielectric layer. This silicon dioxide presents a higher density of defects if compared with the thermal SiO_2 (as the one used to fabricate the samples described in the previous sections). The presence of defects is limited, lower than in the PECVD and it is generated by unsaturated bonds at the dielectric surface [222], [223].

In **Figure 4.58a**, two transfer characteristic curves kept in saturation regime are reported for OFETs fabricated onto both types of silicon dioxides.

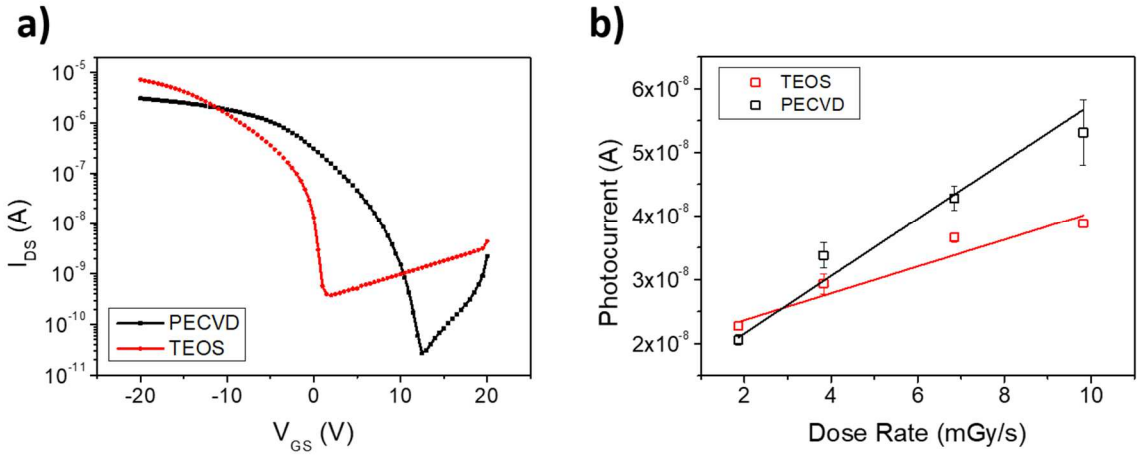

Figure 4.58 *a) Transfer characteristics in saturation regime (V_{DS} = -15 V) and b) photocurrent vs Dose Rate plots for OFETs fabricated on PECVD SiO_2 and TEOS SiO_2.*

The electrical mobility is higher in TEOS samples ($\mu = (3.3 \pm 0.1) \cdot 10^{-2}$ cm^2 V^{-1} s^{-1}) than in PECVD ones ($\mu = (0.014 \pm 0.005)$ cm^2 V^{-1} s^{-1}) that is reasonable because the latter form a more defective interface with the organic semiconductor. PECVD samples show a very positive threshold voltage ($V_{th} = (6.5 \pm 0.2)$ V) which, in p-type OFETs, indicates a strong presence of electron traps as well. On the contrary, the TEOS samples show a slightly negative $V_{th} = (-0.9 \pm 0.2)$ V.

Both types of devices have been tested as radiation detectors irradiating them with X-rays provided by a W-target tube (see **Section 3.7.1.2**). By the dynamic curves it has been possible to calculate the sensitivities as the slope of the fitting curves reported in **Figure 4.58b**. As it is possible to notice, the PECVD samples show a higher sensitivity than the TEOS ones ($S = (1.2 \pm 0.2) \cdot 10^3$ µC Gy^{-1} cm^{-2} and $S = (0.49 \pm 0.07) \cdot 10^3$ µC Gy^{-1} cm^{-2} respectively).

Despite the poorer transport properties, the higher radiation response shown by the PECVD OFETs could be due to the higher number of electron traps related to the PECVD SiO_2/TIPS-Pn interface identified by the shifted V_{th} shown in **Figure 4.58a**.

Important to notice is the fact that in this case the transistors have been irradiated by a different tube compared to the one used for the samples described in the previous section. In particular, this latter is a W-target based tube with a mean energy higher than the Mo-target based one. Moreover, the dose rates employed in these last measurements were lower than the ones used for the previous experiments. These are probably the reasons why the TEOS samples presented a higher sensitivity than the devices fabricated on thermal SiO_2 reported before despite they probably present much more traps for majority carriers.

These preliminary results demonstrated the key role played by the traps at the dielectric/organic semiconductor interface in the enhancement of the PG mechanism.

Another relevant test on this effect has been carried on with a different set of samples realized during my six months stay at the Columbia University in New York (USA), under the supervision of Prof. I. Kymissis. I fabricated several flexible BGBT OFETs presenting the structure depicted in **Figure 3.27c**. I employed a surface treatment to modify the properties of the dielectric/TIPS-Pn interfaces. In particular, I exposed the parylene-C dielectric layer to UV-ozone for different times (i.e. 0, 5, 10, 15 minutes) before depositing the organic semiconductor.

This treatment induced a shift of the threshold voltage towards positive values proportionally to the duration of the treatment (**Figure 4.59a**). **Figure 4.59b** shows how this treatment does not affect the electrical mobility of the OFETs while it has a strong impact on the V_{th}. As observed in the previous cases, for these p-type devices, the direction of this shift indicates the presence of electron traps at the dielectric/organic semiconductor interface. As reported by Kymissis et al. [224], while the unexposed dielectric surface is mostly $-CH_3$ terminated and electroneutral, the UV-treated dielectric surface is partially terminated by electronegative $-COOH$ groups that behave as acceptor-like traps and can attract electrons from TIPS-Pn. The filled traps are almost immobile and form a layer of negative charge which shifts the threshold voltage.

This kind of devices offers another opportunity to further enhance the PG effect exploiting the electron traps induced at the dielectric/organic semiconductor interface by the UV-ozone treatment. Moreover, they allow to transfer the studies conducted so far on Si/SiO_2 substrates onto flexible platforms.

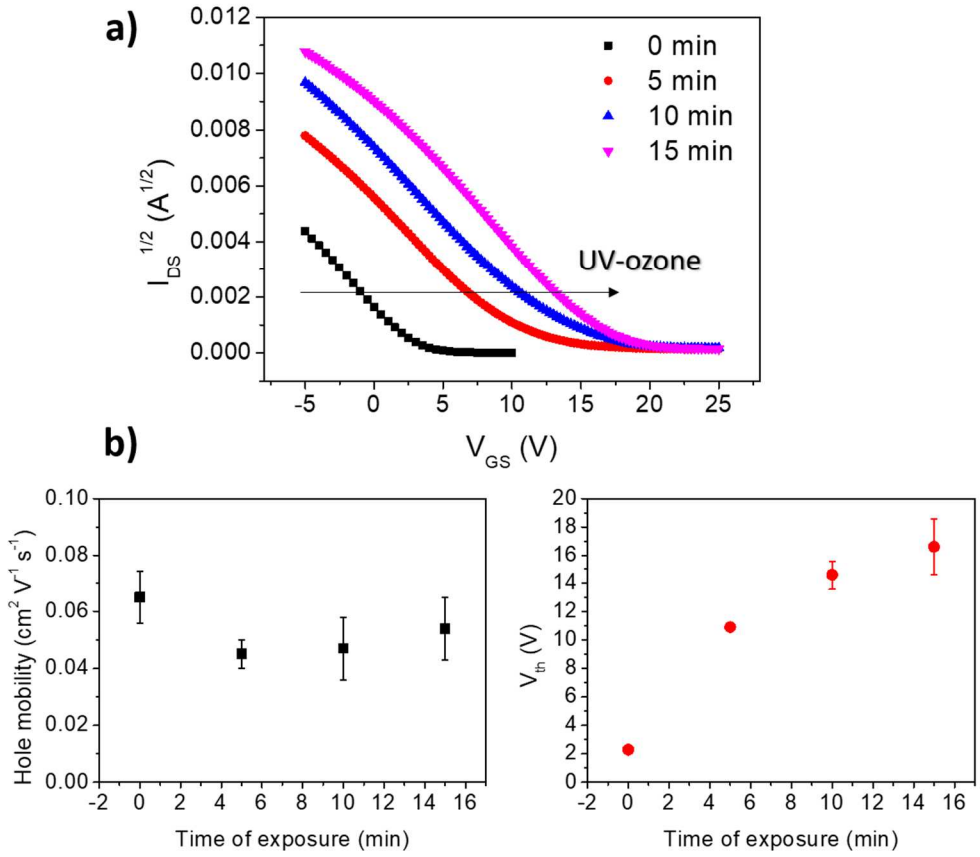

Figure 4.59 a) Transfer characteristics in saturation regime (V_{DS} = -15 V) for samples exposed to UV-ozone for different duration times. The curves clearly indicate a shift of the threshold voltage towards positive bias depending on the time of exposure. Hole mobility (b) and threshold voltage (b) reported as a function of the minutes of UV-ozone exposure.

4.2.2. Increasing of the absorption rate by small molecule tailoring

Another strategy experimented during this work in order to enhance the detection efficiency of the organic semiconductor-based devices exploits an important and peculiar property of this class of materials. In fact, organic semiconductors are easily tailored by chemical processes. Thus, we employed synthesized new small molecules which increase the cross section of interaction between the high energy

photons and the active material of the sensor by the addition of high-Z atoms in the basic molecular structure. This approach allows to overcome the main limitation presented by the blending of organic semiconductors with high-Z nanocomposites (discussed in **Section 2.5.1**) recently proposed by other researchers to increase the efficiency of detection. In fact, in the here reported approach the high-Z elements are directly inserted in the molecular structure of the material avoiding the degradation of the transport properties observed with the implementation of the semiconductor with external species. The results shown in this section are reported in a paper published on *Advanced Functional Materials* in 2018 [225].

We tested the TIPGe-Pn molecule provided by Prof. J. E. Anthony from the University of Kentucky, derived from TIPS-Pn with Ge-substitution in place of the Si atoms. These molecules have been described and depicted in **Section 3.2.2**. Thanks to the much higher Ge atomic number (Z = 32) than the one of Si atoms (Z = 14) the X-ray attenuated fraction of TIPGe-Pn is intrinsically much higher than the TIPS-Pn molecule

(see **Figure 4.60a**), and the attenuation length at an X-ray energy of 17 keV, is ten times shorter (7.8 mm for TIPS-Pn and 0.6 mm for TIPGe-Pn). Moreover, the substitution of Ge for Si leads to a new material with similar solubility and processing parameters as TIPS-Pn.

TIPGe-Pn thin films have been deposited by drop-casting onto interdigitated gold electrodes on flexible plastic substrate as depicted in **Figure 3.26**. Good crystallization and uniform polycrystalline films have been obtained, enabling the efficient flow of electrical current through the fingers of the electrodes. Optical and atomic force microscopy (AFM) images show needle-like crystals, hundreds of

micrometer-long and 200 nm thick (see **Figure 4.60b**). Besides, photocurrent spectroscopy confirms the good optoelectronic properties of the film and its quality. The high and stable photocurrent

signal with a smooth spectrum presenting the known vibronic modes [226], [227] is reported in **Figure 4.60c**. The forbidden energy gap has been extracted from the Tauc formula [228] since the photocurrent signal is well approximated by the absorption spectrum in low absorption condition as at the rising edge of the gap [212]. The calculated energy gap for TIPGe-Pn is (1.60 ± 0.03) eV, slightly larger than the one of TIPS-Pn, (1.56 ± 0.09) eV.

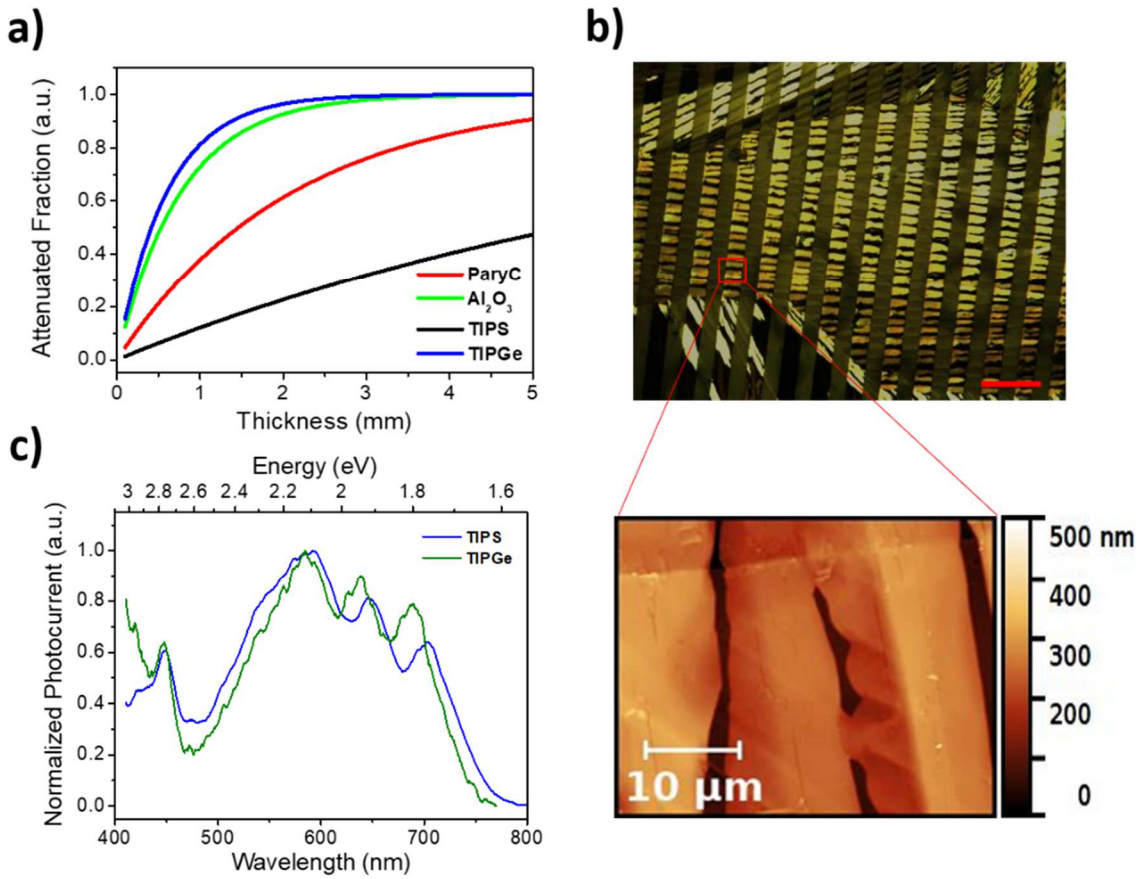

Figure 4.60 *a) X-ray attenuated fraction at energy 17 keV as function of material thickness, showing the much smaller attenuation length of TIPGe-Pn compared to TIPS-Pn. b) Polarized optical microscope image of 200 nm thick microcrystalline layer formed by drop-cast TIPGe-Pn 0.5 wt% solution in toluene onto plastic substrate. Red marker 100 µm. Bottom: AFM image of a few*

crystallites. c) Photocurrent spectra of TIPS-Pn (150 nm thick, blue line) and TIPGe-Pn (200 nm thick, green line) thin films. [225]

To assess the radiation detection performances, I deposited TIPGe-Pn by drop casting onto the BGBC low-voltage OFET structure already described in **Section 3.1** and depicted in **Figure 3.2a**. Important to notice is the fact that the same device architecture had been used to test TIPS-Pn-based devices [229] and so it constitutes an optimal benchmark for the characterization of TIPGe-Pn detecting performance in comparison to what it had been observed with TIPS-Pn-based sensors.

I fabricated OFETs from solutions of TIPGe-Pn at a concentration of 0.5 wt% in toluene or in chlorobenzene solvent. In general, high performing p-type transistors have been obtained operating at very low voltages. **Figure 4.61a** and **b** report the output and the transfer characteristic curves of the optimized device. These indicate a good field effect, no hysteresis, low contact resistance, a very low threshold voltage (< -0.2 V), low leakage current ($< 10^{-9}$ A), and a good ON/OFF ratio (10^2-10^5). Moreover, the average electrical mobility for devices with chlorobenzene solvent is (0.28 ± 0.11) cm^2 V^{-1} s^{-1}, while the highest measured value was 0.4 cm^2 V^{-1} s^{-1}. As shown in **Figure 4.61c**, these electrical mobility values are more than one order of magnitude higher than those reported for TIPS-Pn devices (i.e. $(1.8 \pm 1.0) \cdot 10^{-2}$cm^2 V^{-1} s^{-1}) fabricated exactly on the same substrate, confirming the better transport properties provided by the Ge-based molecules compared with the Si-based ones (see **Section 3.2.2**).

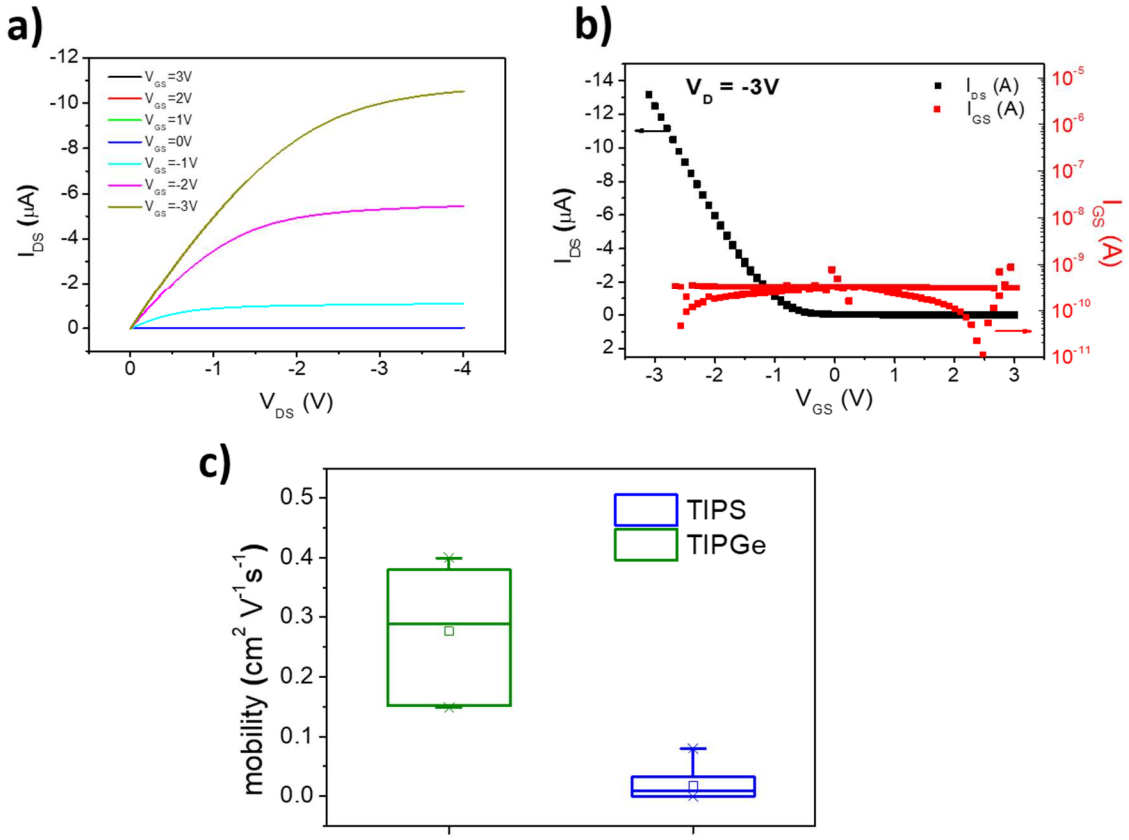

Figure 4.61 *Typical output (a) and transfer characteristic (b) curved acquired by a low-voltage OFET fabricated onto plastic substrate based on TIPGe-Pn semiconductor. c) Electrical mobility comparison between TIPGe-Pn-based and TIPS-Pn-based OFETs fabricated onto the same OFET structure.* [225]

The mechanical flexibility of the devices has been tested stressing the OFETs by incrementally reducing the bending radius and thus increasing the strain on the film. The current variation is small up to strain of 1% (**Figure 4.62**). The transfer characteristic (i.e. the transport properties of the OFETs) returns to the starting point when the samples are restored in the initial flat position (**Figure 4.62b**). This means that no permanent damages are induced in the bending process which lasts 40 minutes. This study confirmed what has been previously reported regarding the mechanical flexibility of TIPS-Pn-based OFETs [101], [230].

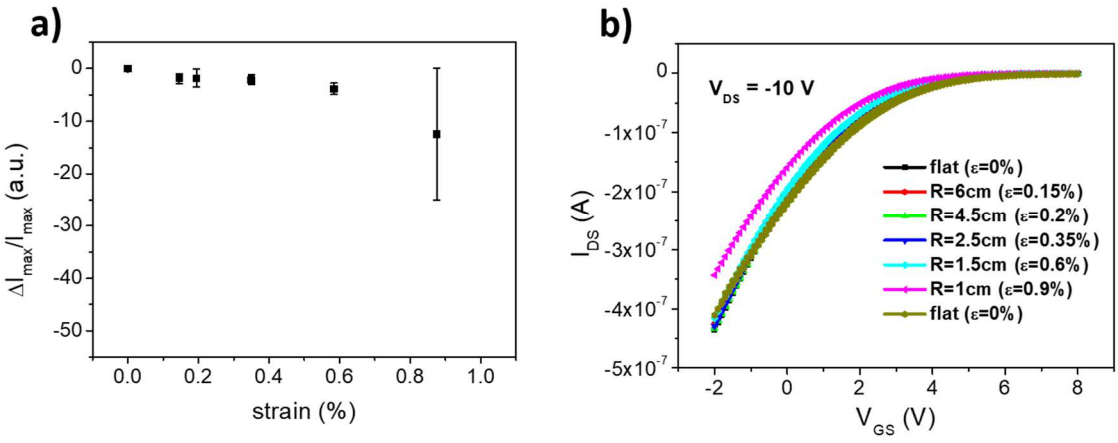

Figure 4.62 *Mechanical stress test of a TIPGe-Pn-based OFET under different bending radius (down to 1 cm). a) Relative current variation under the increasing application of strain. The strain starts to be significant at 0.9%. b) Transfer characteristic curves acquired at different bending radii. The current totally recovers when the flat position is repristinated after the bending test.* [225]

The TIPGe-Pn-based OFETs have been tested as X-rays detectors measuring them under a radiation beam produced by a Mo-target tube (see **Section 3.7.1.1**) and following the procedure described in **Section 4.2**. During the exposures the devices have been kept in saturation regime (V_{GS} = -2 V; V_{DS} = -3 V) in order to maximize the photoresponse. The typical dynamic curve acquired by this class of devices is reported in **Figure 4.63a**. From this, it has been possible to calculate the sensitivity by the linear fit shown in **Figure 4.63b**. The mean sensitivity (averaged over 15 samples) is (3080 ± 20) nC Gy^{-1} ((6.2 ± 0.1) × 10^5 μC Gy^{-1} cm^{-3}), with top recorded value of (4460 ± 50) nC Gy^{-1} ((9.0 ± 0.1) × 10^5 μC Gy^{-1} cm^{-3}).

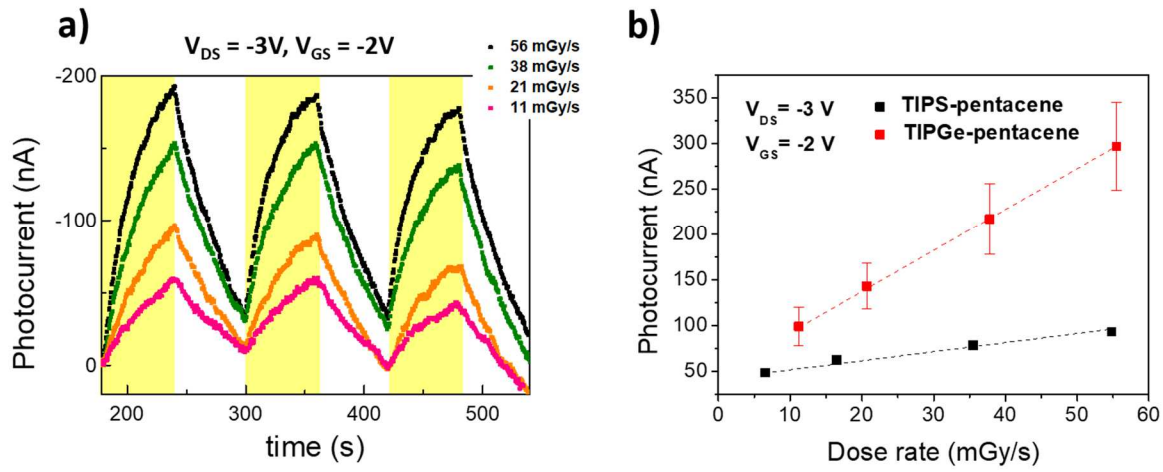

Figure 4.63 *a) Typical dynamic response of the TIPGe-Pn-based detector irradiated by consequent ON/OFF cycles of X-rays at different dose rates. The yellow shaded areas indicate when the beam is ON. b) Comparison between X-rays induced photocurrent at different dose rates for TIPS (black squares) and TIPGe (red squares) [225].*

Table 4.4 and **Figure 4.63b** report the direct comparison with TIPS-Pn thin film detectors fabricated on the same flexible substrate confirming the better performance of TIPGe-Pn. In fact, the average sensitivity of TIPGe-Pn thin film detectors is three times higher than for TIPS-Pn-based devices.

Molecule	*Solution*	*Mobility* ($cm^2V^{-1}s^{-1}$)	*Operative Voltage (V)*	*Film Thickness (nm)*	*Average Sensitivity* ($nCGy^{-1}$)	S_A ($\mu CGy^{-1}cm^{-2}$)	S_V ($\mu CGy^{-1}cm^{-3}$)
TIPS-Pn	0.5wt% in toluene dropcast	0.02 ± 0.01	V_{DS} = -3	150	960 ± 70	3.9 ± 0.3	(2.6 ± 0.2) · 10^5
TIPGe-Pn		0.27 ± 0.09	V_{GS} = -2	200	3080 ± 20	12.3 ± 0.2	(6.2 ± 0.1) · 10^5

Table 4.4 *Comparison of mobility, sensitivity, sensitivity per area and sensitivity per unit of volume for TIPS-Pn and TIPGe-Pn based sensors realized on the same OFET structure.* [225]

Two aspects related to TIPGe-Pn sensitivity are important to notice:

1) The sensitivity per unit of volume is one of the highest reported among solid-state X-ray detectors based on organic and hybrid thin films [152]. The corresponding sensitivity per unit of area is competitive with state-of-art inorganic materials currently used to fabricate large-area detectors (i.e. a-Se which typically presents 25 µC Gy^{-1} cm^{-2}) [124].

2) The lowest detectable dose rate (defined as three times the detector noise, as it has been discussed in **Chapter 2**) from the slope of the linear fit of **Figure 4.64b**, it results equal to 1.66 µGy s^{-1}. **Figure 4.64** reports the photocurrent response of TIPGe-Pn detectors in linear region ($V_{DS} = -0.5V$) at low exposure doses, down to a dose rate of 6.4 µGy s^{-1}. Remarkably, the detectors show a linear response to X-rays over four orders of magnitude in the dose rate range. In addition, the smallest total dose detectable has been measured over an X-ray exposition of 1 s and we could reliably detect down to 12 µGy (**Figure 4.64c**). These values are among the lowest reported for organic and hybrid-based thin films devices and besides, they are below the threshold of regular medical diagnostic (dose rate about 5.5 µGy s^{-1}) [125], [231].

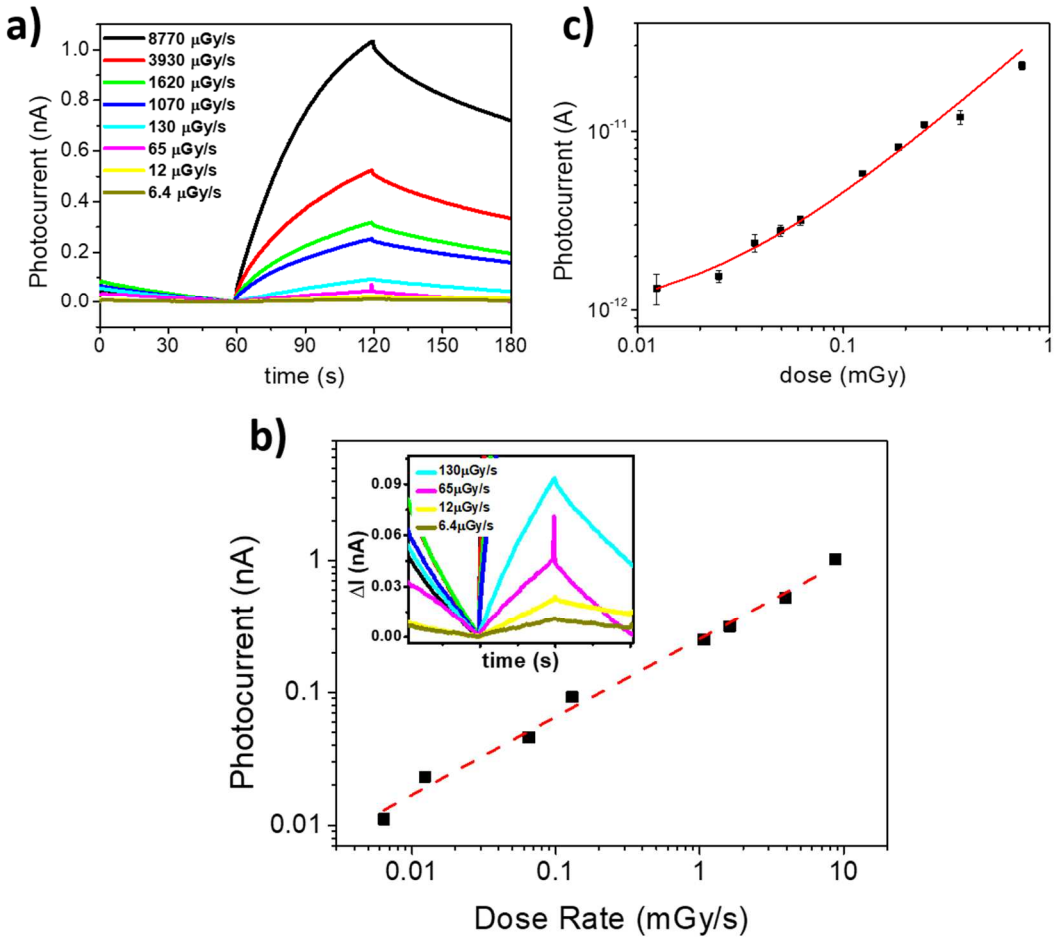

Figure 4.64 *a) Dynamic response of TIPGe-Pn at low dose rates, biased at VDS = −0.5V (linear region). b) X-ray induced photocurrent at very low dose rates, down to 6.4 µGy s⁻¹. Inset: Corresponding photocurrent signal versus time. c) Photocurrent as a function of the relative total integrated doses over 1 s of exposure. Minimum detected total dose equal to 12 µGy.* [225]

So far, it has been shown that the idea of chemical tailoring of organic molecules such as TIPS-Pn to synthetize a new molecule with high-Z atoms intrinsically bonded into the basic molecule (TIPGe-Pn) is effective. In order to confirm the validity of this strategy, the same experiment has been repeated employing another set of organic small-molecule: diF-TES-ADT and its derivative with Ge in place of Si atoms, diF-TEG-ADT. Both these molecules have been described in **Section 3.2.2**. OFETs with the same structure as before have been fabricated with diF-

TES-ADT and diF-TEG-ADT spin coated as active layer (1.2 wt% solution in chlorobenzene).

The morphology of the two films is shown by the AFM images reported in **Figure 4.65**. The diF-TES-ADT crystallized in larger and thicker microstructures (thickness 120 nm) if compared with the diF-TEG-ADT (thickness of 90 nm), but both the films presented a good spatial uniformity.

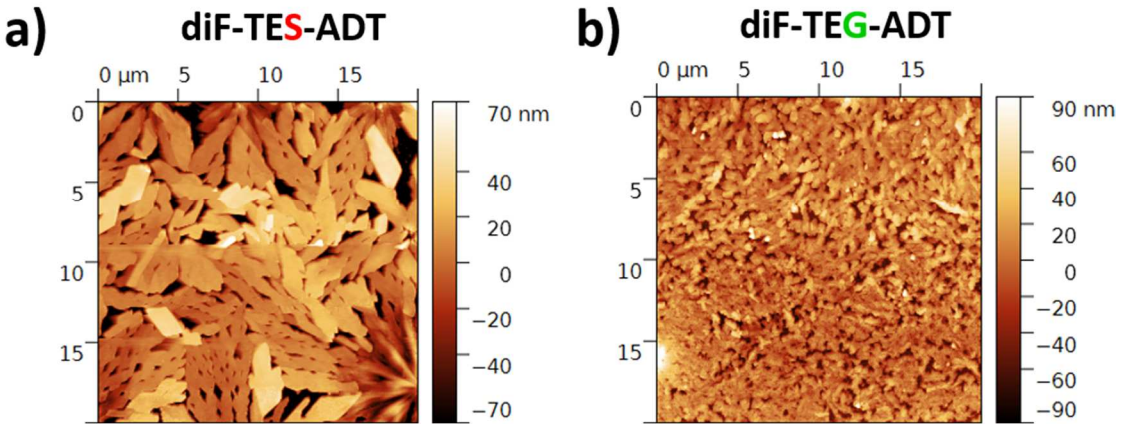

Figure 4.65 *AFM morphology maps of (a) diF-TES-ADT and (b) diF-TEG-ADT thin films.* [225]

Due to the higher-Z elements present in the molecular structure, while the X-ray attenuated fraction is equal to 0.0031% for diF-TES-ADT, it results 0.015% for diF-TEG-ADT. For both materials good field effect mobility in low voltage transistor devices has been obtained and, in spite of the crystal dimensions, diF-TEG-ADT devices show on average a better mobility compared to diF-TES-ADT ones confirming what has been reported in literature and in **Chapter 3** [45]. By the way, for the test under X-rays, devices with comparable mobility values have been measured, in order to explicitly exclude the effects of transport properties on X-ray

sensitivity. **Figure 4.66** reports the X-ray photocurrent versus dose rate of diF-TES-ADT and diF-TEG-ADT transistors, with mobility of (5.2 ± 0.3) × 10^{-2} and (6.9 ± 0.4) × 10^{-2} cm^2 V^{-1} s^{-1}, respectively. The extracted

sensitivity of diF-TEG-ADT-based detectors (3400 ± 400) nC mGy^{-1} cm^{-3} is 40 times higher than the one calculated for diF-TES-ADT devices (see **Table 4.5**).

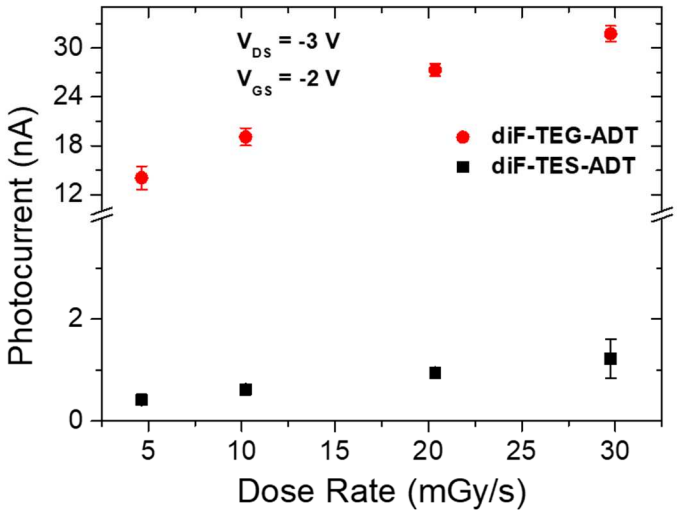

Figure 4.66 *Comparison between X-rays induced photocurrent at different dose rates for diF-TES-ADT (black squares) and diF-TEG-ADT (red circles).* [225]

Molecule	*Solution*	*Mobility* *(cm² V⁻¹ s⁻¹)*	*Operative Voltage*	*Film Thickness (nm)*	*S_V* *(μC Gy⁻¹ cm⁻³)*
diF-TES-ADT	1.2wt% in chlorobenzene spincast	(5.2 ± 0.3) · 10^{-2}	V_{DS} = -3 V	120	80 ± 10
diF-TEG-ADT		(6.9 ± 0.4) · 10^{-2}	V_{GS} = -2 V	90	3400 ± 400

Table 4.5 *Comparison of sensitivity per unit of volume for diF-TES-ADT and diF-TEG-ADT based sensors realized on the same OFET structure and with similar electrical mobilities.* [225]

This crosscheck test confirmed the effectiveness of the here shown strategy, that is, increasing the atomic number of organic molecules by chemical tailoring, that successfully leads to the improvement in X-ray sensitivity of organic thin film detectors.

4.2.2.1. Different activation of photoconductive gain effect

As it has been already discussed in the previous sections, in organic semiconductor-based radiation detectors the generated photocurrent is the product of the gain factor G and the primary collected charges I_{CC}: the gain factor G rises proportionally with the improvement of mobility and with the density of electron traps, while I_{CC} increases with the improvement of X-ray absorption. Considering that both the electrical mobility and the attenuation fraction of the TIPGe-Pn-based OFETs results more than ten times higher than in the TIPS-Pn, the sensitivity values resulted by the first should be higher than what has been obtained.

One possible reason for this discrepancy could be attributed to the different area coverage that has initially been obtained by the two films. In fact, employing the same deposition conditions, the area coverage of TIPS-Pn crystallites is about 76% with small variation between the samples, while the variation of percentage of full coverage in TIPGe-Pn-based devices is relevant, in the range 40–75% (see **Figure 4.67**). If we calculate the potential sensitivity, that is, the sensitivity normalized for the actual coverage as if the full area is covered, we obtain 3.4×10^5 μC Gy^{-1}

cm^{-3} for TIPS-Pn devices, and 21 × 10^5 μC Gy^{-1} cm^{-3} for TIPGe-Pn ones. It is clear that the difference of area coverage between TIPS-Pn and TIPGe-Pn can only partially explain this underestimation.

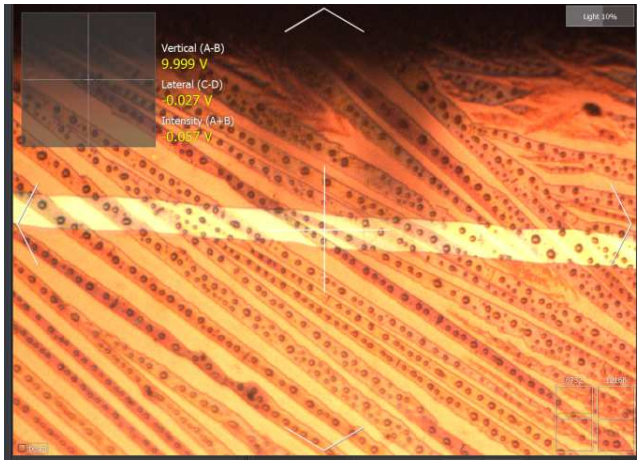

Figure 4.67 *optical image representing the poor area coverage obtained with TIPGe-Pn drop-casted.* [225]

Another possible reason could be related to a different activation of the photoconductive gain effect which rules the amplification of the X-rays induced signal.

In order to deeper investigate this aspect, OFETs fabricated at the Columbia University employing the Pneumatic Nozzle Printing technique have been analyzed. These BGBC OFETs present the structure depicted in **Figure 3.27c**. The Pneumatic Nozzle Printing deposition technique allows to obtain very well packed and uniform thin films both for TIPS-Pn and for TIPGe-Pn as shown by the optical images reported in **Figure 4.68**.

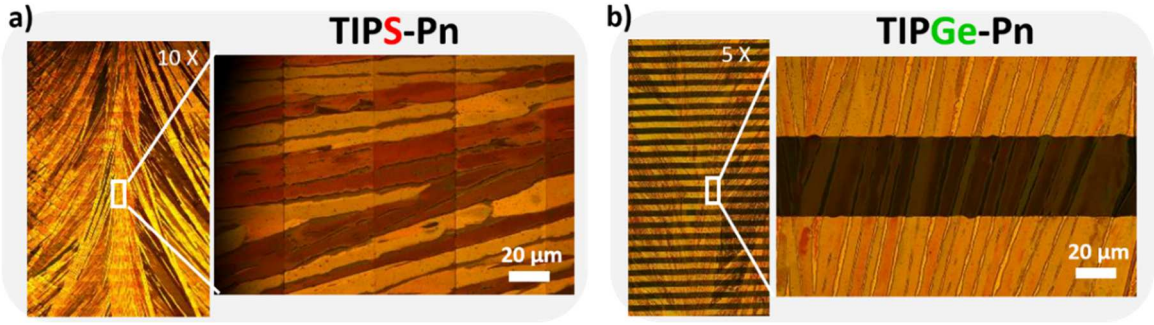

Figure 4.68 *Optical images of (a) TIPS-Pn and (b) TIPGe-Pn thin films deposited by Pneumatic Nozzle Printing at the Columbia University.*

Several OFETs, for each type of molecule, presenting similar electrical mobilities, morphologies (i.e. density of grain boundaries) and sensitivities to the X-rays have been compared and characterized employing photocurrent spectroscopy experiments. In particular, in **Figure 4.69**, a meaningful example which shows the same features observed in photocurrent spectra for TIPGe-Pn and TIPS-Pn OFETs is reported. The OFETs properties are summarized in **Table 4.6**.

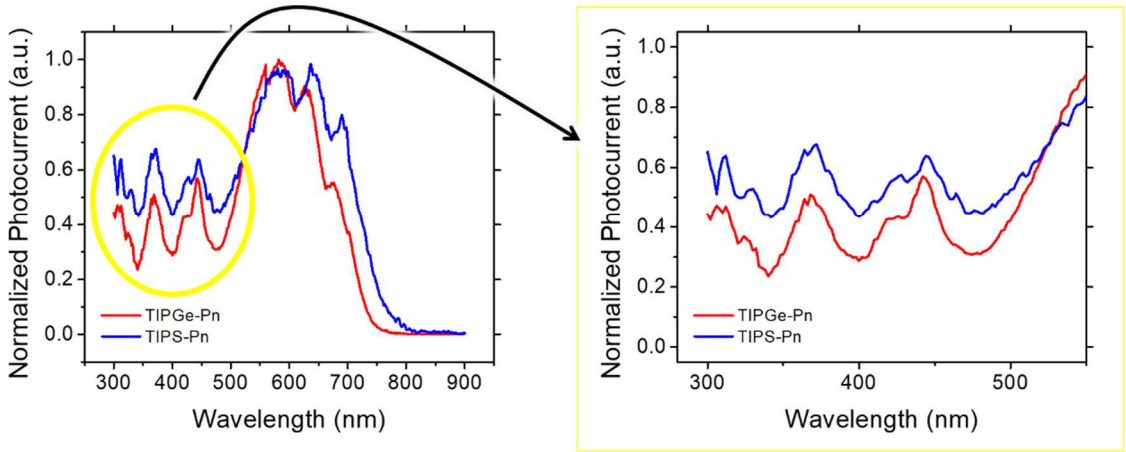

Figure 4.69 *Photocurrent spectra of a TIPS-Pn (blue) and TIPGe-Pn (red) based OFET which share similar electrical mobilities, morphologies (i.e. density of grain boundaries) and sensitivities to the X-rays.*

Molecule	*Grain dimension*	*Mobility* ($cm^2\ V^{-1}\ s^{-1}$)	*Sensitivity* ($\mu C\ Gy^{-1}$)
TIPS-Pn	7 ± 2	0.10 ± 0.02	21.4 ± 0.5
TIPGe-Pn	5.4 ± 0.2	0.09 ± 0.01	21 ± 1

Table 4.6 *Morphological, electrical, and detecting properties of TIPS-Pn and TIPGe-Pn-based OFETs compared in Figure 4.22.*

In the two normalized photocurrent spectra, a large discrepancy between the TIPS-Pn and TIPGe-Pn at low wavelengths (see **Figure 4.69**) can be noticed. In particular, the peaks at 370 nm and 442 nm are smaller for the TIPGe-Pn than for the TIPS-Pn. This aspect can be interpretated considering what I. Kymissis et.al. reported in [224]. They analyzed pentacene-based OFETs comparing the visible photocurrent induced in a UV-ozone treated sample and an identical one with no air or ozone exposure. They demonstrated intensified photocurrent peaks in oxygen-doped samples in the range of 350–480 nm. These peaks are attributed to the formation of excitons and improved dissociation into electrons and holes, owing to the electron trap states formed at the interface between the UV-treated dielectric and the pentacene, which also accounts for positively shifted threshold voltage in the UV-treated sample.

According to that work, the lower intensity of the peaks in the range 300-500nm for TIPGe-Pn could be due to a lower density of those electron traps which are responsible of the photoconductive gain mechanism under X-rays. This could be an additional aspect which lowers the sensitivity of the TIPGe-based radiation sensors with respect to the TIPS-based ones.

4.2.3. Impact of the transport properties on the radiation detection

In this section another aspect which can affect the X-ray detection response of direct organic-based sensor is discussed. These results are reported in [216] and they highlight the impact of the OFETs transport properties on the X-ray sensitivity.

I tested some OFETs presenting the same structure described in **Section 4.2.1.1** and depicted in **Figure 3.27b**. In this case the conditions of deposition (e.g. coating speed) have been kept constant while the addition of an insulating polymer blended with the TIPS-Pn in different concentration has been performed. In fact, as it has been already discussed in **Section 1.2.1.2**, **1.3.1.1** and **3.2.2**, the addition of an insulating polymer such as polystyrene (i.e. PS) to the organic ink has shown to be an effective way to improve thin-film processability and stability, and to boost the performance of TIPS-Pn transistors [52], [232].

In particular, several OFETs based on different TIPS-Pn:PS blending ratios (1:0 i.e. pure TIPS-Pn, 4:1, 2:1, 1:1) have been fabricated and tested.

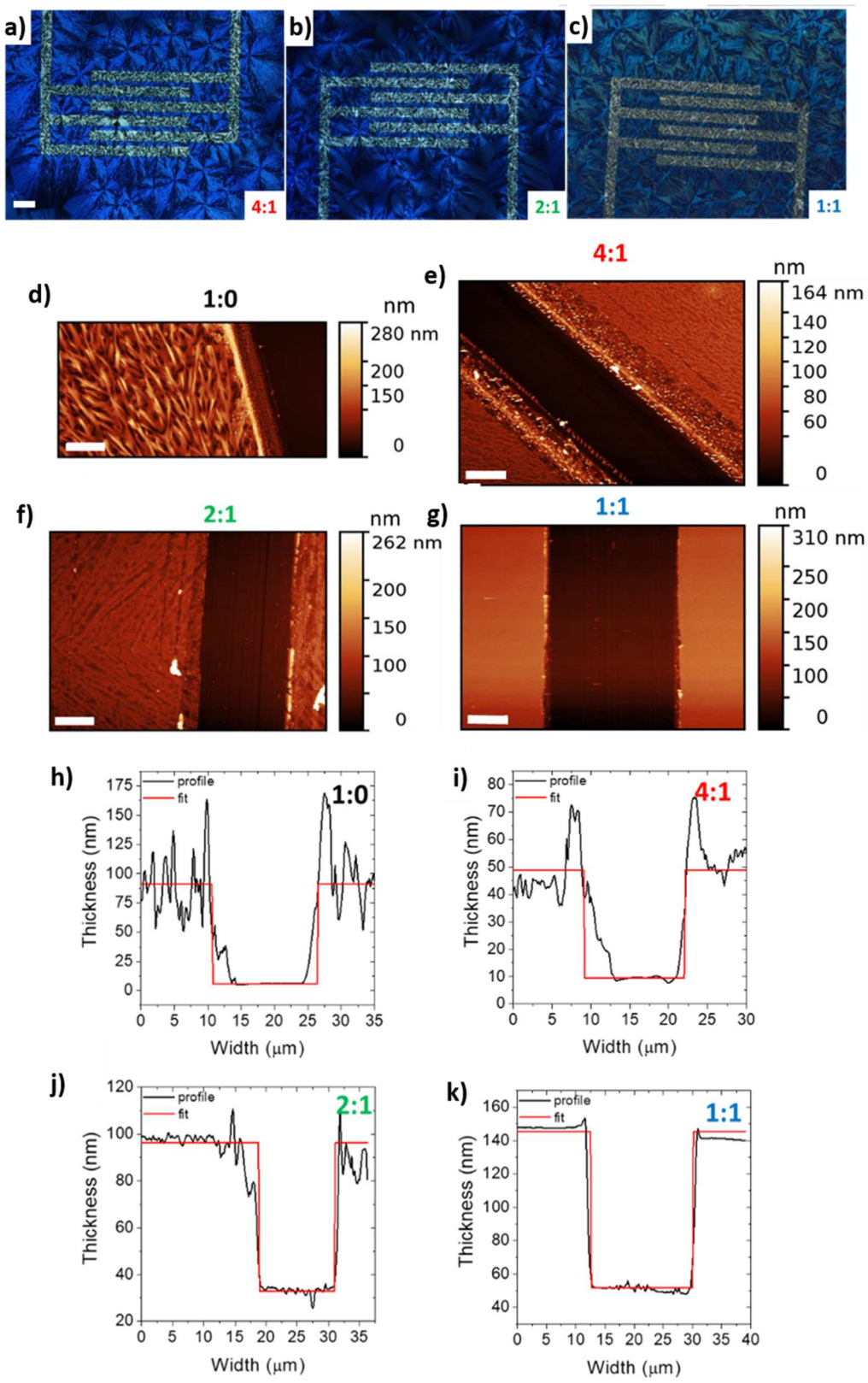

Figure 4.70 *Cross-polarised optical microscope images of TIPS-Pn:PS thin films with different blending ratios (4:1 (a), 2:1 (b), 1:1 (c)). Scale bar: 100 μm. (d-g) Topographic AFM images and (h-k) depth profiles. The blending ratio is indicated on the top of each image. Scale bar: 5 μm.* [216]

In **Figure 4.70a, b, c**, the polarized optical images of the different samples are shown. All the films present a good spatial uniformity and the spherulitic crystallization of the TIPS-Pn already observed for the pure-TIPS-Pn films. Moreover, in **Figure 4.70d-g and h-k**, the AFM images and the extrapolated profiles have been used to further characterize the morphologies and the thicknesses of the different films. As it is summarized in **Table 4.7**, all the thin films presented a thickness in the range between 40 and 90 nm while only the PS-containing films presented a smoother surface demonstrating the uniformity provided by the polymer. This aspect is an indication that TIPS-Pn crystals are embedded in the polymeric matrix.

Blend Ratio	*rms (nm)*	*Thickness (nm)*
1 : 0	37	80 ± 20
4 : 1	6	40 ± 10
2 : 1	9	60 ± 5
1 : 1	2	90 ± 5

Table 4.7 *Roughness (rms) and thin-film thickness for different blend ratios* [216].

A statistical analysis of the main OFET parameters of 1:0, 4:1, 2:1 and 1:1 TIPS-Pn:PS devices was performed employing different batches of samples to test reproducibility (10 devices for each formulation). Statistics on the saturation field effect mobility μ, hole trap density (N_T), on/off ratio (*ON/OFF*) and threshold voltage (V_{th}) are collected in **Figure 4.71** and in **Table 4.8**.

Blend Ratio	I_{on}/I_{off}	*Mobility* ($cm^2\ V^{-1}\ s^{-1}$)	V_{th} (V)	S ($V\ dec^{-1}$)	N_T ($10^{12}\ eV^{-1}\ cm^{-2}$)
1 : 0	$(4 \pm 2) \cdot 10^3$	$(1.0 \pm 0.3) \cdot 10^{-2}$	6 ± 2	1.6 ± 0.4	2.7 ± 0.7
4 : 1	$(3 \pm 2) \cdot 10^5$	$(5 \pm 2) \cdot 10^{-1}$	-1 ± 2	0.6 ± 0.2	1.0 ± 0.3
2 : 1	$(4 \pm 2) \cdot 10^5$	$(5 \pm 3) \cdot 10^{-1}$	-1 ± 1	0.5 ± 0.1	0.8 ± 0.1
1 : 1	$(1.4 \pm 0.9) \cdot 10^5$	$(6 \pm 4) \cdot 10^{-2}$	-2 ± 1	0.7 ± 0.1	1.2 ± 0.2

Table 4.8 *OFET parameters for different ratio of TIPS-Pn:PS blends.* [216]

A comparison between all studied blends shows a general improvement of the electrical performance when PS is added to the ink. In particular, it can be observed that the on/off ratio and the mobility are higher for PS containing devices. For 4:1 and 2:1 blends the average values reach $4 \cdot 10^5$ and 0.5 $cm^2\ V^{-1}\ s^{-1}$, respectively, which represents an increase of almost two orders of magnitude with respect to the pure TIPS-Pn devices. It is important to notice the gradual decrease of the subthreshold swing slope (i.e. S) in the PS-containing devices which indicates a reduction of interfacial trap states for majority carriers (N_T) calculated by Eq. 1.13. Indeed, it has already been reported for various systems of organic semiconductor:PS thin films processed by solution that the crystalline semiconducting layer is formed on top of a PS buffering layer[47], [233], [234]. Thanks to this vertical phase separation, the PS layer in direct contact with the silicon dielectric passivates the surface, reducing the density of hole traps at the dielectric/organic semiconductor interface and thus justifying the observed increased mobility.

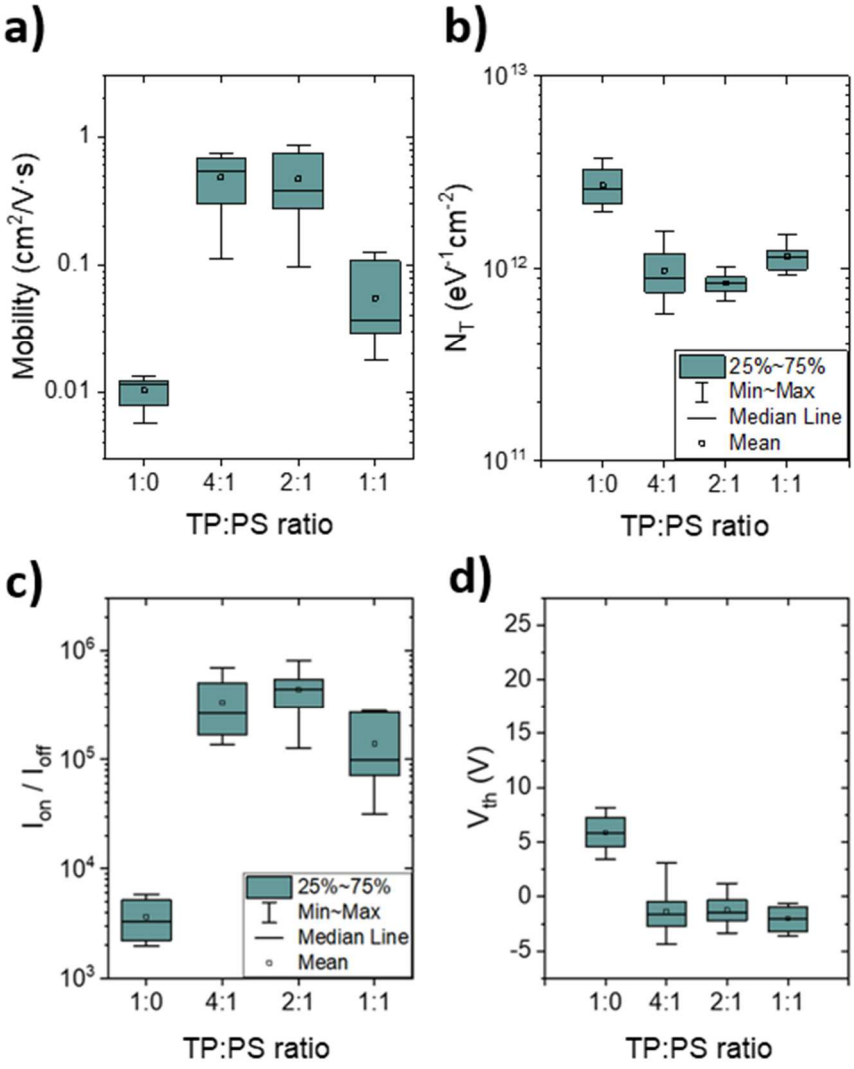

Figure 4.71 *Box-plot statistics for the OFET mobility (a), density of hole traps (b), ON/OFF ratio (c) and threshold voltage (d), obtained from ten devices of each TIPS-Pn:PS blend ratio (1:0, 4:1, 2:1, 1:1).* [216]

The response to X-rays provided by a Mo-target tube was tested for all the proposed TIPS-Pn:PS formulations, 1:0, 4:1, 2:1 and 1:1. **Figure 4.72** shows the estimated sensitivity values, which are higher for PS containing devices, especially for 4:1 and 2:1 blends. Remarkably, an outstanding X-ray sensitivity as high as $1.3 \cdot 10^4$ µC Gy^{-1} cm^{-2}, normalized to the pixel area (indicated by the dashed red square in **Figure 4.54 a**), was obtained, which is the highest value reported for

organic X-ray detectors. The sensitivity is about three and two orders of magnitude higher than the reference value for a-Se and poly-CZT X-ray detectors respectively [124]. As a matter of fact, the gain mechanism in the blended devices is so efficient that the X-ray sensitivity values are comparable with direct detectors based on thick polycrystalline perovskite devices [235].

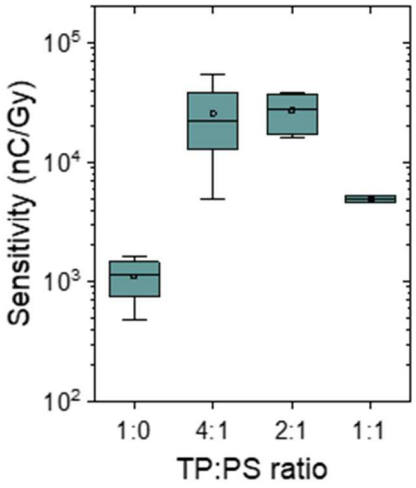

Figure 4.72 *Box-plot statistics for the OFET sensitivity obtained from ten devices of each TIPS-Pn:PS blend ratio (1:0, 4:1, 2:1, 1:1).* [216]

To underline the outperformance achieved by this class of sensors, two graphs reported in a recent review by L. Basiricò et al. are shown in **Figure 4.73** [123]. These plots show the X-ray top sensitivities per unit of area (**Figure 4.73 a**) and of volume (**Figure 4.73 b**) achieved by detectors based on thick/thin active layer of perovskite (red) and organic/hybrid (blue) semiconductors. Both these plots highlight the high sensitivity registered employing TIPS-Pn:PS-based detectors (plotted in yellow) clearly pointing out their potential to real applications. In fact, the top sensitivity value per unit of volume achieved by this class of devices is 3.2 $\cdot$ 10^9 µC Gy^{-1} cm^{-3} which is three orders of magnitude higher than the hybrid

organic/inorganic photodiodes recently reported in literature [145] and four orders of magnitude higher than State-of-the-Art all-organic X-ray detectors [154], [225].

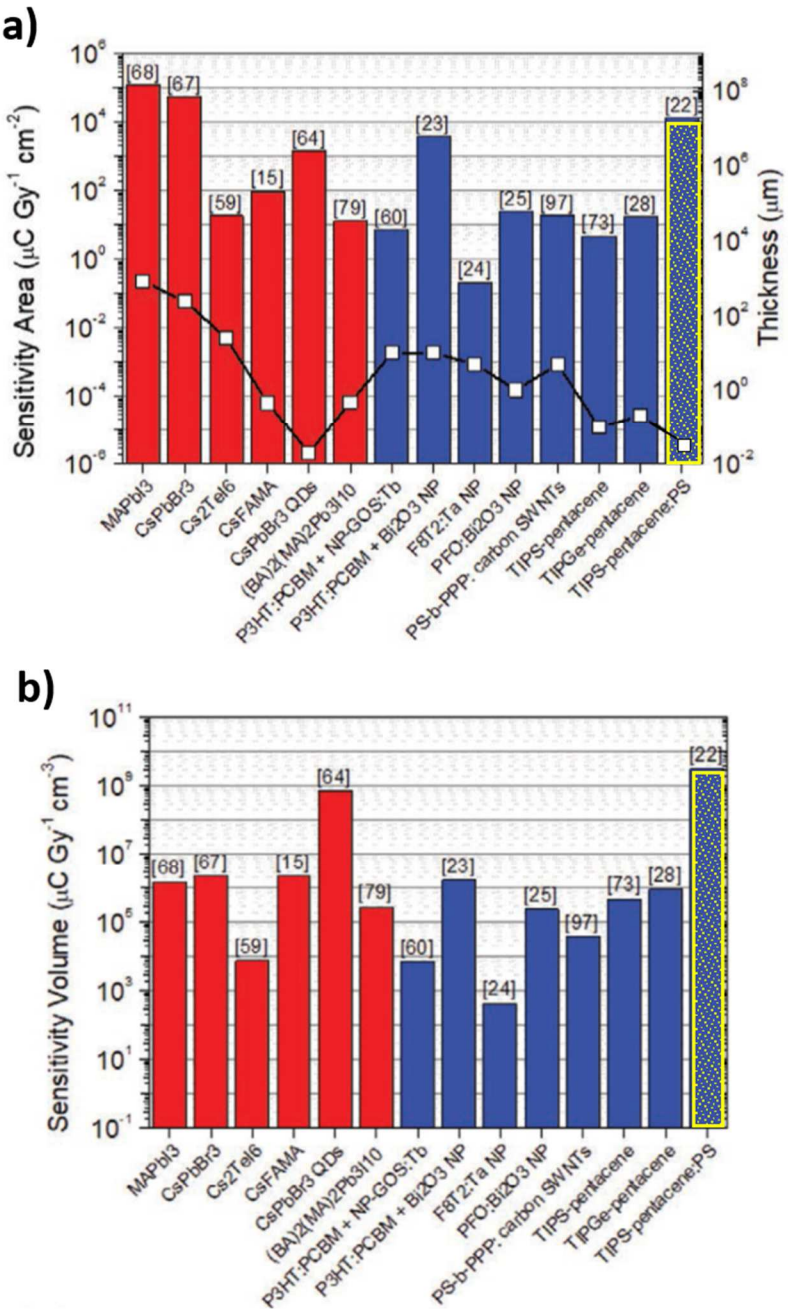

Figure 4.73 *Histogram of the top sensitivity values per a) unit area and b) unit volume for the materials reported as thick/thin active layer of perovskite (red) and organic/hybrid (blue) direct X-ray detectors. In (a) is also reported their variation in thickness (empty black squares—right axis). The sensitivities achieved by the samples described in this Section are highlighted in yellow. The numbers inserted in the plots correspond to the references reported in the review by L. Basiricò et al.* [123].

In order to study the impact of the transport properties on the X-ray detection performance of this class of devices, the trend of X-ray sensitivity versus TIPS-Pn:PS ratio (**Figure 4.72**) has been compared with the OFETs mobilities (**Figure 4.71a**). The two graphs point out a similar behavior meaning that the improvement of the transistor electrical performance, i.e. the hole mobility, due to the PS passivating action for hole traps at the semiconductor/dielectric interface, positively impacts on the detection performance, decreasing the holes transit time τ_t (Eq. 2.13).

However, the detection mechanism based on the photoconductive gain effect is mediated by the presence of traps for minority carriers i.e. electrons in this case, in the organic semiconductor layer (see **Section 4.2.1.1**). The experimentally determined mobility μ and the values of τ_t, τ_r and gain G calculated from the fit of the experimental data for both 1:0 and 4:1 devices with the active layer deposited at different speeds are shown in **Figure 4.74**. The plots clearly show how, for both pure TIPS-Pn samples and blended ones, for similar mobility values, the variation of the photocurrent gain with increasing deposition speed follows the variation of the recombination time (affected by the electron traps).

This demonstrates that both strategies, the first acting on the morphology of the film and the tuning of electron trap density (**Section 4.2.1.1**) and the second enhancing the transport properties by passivating the hole traps at the dielectric/organic semiconductor interface, are two effective and independent tools to control and unprecedentedly boost X-rays sensitivity in organic thin-films.

In the next three subsections, other achievements and studies conducted on this category of samples are discussed.

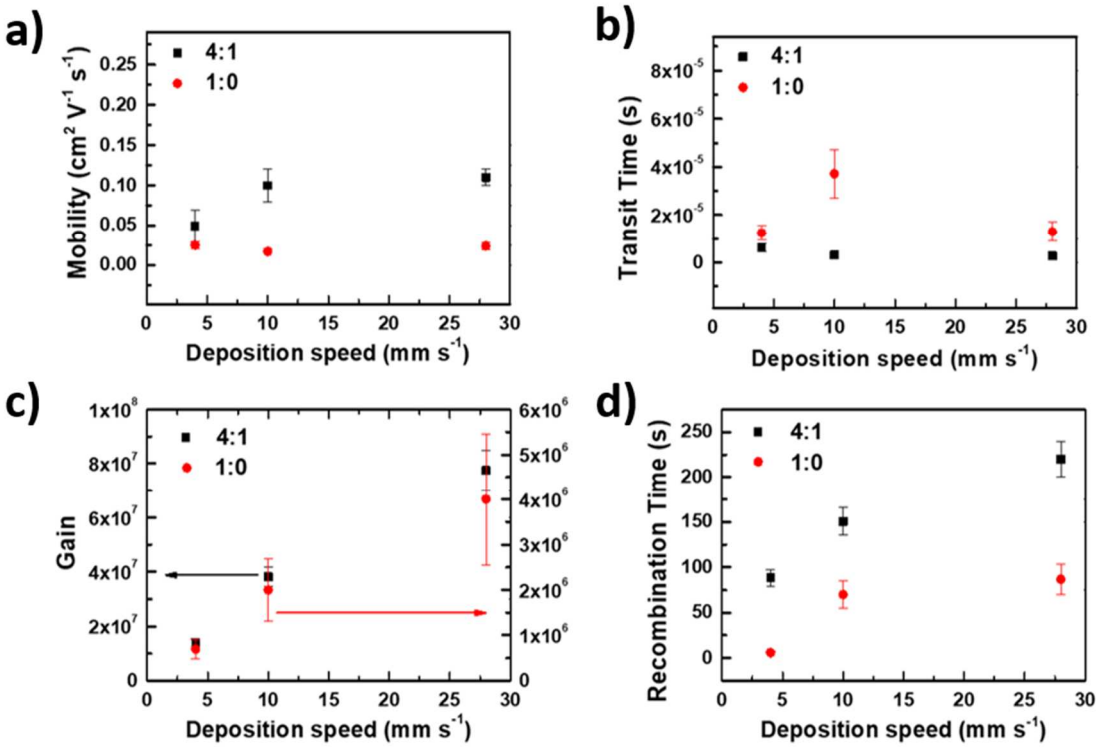

Figure 4.74 *Comparison between pure TIPS-pentacene (1:0) and blended (4:1) devices of: (a) experimentally determined mobility and (b) corresponding transit time; analytically determined (c) photoconductive gain and (d) recombination time, for different deposition speeds. The error bars refer to the statistical fluctuations (SD) of the parameters over 4 samples for each deposition speed.* [216]

Aging

In order to assess the reliability and stability of our devices, the shelf-life of the best performing blends, 4:1 and 2:1 have been investigated, by monitoring the performance of the detectors for up to 80 days. During this period, the devices were stored and measured under dark and ambient conditions. Both the field-effect mobility and the X-ray sensitivity evolution are depicted in **Figure 4.75**. A decrease in the X-ray response of 30-40% was observed after more than 2 months from fabrication, as well as a device mobility drop of 55% in average. These changes are often attributed in the literature to degradation due to ambient humidity, an issue

that is usually avoided by depositing an encapsulation layer on top of the organic film, that is not present in the here reported devices [236], [237]. Indeed, TIPS Pn:PS devices show a more stable behavior than those based on pure TIPS pentacene probably due to the partially passivation provided by the insulating polymer PS.

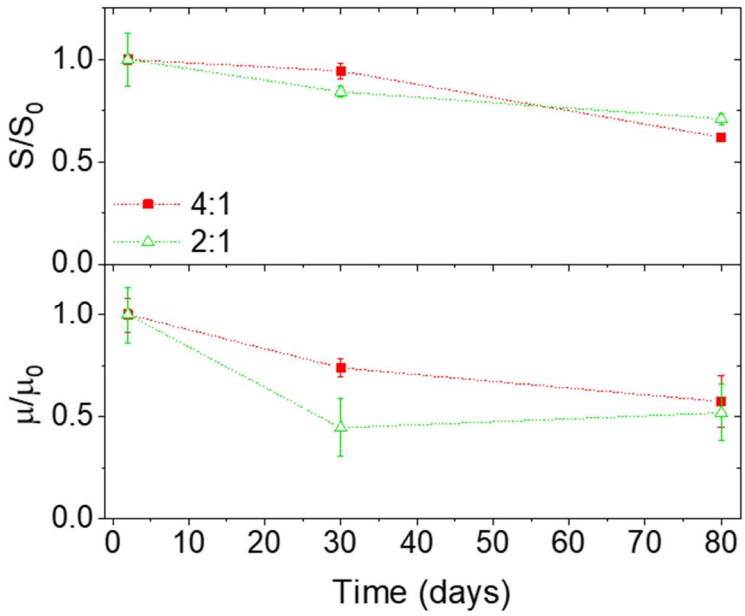

Figure 4.75 *Evolution over time up to 80 days of X-ray sensitivity (up) and field-effect mobility (down) of 4:1 and 2:1 TIPS pentacene:PS devices. It is noteworthy that the here reported devices were not encapsulated. Values have been normalised to the initial values. The error bars refer to the statistical fluctuations of the parameters over 8 samples.*

Limit of Detection

By interposing different Al layers between the Mo-tube and the detector, we attenuated the X-ray beam intensity, reaching few μGy s^{-1}. To achieve this result, we lowered the dark current of the sensor following two roots: the gate electrode has been connected at ground (V_{GS} = 0 V) and the samples have been enclosed in shielding boxes which avoid the illumination of the sensors. The condition of

polarization explains the fast response of the sensor shown in the dynamic reported in **Figure 4.76a**. In this case, in fact, the X-ray response is not mediated by the photoconductive gain effect but it represents the separation and the collection of ionization charges generated by X-ray photon absorption [143].

For these samples, a dose rate down to 35 µGy s^{-1} has been assessed with a linear behavior of the detector response and a calculated sensitivity of (32 ± 2) µC Gy^{-1} cm^{-2} (see **Figure 4.76b**). As in the case of TIPGe-Pn (**Section 4.2.2**) also these results are promising for the implementation of these devices in the medical field where low dose rates are typically employed.

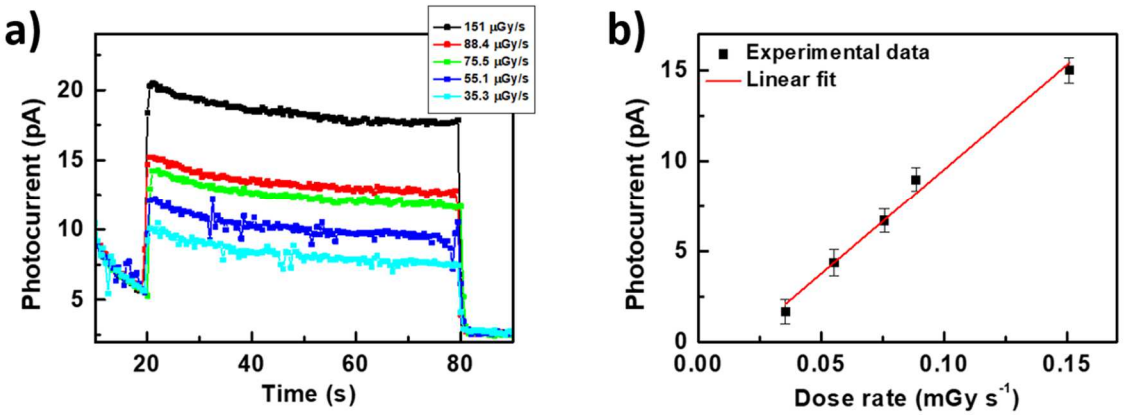

Figure 4.76 *a) X ray induced photocurrent response of a TIPS-Pn:PS 4:1 device at several dose rates, down to 35 µGy s-1. b) Photocurrent versus dose rate, including the linear fit used for the sensitivity calculation. The error bars refer to the statistical fluctuations (SD) of the signal amplitude over three on/off switching cycles of the X-ray beam in the same condition.* [216]

Wheatstone Bridge

As discussed in **Section 2.4.1**, the dark current is an important figure of merit to evaluate the capability of a detector. In this work, exploiting the uniformity

provided by the BAMS deposition technique, a Wheatstone Bridge architecture has been implemented in order to compensate and correct small anomalies (such as bias stress or aging effect) and achieve a stable and low dark current.

The Wheatstone bridge is a widely used device architecture which allows to measure an unknown resistance value and it is typically used in resistive sensor systems. In fact, as illustrated in **Figure 4.77a**, when the bridge is balanced (i.e. the four resistances are equal) the current flowing in the two branches is equal and the voltage difference between the *C* and *D* nodes is $V_{out} = 0$ V. If the bridge is unbalanced (i.e. the four resistances are not equal), the electrical currents flowing in these two branches is different and $V_{out} \neq 0$ V. Therefore, by monitoring the voltage difference between *C* and *D* it is possible to employ the Wheatstone bridge architecture as a detector sensitive to external stimuli able to modify the resistance of at least one of the resistors of the system. As the Wheatstone bridge architecture is very sensitive to small differences in any one of the four resistances, it is crucial to employ a processing technique for large-area deposition that grants a high degree of film uniformity.

Here I show that, thanks to the excellent and uniform properties of the organic devices fabricated with the BAMS technique, a Wheatstone bridge consisting of four 4:1 TIPS-Pn:PS OFETs that operate as resistors has been fabricated, with the layout reported in **Figure 4.77b**. When X-ray photons impact onto the OFETs, the OFET channel resistance decreases due to the photocurrent increase. Thus, the bridge state turns from the balanced to the unbalanced state by exposing to X-rays only two OFETs, *R1* and *R4* in the reported case. In **Figure 4.77c** the voltage difference between the *C* and *D* nodes generated by different dose rates of X-ray radiation is reported. Important to notice is the fact that the dark current is low

and constant as was expected with this type of architecture and that. the Wheatstone bridge responses proportionally to the increase of dose rates (**Figure 4.77**d).

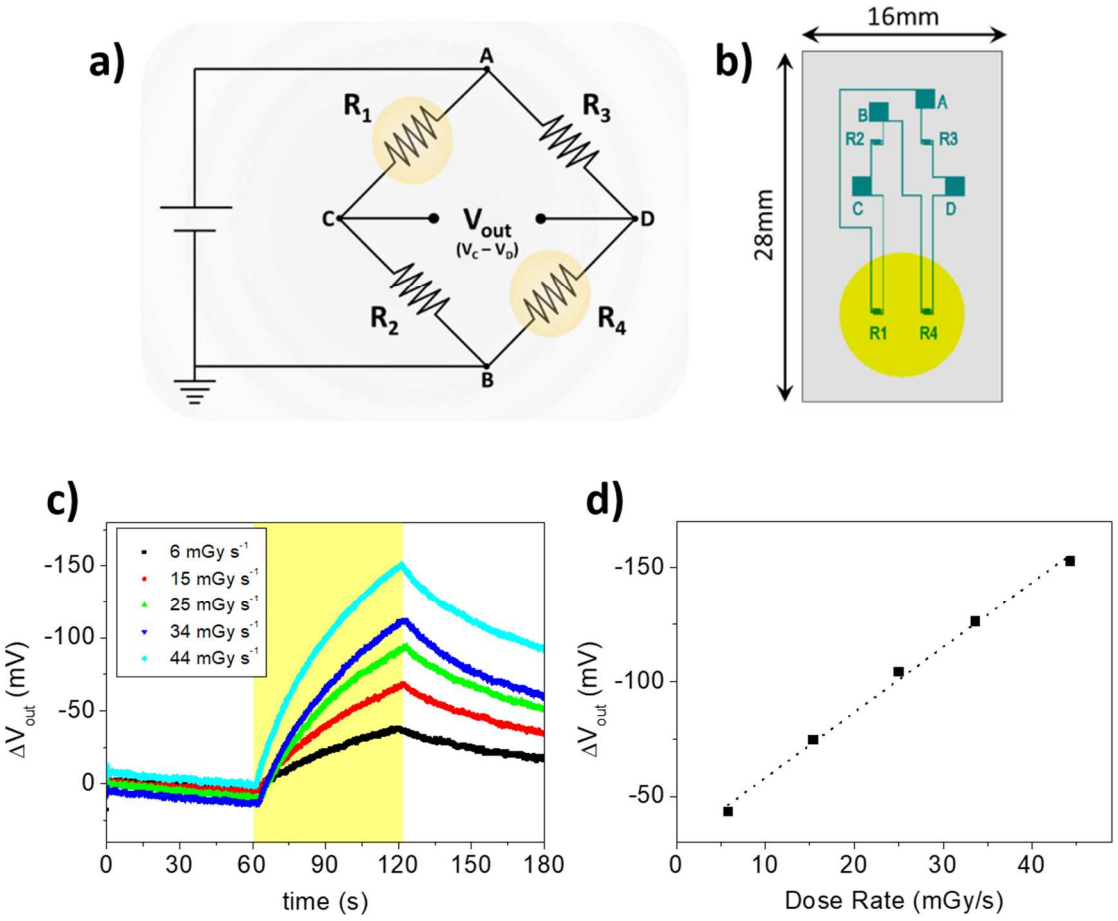

Figure 4.77 *a) Wheatstone bridge circuit and b) schematic representation of the layout designed for the fabrication of the devices. The resistors R_1, R_2, R_3 and R_4 consist in the channel of four different transistors based on 4:1 TIPS-Pn:PS. During the exposure to X-rays, only R_1 and R_4 are irradiated while R_2 and R_3 are kept in dark. Because of the decrease of the channel resistance due to the photocharges generated by the radiation the unbalanced bridge causes a ΔV_{out} between the C and D nodes. (c) ΔV_{out} generated by different intensity of the X-ray beam and applying V_{GS} = -5 V at the gate contacts of the OFETs and -20 V to the entire circuit. d) Linear response of the circuit for different doses of radiation.* [216]

4.2.4. Impact of different geometries and architecture

During this work, a comparison between two different OFETs geometries has been carried on. In particular, the radiation detection performances of BGBC and TGBC OFETs have been compared (see **Section 1.3.1**). The two geometries reported in the comparison have been fabricated at the Columbia University during my six-months abroad period employing printed TIPS-Pn as active layer. In particular, the BGBC OFETs present the structure depicted in **Figure 3.27c** while the TGBC OFETs have been fabricated using the same fabrication processes in order to achieve the structure reported in **Figure 4.78**. In this case, for the gate dielectric several materials have been employed (i.e. Au and Al) and the thickness of the metallic electrode has been tuned between 50nm and 200 nm as well. In order to pattern this last layer, shadow masks have been employed.

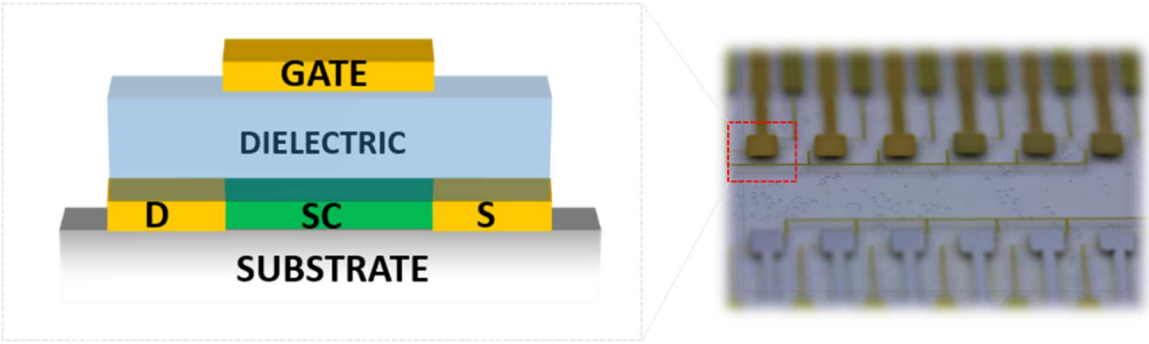

Figure 4.78 *TGBC OFETs structure and picture of the entire device.*

The OFETs have been electrically characterized and the main transport properties for both the two architectures are summarized in the **Table 4.9**.

Bottom Gate – Bottom Contacts				
Gate Thickness (nm)	I_{on}/I_{off}	*Mobility* ($cm^2\ V^{-1}\ s^{-1}$)	V_{th} (V)	*S* ($V\ dec^{-1}$)
60 nm (Au)	$(5 \pm 2) \cdot 10^4$	$(8.5 \pm 1.2) \cdot 10^{-2}$	4.7 ± 1.3	2.1 ± 0.5
Top Gate – Bottom Contacts				
Gate Thickness (nm)	I_{on}/I_{off}	*Mobility* ($cm^2\ V^{-1}\ s^{-1}$)	V_{th} (V)	*S* ($V\ dec^{-1}$)
200 nm (Au)	$(1.5 \pm 0.8) \cdot 10^4$	$(7 \pm 3) \cdot 10^{-3}$	12 ± 6	3.8 ± 0.5
50 nm (Au)	$(1.7 \pm 0.7) \cdot 10^4$	$(9 \pm 4) \cdot 10^{-3}$	13.7 ± 1.1	5.8 ± 0.5
200 nm (Al)	$(6 \pm 5) \cdot 10^3$	$(1.5 \pm 0.4) \cdot 10^{-3}$	12 ± 2	4.3 ± 0.3
50 nm (Al)	$(1.5 \pm 1.0) \cdot 10^4$	$(5.2 \pm 0.8) \cdot 10^{-3}$	8 ± 4	4.6 ± 0.4

Table 4.9 *Electrical parameters calculated for BGBC and TGBC OFETs. All the values represent a statistical analysis conducted over six devices per type.*

While all the different TGBC OFETs share a similar electrical behavior, from the data reported in **Table 4.9**, it is possible to notice that the transport properties are strongly affected by the transistor architecture. In particular, the TGBC OFETs offered poorer electrical performances with respect to the ones obtained by the BGBC. In the top gate the charge mobility is always one order of magnitude lower, as the ON/OFF ratio, the subthreshold swing results higher and finally the threshold voltage is more shifted far from 0 V. All these discrepancies can be due to a different density of traps both for electrons and for holes in the two geometries.

To evaluate their X-ray detection capability, the OFETs have been tested under the radiation produced by the W-target tube (**Section 3.7.1.2**) keeping the devices in saturation regime (V_{GS} = -5 V, V_{DS} = -20 V). While for the BGBC OFETs a sensitivity value has been obtained in line with the values reported so far for analogous devices (top result $S_A = (265 \pm 30)$ µC Gy^{-1} cm^{-2}), for TGBC OFETs poorer performances have been registered. For instance, for the 50 nm Au and 200 nm Al gate electrode devices average sensitivities as $S_A = (24 \pm 4)$ µC Gy^{-1} cm^{-2} and $S_A = (12 \pm 4)$ µC Gy^{-1} cm^{-2} have been measured respectively.

Other experiments should be carried on in order to deeper investigate the discrepancy obtained with the two typologies of OFETs, but some hypothesis can be already formulated.

- The main reason could be attributed to the different transport properties shown by the two. This difference could be due to the different configuration of the semiconductor/dielectric interface or to structural differences. In fact, organic semiconductors from solution are typically deposited under uncontrolled environmental conditions. As the solvent evaporates, moisture and impurities in the air can be trapped in the semiconductor especially where the surface is exposed to the environment despite where it is in contact with the substrate. This factor may become relevant since the first molecular layers of the semiconductor in contact with the dielectric are those that contribute predominantly to the electrical transport in organic field effect transistors. In bottom-gate transistors the semiconductor is deposited on the dielectric, while in top-gate transistors the dielectric is deposited on the semiconductor.

- Another important difference could be related to the interfaces' roughness of the diverse devices. In fact, for BGBC transistors the Parylene C dielectric is directly deposited onto the smooth gate electrode, while for the TGBC devices the insulator is placed on the top of the rougher organic semiconductor. This means that once Parylene C is deposited, in the top-gate transistors we got a dielectric semiconductor interface much rougher than the bottom-gate.

- The presence of structural defects, which can also act as trap states or scattering centers, seems to be in the top-gate transistors the most likely cause for the increase of the threshold voltage and the decrease of mobility. The roughness of the dielectric/semiconductor interface implies that the mean-life time of the charges is shorter, and the recombination is more likely. As a result, the sensitivity of the device is also reduced.

To conclude, it is clear that in order to achieve optimal radiation detection performances employing organic thin film-based devices, the BGBC OFETs offer the most promising properties.

4.2.5. Pneumatic Nozzle Printed Organic Ionizing Radiation Detectors

During my six-months spent at the Columbia University (New York, USA), I worked on the implementation of most of the characteristics here reported in one single device. In particular, I fabricated some OFETs presenting the structure depicted in **Figure 3.27c**. The transistors, presenting a BGBC architecture, have

been patterned by photolithography process and they have been placed in two 6-pixels array as it is shown in **Figure 4.79**.

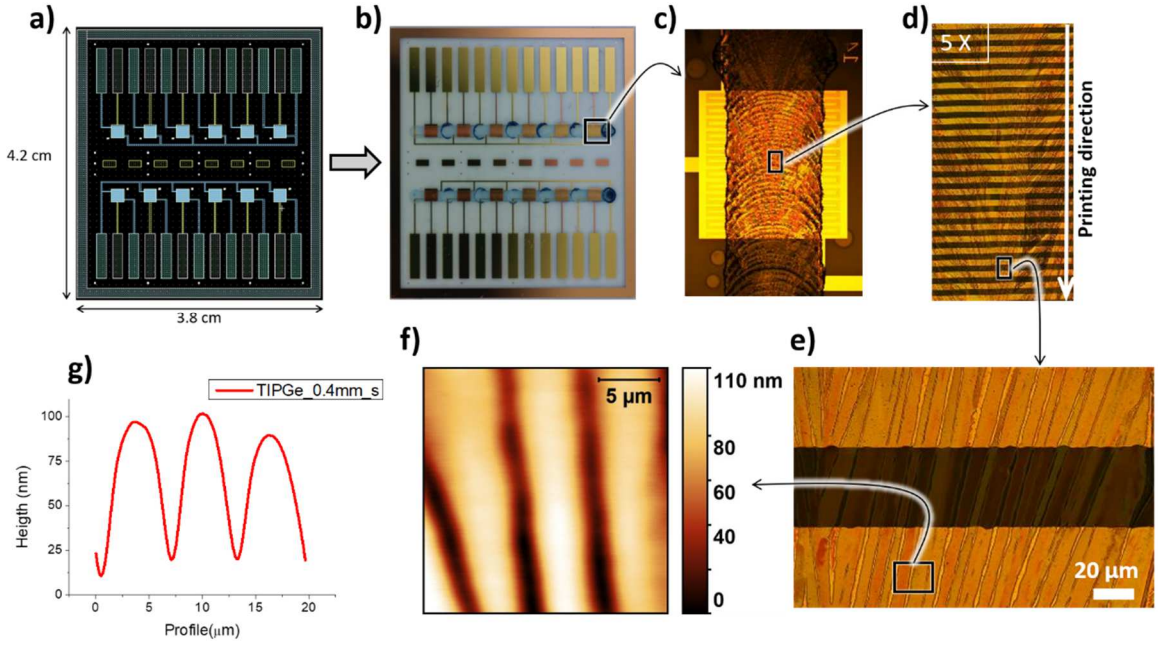

Figure 4.79 *OFETs fabricated during my six months-period spent at the Columbia University (New York). a) Photolithography mask designed by LayoutEditor and real device where two 6-pixel arrays are placed with the source electrode in common and the gate and the drain independent. c,d,e) Cross-polarized optical microscope images of the organic thin films printed on the top. f) Topographic AFM image and g) extracted profile of a printed organic film.*

The organic semiconductors have been deposited from solution by Pneumatic Nozzle Printing which allowed a self-patterning of the layer (as already discussed in **Section 1.2.1.2**). During my work I implemented all the four molecules considered so far (i.e. TIPS-Pn, TIPGe-Pn, diF-TES-ADT, diF-TEG-ADT). As it is shown in **Figure 4.79c, d, e**, this deposition technique allowed to obtain very uniform and well-packed thin films which present microcrystalline structures aligned along the printing direction (i.e. orthogonal to the conductive channel) and with a thickness in the range [100-200] nm. Moreover, tuning the coating speed it has been possible also in this case to reach a full control on the grain dimensions (see **Figure 4.80)** [238].

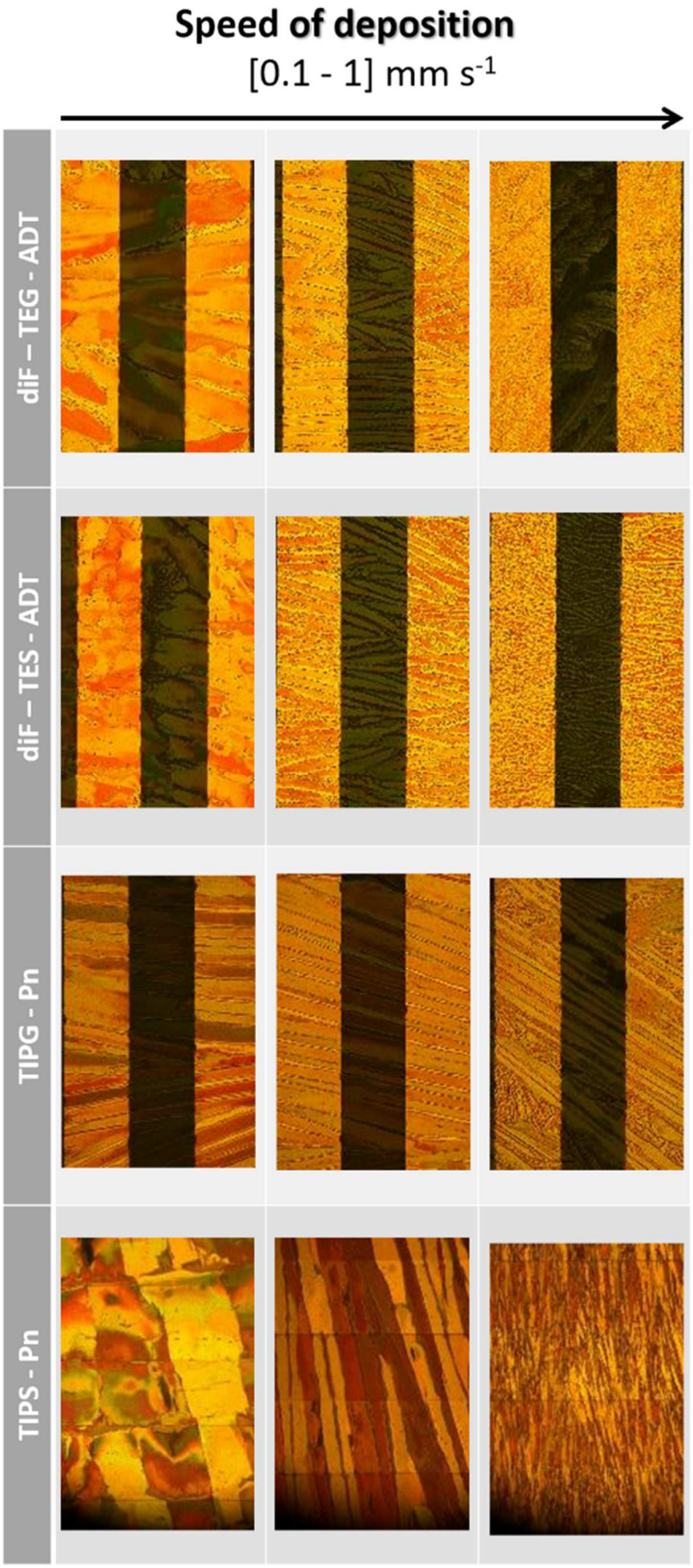

Figure 4.80 *Cross-polarized optical microscope images of TIPS-Pn, TIPGe-Pn, diF-TES-ADT, and diF-TEG-ADT thin films printed at different deposition speed in the range [0.1 – 1] mms^{-1}.*

Thanks to the good-quality films achieved by this deposition technique, good transport properties has been registered as well. The main electrical parameters are listed for each molecule in **Table 4.10**. For all the devices, high ON/OFF ratio and high mobility values in line with the state of the art for flexible devices have been achieved. In particular, the mobility presented by the TIPS-Pn OFETs is one order of magnitude higher than the one reported for the pure-TIPS OFETs fabricated by BASM technique onto Si/SiO_2 substrate (see **Section 4.2.1.1**) [216] and by drop-casting onto flexible foils (see **Section 4.2.2**) [154], [225]. On the contrary, the transport properties of the TIPGe-Pn based OFETs are slightly higher than the performances measured with the drop casted samples reported in **Section 4.2.2** [225]. But most important, in this case the Pneumatic Nozzle Printing strongly improved the area coverage and the film packing (as it has been already mentioned in **Section 4.2.2.1**).

It is important to notice the little deviation of the threshold voltage from 0 V towards positive biases. This aspect could be a sign of the presence of trap states at the interface between the organic semiconductor and the dielectric layer. The highest V_{th} values have been measured for the diF-TEG-ADT-based OFETs and this could be the reason for their anomalous behavior under X-rays. These data are not reported in this work because further investigations are needed.

TIPS-Pn				
Deposition Speed (mm s^{-1})	*I_{on}/I_{off}*	*Mobility (cm^2 V^{-1} s^{-1})*	*V_{th} (V)*	*S (V dec^{-1})*
0.2	$(2.0 \pm 0.7) \cdot 10^5$	$(4 \pm 1) \cdot 10^{-2}$	1 ± 1	1.8 ± 0.4
0.4	$(2 \pm 1) \cdot 10^5$	$(5 \pm 1) \cdot 10^{-2}$	4 ± 1	1.0 ± 0.1
0.6	$(2 \pm 1) \cdot 10^5$	$(9 \pm 2) \cdot 10^{-2}$	3.2 ± 10.5	1.0 ± 0.2

0.8	$(2 \pm 2) \cdot 10^5$	$(6 \pm 1) \cdot 10^{-2}$	4.3 ± 0.3	0.8 ± 0.2
TIPGe-Pn				
Deposition Speed (mm s^{-1})	***I_{on}/I_{off}***	***Mobility (cm^2 V^{-1} s^{-1})***	***V_{th} (V)***	***S (V dec^{-1})***
0.1	$(6 \pm 5) \cdot 10^4$	$(6 \pm 5) \cdot 10^{-2}$	(7.9 ± 0.8)	(1.4 ± 0.4)
0.2	$(3 \pm 5) \cdot 10^5$	$(17 \pm 3) \cdot 10^{-2}$	(5.6 ± 0.3)	(0.7 ± 0.1)
0.4	$(9 \pm 10) \cdot 10^4$	$(13 \pm 1) \cdot 10^{-2}$	(4.3 ± 0.6)	(0.9 ± 0.1)
0.6	$(1 \pm 1) \cdot 10^5$	$(5 \pm 2) \cdot 10^{-2}$	(4.6 ± 0.6)	(0.8 ± 0.1)
diF-TES-ADT				
Deposition Speed (mm s^{-1})	***I_{on}/I_{off}***	***Mobility (cm^2 V^{-1} s^{-1})***	***V_{th} (V)***	***S (V dec^{-1})***
0.2	$(12 \pm 1) \cdot 10^3$	$(15 \pm 1) \cdot 10^{-2}$	(4.8 ± 0.2)	(2.60 ± 0.05)
0.4	$(18 \pm 8) \cdot 10^3$	$(9 \pm 2) \cdot 10^{-2}$	(3.60 ± 0.05)	(2.1 ± 0.3)
0.6	$(8 \pm 9) \cdot 10^4$	$(10 \pm 2) \cdot 10^{-2}$	(2.4 ± 0.2)	(1.8 ± 0.6)
0.8	$(4 \pm 1) \cdot 10^4$	$(8 \pm 1) \cdot 10^{-2}$	(1.8 ± 0.3)	(1.3 ± 0.2)
diF-TEG-ADT				
Deposition Speed (mm s^{-1})	***I_{on}/I_{off}***	***Mobility (cm^2 V^{-1} s^{-1})***	***V_{th} (V)***	***S (V dec^{-1})***
0.2	$(4.9 \pm 0.6) \cdot 10^2$	$(10 \pm 1) \cdot 10^{-2}$	(14.6 ± 0.8)	(6.0 ± 0.3)
0.4	$(3 \pm 2) \cdot 10^3$	$(10 \pm 1) \cdot 10^{-2}$	(11 ± 1)	(4.1 ± 0.8)
0.6	$(9 \pm 7) \cdot 10^2$	$(4 \pm 1) \cdot 10^{-2}$	(13 ± 4)	(5 ± 2)
0.8	$(10 \pm 13) \cdot 10^2$	$(4 \pm 1) \cdot 10^{-2}$	(11 ± 2)	(5 ± 1)

Table 4.10 *Electrical parameters of TIPS-Pn, TIPGe-Pn, diF-TES-ADT, and diF-TEG-ADT - based OFETs printed at different deposition speeds. All the reported values have been calculated from a statistical analysis conducted over 6 OFETs per type.*

All the devices have been characterized as radiation detectors exposing them under X-rays provided by the W-target tube described in **Section 3.7.1.2**. The top

sensitivity values obtained for each molecule are summarized in **Table 4.11** where, also the performances reached by the samples described so far are reported as comparison.

Sample	*Mobility* ($cm^2\ V^{-1}\ s^{-1}$)	*Operative Voltage* (V)	*S* ($\mu C\ Gy^{-1}$)	S_A ($\mu C\ Gy^{-1}\ cm^{-2}$)	S_V ($\mu C\ Gy^{-1}\ cm^{-3}$)	*Reference*
TIPS-Pn *Drop casted*	$(5.2 \pm 0.3) \cdot 10^{-2}$	$V_{DS} = -3$ $V_{GS} = -2$	0.96 ± 0.07	3.9 ± 0.3	$(2.6 \pm 0.2) \cdot 10^{5}$	***Section 4.2.2*** [225]
TIPS-Pn *BAMS*	$(1.7 \pm 0.5) \cdot 10^{-2}$	$V_{DS} = -20$ $V_{GS} = -15$	1.60 ± 0.04	$(3.8 \pm 0.1) \cdot 10^{2}$	$(4.2 \pm 0.1) \cdot 10^{7}$	***Section 4.2.1.1*** [216]
TIPS-Pn *Printed*	$(9 \pm 2) \cdot 10^{-2}$	$V_{DS} = -20$ $V_{GS} = -5$	20.8 ± 1.6	$(5.2 \pm 0.4) \cdot 10^{2}$	$(3.5 \pm 0.3) \cdot 10^{7}$	***Section 4.2.5***
TIPS-Pn:PS *BAMS*	$(5 \pm 2) \cdot 10^{-1}$	$V_{DS} = -20$ $V_{GS} = -15$	54	$1.3 \cdot 10^{4}$	$3.2 \cdot 10^{9}$	***Section 4.2.3*** [216]
TIPGe-Pn *Drop casted*	$(6.9 \pm 0.4) \cdot 10^{-2}$	$V_{DS} = -3$ $V_{GS} = -2$	3.08 ± 0.02	12.3 ± 0.2	$(6.2 \pm 0.1) \cdot 10^{5}$	***Section 4.2.2*** [225]
TIPGe-Pn *Printed*	$(13 \pm 1) \cdot 10^{-2}$	$V_{DS} = -20$ $V_{GS} = -5$	28.4 ± 0.8	$(7.1 \pm 0.2) \cdot 10^{2}$	$(8.9 \pm 0.3) \cdot 10^{7}$	***Section 4.2.5***
diF-TES-ADT *Spin coated*	$(5.2 \pm 0.3) \cdot 10^{-2}$	$V_{DS} = -3$ $V_{GS} = -2$	$(2.4 \pm 0.3) \cdot 10^{-4}$	$(9.6 \pm 1.2) \cdot 10^{-4}$	(80 ± 10)	***Section 4.2.2*** [225]
diF-TES-ADT *Printed*	$(15 \pm 1) \cdot 10^{-2}$	$V_{DS} = -20$ $V_{GS} = -2$	3.2 ± 0.5	$(8.0 \pm 1.3) \cdot 10^{1}$	$(8.0 \pm 1.3) \cdot 10^{6}$	***Section 4.2.5***

Table 4.11 *Summary of the top X-ray sensitivities achieved by the here reported organic thin film-based sensor.*

As it is possible to notice from the values reported in the **Table 4.11**, by adopting most of the strategies illustrated in this chapter allowed to obtain excellent X-ray detection performances.

The printed devices fabricated at the Columbia University well summarize all the characteristics listed in this chapter: they present a BGBC OFET architecture, the Pneumatic Nozzle Printing technique allowed to obtain packed, uniform and well aligned semiconducting layer which on one side makes more effective the grain boundaries as source of electron traps, on the other side it brings an improvement on the transport properties of the devices. Further, by this technique it is possible to deposit from solution the Ge-based molecules which enhance the absorption of the high energy photons. Moreover, by this process it has been possible to fabricate flexible devices easily scalable onto larger areas.

To conclude, the printed TIPGe-Pn-based OFETs reached very high sensitivities ($S_A = (710 \pm 20)$ μC $Gy^{-1}cm^{-2}$; $S_V = (8.9 \pm 0.3) \cdot 10^7$ μC $Gy^{-1}cm^{-3}$). Further improvements could be achieved by implement the polystyrene blending in the printed TIPGe-Pn devices to passivate the hole traps present at the interface with the dielectric and improving the transport properties of the OFETs.

4.2.6. Summary

To conclude this section, a summary about all the strategies studied and implemented in order to understand and control the radiation detection mechanism occurring in organic semiconductor-based devices is given. In order to achieve these results, a deep study of the materials, of the mechanism of interaction radiation-matter and of the device operation has been conducted.

- The advantages gained using a transistor structure instead of a 2-terminal coplanar one have been listed and critically discussed. In particular, it has been explained how by using the polarization condition of the transistor it is possible to control the operation of the sensor as well. It has been demonstrated that the BGBC configuration is the most promising architecture in order to achieve the best detecting performances

- A recap about the mechanism which rules the radiation detection in thin film-based devices has been offered and a detailed study on the role of electron traps in the activation of the photoconductive gain effect has been illustrated. In particular, two main methods in order to investigate different kind of traps have been discussed: tuning the density of grain boundaries and acting on the semiconductor/dielectric interface.

- The employment of new synthetized small molecule with higher-Z elements directly inserted in the molecular structure by chemical tailoring has been exploited to further improve the efficiency of these detectors

- the impact of the transport properties on the radiation detection capability has been discussed. In particular, it has been demonstrated how enhancing the electrical behavior of the transistors (i.e. using a blend with Polystyrene) it is possible to boost the radiation detection performances reaching unprecedent values of sensitivity.

All the here summarized strategies (depicted in **Figure 4.81**) are independent each other and can be separately adopted in order to maximize the X-ray detection efficiency.

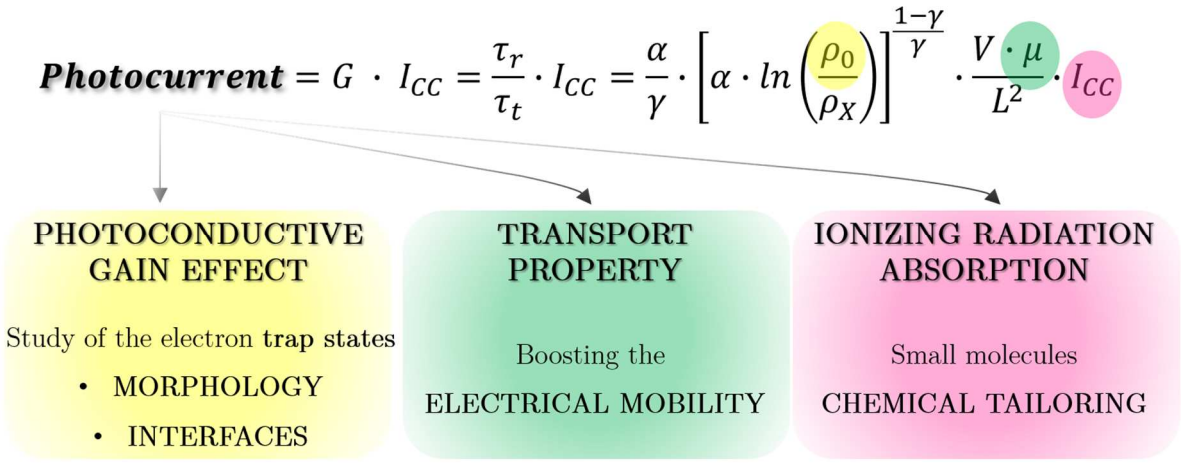

Figure 4.81 *Independent strategies adopted in this thesis in order to boost the X-ray detection efficiency of the organic sensors. Here the photocurrent induced by the radiation is expressed as the product between the photoconductive gain factor G and the photocurrent directly produced by the absorption of photons* I_{CC}.

4.3. X-ray detection in medical application

I tested the potentiality of the organic thin film-based X-ray detectors for their implementation in the field of dental radiography. These results are included in a

more general discussion reported by L. Basiricò et al. in [151], where the assessment of this flexible, large-area and human-tissue like sensing technology is provided for the detection of radiation in several medical fields. In particular, we tested them as bone density analyzers, as medical personal dosimeters for mammography, and finally we show a proof of principle for their implementation as medical imager.

In the field of dental radiography, the technology described so far would offer enormous advantages. The flexibility and conformability, the low operating voltages and the low-cost fabrication are highly desirable properties in this field of application. In this section, the results achieved by the validation of direct organic-based X-ray detectors in actual clinical environment are presented. These measurements have been possible thanks to the collaboration with the *Skan-X Radiology Devices S.p.A* and *Skanray Europe srl and CEI* (*Compagnia Elettronica Italiana*) (Bologna, Italy). They provided us access to two different commercial Dental Radiography irradiation systems. (see also **Section 3.7.2**) that allowed us to conduce the measurements in the real operation conditions employed for dental radiography. In particular, these applications require energies around a peak kilovoltage of 70 kVp, low irradiation doses down to few µGy and short irradiation pulses of the order of hundreds of ms.

For these experiments, co-planar devices presenting the structure depicted in **Figure 3.26** and fabricated onto plastic polymeric foils have been employed. The active layer of the sensors is a TIPGe-Pn thin film deposited from solution by drop casting. The devices have been enclosed in metallic box in order to screen the electrical noise during the measurements and to keep the samples in dark for the lowering of the dark-current.

The dynamic responses for 0.5, 1, 1.5, 2 s of irradiation at 70 kVp from the W-target X-ray tube are reported in **Figure 4.82a**.

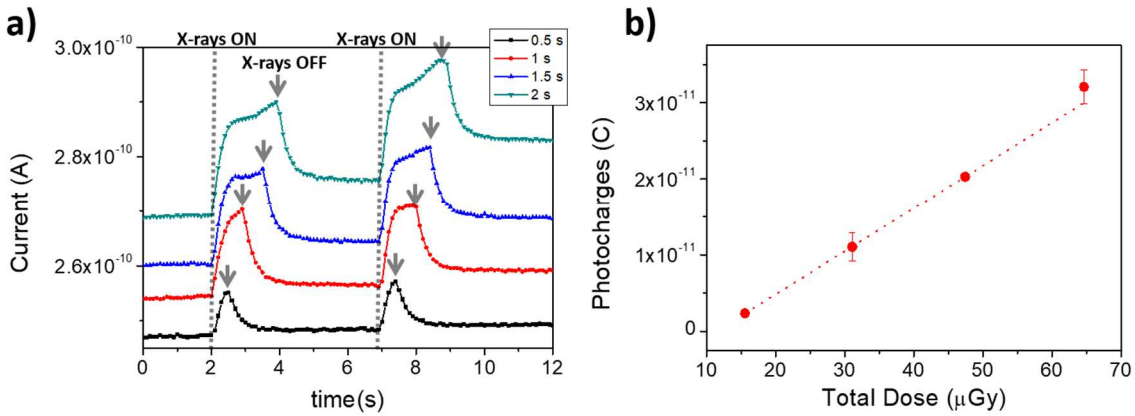

Figure 4.82 *a) Current response of the detector to the X-ray beam provided by a W-target X-ray tube operated at 70 kVp accelerating voltage and 4mA filament current, for different exposition time windows: 0.5, 1, 1.5, 2 s. The vertical grey dashed lines indicate when the X-ray tube is turned on while the grey arrows when it is switched off. b) Plot of the corresponding generated photocharges as a function of the total dose impinged on the detector for the different exposure times.* [151]

In this case, the X-ray flux is kept constant by setting the anodic current at 4 mA, therefore decreasing the exposure time leads to the decrease of the total dose impinging on the detector in the range [15.5-64.6] µGy. The dynamical response to X-rays is the one typical of organic thin films-based devices and it is clearly distinguishable from the background down to 15.5 µGy of total dose. The integral of the peaks present in the dynamic curve correspond to the amount of charges generated in the organic layer by the interaction with the radiation. These data are plotted in **Figure 4.82b** as a function of the corresponding total X-rays dose and from the slope of the linear fit of this curve, a sensitivity of $1.6 \cdot 10^5$ µC Gy^{-1} cm^{-3} has been obtained. This value is in-line with that reported for analogous devices considering the detector structures [153] and the organic semiconductor employed

[225], characterized at much higher Xray doses and lower energies (5–30 mGy s^{-1}; 35 kVp). In order to test the detector performance under short pulses of X-rays and to validate it in actual measurement conditions for medical imaging application, we expose it to a pulsed X-ray beam (duration 100ms) provided by a commercial dental radiography system (see **Section 3.7.2**). The detectors respond to the 100ms X-ray pulses with clean and steep output signals with an amplitude proportional to the impinging dose rate, demonstrating to be able to follow the typical frame rates of a commercial dental radiographic apparatus. Both the dynamic response and the sensitivity curve are reported in **Figure 4.83a, b**. Further, from the baseline of the measurement reported in **Figure 4.83a** the noise of the system has been calculated as three times the root mean square of the experimental data, obtaining the value of 1.5 pA. Combining this value with the plot reported in **Figure 4.83b**, the lowest detectable dose has been extrapolated and it results 12 µGy. This value confirmed the potentiality of the employment of this class of detectors in the field of dental radiography where few µGy of radiation for the diagnostic exams are delivered.

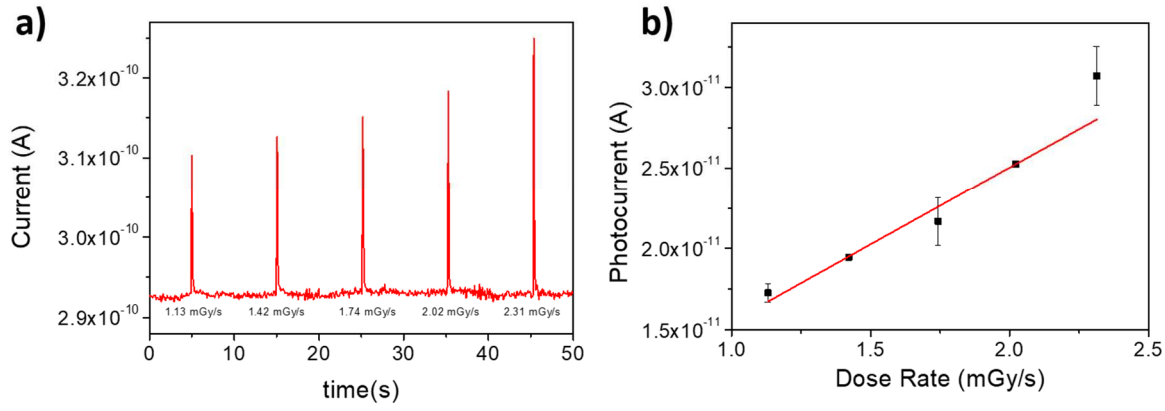

Figure 4.83 *Dynamic signal response to 100ms X-rays pulses at different dose rates provided by the Intraskan DC machine and (b) the corresponding plot of X-ray induced photocurrent as a function of the dose rate.* [151]

It is important to note, regarding the fast response here reported, that even if the radiation detection mechanism occurring in these devices is mediated by electron traps (i.e.PG mechanism) and so it presents long characteristic times, also with very short pulses of radiation the sensor is able to generate a clear peak of photocurrent. This confirms what has already been discussed in **Section 4.2** and depicted in the graph in **Figure 4.51** .

Finally, working at low doses and short pulses strongly improves the signal stability. In fact, while at higher doses these sensors present a limited and reversable degradation, in this range of doses a deviation small of 2.7% for 10 subsequent repetitions of 500ms X-rays exposure has been recorded (**Figure 4.84**).

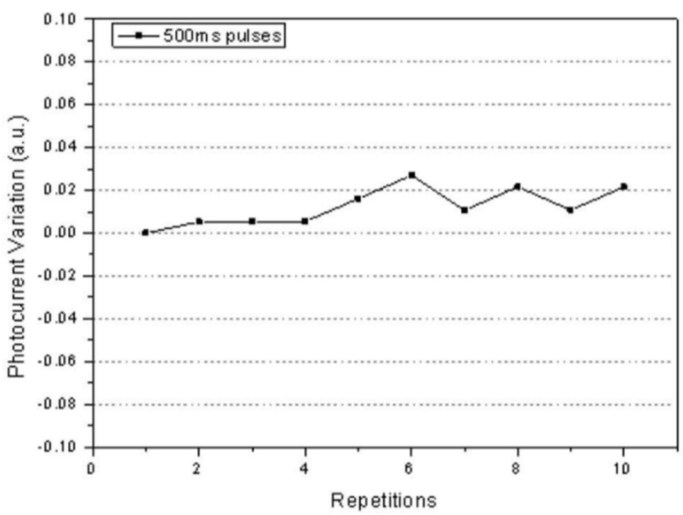

Figure 4.84 *Normalized signal amplitude variation for 500ms X-ray pulses exposure over 10 repetitions.* [151]

4.4. Proton detection

In the framework of the INFN CSN5 *FIRE - Flexible organic Ionizing Radiation dEtectors* project, the study of proton direct detection by organic thin film-based

sensors has been carried out. The properties which made the organic semiconductors appealing for their implementation as active layer in direct X-ray radiation detectors (see **Section 2.5.1)**, are also valid for the detection of protons. The mechanical flexibility and conformability, the large-area, the low cost of production and finally the human tissue-like behavior in terms of absorption make them promising candidate in order to overcome the main limitation presented by the commonly used proton detectors. Therefore, with the aim to assess the potentiality of this class of sensors in the field of proton therapy, two main experiments have been conducted. The first one took place at LABEC – Laboratorio di Tecniche Nucleari Applicate ai Beni Culturali (Florence, Italy) (**Section 3.7.4.1**) where 5 MeV protons have been detected. The energies and the fluxes employed during this experiment are of the order of the end-of-range values for proton therapy beams, in particular of the energies of scattered protons reaching internal healthy tissues surrounding the target. These results are discussed in **Section 4.4.1**. The second experiment provided the results shown in **Section 4.4.2** and they have been collected at TIFPA Proton Therapy Center (TN) (**Section 3.7.4.2**). In this case, the typical energies and fluxes involved in the treatment for the primary beam have been tested.

4.4.1. LABEC – 5 MeV proton beams

In order to detect the 5 MeV protons provided by the 3 MV Tandetron present at LABEC, several co-planar devices as the one depicted in **Figure 4.47a** have been employed. The active layer of the sensors is formed by TIPGe-Pn deposited from solution by drop casting and presenting a thickness of 150 nm. The devices have

been fabricated directly onto a 125 µm thick plastic foil (i.e. PET or PEN). In particular, we fabricated and tested samples with two different geometries: same channel length (i.e. the distance between the fingers of the electrodes) of L = 30 µm and two different width, i.e. W = 205.5 mm (W/L = 6850) and W = 45 mm (W/L = 1500). The irradiation setup and the system involved for the beam monitoring are described in **Section 3.7.4.1**.

After passing all the layers interposing between the proton source and the sensor, protons loose about 390 keV keV, as calculated with the SRIM Monte Carlo code [213]. **Figure 4.85** reports the SRIM simulation of the Linear Transfer Energy (LET) of each proton in the TIPGe film and in the plastic substrate.

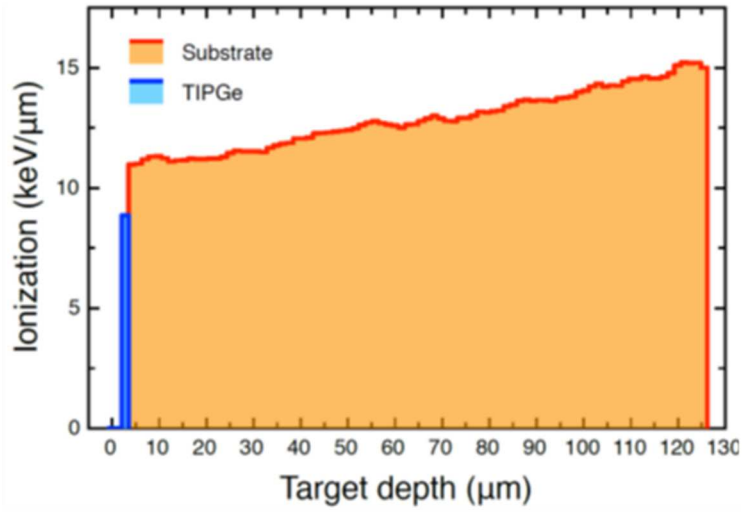

Figure 4.85 *SRIM simulated curve of the energy released by the proton beam in the organic semiconducting layer (150 nm thick) and in the plastic substrate (125 µm thick).*

The total released energy, given by the integral of the curves, in the plastic substrate is much higher than the one deposited in the organic semiconductor, due to the significantly different layer thicknesses. In particular, the energy lost by each

proton within the TIPGe-Pn layer is on average 1.55 keV, while the energy absorbed by the plastic substrate is about 1590 keV. Such difference has been effectively exploited to implement a proton detector able to simultaneously operate, as detailed in the following, in two distinct modes:

- *real-time mode*, exploiting the absorption of the organic thin film
- *integration-mode,* based on the absorption within the plastic substrate,

During the irradiation, the sensors were polarized at low voltages (<1 V) in order to collect the charges generated by anelastic interactions of protons with the electrons of the semiconducting layer. The detectors performance has been tested under consecutive ON/OFF cycles of exposure to 5 MeV proton beam, tuning the fluence of particles impinging onto the devices in the range between $3.5 \cdot 10^{9}$ $H^{+}cm^{-2}$ and $8.7 \cdot 10^{11}$ $H^{+}cm^{-2}$.

Figure 4.86 reports the typical dynamic current response, where the colored areas of the graphs represent the time windows of proton irradiation. The measurements have been carried out either keeping the exposure time constant (t = 10 s, **Figure 4.86a**), or varying it between 10 s and 30 s (**Figure 4.86b**).

Figure 4.86c zooms into one of the peaks reported in **Figure 4.86a** and **Figure 4.86b**, highlighting the typical curve of response to proton irradiation by the detector. The shadowed area indicates the total collected charges during the interval of exposure to the flux of protons. The small spikes during proton irradiation are due to the small metal plate of the chopper necessary for the accurate evaluation of the beam flux (as described in **Section 3.7.4.1**). As in the X-ray case, due to the energy absorption from the impinging radiation, electron-hole pairs are generated within the organic semiconductor and the electrical current

measured between the two electrodes increases by ΔI. When the beam is switched off, the current has an initial fast drop due to the recombination of the charges, followed by a slower decay. As it has been already discussed, the shape of the dynamic curve is a fingerprint for the PG mechanism which rules the detection of ionizing radiation by thin-film organic semiconductor-based sensors.

For each exposure cycle, the radiation dose absorbed by the sensor has been calculated by Equation 4.1:

$$D = \frac{E_{abs} \cdot N_{prot}}{\rho_{TIPGe-Pn} \cdot Volume} \tag{4.1}$$

where E_{abs} is the simulated value of the energy released by each proton to the organic thin film (LET), N_{prot} is the number of protons impinging onto the sensor and monitored by the rotating beam chopper, $\rho_{TIPG\text{-}Pn}$ and $Volume$ are respectively the density and the volume of the TIPGe-Pn active layer. The proton-induced charges collected during each exposure cycle have been calculated as the integral of the photocurrent peaks (i.e. the colored shadow in **Figure 4.86c**).

Figure 4.86d reports the collected charges as a function of the total proton dose for four samples: two samples with W/L = 1500 (black dots) and two samples with W/L = 6850 (red dots). The response of all tested detectors is linear with increasing radiation dose in a wide range of doses between 40 Gy and 11 kGy. Different samples with equal geometry lay on the same fit line, assessing the reproducibility and the repeatability of the detection response. From the plots in **Figure 4.86d**, the sensitivity of the detector (i.e. the induced charges collected per unit of absorbed dose) has been extracted as the slope of the linear fitting curve, reaching the values of $S_{W/L=1500} = (5.15 \pm 0.13)$ pC Gy^{-1} and $S_{W/L=6850} = (3.40 \pm 0.18)$ pC Gy^{-1}. The different responses achieved with the two geometries can be ascribed to the

different electrical efficiency for the extraction/injection of the induced charges by the electrodes.

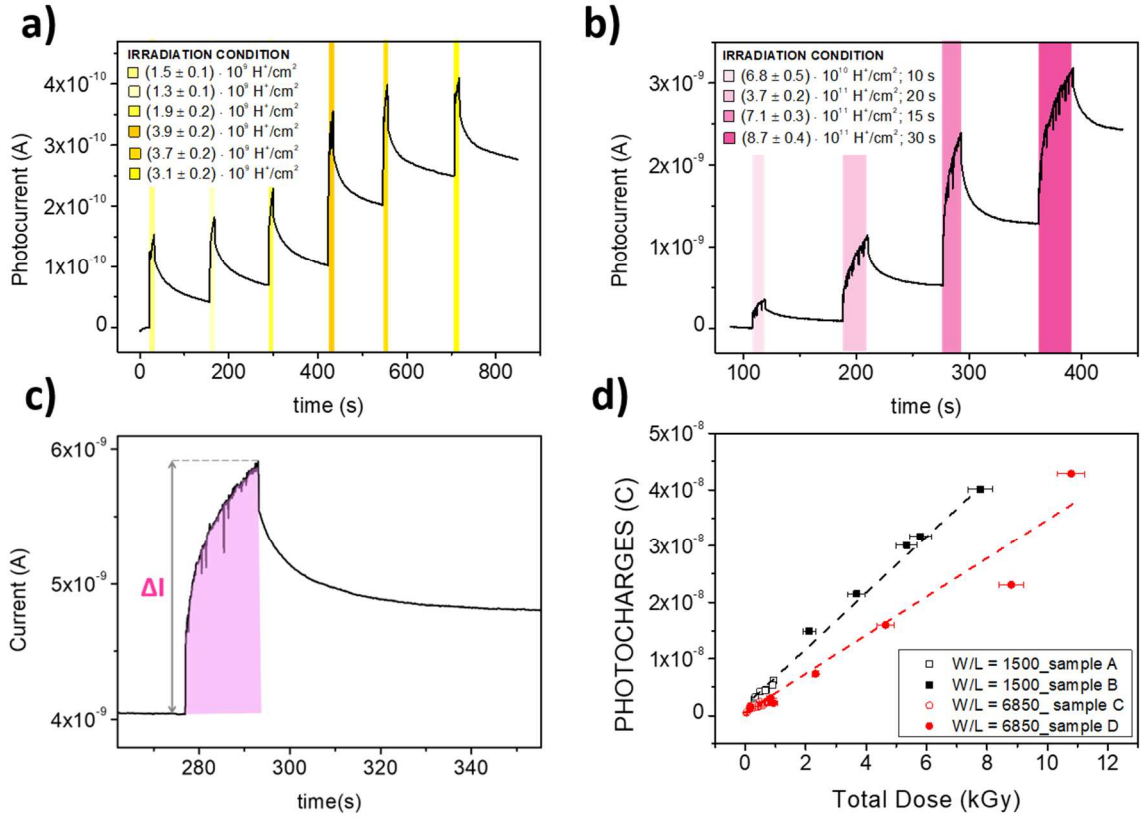

Figure 4.86 *a) and b) Photocurrent vs. time response of the detectors irradiated by subsequent ON/OFF cycles of protons tuning the incident fluences (3.5 · 10^0 - 9 · 10^{11} H^+cm^{-2}). The detectors have been tested keeping the exposure time constant t = 10 s (a) or varying it between 10 s and 30 s (b). During the measurements, an electric field (applied bias < 1 V) was imposed to the organic semiconducting layer. The time window of the irradiation is colored in the graphs and the color intensity of the boxes indicates the intensity of the proton beam. c) Highlight of dynamic response of the detector. The slow increase of the current indicates photoconductive gain effect. The photocurrent (ΔI) is calculated as the difference between maximum peak current and the baseline current before the irradiation. The integral of the plot (colored in pink) represents the total charge induced by the protons. d) Plots of the collected charges in function of the total dose of protons for two different W/L are shown. The black squares correspond to W/L = 1500 while the red circles represent W/L = 6850. In both cases the graphs indicate a linear response of the detector in a wide range of fluences (40 Gy - 11 · 10^3 Gy).*

The limit of detection has been calculated as:

$$LOD = \frac{3 \cdot RMS_{signal}}{Sensitivity} \tag{4.2}$$

Where RMS_{signal} is the root mean square of the current flowing in the device in dark condition and the *Sensitivity* is the higher sensitivity obtained. By applying this definition, a LOD down to (30 ± 6) cGy s^{-1} has been estimated.

The linearity of the real-time response holds even after 28.5 kGy of proton irradiation, assessing the reliability and the radiation hardness of TIPGe-Pn -based detectors.

Up to now, we discussed the sensor's detection mechanism in *real-time* mode, based on the interaction between the proton beam and the organic thin film. However, the persistent current turns to be reproducible and scale with the total absorbed dose. Hereafter, we discuss how to exploit the gradual baseline shift induced by multiple successive exposures, to implement an *integration-mode* operation, following the irradiation history of the sensor.

Figure 4.87 reports the current-voltage characteristics (IV) of a TIPGe-Pn detector before and after proton irradiation, and after up to 3 months storage in the dark. The increase of conductivity of the organic layer due to the interaction with the proton beam is evident. The conductivity raises from (1.93 ± 0.08) · 10^{-6} S m^{-1} to (36.4 ± 0.1) · 10^{-6} S m^{-1} after 66 nC of incident protons. The effect is reversible, in fact, despite the long relaxation time, full recovery occurs after 3 months (conductivity of (1.88 ± 0.07) · 10^{-6} S m^{-1}).

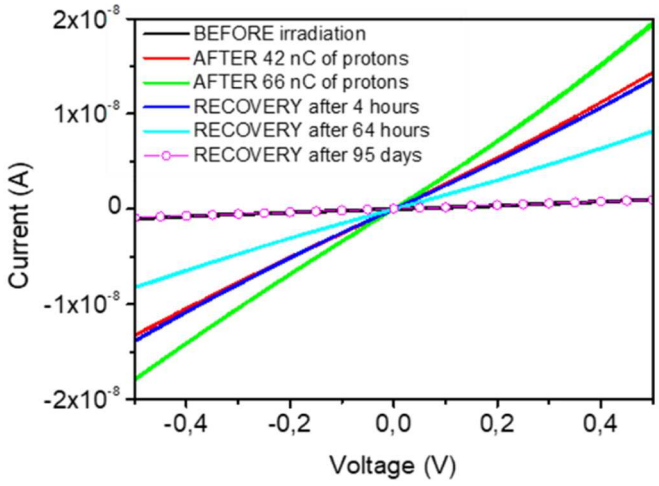

Figure 4.87 *Current-Voltage curves acquired before (black) the irradiation, after 2.5 · 10^{11} incident protons (42 nC, red line), after 4 · 10^{11} incident protons (66 nC, green line), after four hours (blue line), sixty-four hours (light blue line), ninety-five days (pink line and dots) of storage in dark. The graph shows the increase of conductivity of the organic semiconducting layer due to the irradiation.*

Looking closely at the typical dynamic response curve of the detector to proton irradiation (see **Figure 4.88a**), the total proton irradiation-induced current can be considered composed by two different contributions. The first one is the *real-time* response as a result of energy released in the organic semiconductor layer and photoconductive gain effect. This has been already discussed before and called ΔI. The second contribution, here denoted as I_0, represents the current baseline shift due to the fixed charges trapped in the plastic substrate after each proton beam exposure and depends on the irradiation history of the detector. In analogy to the procedure described above, the total induced charges (i.e. the integral of the green area highlighted in the dynamic curve of **Figure 4.88a**) and the dose corresponding to each exposure can be calculated (following the procedure indicated previously). The integrated amount of charges generated in the substrate, responsible for the current baseline shift (and of its long relaxation time), is linearly dependent on the

integrated dose of proton irradiation received by the detectors. From the linear fit of the curve reported in **Figure 4.88b**, the sensitivity of the detector, here thus operating in an *integration-mode*, results S = (6.97 ± 0.18) · 10^{-1} pC Gy^{-1}. The generation of charges in polymeric foils following proton irradiation is an effect known in the literature [239]–[243] and is well justified in the here presented devices, fabricated onto a 125 μm thick plastic substrate absorbing a consistent fraction of the proton energy (about 1590 keV per H^+, as already discussed).

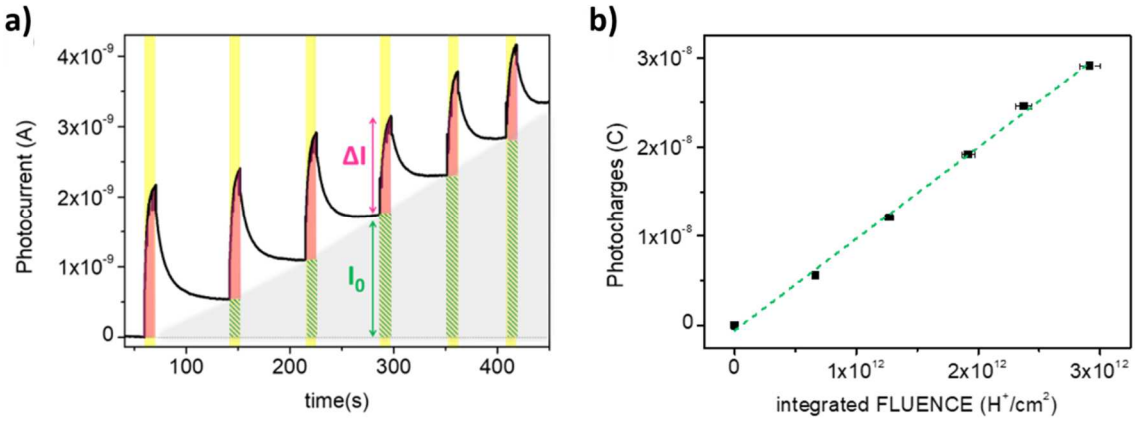

Figure 4.88 *a) Dynamic curve (black line) of the current response of the detector to different fluences of incident protons ((4.5 · 10^{11} – 6.6 · 10^{11}) H^+cm^{-2}). Two different contributions can be distinguished: ΔI (pink shadow) is the* real-time *response proportional to the dose (already described in* ***Figure 4.86****), while I_0 (green shadow) represents the baseline shift due to the fixed charges trapped in the plastic substrate. b) Linear increase of the total charges generated in the plastic substrate as a function of the integrated dose which irradiates the sample.*

These proton-induced charges, accumulated in the plastic substrate, act as a bottom-gate effect for the organic semiconductor layer, increasing its electrical conductivity. This effect can in fact be assimilated to what occurs in a field effect transistor (**Figure 4.89**) where the gate electrode is used to tune the density of charges flowing in the thin

channel at the semiconductor/dielectric interface, between the source and drain electrodes. Here, as the charges induced in the plastic substrate have a long lifetime (as assessed by the IV curves reported in **Figure 4.87**), this gating effect adds up after each proton exposure, with a contribution proportional to the actual dose received, thus allowing to quantitatively monitor the irradiation history of the detector.

It is noteworthy that to collect and to exploit the information accumulated within the plastic substrate, the organic semiconducting layer and its interface with the substrate play an essential role, as they permit to transduce into a source-drain current the information stored in the static charges induced in the by proton irradiation.

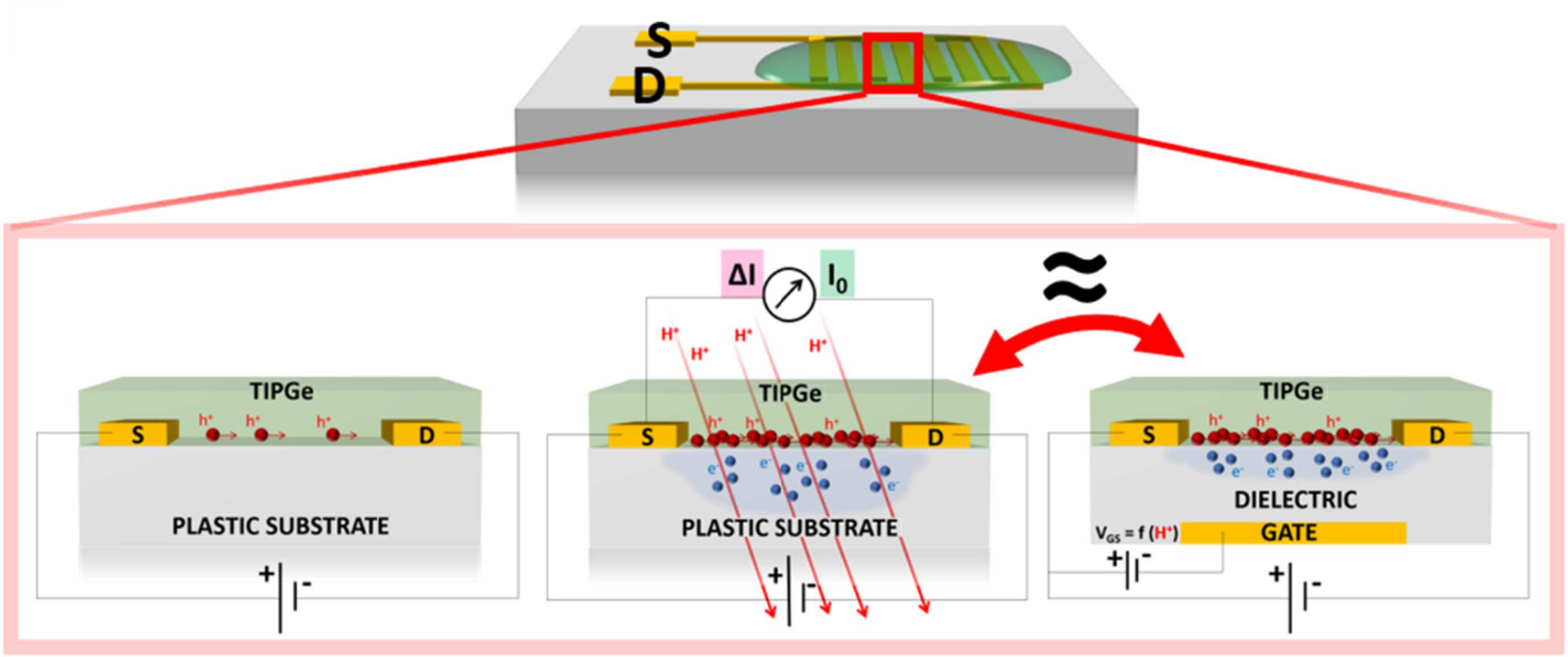

Figure 4.89 *Schematics of the detector integration-mode operation: the protons irradiating the sample generate charges in the polymeric foil with a very long relaxation time. These trapped negative charges induce an increase of the semiconductor conductivity leading to higher source-drain current in the organic thin film. This effect is similar to what happens in an Organic Field Effect Transistor (OFET) structure, where the gate electrode is typically used to tune the current flowing between the source and the drain electrodes. In this case, the irradiated polymeric substrate of the sensor acts as the bottom gate electrode of an OFET structure creating a gating effect proportional to the integrated dose of irradiating protons.*

4.4.2. TIFPA – 70 MeV proton beams

In this paragraph, preliminary results achieved by exposing organic-based devices under 70MeV protons provided by the Proton Therapy Center TIFPA – Trento Institute for Fundamental Physics and Applications (Trento, Italy) Proton Therapy Center are illustrated. These data demonstrate the potentiality of these novel class of direct detectors for their implementation in proton dosimetry for medical therapy. These represent the first measurements which should be followed by deeper investigation in actual medical environment for a more solid interpretation of the detection mechanism occurring in organic-based sensors exposed to higher energy protons.

Co-planar devices as the one employed at LABEC (see **Figure 3.26**) have been exposed to a 70 MeV proton beams varying the fluences of irradiation in the range between [4 - 10] $\cdot$ 10^{10} protons cm^{-2}.

The irradiation experiment has been conducted interposing several solid water layers between the proton source and the samples. These polymeric panels present a density of (1.032 $\pm$ 0.005) g cm^{-3} which simulate well the human tissues passed through the protons during a medical treatment. Varying their thicknesses, we could assess the detection response of the device as it would be placed in different position inside a human body. In **Figure 4.90**, the dynamic curves measured during the ON/OFF exposition cycles are shown for different solid water thicknesses (indicated by the numbers reported in the single plots). The yellow squares indicate the time interval during which the beam was turned on.

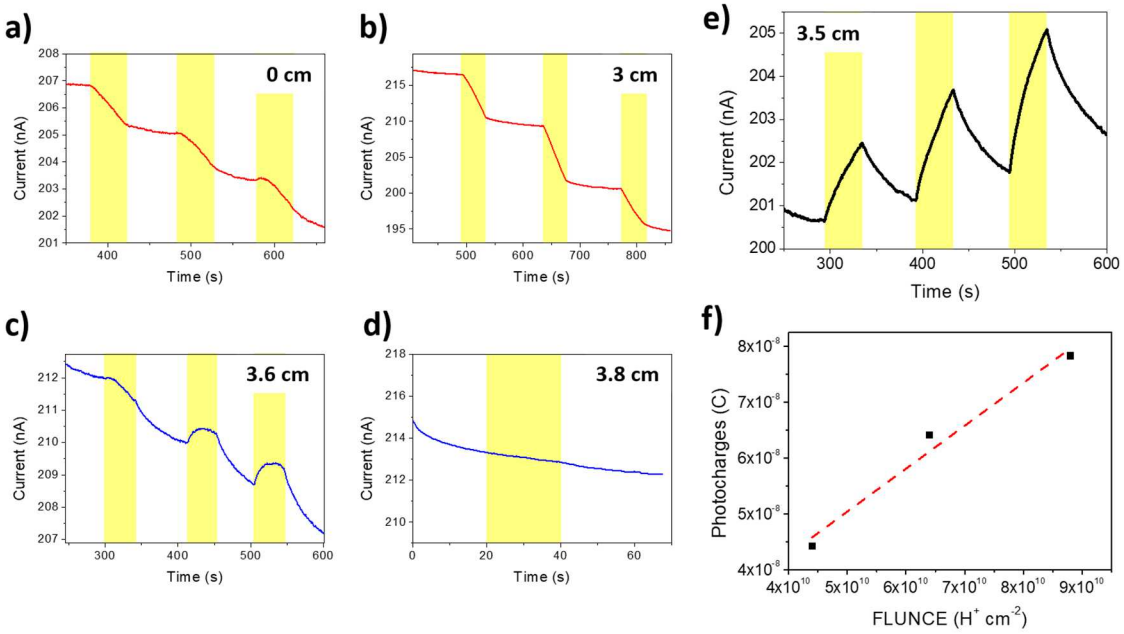

Figure 4.90 *Dynamic response of the organic thin film-based device exposed to three subsequent ON/OFF cycles of increasing fluences (in the range between [4 - 10] · 10^{10} protons cm^{-2}) of 70 MeV protons. Different thicknesses of solid water have been interposed between the proton source and the sample, in particular (a) 0 cm, (b) 3 cm, (c) 3.6 cm, (d) 3.8 cm, (e) 3.5 cm. (f) Charges induced by the three exposures reported in (e) plotted as a function of the correspondent fluence of protons.*

As it is demonstrated by these plots, the detector responds to the beam showing a clear increase of the current due to the absorption of protons only when a specific amount of solid water is placed in front of it (**Figure 4.90e**). In fact, in this case the sensor shows an increase of the current which linearly depends on the fluence of the proton beam. This trend is shown in **Figure 4.90f** where a sensitivity of (7.7 ± 1.1) · 10^{-19} C protons^{-1} cm^{-2} has been calculated.

On the contrary, when the solid layer thicknesses are either lower or higher than this specific amount (i.e. 3.5 cm) the detector doesn't exhibit a clear response. In more detail, for lower thicknesses (**Figure 4.90c, d**) the sensor shows a decrease of the current during the exposures which seems not depending on the proton fluences. On the opposite side, for slightly higher thicknesses (**Figure 4.90c**) the current

increases due to the absorption of protons but the proportionality with the intensity of the beam is lost. For much higher solid water thicknesses, the detector does not show any change induced by the irradiation (**Figure 4.90d**).

These differences are related to the change of the Bragg peak position due to the different layers which the protons have to pass through before reaching the sensor.

By the data collected so far, only a speculative interpretation of these measurements can be given and further experiments and simulations should be carried out in order to confirm it. As it has been introduced in **Section 2.2.2**, protons interact with matter in a different way compared to high energy photons. In particular, the graph reported in **Figure 2.19** clearly depicts the difference between the two in releasing energy during their pathways. One can deduce that interposing 3.5 cm of solid water moves the Bragg peak exactly on the active layer of the sensor achieving the clearer response by the detector. On the contrary, when thinner solid water layers are placed in front of the sample, the Bragg peak moves behind the organic detector and the energy released in the semiconducting layer is not enough to produce an increase of current. Indeed, with the release of this amount of energy the protons activate other mechanisms within the organic semiconductors which bring a decrease of the current. More important, when the thickness of the solid water interposed between the proton source and the detector is much higher than 3.5 cm, the Brag peak falls before the sensor position and the detector correctly responds as no protons is present at that larger depth. This last aspect is very appealing thinking about a possible application for this class of devices. In fact, in addition to the monitoring of the dose delivered at the tumor during the treatments, the monitoring of the surrounding healthy tissues is a crucial aspect. The human tissue equivalence and the mechanical flexibility together with

these last results confirm the great potential of direct organic thin film-based detectors for their employment as radiation detectors able to assess in real-time the presence of unwanted extra radiation doses delivered onto the healthy tissues surrounding the tumor during a medical treatment.

5.

Ionizing Radiation Detectors based on High Mobility Amorphous Oxide Semiconductors (ROXFET)

In this fifth chapter, the main results regarding the employment of thin film transistors based on high mobility amorphous oxide semiconductors as radiation detectors are shown. In particular, in the first section a brief description of the TFTs structure and electrical behavior is provided. Following, the X-ray detection experiments which allowed to assess the sensing performances of these devices are described with a comparison between the standard RADiation sensitive Field Effect Transistor (RADFET) [244] and the here presented Radiation sensitive OXide semiconductor Field Effect Transistor (ROXFET). Thus, the following paragraph is focused on the innovative dielectric layer implemented in these devices and the impact of the thickness of this insulator on the detection performances is illustrated. Finally, the integration of these sensors with a passive RFID chip for the readout of the dosimeter is shown. At the end, the proof of concept for the detection of high energy gamma rays by this class of detectors is demonstrated.

5.1. High Mobility Amorphous Oxides Thin Film Transistors

The radiation detection capability of Amorphous Oxide Semiconductor TFTs have been tested employing the devices described in **Section 3.1** and depicted in **Figure 3.28**. The basic structure of the TFTs is also reported in **Figure 5.91**.

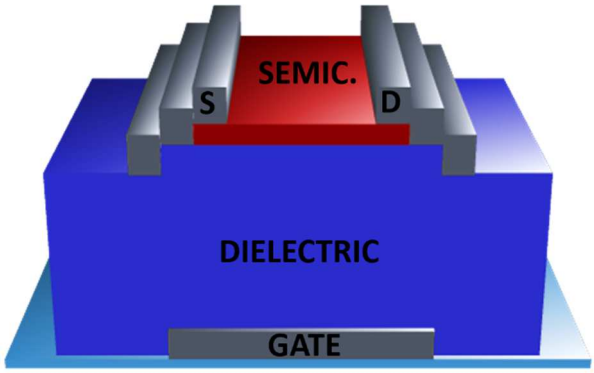

Figure 5.91 *Schematic of the thin film transistor based on amorphous oxide semiconductors.*

The transistors have been fabricated following the procedures shown in **Section 3.1**. In particular, thirty-six BGBC TFTs have been placed in four 3 x 3 matrixes as it is shown in **Figure 5.92**. They have been fabricated onto PEN foils in order to obtain fully flexible devices (see **Figure 5.92e**). The dimensions of the transistors are W = 320 µm and L = 20 µm presenting a linear channel as depicted in **Figure 5.92d**. This layout allowed to electrically connect all the nine TFTs forming the same 3 x 3 matrix at the same time, using the multiplexer system described in **Section 3.4** (see **Figure 3.36**). This method leads the possibility to characterize

more than one device at the same time, leading to assess the statistical uniformity of transport properties and radiation detection performances. This is an essential task in order to prove the potentiality of this technology for the development of large area systems.

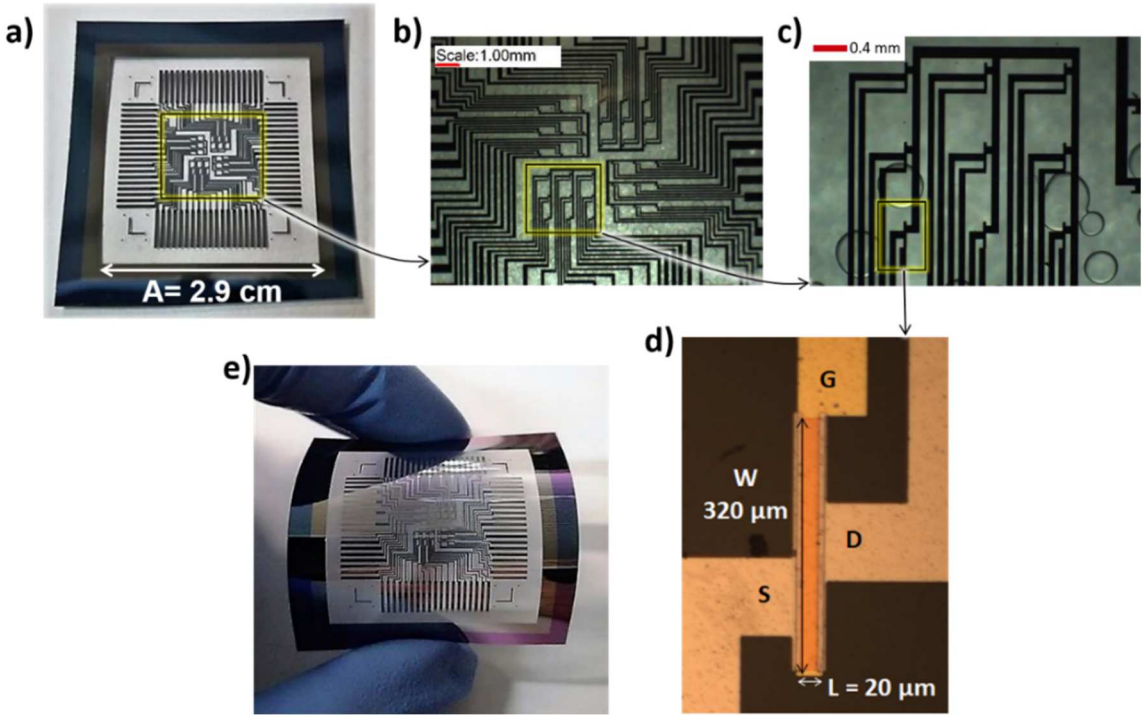

Figure 5.92 *a-c) The entire layout of the AOS TFTs matrix is here depicted. The 36 TFTs have been placed in four different 3 x 3 matrixes in which the source electrode is in common and the drain and the gate are independent for each transistor. d) The single pixel is constituted by a TFT with a linear channel (L = µm, W = 320 µm). e) The devices have been fabricated onto PEN 125 µm thick foils in order to achieve fully flexible detectors.*

The TFTs have been electrically tested as described in **Section 3.4**. A typical transfer characteristic in saturation regime acquired for nine TFTs laying in the same matrix is reported in **Figure 5.93** where the great spatial uniformity achieved by this fabrication process is demonstrated.

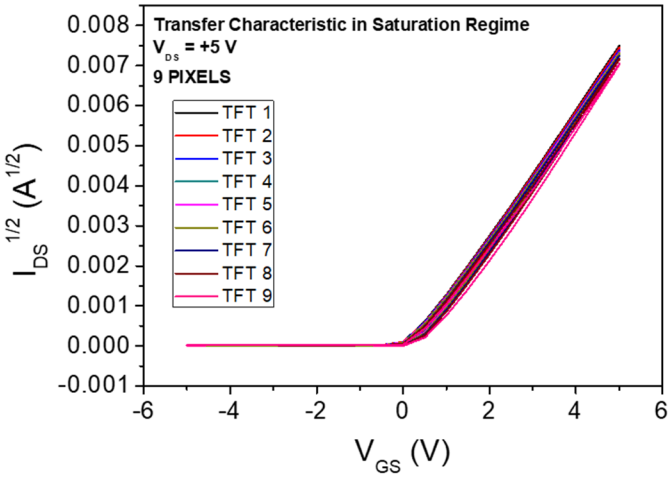

Figure 5.93 *Transfer characteristics in saturation regime for nine TFTs laying in the same matrix.*

Depending on the dielectric thickness, the transistors show mobilities in the range of 10 to 22 $cm^2\,V^{-1}\,s^{-1}$, a steep subthreshold swing S (0.16 to 0.35 V/decade), low leakage currents (<1 pA) (see **Table 5.12**), and stable operation up to frequencies of 1 MHz (see **Figure 5.94**).

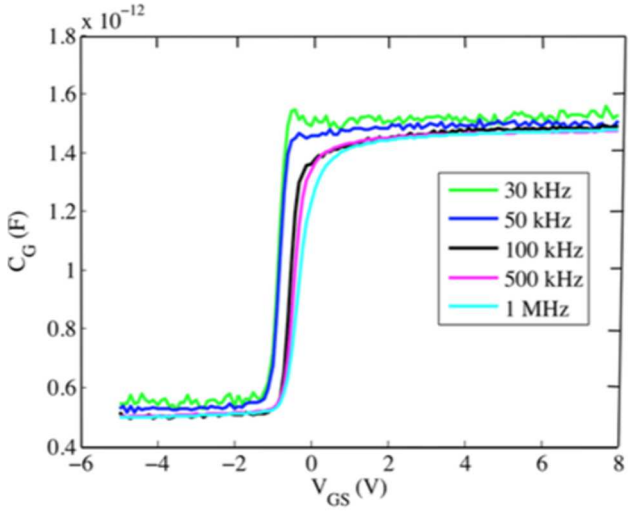

Figure 5.94 *Gate capacitance at different AC frequencies as a function of gate voltage. The capacitance rises when the conductive channel is formed, and the transistor is switched on* [245].

Dielectric Thickness (nm)	*Mobility* ($cm^2\ V^{-1}\ s^{-1}$)	*Leackage current @ 5 V (pA)*	*S* ($V\ dec^{-1}$)	N_T ($10^{11}\ eV^{-1}\ cm^{-2}$)
114	(29.4 ± 1.7)	0.250 ± 0.005	0.16 ± 0.01	5.9 ± 0.9
205	(22.5 ± 1.8)	0.150 ± 0.005	0.27 ± 0.04	8.7 ± 1.0
293	(17.3 ± 1.8)	0.10 ± 0.01	0.30 ± 0.10	7.3 ± 1.0
352	(12.0 ± 0.4)	0.05 ± 0.01	0.35 ± 0.13	8.5 ± 1.1

Table 5.12 *Electrical parameters describing TFTs with different dielectric thicknesses* [245].

5.2. X-ray detection

The results reported in this section have been published by T. Cramer et al. in 2018 [245] and they emerged from a collaboration with the Faculdade de Ciências e Tecnologia of the Universidade Nova de Lisboa (Portugal) and with the Company Tagsys RFID.

The sensors have been tested exposing them under X-rays produced by a Mo-target tube kept at 35 kV and varying the doses in the range [5 – 75] mGy. The TFTs have been electrically connected as described in **Section 3.4**. During the X-ray exposure, the three terminals of the TFTs have been kept at ground potential, while transfer characteristics have been acquired during the irradiation every 2 s in a time interval of 6 ms as depicted in **Figure 5.95a**. Thus, the parameters of the

TFTs have been extracted from the transfer characteristics acquired in saturation regime (**Figure 5.95b**).

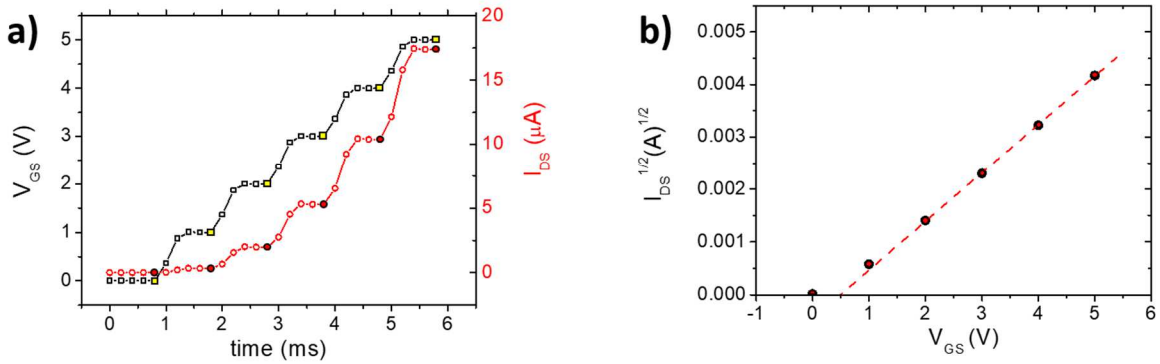

Figure 5.95 *Determination of TFT threshold voltage in radiation experiments. a) Transfer characteristics acquired in a 6 ms time interval applying a voltage ramp to the gate electrode. The filled points are the ones considered for the electrical characterization. b) Linear fit to the plot of VG vs* $I_{DS}^{1/2}$ *was used to determine the threshold voltage. For the rest of the time all terminals of the TFT were connected to ground* [245].

In the following paragraphs, the detection response physical mechanism of the sensors is described. The innovative structure of the dielectric, which in this case plays the role of the sensing active layer, is shown focusing on the detection mechanism which induces the radiation-response. Finally, the integration of a readout system formed by a low-cost CMOS radiofrequency identification (RFID) tag is illustrated.

5.2.1. Radiation-sensitive OXide semiconductor FET: the ROXFET

The radiation-sensitive Field Effect Transistor (RADFET) which employs a thick silicon oxide (SiO_2) layer as the active volume for high-energy radiation detection is a very diffuse sensing technology employed in several fields of application (see **Section 2.5.2** and **Figure 5.97a**). It offers numerous advantages such as the small size, the ability to permanently store accumulated dose, the dose-rate independence, and the ease of readout. However, many drawbacks related to this class of sensors are still present such as the incompatibility of the CMOS technologies with flexible polymeric substrates and the low stopping power offered by SiO_2 which causes poor sensitivities spanning in the range [0.05 – 0.3] V Gy^{-1}.

With the aim of overcoming these two main limitations, we introduced the radiation-sensitive oxide semiconductor Field Effect Transistor (i.e. ROXFET). These devices are based on a-IGZO as semiconductor (see **Section 3.2.3**) and on a multilayer dielectric containing tantalum oxide and silicon dioxide (**Section 3.2.4.2**). The use of HMOSs as the active materials for the development of TFTs make them compatible with low-temperature processes which allow to fabricate flexible devices onto polymeric foils (as already discussed in **Chapter 1**). Second, the multilayer dielectric formed both by multilayers of sputtered SiO_2 and Ta_2O_5 enormously improved the performance of AOS TFTs both in terms of sensitivity and of operating voltages.

In ones considers the higher Z number of Ta if compared with Si ($Z_{Si} = 14$, $Z_{Ta} = 73$), the introduction of Tantalum Oxide brings an increase of the attenuation fraction by the active layer of the sensor and thus an increment of the corresponding

sensitivity (see **Figure 5.96**). The high content of high-Z tantalum atoms leads to 50 times shorter photon mean-free path than in pure SiO_2 dielectrics at the assessed X-ray energies that are beyond the Tantalum X-ray absorption L-edge. Moreover, the Ta_2O_5 ($k = 44$) belongs to a category of dielectric called *high-k insulators* [246] which allows the TFT to work at very low voltages (or even in passive mode) still ensuring an effective separation of the electron-hole pairs generated by the radiation absorption thanks to the inner electric field built up by the dielectric layer itself.

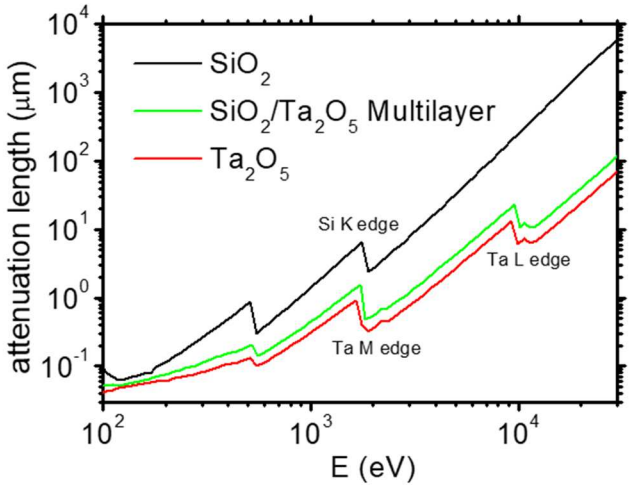

Figure 5.96 *Calculated attenuation length spectra for silicon dioxide and tantalum penta-oxide based on NIST data base* [245].

As in the RADFET systems, the absorption of radiation in this kind of devices induces the generation of a net-positive charge accumulated in the dielectric layer (see **Figure 5.97**). This provokes a shift of the transfer curve to negative gate voltages which is well illustrated by the graph reported in **Figure 2.25b**. No other TFT parameters such as subthreshold slope or mobility is affected, simultaneously confirming the radiation sensitivity of the transistor structure and the radiation hardness of oxide semiconductor transport properties [247].

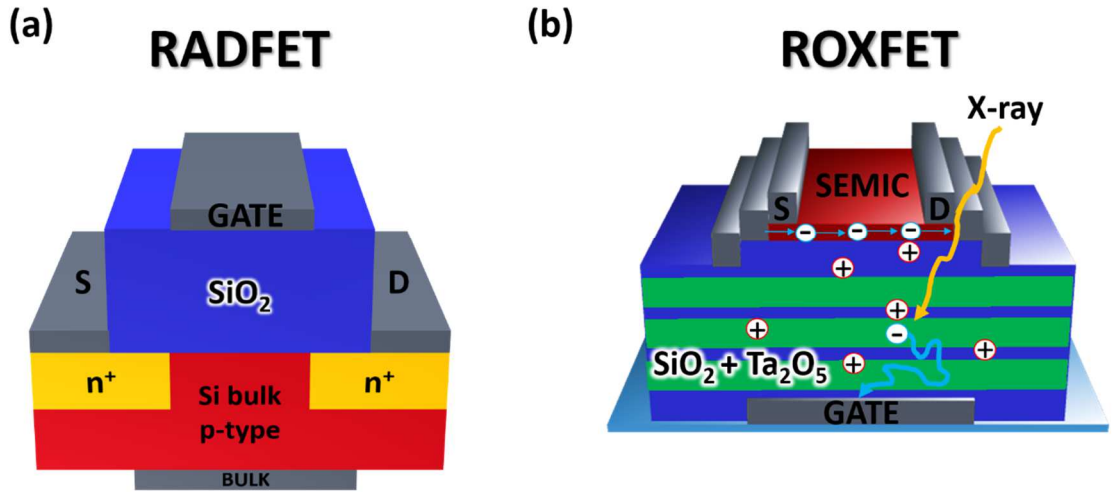

Figure 5.97 *Schemes (not in scale) of the (a) RADFET where a unique SiO_2 dielectric layer is present and (b) ROXFET where a stacked multilayer is inserted. In (b) the generation of trapped positive charge in the dielectric as a consequence of X-ray absorption is shown* [245].

Figure 5.98a, shows the threshold voltage shift towards negative values for different total dose of radiation absorbed during one second of exposure. In **Figure 5.98b** it is possible to notice that the ΔV_{th} scales linearly with the exposure dose, thus allowing to define a sensitivity S in units of Volts per Gray. Here, the sensitivity value amounts to $S = (3.4 \pm 0.2)$ V Gy^{-1}, outperforming typical CMOS RADFET devices by about an order of magnitude.

The integration mode operation of this kind of detector is well summarized and demonstrated by the graph reported in **Figure 5.98c**. Here, 30 mGy of total radiation has been delivered to the sensor in different ways. The black curve indicates the single-step delivery, while the red and the green curves show the response due to two or three consequent exposures of 15 mGy and 10 mGy respectively. As it is possible to see, the final threshold voltage depends only on the total dose and it is independent on the dose rate.

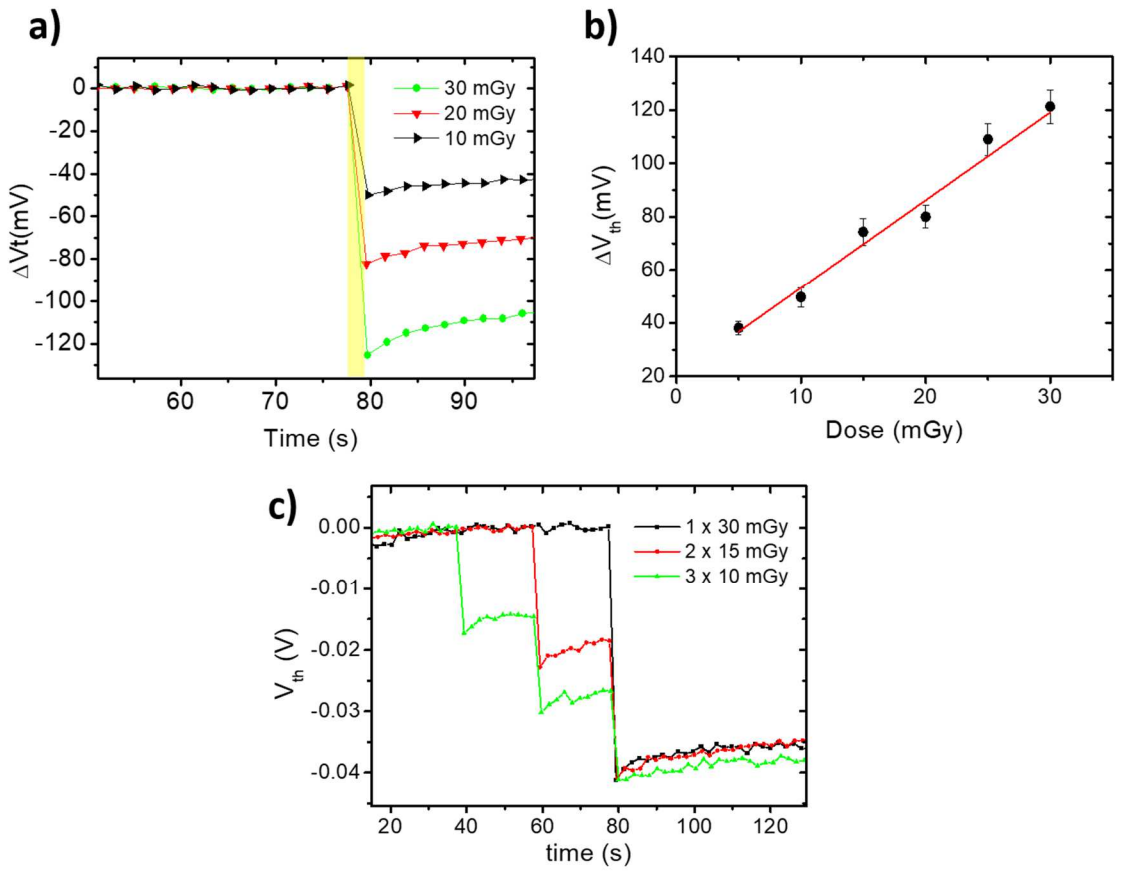

Figure 5.98 *a) Threshold voltage shift of TFTs due to 1 s X-rays exposure of three different doses. b) ΔVth reported as a function of the total dose of exposure. From this graph it is possible to calculate the sensitivity of the sensor as the slop of the fitting curve. It results S = (3.4 ± 0.2) V Gy⁻¹. c) The threshold voltage of the oxide transistor as a function of time. Three different situations are compared: one exposure of 30 mGy (black), two consecutive exposures of 15 mGy each (red) and three exposures of 10 mGy each (green). This graph illustrates the integration mode operation of this class of detectors* [245].

When observing the ROXFET response on a longer time scale, it is possible to notice (**Figure 5.99a**) that the threshold voltage returns to the initial value after exposure, thus indicating the annealing of positive ionization charge in the dielectric. The dynamics of the annealing process cannot be described by a single exponential but has contributions at different time scales resulting in a stretched exponential behavior (see Eq. 5.1).

$$\frac{V_{th}(t) - V_{th}(t=\infty)}{|V_{th}(t=0) - V_{th}(t=\infty)|} = exp\left[-\left(\frac{t}{\tau}\right)^{\gamma}\right] \qquad (5.1)$$

The dynamics is independent on dose, and, after normalization, all time traces superimpose on a universal curve, as shown in **Figure 5.99b**. Quantitatively, this behavior is described by a stretched exponential using a time constant of $\tau = 17.9$ min and an exponent of $\gamma = 0.67$. Stretched exponential behavior (as the one which describes the PG relaxation in organic-based sensors in **Chapter 4**) results from processes that follow a distribution of time constants, characteristic for transport in amorphous, disordered energy landscapes [248], [249]. Here, the behavior is attributed to trap states in the dielectric that are distributed in their characteristic energy and therefore keep the ionization charges captured for different characteristic time scales.

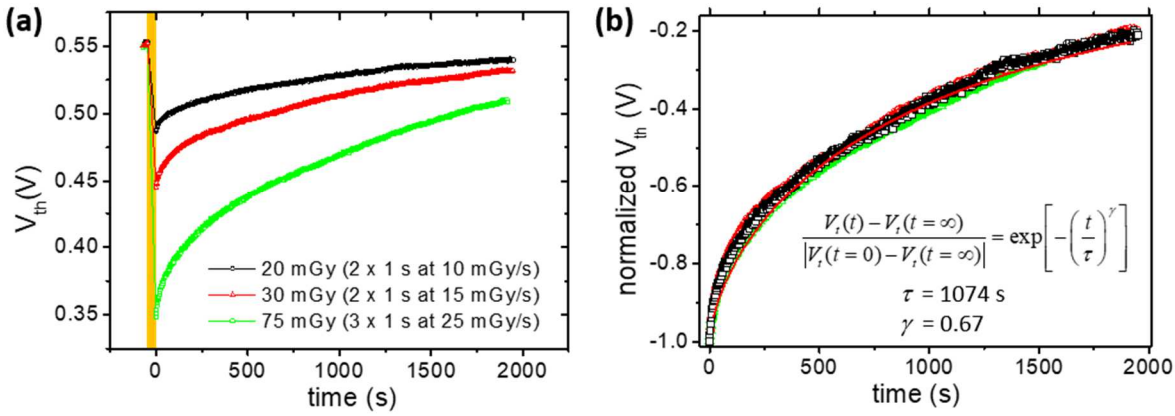

Figure 5.99 *a) Threshold voltage as a function of time after x-ray exposures at different total doses: recombination processes lead to the annealing of trapped charges in the dielectric on a slow time scale. b) Normalized threshold voltage shift for different exposure doses: the threshold recovers its initial value following the universal stretched exponential indicated in the graph* [245].

In comparison to silicon oxide–based RADFET sensors, in the case of ROXFET the annealing happens on faster time scales, and corrections have to be included when the sensor is used as an integrative dosimeter over long time scales. Moreover, it has been demonstrated that the trap annealing time can be further shortened by increasing temperature (see **Figure 5.100a**) or by applying electric fields across the dielectric (**Figure 5.100b**). In this way, it is possible to easily reset the dosimeter to its initial state and to reuse the device [250].

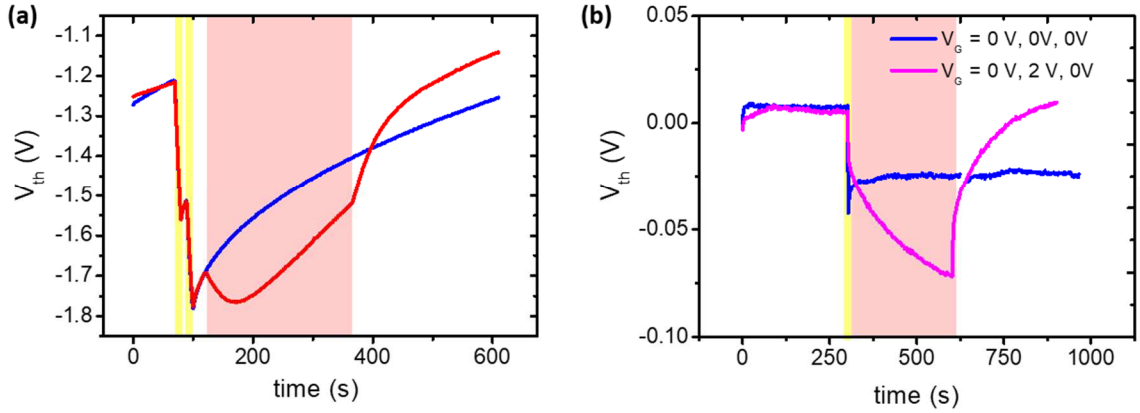

Figure 5.100 *a) Acceleration of the ROXFET recovery by heating the sample with aa IR-lamp. The blue line shows a TFT that was exposed to 2 x 300 mGy doses (yellow bars) and then left at room temperature. The red line results from the same exposure with the difference that the TFT was heated to 80°C with a IR lamp during the time indicated with the red box. b) Acceleration of the ROXFET recovery by applying a gate voltage to the TFTs. The graph reports the threshold voltage as a function of time before and after exposure to 15 mGy of X-ray (indicated by the yellow bar). Without application of a potential (V_{GS}=0), the device maintains a stable threshold voltage after exposure and returns only on a long time-scale to the original threshold value. By applying V_{GS}=2V after exposure, annealing processes accelerate and in addition bias stress occurs, shifting the threshold to negative values. Importantly, when applying again 0V after 300 s, the device recovers from bias stress and returns to the original threshold value, demonstrating that no trapped charge is left in the dielectric* [245].

5.2.2. Dielectric thickness impact

The dielectric of the proposed ROXFET plays a crucial role in obtaining high x-ray sensitivity and a high signal-to-noise ratio for dosimeter applications. In particular, it has to combine low leakage and high permittivity with high X-ray cross section and high quantum efficiency as it has already been discussed in **Section 3.2.4.2**. For this purpose, the stacked 7-multilayer dielectric depicted in the inset in **Figure 5.101** has been employed. The role of Ta_2O_5 has already been discussed while the SiO_2 layers have been incorporated both for the lowering of the leackage current below 1 pA and in order to achieve a less defective interface with the a-IGZO oxide semiconductor [251].

In order to investigate in more detail, the role of the dielectric in the detection of X-rays, several devices presenting different insulator total thicknesses have been tested. The total thickness of the dielectric has been varied between 110 and 380 nm nm, but the ratio of total Ta_2O_5 + SiO_2 to SiO_2 layer thickness has been kept constant at a value of $d_{Ta}/d_{Si} = 3.5$. **Figure 5.101** shows how the capacitance scales with the dielectric layer thickness. As expected, a reciprocal relation is shown, where the intercept is related to the interfacial layer of silicon oxide. The data fit well to a multilayer structure with alternating layers [246], yielding an effective permittivity of $\varepsilon_r = 13.4$. Because of this increased permittivity, the specific capacitance results 25 nF cm^{-2} for the TFTs with the thickest dielectric (382 nm), assuring a steep subthreshold slope and low-voltage operation.

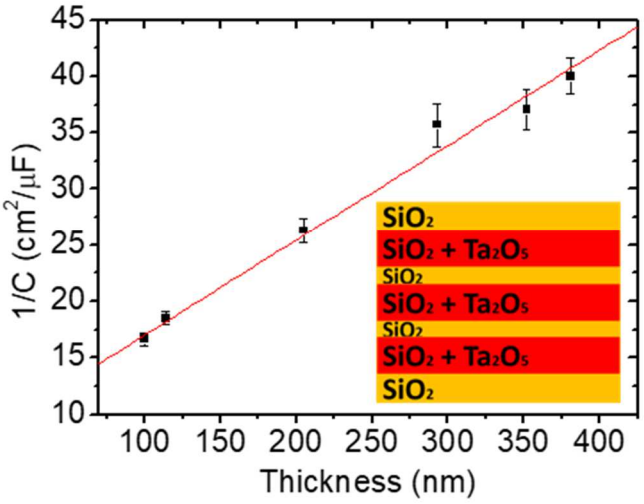

Figure 5.101 *Inverse dependence of the reciprocal of specific capacitance with the multilayer dielectric total thickness. From this graph the effective permittivity of the stacked structure has been calculated and it results* $\varepsilon_r = 13.4$*. The inset shows the multilayer structure of the dielectric* [245].

Next, the impact of the multilayer dielectric thickness on X-ray sensitivity has been evaluated. **Figure 5.102a** shows the threshold voltage shifts obtained at different X-ray doses for transistors with different dielectric thickness. For each tested device, a linear relation is obtained, and the resulting slope is reported in **Figure 5.102b** as X-ray sensitivity as a function of layer thickness. From this latter graph, a quantitative analysis has been carried out in order to assess relevant parameters for the conversion of photons into ionization charge in these materials. Here, the increase of sensitivity follows a quadratic dependency, similar to what happens in classical RADFET dosimeters. In fact, after the absorption of energy by the impinging radiation, it is possible to assume that the ionization charge density σ is distributed equally in the dielectric. The ionization charge is counterbalanced on one site of the dielectric by mobile electron carriers causing a shift in the transistor threshold:

$$\Delta V_{th} = \frac{\sigma(d)}{2c(d)} \tag{5.2}$$

Where both σ and the specific capacitance of the dielectric c depend on the dielectric layer thickness d. This is the reason for the quadratic behavior observed in **Figure 5.102b**.

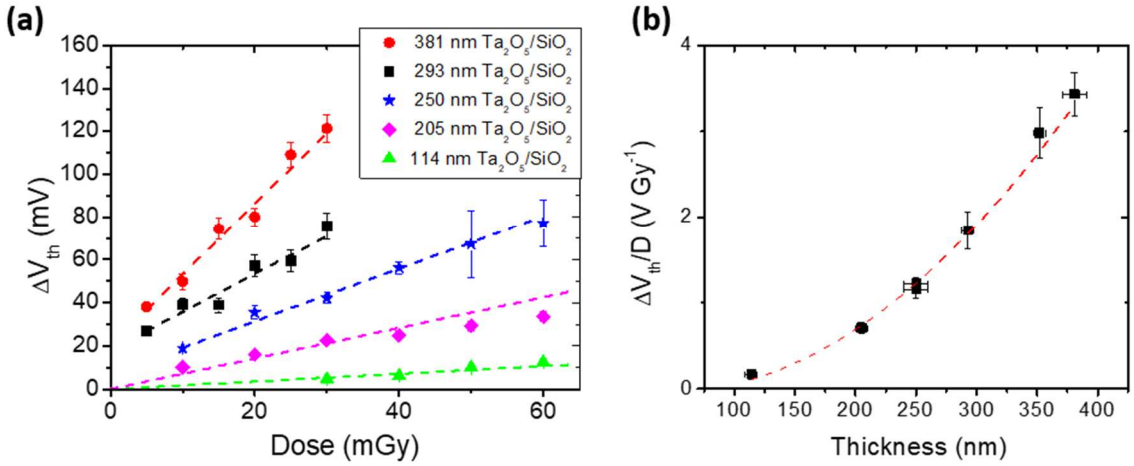

Figure 5.102 *a) Threshold voltage shift as a function of total dose for oxide transistors with different dielectric layer thicknesses. b) X-ray sensitivity, defined as the threshold voltage shift per dose, as a function of dielectric thickness. The line represents the quadratic fit described in the text* [245].

It is possible to extract the quantum efficiency of the sensor considering the following. The amount of ionization charge that is produced in the dielectric depends on radiation dose ΔD (expressed in air kerma). Knowing the X-ray photon absorption length λ it is possible to estimate the amount of absorbed energy ΔE as:

$$\Delta E\ (d) = \frac{\Delta D\ d}{c_{m,air}\ \lambda} \tag{5.3}$$

The amount of charge produced depends then on the electron-hole-pair formation energy $W_{\pm}$ and the internal quantum efficiency of the process QE_I that is limited due to recombination processes and thermal dissipation

$$\sigma\,(d) = \frac{QE_I\; e\; \Delta E(d)}{W_{\pm}} \tag{5.4}$$

If one indicates the specific capacitance of the dielectric as

$$\frac{1}{c} = \frac{d}{\varepsilon_r \varepsilon_0} \tag{5.5}$$

Combining all these equations (Eq. 5.2-Eq. 5.5) it is possible to express the sensitivity of the detector as:

$$S = \frac{\Delta V_{th}}{\Delta D} = \frac{QE_I\; e}{2c_{m,air}\lambda\varepsilon_r\varepsilon_0 W_{\pm}}\, d^2 \tag{5.6}$$

Then, fitting the curve reported in **Figure 5.102b**, from the extraction of the slope it has been possible to calculate the internal quantum efficiency of the sensor. In particular, setting the Mo-Kα line (17 keV) as the relevant photon energy to obtain values for $c_{m,air}$ and λ, $W_{\pm}$ = 12.9 eV that is three times the bandgap reported for Ta_2O_5, the internal quantum efficiency QE_I results 16%.

5.2.3. Readout system based on RFID

This optimized multilayer dielectric endows the ROXFET with an increased X-ray sensitivity (i.e. one order of magnitude higher than the typical values reported for the standard CMOS RADFET), a high-frequency operation, and a steep

subthreshold behavior. The combination of these properties leads to the possibility of directly combine a ROXFET-based dosimeter with a passive RFID chip to achieve a low-cost x-ray dosimeter tag, as shown in **Figure 5.103**.

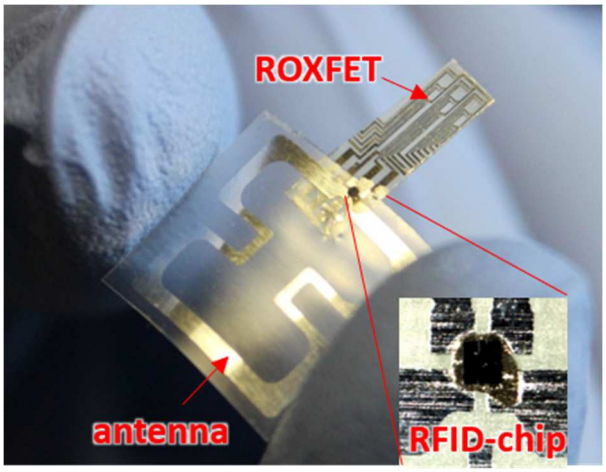

Figure 5.103 *Picture of flexible RFID X-ray sensor tag* [245].

The main purpose of such an X-ray tag is to provide information upon wireless interrogation if the integrated absorbed radiation dose has overcome a certain programmable threshold. Upon the RFID reader command, the integrated RFID tag probes the channel impedance Z of the ROXFET that has changed its value in case of radiation exposure.

A simple version of such a functionality is implemented in commercial RFID chips as a tamper alarm and switching occurs if the measured impedance varies from below 2 MΩ to above 20 MΩ. X-ray exposure can actually induce such an order-of-magnitude variation in the ROXFET channel impedance because of the resulting charging of the dielectric and the threshold voltage shift that is large enough to turn the transistor from an off state to an on state. This switch of state is then

communicated by the RFID chip in the digital information that is contained in the reflected RF signal.

To set the point of work of the unexposed device, a capacitance has been connected between gate and source and it has been charged with a programming voltage V_C as it is illustrated in **Figure 5.104**.

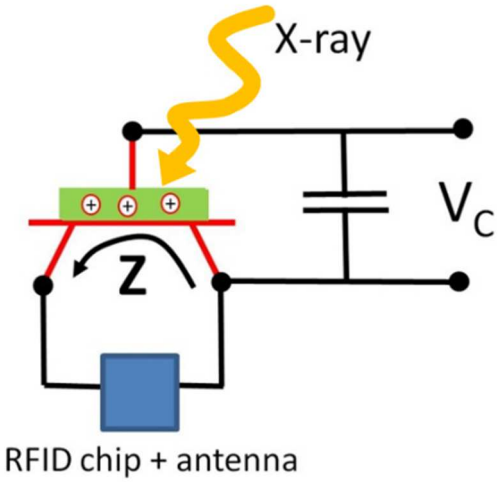

Figure 5.104 *Electrical circuit diagram showing how the radiation sensitive oxide TFT is connected to the commercial RFID sensor and how the programming voltage VC is applied* [245].

Figure 5.105 illustrates the impact of V_C on channel impedance at the relevant probing frequency of the RFID tag (1 kHz). At V_C values below 0 V, the channel is in the off state and the impedance is >20 MΩ, so the RFID tag remains in the off state (i.e. 0). Here, the impedance of the ROXFET in the off-state results mostly from the parasitic capacitance due to overlap between gate and source/drain electrodes rather than OFF current flowing in the semiconductor when the transistor is switched off. Moving to positive V_C values, charge carriers accumulate in the channel, the transistor turns on, and the impedance drops. Within an interval

of 0.6 V, the channel impedance lowers an order of magnitude down to <2 MΩ, and the RFID chip changes its memory status.

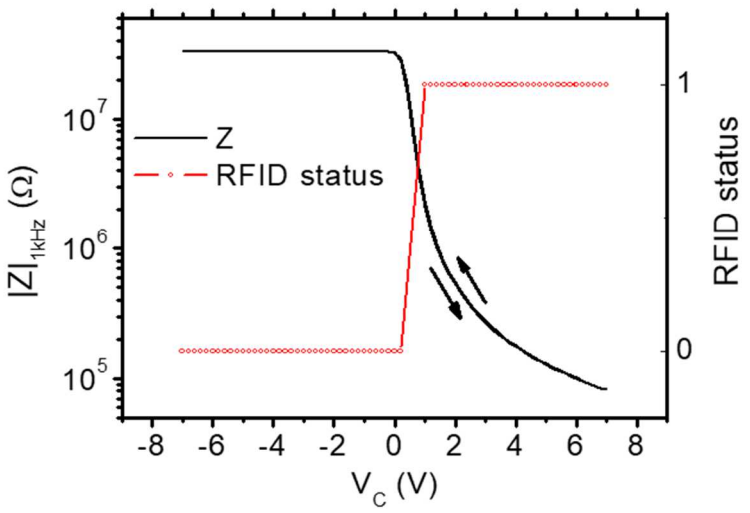

Figure 5.105 *TFT channel impedance Z as a function of V_C. The RFID switches its status in a narrow interval (i.e.0.6V) close to the turn-on voltage of the transistor when the impedance of the device drops down because of the creation of the conductive channel* [245].

Figure 5.106a shows how X-ray exposure affects channel impedance. Three dosimeter tags are compared, after being initially charged with different (negative) V_C voltages to program different X-ray threshold doses. In the initial states, all dosimeters are in the high-impedance state, and the impedance remains high and constant also after the voltage source used to program V_C is removed. This aspect is very important in order to demonstrate the possibility to operate the sensing system in passive mode and it has been possible thanks to the very low leakage current presented by the TFTs. At t = 0, the devices have been exposed to X-ray, and the impedances start to drop during exposure. The reduction in impedance continues until the X-ray exposure is stopped, as indicated by the arrows in the figure. Charging of the capacitance with the V_C voltage

allowed to program the X-ray threshold dose by controlling the impedance variation during X-ray exposure. In fact, because of the V_C voltage, an electric field builds up across the multilayer dielectric of the ROXFET. Before ionization charges can induce carrier accumulation in the channel by field effect causing the drop of the impedance, they have to compensate the V_C field. Accordingly, it is possible to observe that more negative V_C voltages require longer exposure times to sufficiently decrease the channel impedance for RFID status switching. Moreover, **Figure 5.106b** shows the dependence of the critical dose needed to switch the RFID state as a function of V_C voltage. The graph demonstrates that the ROXFET-based, passive RFID dosimeter allows to detect programmable threshold doses in the range of hundreds of milligrays.

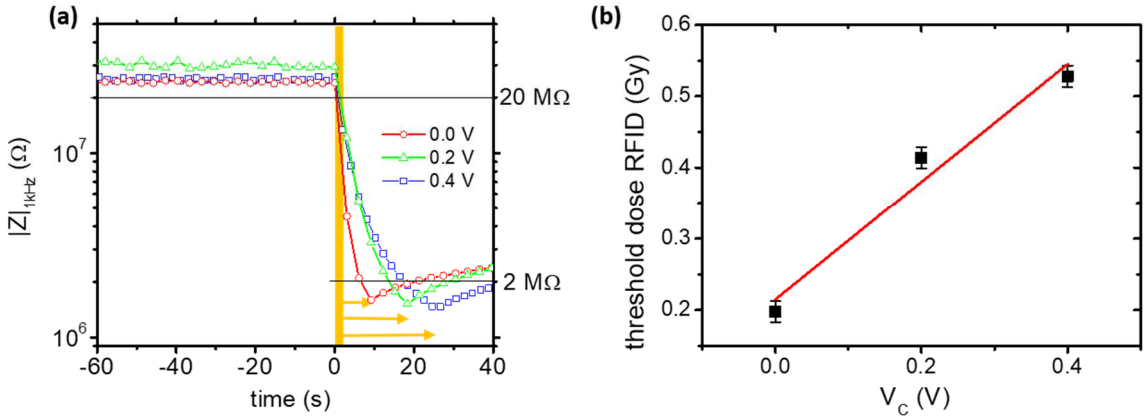

Figure 5.106 *Channel impedance Z as a function of time for different RFID programming voltages V_C. At time = 0, the sensor has been exposed to X-ray (30 mGy s^{-1}) for the indicated amount of time, leading to an order-of-magnitude decrease in Z and switching the RFID status. The amount of exposing time needed to achieve the switch depends on the programmed V_C. b) Threshold dose necessary to switch RFID status as a function of V_C.*

5.3. Gamma-ray detection

AOS TFTs have been investigated also under γ sources of Cd^{109} and Cs^{137} at the *Istituto Nazionale di Astrofisica* (INAF, CNR Bologna). The experimental setup and the activity of the sources have been described in **Section 3.7.3** while the sensor characterization followed the same procedure illustrated in the previous section. In particular, in this case the fast transfer characteristic has been acquired every five minutes.

Figure 5.107 shows the preliminary results about the threshold voltage shift caused by the absorption of gamma rays produced by (**a**) Cd^{109} and (**b**) Cs^{137} during twenty-five minutes of exposure. The clear shift of V_{th} towards negative values indicates that also in this range of energies the sensor is sensible and the RADFET effect is effective.

These represent only a proof of concept showing the potentiality of this class of sensors in order to be implemented also as gamma ray detectors but for a deeper and more quantitative interpretation of the results, further measurements are needed.

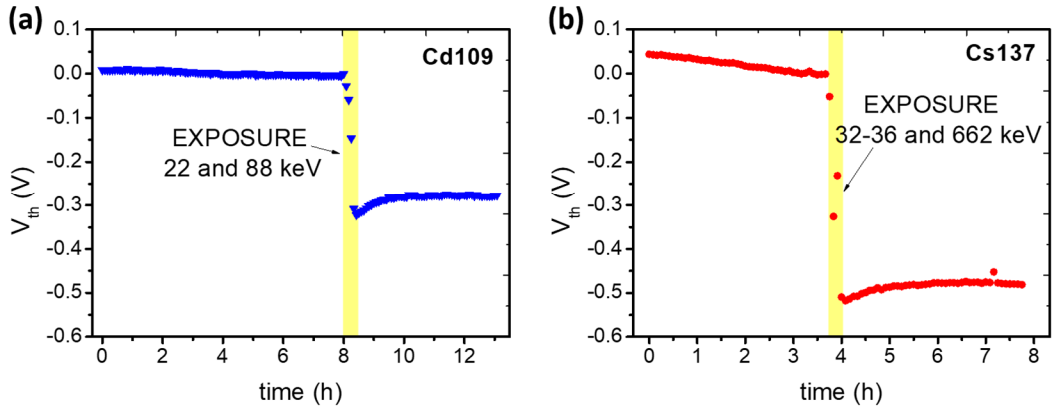

Figure 5.107 *Threshold voltage as a function of time during the exposure of the sensor to gamma rays produced by (a) Cd^{109} and (b) Cs^{137} sources kept at 1 cm from the TFT. The yellow boxes indicate the time interval during which the sample has been exposed (i.e. 25 minutes).*

Conclusions

In this thesis I researched and demonstrated the potential of thin film devices based on organic semiconductors and high mobility metal oxides to be employed as flexible and large area solid state ionizing radiation detectors. Both these classes of materials offer the possibility to be deposited by low cost and low temperature processes directly onto large area thin polymeric foils. It is shown and assessed how they are able to provide a reliable real-time detection of X-rays, gamma-rays and protons operating at very low voltages and in ambient conditions.

Ionizing radiation detectors based on organic semiconductors offer a unique property which is related to their chemical composition: the low-Z elements forming these materials render them human-tissue equivalent in terms of radiation absorption. This feature is very appealing for the development of sensing platforms for the direct and in-situ monitoring of dose delivery during medical diagnostic exams and radiation-based therapies. On the other side, this aspect makes the detection challenging because of the poor absorption of high energy radiation. In this work, I demonstrated several pathways to be implemented in order to boost the efficiency of these sensors maintaining the thin films architecture and thus the mechanical flexibility of the system. First, I demonstrated how, by exploiting the transistor structure it is possible to tune the detection response of the sensors acting on the polarization conditions. Second, a deep study of the mechanism of interaction between the X-rays and the organic semiconductors has been carried out to understand, model and control the photoconductive gain phenomenon which

rules the response of this class of sensors. Therefore, I analyzed and controlled the role of the active traps responsible for the amplification of the radiation induced signal. To this aim I investigated the impact of the grain boundaries present in organic semiconducting thin films and the impact of the organic semiconductor/dielectric interfaces. I exploited another unique property offered by organic materials which is the ease of tailoring of the molecular structure by chemical processes. This aspect leads to the possibility of introducing high-Z elements directly in the organic small molecule, thus s increasing the cross section of interaction between the high energy photons and the active layer of the sensors. Following this idea, I demonstrated the enhancement of the sensitivity to radiation due to the employment of novel synthetized organic small molecules where the silicon atoms have been substituted by germanium ones. The role and the impact of the charge transport properties of the electronic devices on their sensing capability has been studied. I demonstrated that the blending of the organic semiconductors with an insulating polymer (i.e. polystyrene) passivates hole traps at the interface with the dielectric layer, leading to an improvement of the electrical mobility of the transistors. This feature provided an increased charge collection which, in turn, provoked an enhancement of the sensors' sensitivities. Finally, exploiting an innovative deposition technique from solution (i.e. Pneumatic Nozzle Printing) performed at the Columbia University, it has been possible to fabricate highly performing detectors. This technique allows to deposit the organic semiconductors in a highly controlled way obtaining very aligned and very well packed microcrystalline structures.

Combining all these strategies I reached the record sensitivity values among the direct ionizing radiation detectors based on organic semiconductors both for rigid ($S = 1.3 \cdot 10^4$ µC $Gy^{-1}cm^{-2}$) and flexible ($S = 7.1 \cdot 10^2$ µC $Gy^{-1}cm^{-2}$) substrates. These

performances are comparable or even higher than the results reported in the literature for direct hybrid radiation detectors based on thin and thick layers of perovskites, another class of very promising semiconducting materials for photovoltaics and radiation detection devices.

The promising performances demonstrated by this novel class of direct ionizing radiation detectors have been assessed in actual medical environments. In particular, in this thesis I report the results achieved testing real X-rays sources employed in the field of dental radiography. Here, the detectors are typically irradiated by very short pulses of radiation (i.e. 100 ms) at the typical doses employed during this kind of diagnostic exams (i.e. few tens of µGy) and the detectors fabricated and characterized in this research work responded linearly with the increase of the radiation dose.

Organic semiconducting-based devices have been tested also for the detection of proton beams (5 MeV and 70 MeV) These values are of interest for proton therapy applications, the lower energy corresponding to the typical energy of the end of range of the accelerated ions while the latter is the energy of the primary beam. Ionizing radiation detectors based on organic semiconductors demonstrated to properly operate both as real-time and as integrator dosimeter, exploiting the coupling of the device with the plastic substrate.

Ionizing radiation detectors based on metal oxides have been fabricated and characterized, following a novel device concept and geometry, that we labeled ROXFET (radiation-sensitive oxide semiconductor Field Effect Transistor) and that overcomes the main drawbacks of the standard RADFET (radiation-sensitive Field Effect Transistor) sensors. In fact, by employing the amorphous high mobility oxide semiconductors (i.e. a-IGZO) instead of silicon in the CMOS technology it

has been possible to fabricate flexible devices scalable onto large area, still keeping excellent performances in terms of transport properties. On the other side, the implementation of a stacked multilayer dielectric formed by SiO_2 and Ta_2O_5 allowed to improve the absorption rate of the high energy photons leading to an outperforming sensitivity S = (3.4 ± 0.2) V Gy^{-1}, one order of magnitude higher than the typical value reported for the standard CMOS RADFETs. A proof of principle for the detection of gamma-rays by this class of sensors has been provided. This ROXFET sensing concept offers the additional possibility of coupling the detector with a wireless readout system based on a passive RFID chip, very interesting for a fully passive monitoring of received radiation dose.

Bibliography

[1] W. S. Wong and A. Salleo, *Flexible Electronics - Materials and Applications*, vol. 53, no. 9. Springer International Publishing, 2009.

[2] A. You, M. A. Y. Be, and I. In, "Schottky-barrier characteristics of metal – amorphous-silicon diodes," *Appl. Phys. Lett.*, vol. 602, no. August 2008, 1976.

[3] H. Okaniwa, K. Nakatani, M. Yano, M. Asano, and K. Suzuki, "Preparation and properties of a-si: H solar cells on organic polymer film substrate," *Jpn. J. Appl. Phys.*, vol. 21, no. S2, pp. 239–244, 1982.

[4] P. M. Smith, P. G. Carey, and T. W. Sigmon, "Excimer laser crystallization and doping of silicon films on plastic substrates," *Appl. Phys. Lett.*, vol. 70, no. 3, pp. 342–344, 1997.

[5] N. D. Young, G. Harkin, R. M. Bunn, D. J. Mcculloch, R. W. Wilks, and A. G. Knapp, "Polysilicon TFT ' s on Glass and Polymer Substrates," *IEEE Electron Device Lett.*, vol. 18, no. 1, pp. 19–20, 1997.

[6] S. J. Kim, K. Choi, B. Lee, Y. Kim, and B. H. Hong, "Materials for Flexible, Stretchable Electronics: Graphene and 2D Materials," *Annu. Rev. Mater. Res.*, vol. 45, no. 1, pp. 63–84, 2015.

[7] S. Park, M. Vosguerichian, and Z. Bao, "A review of fabrication and applications of carbon nanotube film-based flexible electronics," *Nanoscale*, vol. 5, no. 5. The Royal Society of Chemistry, pp. 1727–1752, 07-Mar-2013.

[8] L. Xiang, H. Zhang, Y. Hu, and L. M. Peng, "Carbon nanotube-based flexible electronics," *Journal of Materials Chemistry C*, vol. 6, no. 29. Royal Society of Chemistry, pp. 7714–7727, 26-Jul-2018.

[9] M. Kaltenbrunner *et al.*, "Flexible high power-per-weight perovskite solar cells with chromium oxide-metal contacts for improved stability in air," *Nat. Mater.*, vol. 14, no. 10, pp. 1032–1039, Oct. 2015.

[10] M. Caironi and N. Yong-Young, *Large Area and Flexible Electronics*. Wiley-VCH Verlag, 2015.

[11] J. Liu *et al.*, "Flexible, Printable Soft-X-Ray Detectors Based on All-Inorganic Perovskite Quantum Dots," *Adv. Mater.*, vol. 31, no. 30, p. 1901644, Jun. 2019.

[12] H. Mescher *et al.*, "Flexible Inkjet-Printed Triple Cation Perovskite X-ray Detectors," *ACS Appl. Mater. Interfaces*, vol. 12, no. 13, pp. 15774–15784, Apr. 2020.

[13] J. Zhao *et al.*, "Perovskite-filled membranes for flexible and large-area direct-conversion X-ray detector arrays," *Nat. Photonics*, vol. 14, no. 10, pp. 612–617, Oct. 2020.

[14] S. Demchyshyn *et al.*, “Designing Ultraflexible Perovskite X-Ray Detectors through Interface Engineering,” *Adv. Sci.*, p. 2002586, Nov. 2020.

[15] V. Pecunia, A. Sahel, S. Henning, and C. Eugenio, *Organic and Oxide Flexible Analogue Electronics*, vol. 4015, no. May. Cambridge University Press, 2018.

[16] I. Kymissis, *Organic Field Effect Transistors Theory , Fabrication and Characterization*. 2009.

[17] S. R. Forrest, “Electronic Appliances on Plastic,” *Nature*, vol. 428, no. 6986, pp. 911–918, 2004.

[18] H. Bronstein, C. B. Nielsen, B. C. Schroeder, and I. McCulloch, “The role of chemical design in the performance of organic semiconductors,” *Nature Reviews Chemistry*, vol. 4, no. 2. Nature Research, pp. 66–77, 01-Feb-2020.

[19] V. Coropceanu, J. Cornil, D. A. da Silva Filho, Y. Olivier, R. Silbey, and J. L. Brédas, “Charge transport in organic semiconductors,” *Chemical Reviews*, vol. 107, no. 4. American Chemical Society , pp. 926–952, Apr-2007.

[20] Ian Fleming, *Molecular Orbitals and Organic Chemical Reactions*. 2010.

[21] S. Fratini, M. Nikolka, A. Salleo, G. Schweicher, and H. Sirringhaus, “Charge transport in high-mobility conjugated polymers and molecular semiconductors,” *Nat. Mater.*, vol. 19, no. 5, pp. 491–502, 2020.

[22] N. Tessler, Y. Preezant, N. Rappaport, and Y. Roichman, “Charge transport in disordered organic materials and its relevance to thin-film devices: A tutorial review,” *Adv. Mater.*, vol. 21, no. 27, pp. 2741–2761, 2009.

[23] G. Horowitz, “Organic Field-Effect Transistors,” *Adv. Mat.*, 1998. [Online]. Available: https://onlinelibrary.wiley.com/doi/epdf/10.1002/%28SICI%291521-4095%28199803%2910%3A5%3C365%3A%3AAID-ADMA365%3E3.0.CO%3B2-U. [Accessed: 05-Aug-2020].

[24] H. Sirringhaus, “Device physics of solution-processed organic field-effect transistors,” *Adv. Mater.*, vol. 17, no. 20, pp. 2411–2425, 2005.

[25] C. D. Dimitrakopoulos and P. R. L. Malenfant, “Organic thin film transistors for large area electronics,” *Adv. Mater.*, vol. 14, no. 2, pp. 99–117, 2002.

[26] Ana Kohler and Heinz Bassler, *Electronic Processes in Organic Semiconductors*. 2015.

[27] N. F. Mott, “ON THE TRANSITION TO METALLIC CONDUCTION IN SEMICONDUCTORS,” *Can. J. Phys.*, vol. 34, no. 12A, pp. 1356–1368, Dec. 1956.

[28] E. M. Conwell, “Impurity band conduction in germanium and silicon,” *Phys. Rev.*, vol. 103, no. 1, pp. 51–61, Jul. 1956.

[29] A. Miller and E. Abrahams, “Impurity conduction at low concentrations,” *Phys. Rev.*, vol. 120, no. 3, pp. 745–755, Nov. 1960.

[30] W. Warta and N. Karl, “Hot holes in naphthalene: High, electric-field-dependent mobilities,” *Phys. Rev. B*, vol. 32, no. 2, pp. 1172–1182, Jul. 1985.

[31] T. Holstein, “Studies of polaron motion. Part I. The molecular-crystal model,” *Ann. Phys. (N. Y).*, vol. 8, no. 3, pp. 325–342, Nov. 1959.

[32] S. Verlaak, V. Arkhipov, and P. Heremans, “Modeling of transport in polycrystalline organic semiconductor films,” *Appl. Phys. Lett.*, vol. 82, no. 5, pp. 745–747, Feb. 2003.

[33] G. Horowitz, R. Hajlaoui, and P. Delannoy, “Temperature Dependence of the Field-Effect Mobility of Sexithiophene. Determination of the Density of Traps,” *J. Phys. III*, vol. 5, no. 4, pp. 355–371, Apr. 1995.

[34] G. Horowitz and M. E. Hajlaoui, “Mobility in polycrystalline oligothiophene field-effect transistors dependent on grain size,” *Adv. Mater.*, vol. 12, no. 14, pp. 1046–1050, Jul. 2000.

[35] Y. Diao, L. Shaw, Z. Bao, and S. C. B. Mannsfeld, “Morphology control strategies for solution-processed organic semiconductor thin films,” 2014.

[36] C.-H. Kim *et al.*, “Strongly Correlated Alignment of Fluorinated 5,11-Bis(triethylgermylethynyl)anthradithiophene Crystallites in Solution-Processed Field-Effect Transistors,” *ChemPhysChem*, vol. 15, no. 14, pp. 2913–2916, Oct. 2014.

[37] M. M. Payne, S. R. Parkin, J. E. Anthony, C. C. Kuo, and T. N. Jackson, “Organic field-effect transistors from solution-deposited functionalized acenes with mobilities as high as 1 cm2/V · s,” *J. Am. Chem. Soc.*, vol. 127, no. 14, pp. 4986–4987, 2005.

[38] A. F. Paterson *et al.*, “Recent Progress in High-Mobility Organic Transistors: A Reality Check,” *Adv. Mater.*, vol. 30, no. 36, pp. 1–33, 2018.

[39] Z. A. Lamport *et al.*, “A simple and robust approach to reducing contact resistance in organic transistors,” *Nat. Commun.*, vol. 9, no. 1, 2018.

[40] J. Panidi *et al.*, “Remarkable Enhancement of the Hole Mobility in Several Organic Small-Molecules, Polymers, and Small-Molecule:Polymer Blend Transistors by Simple Admixing of the Lewis Acid p-Dopant B(C $_6$ F $_5$) $_3$,” *Adv. Sci.*, vol. 5, no. 1, p. 1700290, Jan. 2018.

[41] Y. Xu, C. Liu, D. Khim, and Y. Y. Noh, “Development of high-performance printed organic field-effect transistors and integrated circuits,” *Phys. Chem. Chem. Phys.*, vol. 17, no. 40, pp. 26553–26574, Oct. 2015.

[42] H. Sun, Q. Wang, J. Qian, Y. Yin, Y. Shi, and Y. Li, “Unidirectional coating technology for organic field-effect transistors: Materials and methods,” *Semicond. Sci. Technol.*, vol. 30, no. 5, pp. 1–17, May 2015.

[43] Z. A. Lamport, H. F. Haneef, S. Anand, M. Waldrip, and O. D. Jurchescu, “Tutorial: Organic field-effect transistors: Materials, structure and operation,” *J. Appl. Phys.*, vol. 124, no. 7, Aug. 2018.

[44] P. J. Diemer *et al.*, “Vibration-Assisted Crystallization Improves Organic/Dielectric

Interface in Organic Thin-Film Transistors," *Adv. Mater.*, vol. 25, no. 48, pp. 6956–6962, Dec. 2013.

[45] Y. Mei *et al.*, "High Mobility Field-Effect Transistors with Versatile Processing from a Small-Molecule Organic Semiconductor," *Adv. Mater.*, vol. 25, no. 31, pp. 4352–4357, Aug. 2013.

[46] O. Goto *et al.*, "Organic Single-Crystal Arrays from Solution-Phase Growth Using Micropattern with Nucleation Control Region," *Adv. Mater.*, vol. 24, no. 8, pp. 1117–1122, Feb. 2012.

[47] Y. Yuan *et al.*, "Ultra-high mobility transparent organic thin film transistors grown by an off-centre spin-coating method," *Nat. Commun.*, vol. 5, Jan. 2014.

[48] S. Galindo, A. Tamayo, F. Leonardi, and M. Mas-Torrent, "Control of Polymorphism and Morphology in Solution Sheared Organic Field-Effect Transistors," *Adv. Funct. Mater.*, vol. 27, no. 25, pp. 1–9, 2017.

[49] J. Jang *et al.*, "Highly crystalline soluble acene crystal arrays for organic transistors: Mechanism of crystal growth during dip-coating," *Adv. Funct. Mater.*, vol. 22, no. 5, pp. 1005–1014, Mar. 2012.

[50] R. R. Søndergaard, M. Hösel, and F. C. Krebs, "Roll-to-Roll fabrication of large area functional organic materials," *Journal of Polymer Science, Part B: Polymer Physics*, vol. 51, no. 1. John Wiley & Sons, Ltd, pp. 16–34, 01-Jan-2013.

[51] F. G. del Pozo *et al.*, "Single Crystal-Like Performance in Solution-Coated Thin-Film Organic Field-Effect Transistors," *Adv. Funct. Mater.*, vol. 26, no. 14, pp. 2379–2386, Apr. 2016.

[52] I. Temiño, F. G. Del Pozo, M. R. Ajayakumar, S. Galindo, J. Puigdollers, and M. Mas-Torrent, "A Rapid, Low-Cost, and Scalable Technique for Printing State-of-the-Art Organic Field-Effect Transistors," *Adv. Mater. Technol.*, vol. 1, no. 5, p. 1600090, Aug. 2016.

[53] S. Yang, S. Park, J. Bintinger, Y. Bonnassieux, and I. Kymissis, "P-99: Pneumatic Nozzle Printing as a Versatile Approach to Crystal Growth Management and Patterning of Printed Organic Thin Film Transistors," *SID Symp. Dig. Tech. Pap.*, vol. 47, no. 1, pp. 1502–1505, May 2016.

[54] C. Koutsiaki *et al.*, "Efficient combination of Roll-to-Roll compatible techniques towards the large area deposition of a polymer dielectric film and the solution-processing of an organic semiconductor for the field-effect transistors fabrication on plastic substrate," *Org. Electron.*, vol. 73, pp. 231–239, Oct. 2019.

[55] H. F. Haneef, A. M. Zeidell, and O. D. Jurchescu, "Charge carrier traps in organic semiconductors: a review on the underlying physics and impact on electronic devices," *J. Mater. Chem. C*, vol. 8, p. 759, 2020.

[56] H. H. Choi *et al.*, "Hall Effect in Polycrystalline Organic Semiconductors: The Effect of

Grain Boundaries," *Adv. Funct. Mater.*, vol. 30, no. 20, pp. 1–11, 2020.

[57] D. Natali and M. Caironi, "Charge injection in solution-processed organic field-effect transistors: Physics, models and characterization methods," *Advanced Materials*, vol. 24, no. 11. John Wiley & Sons, Ltd, pp. 1357–1387, 15-Mar-2012.

[58] T. Kamiya and H. Hosono, "Material characteristics and applications of transparent amorphous oxide semiconductors," *NPG Asia Mater.*, vol. 2, no. 1, pp. 15–22, 2010.

[59] T. Kamiya, K. Nomura, and H. Hosono, "Origins of High Mobility and Low Operation Voltage of Amorphous Oxide TFTs: Electronic Structure, Electron Transport, Defects and Doping*," *J. Disp. Technol.*, vol. 5, no. 12, pp. 468–483, 2009.

[60] T. Kamiya, K. Nomura, and H. Hosono, "Present status of amorphous In-Ga-Zn-O thin-film transistors," *Sci. Technol. Adv. Mater.*, vol. 11, no. 4, 2010.

[61] D. Adler, L. P. Flora, and S. D. Senturia, "Electrical conductivity in disordered systems," *Solid State Commun.*, vol. 12, no. 1, pp. 9–12, Jan. 1973.

[62] K. Ide, K. Nomura, H. Hosono, and T. Kamiya, "Electronic Defects in Amorphous Oxide Semiconductors: A Review," *Phys. status solidi*, vol. 216, no. 5, p. 1800372, Mar. 2019.

[63] T. Kamiya, K. Nomura, and H. Hosono, "Present status of amorphous In-Ga-Zn-O thin-film transistors," *Science and Technology of Advanced Materials*, vol. 11, no. 4. Taylor & Francis, Aug-2010.

[64] R. F. P. Martins *et al.*, "Recyclable, flexible, low-power oxide electronics," *Adv. Funct. Mater.*, vol. 23, no. 17, pp. 2153–2161, 2013.

[65] E. Fortunato, P. Barquinha, and R. Martins, "Oxide Semiconductor Thin-Film Transistors: A Review of Recent Advances," *Adv. Mater.*, vol. 24, no. 22, pp. 2945–2986, Jun. 2012.

[66] C. Fernandes *et al.*, "A sustainable approach to flexible electronics with zinc-tin oxide thin-film transistors," *Adv. Electron. Mater*, vol. 1800032, pp. 1–10, 2018.

[67] H. Yanagi, Y. Koyamaishi, C. Sato, and Y. Kimura, "Transparent semiconducting amorphous cadmium-gallium-Tin oxide films by magnetron sputtering with water vapor," *Appl. Phys. Lett.*, vol. 110, no. 25, p. 252107, Jun. 2017.

[68] L. Prušáková, P. Hubík, A. Aijaz, T. Nyberg, and T. Kubart, "Room Temperature Reactive Deposition of InGaZnO and ZnSnO Amorphous Oxide Semiconductors for Flexible Electronics," *Coatings*, vol. 10, no. 1, p. 2, Dec. 2019.

[69] K. Ellmer, "Magnetron sputtering of transparent conductive zinc oxide: Relation between the sputtering parameters and the electronic properties," *J. Phys. D. Appl. Phys.*, vol. 33, no. 4, p. R17, Feb. 2000.

[70] J. W. Park, B. H. Kang, and H. J. Kim, "A Review of Low-Temperature Solution-Processed Metal Oxide Thin-Film Transistors for Flexible Electronics," *Adv. Funct. Mater.*, vol. 30, no. 20, pp. 1–40, 2020.

[71] S. J. Kim, S. Yoon, and H. J. Kim, "Review of solution-processed oxide thin-film transistors," *Jpn. J. Appl. Phys.*, vol. 53, 2014.

[72] J. Socratous *et al.*, "Electronic structure of low-temperature solution-processed amorphous metal oxide semiconductors for thin-film transistor applications," *Adv. Funct. Mater.*, vol. 25, no. 12, pp. 1873–1885, 2015.

[73] B. Park *et al.*, "Solution-Processed Rad-Hard Amorphous Metal-Oxide Thin-Film Transistors," *Adv. Funct. Mater.*, vol. 28, no. 47, pp. 1–11, 2018.

[74] Q. Li *et al.*, "Review of printed electrodes for flexible devices," *Front. Mater.*, vol. 5, no. January, pp. 1–14, 2019.

[75] A. Nathan *et al.*, "Flexible electronics: The next ubiquitous platform," *Proc. IEEE*, vol. 100, no. SPL CONTENT, pp. 1486–1517, 2012.

[76] J. W. Ward *et al.*, "Solution-Processed Organic and Halide Perovskite Transistors on Hydrophobic Surfaces," *ACS Appl. Mater. Interfaces*, vol. 9, no. 21, pp. 18120–18126, May 2017.

[77] D. Braga and G. Horowitz, "High-Performance organic field-effect transistors," *Adv. Mater.*, vol. 21, no. 14–15, pp. 1473–1486, 2009.

[78] M. Kim *et al.*, "Donor–Acceptor-Conjugated Polymer for High-Performance Organic Field-Effect Transistors: A Progress Report," *Adv. Funct. Mater.*, vol. 30, no. 20, pp. 1–25, 2020.

[79] K. Nomura, H. Ohta, K. Ueda, T. Kamiya, M. Hirano, and H. Hosono, "Thin-film transistor fabricated in single-crystalline transparent oxide semiconductor," *Science (80-.).*, vol. 300, no. 5623, pp. 1269–1272, 2003.

[80] K. Nomura, H. Ohta, A. Takagi, T. Kamiya, M. Hirano, and H. Hosono, "Room-temperature fabrication of transparent flexible thin-film transistors using amorphous oxide semiconductors," *Nature*, vol. 432, no. 7016, pp. 488–492, Nov. 2004.

[81] P. G. Bahubalindruni *et al.*, "Influence of Channel Length Scaling on InGaZnO TFTs Characteristics: Unity Current-Gain Cutoff Frequency, Intrinsic Voltage-Gain, and On-Resistance," *J. Disp. Technol.*, vol. 12, no. 6, pp. 515–518, Jun. 2016.

[82] R. Barros *et al.*, "Role of Structure and Composition on the Performances of P-Type Tin Oxide Thin-Film Transistors Processed at Low-Temperatures," *Nanomaterials*, vol. 9, no. 3, p. 320, Mar. 2019.

[83] Y. Kuo, "Thin film transistor technology-Past, present, and future," *Electrochem. Soc. Interface*, vol. 22, no. 1, pp. 55–61, 2013.

[84] D. Kang *et al.*, "Amorphous gallium indium zinc oxide thin film transistors: Sensitive to oxygen molecules," *Appl. Phys. Lett.*, vol. 90, no. 19, pp. 4–7, 2007.

[85] J. S. Park, W. J. Maeng, H. S. Kim, and J. S. Park, "Review of recent developments in amorphous oxide semiconductor thin-film transistor devices," *Thin Solid Films*, vol. 520,

no. 6, pp. 1679–1693, 2012.

[86] J. Sheng, H.-J. Jeong, K.-L. Han, T. Hong, and J.-S. Park, "Review of recent advances in flexible oxide semiconductor thin-film transistors," *J. Inf. Disp.*, vol. 18, no. 4, pp. 159–172, Oct. 2017.

[87] H. I. Un, J. Y. Wang, and J. Pei, "Recent Efforts in Understanding and Improving the Nonideal Behaviors of Organic Field-Effect Transistors," *Adv. Sci.*, vol. 6, no. 20, 2019.

[88] T. Yang *et al.*, "Understanding, Optimizing, and Utilizing Nonideal Transistors Based on Organic or Organic Hybrid Semiconductors," *Adv. Funct. Mater.*, vol. 30, no. 20, pp. 1–39, 2020.

[89] G. Horowitz, R. Hajlaoui, H. Bouchriha, R. Bourguiga, and M. Hajlaoui, "Concept of `threshold voltage' in organic field-effect transistors," *Adv. Mater.*, vol. 10, no. 12, pp. 923–927, Jan. 1998.

[90] X. Jia, C. Fuentes-Hernandez, C. Y. Wang, Y. Park, and B. Kippelen, "Stable organic thin-film transistors," *Sci. Adv.*, vol. 4, no. 1, p. eaao1705, Jan. 2018.

[91] P. J. Diemer *et al.*, "Vibration-Assisted Crystallization Improves Organic/Dielectric Interface in Organic Thin-Film Transistors," *Adv. Mater.*, vol. 25, no. 48, pp. 6956–6962, Dec. 2013.

[92] Y. H. Noh, S. Young Park, S. M. Seo, and H. H. Lee, "Root cause of hysteresis in organic thin film transistor with polymer dielectric," *Org. Electron.*, vol. 7, no. 5, pp. 271–275, Oct. 2006.

[93] T. D. Anthopoulos, Y. Y. Noh, and O. D. Jurchescu, "Emerging Thin-Film Transistor Technologies and Applications," *Adv. Funct. Mater.*, vol. 30, no. 20, pp. 1–2, 2020.

[94] H. Kleemann, K. Krechan, A. Fischer, and K. Leo, "A Review of Vertical Organic Transistors," *Adv. Funct. Mater.*, vol. 30, no. 20, 2020.

[95] Y. Wakayama and R. Hayakawa, "Antiambipolar Transistor: A Newcomer for Future Flexible Electronics," *Adv. Funct. Mater.*, vol. 30, no. 20, pp. 1–11, 2020.

[96] S. Lai, F. Antonio Viola, P. Cosseddu, and A. Bonfiglio, "Floating Gate, Organic Field-Effect Transistor-Based Sensors towards Biomedical Applications Fabricated with Large-Area Processes over Flexible Substrates," 2018.

[97] F. A. Viola, A. Spanu, P. C. Ricci, A. Bonfiglio, and P. Cosseddu, "Ultrathin, flexible and multimodal tactile sensors based on organic field-effect transistors," *Sci. Rep.*, vol. 8, no. 1, pp. 1–8, 2018.

[98] G. Casula, S. Lai, L. Matino, F. Santoro, A. Bonfiglio, and P. Cosseddu, "Printed, Low-Voltage, All-Organic Transistors and Complementary Circuits on Paper Substrate," *Adv. Electron. Mater.*, vol. 6, no. 5, pp. 1–9, 2020.

[99] G. E. Bonacchini *et al.*, "Tattoo-Paper Transfer as a Versatile Platform for All-Printed Organic Edible Electronics," *Adv. Mater.*, vol. 30, no. 14, pp. 1–8, 2018.

[100] H. Matsui, Y. Takeda, and S. Tokito, "Flexible and printed organic transistors: From materials to integrated circuits," *Organic Electronics*, vol. 75. Elsevier B.V., p. 105432, 01-Dec-2019.

[101] S. Lai *et al.*, "Morphology Influence on the Mechanical Stress Response in Bendable Organic Field-Effect Transistors with Solution-Processed Semiconductors," *Adv. Electron. Mater.*, vol. 4, no. 10, p. 1700271, Oct. 2018.

[102] S. Duan *et al.*, "Solution-Processed Centimeter-Scale Highly Aligned Organic Crystalline Arrays for High-Performance Organic Field-Effect Transistors," *Adv. Mater.*, vol. 32, no. 12, pp. 1–8, 2020.

[103] J. Sheng, H.-J. Jeong, K.-L. Han, T. Hong, and J.-S. Park, "Review of recent advances in flexible oxide semiconductor thin-film transistors," *J. Inf. Disp.*, vol. 18, no. 4, pp. 159–172, Oct. 2017.

[104] Y. H. Kim, E. Lee, J. G. Um, M. Mativenga, and J. Jang, "Highly robust neutral plane oxide TFTs withstanding 0.25mm bending radius for stretchable electronics," *Sci. Rep.*, vol. 6, no. May, pp. 1–8, 2016.

[105] Y. S. Rim *et al.*, "Printable Ultrathin Metal Oxide Semiconductor-Based Conformal Biosensors," *ACS Nano*, vol. 9, no. 12, pp. 12174–12181, Oct. 2015.

[106] G. Han, S. Cao, Q. Yang, W. Yang, T. Guo, and H. Chen, "High-Performance All-Solution-Processed Flexible Photodetector Arrays Based on Ultrashort Channel Amorphous Oxide Semiconductor Transistors," *ACS Appl. Mater. Interfaces*, vol. 10, no. 47, pp. 40631–40640, Nov. 2018.

[107] Y. S. Rim *et al.*, "Ultrahigh and Broad Spectral Photodetectivity of an Organic-Inorganic Hybrid Phototransistor for Flexible Electronics," *Adv. Mater.*, vol. 27, no. 43, pp. 6885–6891, Nov. 2015.

[108] G. F. Knoll, *Radiation Detection and Measuremnt*. John Wiley & Sons, Inc., 1980.

[109] S. Mobilio, F. Boscherini, and C. Menenghini, *Synchrotron Radiation. Basics, Methods and Applications*. Springer, 2015.

[110] J. Als-Nielsen and D. McMorrow, *Elements of Modern X-ray Physics: Second Edition*. Wiley, 2011.

[111] F. B. Dunning and R. G. Hulet, *Atomic, Molecular, and Optical Physics: Charged Particles*. Academic Press, 1995.

[112] R. D. Evans, *The Atomic Nucleus*. McGraw-Hill Book Company, 1955.

[113] H. Paganetti, *Proton Therapy Physics*. CRC Press, 2012.

[114] W. R. Leo, *Nuclear and Particle A How-to Approach*. Springer, 1994.

[115] O. Desouky and G. Zhou, "Biophysical and radiobiological aspects of heavy charged particles," *J. Taibah Univ. Sci.*, vol. 10, no. 2, pp. 187–194, Apr. 2016.

[116] E. B. Podgorsac, *Review of Radiation Oncology Physics: A Handbook for Teachers and Students*. International Atomic Energy Agency, 2005.

[117] A. Ciavatti, "Transport Properties and Novel Sensing Applications of Organic Semiconducting Crystals," University of Bologna.

[118] ICRP, "1990 Recommendations of the International Commission on Radiological Protection," *Pergamon Press*, vol. ICRP Pubbl, 1991.

[119] A. Mirzaei, J. S. Huh, S. S. Kim, and H. W. Kim, "Room Temperature Hard Radiation Detectors Based on Solid State Compound Semiconductors: An Overview," *Electronic Materials Letters*, vol. 14, no. 3. The Korean Institute of Metals and Materials, pp. 261–287, 01-May-2018.

[120] J. Seco, B. Clasie, and M. Partridge, "Review on the characteristics of radiation detectors for dosimetry and imaging," *Phys. Med. Biol.*, vol. 59, no. 20, pp. R303–R347, 2014.

[121] B. Fraboni, A. Ciavatti, L. Basiricò, and A. Fraleoni-Morgera, "Organic semiconducting single crystals as solid-state sensors for ionizing radiation," *Faraday Discuss.*, vol. 174, no. 0, pp. 219–234, Sep. 2014.

[122] S. Kasap *et al.*, "Amorphous and polycrystalline photoconductors for direct conversion flat panel x-ray image sensors," *Sensors*, vol. 11, no. 5. pp. 5112–5157, May-2011.

[123] L. Basiricò, A. Ciavatti, and B. Fraboni, "Solution-Grown Organic and Perovskite X-Ray Detectors: A New Paradigm for the Direct Detection of Ionizing Radiation," *Adv. Mater. Technol.*, vol. 2000475, 2020.

[124] M. Z. Kabir and S. Kasap, "Photoconductors for X-Ray Image Detectors," *Springer Handb. Electron. Photonic Mater.*, pp. 1125–1147, 2017.

[125] I. Clairand *et al.*, "Use of active personal dosemeters in interventional radiology and cardiology: Tests in laboratory conditions and recommendations - ORAMED project," in *Radiation Measurements*, 2011, vol. 46, no. 11, pp. 1252–1257.

[126] M. Bruzzi, C. Talamonti, N. Calisi, S. Caporali, and A. Vinattieri, "First proof-of-principle of inorganic perovskites clinical radiotherapy dosimeters ARTICLES YOU MAY BE INTERESTED IN First proof-of-principle of inorganic perovskites clinical radiotherapy dosimeters," vol. 7, p. 51101, 2019.

[127] M. Thompson, S. L. R. Ellison, and R. Wood, "Harmonized guidelines for single-laboratory validation of methods of analysis (IUPAC Technical Report)," *Pure Appl. Chem.*, vol. 74, no. 5, pp. 835–855, Jan. 2002.

[128] F. Chen *et al.*, "Direct-conversion X-ray detector using lateral amorphous selenium structure," *IEEE Sens. J.*, vol. 11, no. 2, pp. 505–509, 2011.

[129] A. Owens and A. Peacock, "Compound semiconductor radiation detectors," in *Nuclear Instruments and Methods in Physics Research, Section A: Accelerators, Spectrometers, Detectors and Associated Equipment*, 2004, vol. 531, no. 1–2, pp. 18–37.

[130] W. Zhao and J. A. Rowlands, "X-ray imaging using amorphous selenium: Feasibility of a flat panel self-scanned detector for digital radiology," *Med. Phys.*, vol. 22, no. 10, pp. 1595–1604, Oct. 1995.

[131] S. Yakunin *et al.*, "Detection of X-ray photons by solution-processed lead halide perovskites," *Nat. Photonics*, vol. 9, no. 7, pp. 444–449, 2015.

[132] M. Hu *et al.*, "Large and Dense Organic-Inorganic Hybrid Perovskite CH3NH3PbI3 Wafer Fabricated by One-Step Reactive Direct Wafer Production with High X-ray Sensitivity," *ACS Appl. Mater. Interfaces*, vol. 12, no. 14, pp. 16592–16600, Apr. 2020.

[133] M. J. Griffith, S. Cottam, J. Stamenkovic, J. A. Posar, and M. Petasecca, "Printable Organic Semiconductors for Radiation Detection: From Fundamentals to Fabrication and Functionality," *Front. Phys.*, vol. 8, no. March, pp. 1–21, 2020.

[134] B. Fraboni *et al.*, "Organic Semiconducting Single Crystals as Next Generation of Low-Cost, Room-Temperature Electrical X-ray Detectors," *Adv. Mater.*, vol. 24, no. 17, pp. 2289–2293, May 2012.

[135] A. Ciavatti *et al.*, "Toward Low-Voltage and Bendable X-Ray Direct Detectors Based on Organic Semiconducting Single Crystals," *Adv. Mater.*, vol. 27, no. 44, pp. 7213–7220, Nov. 2015.

[136] L. Basirico *et al.*, "Solid State Organic X-Ray Detectors Based on Rubrene Single Crystals," *IEEE Trans. Nucl. Sci.*, vol. 62, no. 4, pp. 1791–1797, 2015.

[137] G. Pipan *et al.*, "Direct Inkjet Printing of TIPS-Pentacene Single Crystals onto Interdigitated Electrodes by Chemical Confinement," *Adv. Mater. Interfaces*, vol. 5, no. 3, p. 1700925, Feb. 2018.

[138] F. A. Boroumand, M. Zhu, A. B. Dalton, J. L. Keddie, P. J. Sellin, and J. J. Gutierrez, "Direct x-ray detection with conjugated polymer devices," *Appl. Phys. Lett.*, vol. 91, no. 3, p. 033509, Jul. 2007.

[139] A. Intaniwet, C. A. Mills, M. Shkunov, H. Thiem, J. L. Keddie, and P. J. Sellin, "Characterization of thick film poly(triarylamine) semiconductor diodes for direct x-ray detection," *J. Appl. Phys.*, vol. 106, no. 6, p. 064513, Sep. 2009.

[140] A. Intaniwet, C. A. Mills, P. J. Sellin, M. Shkunov, and J. L. Keddie, "Achieving a stable time response in polymeric radiation sensors under charge injection by X-rays," *ACS Appl. Mater. Interfaces*, vol. 2, no. 6, pp. 1692–1699, Jun. 2010.

[141] A. Intaniwet, C. A. Mills, M. Shkunov, P. J. Sellin, and J. L. Keddie, "Heavy metallic oxide nanoparticles for enhanced sensitivity in semiconducting polymer x-ray detectors," *Nanotechnology*, vol. 23, no. 23, p. 235502, Jun. 2012.

[142] C. A. Mills *et al.*, "Enhanced x-ray detection sensitivity in semiconducting polymer diodes containing metallic nanoparticles," *J. Phys. D. Appl. Phys.*, vol. 46, no. 27, p. 275102, Jul. 2013.

[143] A. Ciavatti *et al.*, "Dynamics of direct X-ray detection processes in high-Z Bi2O3

nanoparticles-loaded PFO polymer-based diodes," *Appl. Phys. Lett.*, vol. 111, no. 18, p. 183301, Oct. 2017.

[144] G. N. Ankah *et al.*, "PbS quantum dot based hybrid-organic photodetectors for X-ray sensing," *Org. Electron.*, vol. 33, pp. 201–206, Jun. 2016.

[145] H. M. Thirimanne *et al.*, "High sensitivity organic inorganic hybrid X-ray detectors with direct transduction and broadband response," *Nat. Commun.*, 2018.

[146] P. Büchele *et al.*, "X-ray imaging with scintillator-sensitized hybrid organic photodetectors," *Nat. Photonics*, vol. 9, no. 12, pp. 843–848, Nov. 2015.

[147] A. Intaniwet, J. L. Keddie, M. Shkunov, and P. J. Sellin, "High charge-carrier mobilities in blends of poly(triarylamine) and TIPS-pentacene leading to better performing X-ray sensors," *Org. Electron.*, vol. 12, no. 11, pp. 1903–1908, Nov. 2011.

[148] H. Han *et al.*, "Enhancement of X-ray detection by single-walled carbon nanotube enriched flexible polymer composite," *Nanoscale Res. Lett.*, vol. 9, no. 1, pp. 1–7, Dec. 2014.

[149] A. M. Zeidell *et al.*, "Organic Field-Effect Transistors as Flexible, Tissue-Equivalent Radiation Dosimeters in Medical Applications," *Adv. Sci.*, vol. 7, no. 18, p. 2001522, Sep. 2020.

[150] J. A. Posar *et al.*, "Characterization of a plastic dosimeter based on organic semiconductor photodiodes and scintillator," *Phys. Imaging Radiat. Oncol.*, vol. 14, no. February, pp. 48–52, 2020.

[151] L. Basiricò *et al.*, "Medical Applications of Tissue-Equivalent, Organic-Based Flexible Direct X-Ray Detectors," *Front. Phys.*, vol. 8, no. February, pp. 1–11, 2020.

[152] L. Basiricò, A. Ciavatti, and B. Fraboni, "Solution-Grown Organic and Perovskite X-Ray Detectors: A New Paradigm for the Direct Detection of Ionizing Radiation," *Adv. Mater. Technol.*, p. 2000475, Aug. 2020.

[153] L. Basiricò, A. Ciavatti, T. Cramer, P. Cosseddu, A. Bonfiglio, and B. Fraboni, "Direct X-ray photoconversion in flexible organic thin film devices operated below 1 V," *Nat. Commun.*, vol. 7, no. 1, p. 13063, Dec. 2016.

[154] S. Lai, P. Cosseddu, L. Basiricò, A. Ciavatti, B. Fraboni, and A. Bonfiglio, "A Highly Sensitive, Direct X-Ray Detector Based on a Low-Voltage Organic Field-Effect Transistor," *Adv. Electron. Mater.*, vol. 3, no. 8, p. 1600409, Aug. 2017.

[155] R. A. Price, C. Benson, M. J. Joyce, and K. Rodgers, "Development of a RadFET Linear Array for Intracavitary in vivo Dosimetry During External Beam Radiotherapy and Brachytherapy," *IEEE Trans. Nucl. Sci.*, vol. 51, no. 4, 2004.

[156] A. B. Rozenfeld, G. Biasi, M. Petasecca, M. L. F. Lerch, G. Villani, and V. Feygelman, "Semiconductor dosimetry in modern external-beam radiation therapy," *Phys. Med. Biol.*, Jun. 2020.

[157] G.-W. Luo, Z.-Y. Qi, X.-W. Deng, and A. Rosenfeld, "Investigation of a pulsed current

annealing method in reusing MOSFET dosimeters for *in vivo* IMRT dosimetry," *Med. Phys.*, vol. 41, no. 5, p. 051710, Apr. 2014.

[158] S. Alshaikh, M. Carolan, M. Petasecca, M. Lerch, P. Metcalfe, and A. Rosenfeld, "Direct and pulsed current annealing of p-MOSFET based dosimeter: The 'MOSkin,'" *Australas. Phys. Eng. Sci. Med.*, vol. 37, no. 2, pp. 311–319, 2014.

[159] F. Fuschino *et al.*, "A wireless transmission low-power radiation sensor for in vivo dosimetry," *J. Instrum.*, vol. 9, no. 2, p. C02016, Feb. 2014.

[160] M. Arsalan, A. Shamim, M. Shams, N. G. Tarr, and L. Roy, "Ultra low power CMOS-based sensor for on-body radiation dose measurements," *IEEE J. Emerg. Sel. Top. Circuits Syst.*, vol. 2, no. 1, pp. 34–41, Mar. 2012.

[161] M. Brucoli *et al.*, "Investigation on Passive and Autonomous Mode Operation of Floating Gate Dosimeters," *IEEE Trans. Nucl. Sci.*, vol. 66, no. 7, pp. 1620–1627, Jul. 2019.

[162] A. G. Holmes-Siedle, J. O. Goldsten, R. H. Maurer, and P. N. Peplowski, "RADFET dosimeters in the belt: The Van Allen Probes on day 365," in *Proceedings of the European Conference on Radiation and its Effects on Components and Systems, RADECS*, 2013.

[163] S. Giordanengo, L. Manganaro, and A. Vignati, "Review of technologies and procedures of clinical dosimetry for scanned ion beam radiotherapy," 2017.

[164] M. Carrara *et al.*, "Semiconductor real-time quality assurance dosimetry in brachytherapy," *Brachytherapy*, vol. 17, no. 1. Elsevier Inc., pp. 133–145, 01-Jan-2018.

[165] P. Metcalfe *et al.*, "Review of four novel dosimeters developed for use in radiotherapy," *J. Phys. Conf. Ser.*, vol. 444, no. 1, 2013.

[166] I. S. Kwan *et al.*, "Skin dosimetry with new MOSFET detectors," *Radiat. Meas.*, vol. 43, no. 2–6, pp. 929–932, Feb. 2008.

[167] K. Legge *et al.*, "Real-time in vivo rectal wall dosimetry using MOSkin detectors during linac based stereotactic radiotherapy with rectal displacement."

[168] M. Carrara *et al.*, "Clinical application of MOSkin dosimeters to rectal wall in vivo dosimetry in gynecological HDR brachytherapy," *Phys. Medica*, vol. 41, pp. 5–12, Sep. 2017.

[169] A. A. Romanyukha *et al.*, "Applications of MOSkin dosimeters for quality assurance in gynecological HDR brachytherapy: An in-phantom feasibility study," *Radiat. Meas.*, vol. 106, pp. 399–404, Nov. 2017.

[170] S. M. Pejović, M. M. Pejović, and M. Živanović, "Small dose effect in RADFET with thick gate oxide," *Appl. Radiat. Isot.*, vol. 152, pp. 72–77, Oct. 2019.

[171] M. Durante and J. S. Loeffler, "Charged particles in radiation oncology," *Nature Reviews Clinical Oncology*, vol. 7, no. 1. Nature Publishing Group, pp. 37–43, 01-Jan-2010.

[172] S. Giordanengo, L. Manganaro, and A. Vignati, "Review of technologies and procedures of

clinical dosimetry for scanned ion beam radiotherapy," *Phys. Medica*, vol. 43, no. October, pp. 79–99, 2017.

[173] R. P. Johnson, "Review of medical radiography and tomography with proton beams," *Reports on Progress in Physics*, vol. 81, no. 1. Institute of Physics Publishing, p. 016701, 01-Jan-2018.

[174] S. Braccini *et al.*, "Segmented ionization chambers for beam monitoring in hadrontherapy," *Mod. Phys. Lett. A*, vol. 30, no. 17, Jun. 2015.

[175] M. T. Gillin *et al.*, "Commissioning of the discrete spot scanning proton beam delivery system at the University of Texas M.D. Anderson Cancer Center, Proton Therapy Center, Houston," *Med. Phys.*, vol. 37, no. 1, pp. 154–163, 2010.

[176] A. Mirandola *et al.*, "Dosimetric commissioning and quality assurance of scanned ion beams at the Italian National Center for Oncological Hadrontherapy," *Med. Phys.*, vol. 42, no. 9, pp. 5287–5300, Sep. 2015.

[177] B. Arjomandy, N. Sahoo, X. Ding, and M. Gillin, "Use of a two-dimensional ionization chamber array for proton therapy beam quality assurance," *Med. Phys.*, vol. 35, no. 9, pp. 3889–3894, Aug. 2008.

[178] S. Dhanesar *et al.*, "Quality assurance of proton beams using a multilayer ionization chamber system," *Med. Phys.*, vol. 40, no. 9, p. 092102, Aug. 2013.

[179] Y. Hara, T. Furukawa, K. Mizushima, E. Takeshita, T. Shirai, and K. Noda, "Application of radiochromic film for quality assurance in the heavy-ion beam scanning irradiation system at HIMAC," *Nucl. Instruments Methods Phys. Res. Sect. B Beam Interact. with Mater. Atoms*, vol. 331, pp. 253–256, Jul. 2014.

[180] S. Russo *et al.*, "Characterization of a commercial scintillation detector for 2-D dosimetry in scanned proton and carbon ion beams," *Phys. Medica*, vol. 34, pp. 48–54, Feb. 2017.

[181] K. Legge *et al.*, "Real-time in vivo rectal wall dosimetry using MOSkin detectors during linac based stereotactic radiotherapy with rectal displacement," *Radiat. Oncol.*, vol. 12, no. 1, p. 41, Feb. 2017.

[182] Y. Akino, A. Gautam, L. Coutinho, J. Würfel, and I. J. Das, "Characterization of a new commercial single crystal diamond detector for photon-and proton-beam dosimetry," in *Journal of Radiation Research*, 2015, vol. 56, no. 6, pp. 912–918.

[183] J. L. Cantley *et al.*, "Real-time *in vivo* dosimetry for SBRT prostate treatment using plastic scintillating dosimetry embedded in a rectal balloon: a case study," *J. Appl. Clin. Med. Phys.*, vol. 17, no. 6, pp. 305–311, Nov. 2016.

[184] L. Lin *et al.*, "Use of a novel two-dimensional ionization chamber array for pencil beam scanning proton therapy beam quality assurance," *J. Appl. Clin. Med. Phys.*, vol. 16, no. 3, pp. 270–276, May 2015.

[185] P. Cosseddu, S. Lai, M. Barbaro, and A. Bonfiglio, "Ultra-low voltage, organic thin film transistors fabricated on plastic substrates by a highly reproducible process," *Appl. Phys.*

Lett., vol. 100, no. 9, pp. 1–6, 2012.

[186] J. E. Anthony, "The larger acenes: Versatile organic semiconductors," *Angewandte Chemie - International Edition*, vol. 47, no. 3. John Wiley & Sons, Ltd, pp. 452–483, 04-Jan-2008.

[187] J. E. Anthony, "The larger acenes: Versatile organic semiconductors," *Angewandte Chemie - International Edition*, vol. 47, no. 3. John Wiley & Sons, Ltd, pp. 452–483, 04-Jan-2008.

[188] J. E. Anthony, "Functionalized acenes and heteroacenes for organic electronics," *Chemical Reviews*, vol. 106, no. 12. American Chemical Society , pp. 5028–5048, Dec-2006.

[189] J. E. Anthony, D. L. Eaton, and S. R. Parkin, "A Road Map to Stable, Soluble, Easily Crystallized Pentacene Derivatives," *Org. Lett.*, vol. 4, no. 1, pp. 15–18, 2002.

[190] A. J. Petty *et al.*, "Computationally aided design of a high-performance organic semiconductor: The development of a universal crystal engineering core," *Chem. Sci.*, vol. 10, no. 45, pp. 10543–10549, Nov. 2019.

[191] J. E. Anthony, J. S. Brooks, D. L. Eaton, and S. R. Parkin, "Functionalized Pentacene: Improved Electronic Properties from Control of Solid-State Order," *J. Am. Chem. Soc*, vol. 123, no. 9, p. 45, 2001.

[192] S. Wang, X. Zhao, Y. Tong, Q. Tang, and Y. Liu, "Directly Spin Coating a Low-Viscosity Organic Semiconductor Solution onto Hydrophobic Surfaces: Toward High-Performance Solution-Processable Organic Transistors," *Adv. Mater. Interfaces*, vol. 7, no. 8, p. 1901950, Apr. 2020.

[193] Y. Diao *et al.*, "Solution coating of large-area organic semiconductor thin films with aligned single-crystalline domains," *Nat. Mater.*, vol. 12, no. 7, pp. 665–671, 2013.

[194] J. A. Lim, H. S. Lee, W. H. Lee, and K. Cho, "Control of the morphology and structural development of solution-processed functionalized acenes for high-performance organic transistors," *Adv. Funct. Mater.*, vol. 19, no. 10, pp. 1515–1525, 2009.

[195] J. Chen, D. C. Martin, and J. E. Anthony, "Morphology and molecular orientation of thin-film bis(triisopropylsilylethynyl) pentacene," *J. Mater. Res.*, vol. 22, no. 6, 2007.

[196] C. P. L. Rubinger, H. F. Haneef, C. Hewitt, D. Carroll, J. E. Anthony, and O. D. Jurchescu, "Influence of solvent additives on the morphology and electrical properties of diF-TES ADT organic field-effect transistors," *Org. Electron.*, vol. 68, no. December 2018, pp. 205–211, 2019.

[197] S. Subramanian, K. P. Sung, S. R. Parkin, V. Podzorov, T. N. Jackson, and J. E. Anthony, "Chromophore fluorination enhances crystallization and stability of soluble anthradithiophene semiconductors," *J. Am. Chem. Soc.*, vol. 130, no. 9, pp. 2706–2707, Mar. 2008.

[198] K. Paudel, G. Giesbers, J. Van Schenck, J. E. Anthony, and O. Ostroverkhova, "Molecular packing-dependent photoconductivity in functionalized anthradithiophene crystals," *Org. Electron.*, vol. 67, pp. 311–319, Apr. 2019.

[199] J. C. Sorli *et al.*, "Impact of Atomistic Substitution on Thin-Film Structure and Charge Transport in a Germanyl-ethynyl Functionalized Pentacene," *Chem. Mater.*, vol. 31, no. 17, pp. 6615–6623, 2019.

[200] C.-H. Kim *et al.*, "Strongly Correlated Alignment of Fluorinated 5,11-Bis(triethylgermylethynyl)anthradithiophene Crystallites in Solution-Processed Field-Effect Transistors," *ChemPhysChem*, vol. 15, no. 14, pp. 2913–2916, Oct. 2014.

[201] S. Riera-Galindo, F. Leonardi, R. Pfattner, and M. Mas-Torrent, "Organic Semiconductor/Polymer Blend Films for Organic Field-Effect Transistors," *Adv. Mater. Technol.*, vol. 4, no. 9, pp. 1–20, 2019.

[202] C. Teixeira da Rocha, K. Haase, Y. Zheng, M. Löffler, M. Hambsch, and S. C. B. Mannsfeld, "Solution Coating of Small Molecule/Polymer Blends Enabling Ultralow Voltage and High-Mobility Organic Transistors," *Adv. Electron. Mater.*, vol. 4, no. 8, pp. 1–9, 2018.

[203] A. Kiazadeh *et al.*, "Improving positive and negative bias illumination stress stability in parylene passivated IGZO transistors," *Appl. Phys. Lett.*, vol. 109, no. 5, 2016.

[204] P. Barquinha, R. Martins, L. Pereira, and E. Fortunato, *Transparent Oxide Electronics*. John Wiley & Sons, Ltd, 2012.

[205] Bhushan Bharat, *Encyclopedia of Nanotechnology*, vol. 53, no. 9. Springer, 2012.

[206] C. H. Kim *et al.*, "Decoupling the Effects of Self-Assembled Monolayers on Gold, Silver, and Copper Organic Transistor Contacts," *Adv. Mater. Interfaces*, vol. 2, no. 2, pp. 1–9, 2015.

[207] P. S. Corporation, "Park NX-10 AFM user's manual." 2013.

[208] T. Sueyoshi, H. Fukagawa, M. Ono, S. Kera, and N. Ueno, "Low-density band-gap states in pentacene thin films probed with ultrahigh-sensitivity ultraviolet photoelectron spectroscopy," *Appl. Phys. Lett.*, vol. 95, no. 18, pp. 3–6, 2009.

[209] K. Lee *et al.*, "Interfacial trap density-of-states in pentacene- and ZnO-based thin-film transistors measured via novel photo-excited charge-collection spectroscopy," *Adv. Mater.*, vol. 22, no. 30, pp. 3260–3265, 2010.

[210] Z. Jia, L. Banu, and I. Kymissis, "Photocurrent study of oxygen-mediated doping states in pentacene thin-film transistors," *IEEE Trans. Electron Devices*, vol. 57, no. 2, pp. 380–384, 2010.

[211] A. Masurkar and I. Kymissis, "Photocurrent measurements of pentacene-based devices," *Applied Physics Reviews*, vol. 2, no. 3. American Institute of Physics Inc., p. 031101, 01-Sep-2015.

[212] Richard H. Bube, *Photoconductivity of Solids*. John Wiley & Sons, Inc., 1960.

[213] J. F. Ziegler, M. D. Ziegler, and J. P. Biersack, "SRIM - The stopping and range of ions in matter (2010)," *Nucl. Instruments Methods Phys. Res. Sect. B Beam Interact. with Mater.*

Atoms, vol. 268, no. 11–12, pp. 1818–1823, Jun. 2010.

[214] M. Chiari, A. Migliori, and P. A. Mandoò, "Measurement of low currents in an external beam set-up," *Nucl. Instruments Methods Phys. Res. Sect. B Beam Interact. with Mater. Atoms*, vol. 188, no. 1–4, pp. 162–165, 2002.

[215] F. Tommasino *et al.*, "Proton beam characterization in the experimental room of the Trento Proton Therapy facility," *Nucl. Instruments Methods Phys. Res. Sect. A Accel. Spectrometers, Detect. Assoc. Equip.*, vol. 869, pp. 15–20, Oct. 2017.

[216] I. Temiño *et al.*, "Morphology and mobility as tools to control and unprecedentedly enhance X-ray sensitivity in organic thin-films," *Nat. Commun.*, vol. 11, no. 1, pp. 1–10, 2020.

[217] G. Giri *et al.*, "Tuning charge transport in solution-sheared organic semiconductors using lattice strain," *Nature*, vol. 480, no. 7378, pp. 504–508, 2011.

[218] S. Riera-Galindo, A. Tamayo, and M. Mas-Torrent, "Role of Polymorphism and Thin-Film Morphology in Organic Semiconductors Processed by Solution Shearing," *ACS Omega*, vol. 3, no. 2, pp. 2329–2339, 2018.

[219] A. Tamayo, S. Riera-Galindo, A. O. F. Jones, R. Resel, and M. Mas-Torrent, "Impact of the Ink Formulation and Coating Speed on the Polymorphism and Morphology of a Solution-Sheared Thin Film of a Blended Organic Semiconductor," *Adv. Mater. Interfaces*, vol. 6, no. 22, p. 1900950, Nov. 2019.

[220] K. D. G. I. Jayawardena *et al.*, "Millimeter-Scale Unipolar Transport in High Sensitivity OrganicInorganic Semiconductor X-ray Detectors," *ACS Nano*, vol. 13, no. 6, pp. 6973–6981, 2019.

[221] M. P. A. Nanayakkara *et al.*, "Ultra-Low Dark Current Organic–Inorganic Hybrid X-Ray Detectors," *Adv. Funct. Mater.*, p. 2008482, Nov. 2020.

[222] D. Goghero, A. Goullet, and J. P. Landesman, "Structural and electrical properties of SiO2 films deposited on Si substrates from tetraethoxysilane/oxygen plasmas," *Solid. State. Electron.*, vol. 49, no. 3, pp. 369–376, 2005.

[223] C. Wöll, *Physical and Chemical Aspects of Organic Electronics*. 2009.

[224] Z. Jia, L. Banu, and I. Kymissis, "Photocurrent study of oxygen-mediated doping states in pentacene thin-film transistors," *IEEE Trans. Electron Devices*, vol. 57, no. 2, pp. 380–384, Feb. 2010.

[225] A. Ciavatti *et al.*, "Boosting Direct X-Ray Detection in Organic Thin Films by Small Molecules Tailoring," *Adv. Funct. Mater.*, p. 1806119, Dec. 2018.

[226] R. J. Davis *et al.*, "Determination of energy level alignment at interfaces of hybrid and organic solar cells under ambient environment," *J. Mater. Chem.*, vol. 21, no. 6, pp. 1721–1729, Feb. 2011.

[227] L. Basiricò *et al.*, "Space Environment Effects on Flexible, Low-Voltage Organic Thin-Film

Transistors," *ACS Appl. Mater. Interfaces*, vol. 9, no. 40, pp. 35150–35158, Oct. 2017.

[228] J. Tauc, R. Grigorovici, and A. Vancu, "Optical Properties and Electronic Structure of Amorphous Germanium," *Phys. status solidi*, vol. 15, no. 2, pp. 627–637, Jan. 1966.

[229] S. Lai, P. Cosseddu, L. Basiricò, A. Ciavatti, B. Fraboni, and A. Bonfiglio, "A Highly Sensitive, Direct X-Ray Detector Based on a Low-Voltage Organic Field-Effect Transistor," *Adv. Electron. Mater.*, vol. 3, no. 8, p. 1600409, Aug. 2017.

[230] T. Cramer *et al.*, "Direct imaging of defect formation in strained organic flexible electronics by Scanning Kelvin Probe Microscopy," *Sci. Rep.*, vol. 6, no. 1, pp. 1–9, Dec. 2016.

[231] D. R. Shearer and M. Bopaiah, "Dose rate limitations of integrating survey meters for diagnostic x-ray surveys," *Health Phys.*, vol. 79, no. 2 SUPPL., 2000.

[232] R. Hamilton *et al.*, "High-performance polymer-small molecule blend organic transistors," *Adv. Mater.*, vol. 21, no. 10–11, pp. 1166–1171, Mar. 2009.

[233] A. Pérez-Rodríguez, I. Temiño, C. Ocal, M. Mas-Torrent, and E. Barrena, "Decoding the Vertical Phase Separation and Its Impact on C8-BTBT/PS Transistor Properties," *ACS Appl. Mater. Interfaces*, vol. 10, no. 8, pp. 7296–7303, Feb. 2018.

[234] K. Zhao *et al.*, "Vertical Phase Separation in Small Molecule:Polymer Blend Organic Thin Film Transistors Can Be Dynamically Controlled," *Adv. Funct. Mater.*, vol. 26, no. 11, pp. 1737–1746, Mar. 2016.

[235] Y. C. Kim *et al.*, "Printable organometallic perovskite enables large-area, low-dose X-ray imaging," *Nature*, vol. 550, no. 7674, pp. 87–91, 2017.

[236] S. H. Kim, W. M. Yoon, M. Jang, H. Yang, J. J. Park, and C. E. Park, "Damage-free hybrid encapsulation of organic field-effect transistors to reduce environmental instability," *J. Mater. Chem.*, vol. 22, no. 16, pp. 7731–7738, Apr. 2012.

[237] F. De Angelis, S. Cipolloni, L. Mariucci, and G. Fortunato, "Aging effects in pentacene thin-film transistors: Analysis of the density of states modification," *Appl. Phys. Lett.*, vol. 88, no. 19, p. 193508, May 2006.

[238] S. Yang, S. Park, J. Bintinger, Y. Bonnassieux, J. Anthony, and I. Kymissis, "Employing Pneumatic Nozzle Printing for Controlling the Crystal Growth of Small Molecule Organic Semiconductor for Field-Effect Transistors," *Adv. Electron. Mater.*, vol. 4, no. 6, pp. 4–9, 2018.

[239] M. Saito, F. Nishiyama, K. Kobayashi, S. Nagata, and K. Takahiro, "Reduction of light elements loss in polymer foils during MeV-proton irradiation by application of an aluminum coating," *Nucl. Instruments Methods Phys. Res. Sect. B Beam Interact. with Mater. Atoms*, vol. 268, no. 19, pp. 2918–2922, 2010.

[240] R. Mishra *et al.*, "Optical and electrical properties of some electron and proton irradiated polymers," *Nucl. Instruments Methods Phys. Res. Sect. B Beam Interact. with Mater. Atoms*, vol. 168, no. 1, pp. 59–64, 2000.

[241] J. Čermák *et al.*, "Proton irradiation induced changes in glass and polyethylene terephthalate substrates for photovoltaic solar cells," *Sol. Energy Mater. Sol. Cells*, vol. 186, no. June, pp. 284–290, 2018.

[242] E. H. Lee, "Ion-beam modification of polymeric materials - fundamental principles and applications," *Nucl. Instruments Methods Phys. Res. Sect. B Beam Interact. with Mater. Atoms*, vol. 151, no. 1–4, pp. 29–41, 1999.

[243] N. L. Singh, N. Shah, C. F. Desai, K. P. Singh, and S. K. Arora, "Modification of polyethylene terephthalate by proton irradiation," *Radiat. Eff. Defects Solids*, vol. 159, no. 8–9, pp. 475–482, 2004.

[244] A. Holmes-Siedle and L. Adams, "RADFET: A review of the use of metal-oxide-silicon devices as integrating dosimeters," *Int. J. Radiat. Appl. Instrumentation. Part C. Radiat. Phys. Chem.*, vol. 28, no. 2, pp. 235–244, Jan. 1986.

[245] T. Cramer *et al.*, "Passive radiofrequency x-ray dosimeter tag based on flexible radiation-sensitive oxide field-effect transistor," *Sci. Adv.*, vol. 4, no. 6, p. eaat1825, 2018.

[246] C. Chaneliere, J. L. Autran, R. A. B. Devine, and B. Balland, "Tantalum pentoxide (Ta2O5) thin films for advanced dielectric applications," *Materials Science and Engineering R: Reports*, vol. 22, no. 6. Elsevier BV, pp. 269–322, 25-May-1998.

[247] T. Cramer *et al.*, "Radiation-Tolerant Flexible Large-Area Electronics Based on Oxide Semiconductors," *Adv. Electron. Mater.*, vol. 2, no. 7, pp. 1–8, 2016.

[248] B. Sturman, E. Podivilov, and M. Gorkunov, "Origin of stretched exponential relaxation for hopping-transport models," *Phys. Rev. Lett.*, vol. 91, no. 17, p. 176602, Oct. 2003.

[249] J. Luo, A. U. Adler, T. O. Mason, D. Bruce Buchholz, R. P. H. Chang, and M. Grayson, "Transient photoresponse in amorphous In-Ga-Zn-O thin films under stretched exponential analysis," *J. Appl. Phys.*, vol. 113, no. 15, 2013.

[250] J. Lipovetzky, E. G. Redin, and A. Faigón, "Electrically erasable metal-oxide-semiconductor dosimeters," in *IEEE Transactions on Nuclear Science*, 2007, vol. 54, no. 4, pp. 1244–1250.

[251] J. Liu, D. B. Buchholz, J. W. Hennek, R. P. H. Chang, A. Facchetti, and T. J. Marks, "All-amorphous-oxide transparent, flexible thin-film transistors. Efficacy of bilayer gate dielectrics," *J. Am. Chem. Soc.*, vol. 132, no. 34, pp. 11934–11942, Sep. 2010.

Acknowledgements

First of all, I would like to thank my supervisor Prof. Beatrice Fraboni for giving me the possibility to start the PhD program and to be introduced in the world of scientific research. Thank you for all the support, teachings, and advices you offered me in these long, exciting and hard years. Without your experience, your leadership and your passion for science this thesis would have not be possible!

A special thanks to Dr. Laura Basiricò and Dr. Andrea Ciavatti. Thank you very much for your personal support and for your concrete scientific contributions. Thank you for introducing me in the world of radiation detection and for teaching me how to become a scientist. You taught me a lot and your patience and your advices made these years better!

I would like to thank Prof. Tobias Cramer for his fundamental contribution in the research on ROXFET and for his precious teachings and discussions.

A special thanks to Professor Ioannis Kymissis who offered me the possibility to spend an incredible semester at the Columbia University in NYC. Thank you for all your teachings on organic electronics and for your numerous ideas. I would also like to specially thank all the CLUE lab team: Caroline, Keith, Jose, Stelios, Chrissy, Vikrant, Kevin, Zicong, Zach: thank you for hosting me in your research group and for letting me feel at home even so far from my place.

I would like to acknowledge Dr. Marta Mas Torrent, Dr. Inés Temiño and Adrian Tamayo for our fruitful collaboration on the study of organic semiconductor-based radiation detectors. A special thanks to Inés for the great time spent together here in Bologna with Maria.

I would like also to thank Prof. John Anthony from the University of Kentucky for providing the new synthetized organic small molecules employed in this thesis,

I would like to thank Prof. Pedro Barquinha, Prof. Rodrigo Martins and Prof. Elvira Fortunato for the realization of the AOS-based TFTs employed for the realization of the ROXFETs.

I would also like to thank Dr. Massimo Chiari from the LABEC (INFN FI, Italy) and the TIFPA Center (TN, Italy) for offering me the possibility to perform the proton irradiation experiments.

I would like to acknowledge the *Fondazione Bruno Kessler* (TN, Italy) for providing the Si/SiO_2 wafers employed in this thesis, *TAGSYS RFID* for providing the CMOS RFID TAG implemented for the realization of the read-out system of the ROXFET, and *CEI - Skanray Europe Srl.* for offering me the possibility to perform some irradiation experiments in actual clinical environments.

I would like to thank Prof. Annalisa Bonfiglio, Prof. Piero Cosseddu and Prof. Stefano Lai from the University of Cagliari for the fabrication of the ultra low-voltage OFETs employed in this thesis as ionizing radiation detectors.

I would also like to thank Prof. Alberto Quaranta and Dr. Enrico Zanazzi for the SRIM simulations employed to interpret the results obtained by the proton irradiation experiments.

I would like to thank all the master students who worked on this project during these years: Giorgio Pacioni, Francesco Maccaferri, Francesco Mariotti and Maria Pereira.

A particular thanks to all my colleagues at the Department of Physics and Astronomy (UNIBO) Maria Antonietta, Francesco, Nicola, Alberto, Luca, Matteo, Giovanni, Luca, Filippo, Pier, Marta, Ferdinand, Leo, Laura, Vito, Tommaso!

Finally, I would like to acknowledge the INFN CSN5 FIRE project and the Marco Polo funding for the financial supports.